Investigations on the efficiency of truck axles and their hypoid gear set : A thermo-mechanical model

Charlotte Fossier

N°d'ordre NNT : 2018LYSEI019

THESE de DOCTORAT DE L'UNIVERSITE DE LYON
opérée au sein de
INSA-LYON

Ecole Doctorale N° ED162
MEGA
(MECANIQUE, ENERGETIQUE, GENIE CIVIL, ACOUSTIQUE)

Spécialité de doctorat : Génie Mécanique

Soutenue publiquement le 14/03/2018, par :
Charlotte FOSSIER

Investigations on the efficiency of truck axles and their hypoid gear set: A thermo-mechanical model

---

Devant le jury composé de :

Seabra, Jorge	Professeur	FEUP	Président Rapporteur
Berier, Vincent	Ingénieur	VOLVO GROUP – RT	Examinateur
Changenet, Christophe	Docteur HDR	ECAM LYON	Directeur de thèse
Dini, Daniele	Professeur	IMPERIAL COLLEGE LONDON	Examinateur
Fabre, Agnès	Docteur HDR	ENSAM	Rapporteure
Ville, Fabrice	Professeur	INSA-LYON	Directeur de thèse

Département FEDORA – INSA Lyon - Ecoles Doctorales – Quinquennal 2016-2020

SIGLE	ÉCOLE DOCTORALE	NOM ET COORDONNEES DU RESPONSABLE
CHIMIE	**CHIMIE DE LYON** **http://www.edchimie-lyon.fr** Sec. : Renée EL MELHEM Bât. Blaise PASCAL, 3e étage **secretariat@edchimie-lyon.fr** INSA : R. GOURDON	M. Stéphane DANIELE Institut de recherches sur la catalyse et l'environnement de Lyon IRCELYON-UMR 5256 Équipe CDFA 2 Avenue Albert EINSTEIN 69 626 Villeurbanne CEDEX **directeur@edchimie-lyon.fr**
E.E.A.	**ÉLECTRONIQUE, ÉLECTROTECHNIQUE, AUTOMATIQUE** **http://edeea.ec-lyon.fr** Sec. : M.C. HAVGOUDOUKIAN **ecole-doctorale.eea@ec-lyon.fr**	M. Gérard SCORLETTI École Centrale de Lyon 36 Avenue Guy DE COLLONGUE 69 134 Écully Tél : 04.72.18.60.97 Fax 04.78.43.37.17 **gerard.scorletti@ec-lyon.fr**
E2M2	**ÉVOLUTION, ÉCOSYSTÈME, MICROBIOLOGIE, MODÉLISATION** **http://e2m2.universite-lyon.fr** Sec. : Sylvie ROBERJOT Bât. Atrium, UCB Lyon 1 Tél : 04.72.44.83.62 INSA : H. CHARLES **secretariat.e2m2@univ-lyon1.fr**	M. Fabrice CORDEY CNRS UMR 5276 Lab. de géologie de Lyon Université Claude Bernard Lyon 1 Bât. Géode 2 Rue Raphaël DUBOIS 69 622 Villeurbanne CEDEX Tél : 06.07.53.89.13 **cordey@univ-lyon1.fr**
EDISS	**INTERDISCIPLINAIRE SCIENCES-SANTÉ** **http://www.ediss-lyon.fr** Sec. : Sylvie ROBERJOT Bât. Atrium, UCB Lyon 1 Tél : 04.72.44.83.62 INSA : M. LAGARDE **secretariat.ediss@univ-lyon1.fr**	Mme Emmanuelle CANET-SOULAS INSERM U1060, CarMeN lab, Univ. Lyon 1 Bâtiment IMBL 11 Avenue Jean CAPELLE INSA de Lyon 69 621 Villeurbanne Tél : 04.72.68.49.09 Fax : 04.72.68.49.16 **emmanuelle.canet@univ-lyon1.fr**
INFOMATHS	**INFORMATIQUE ET MATHÉMATIQUES** **http://edinfomaths.universite-lyon.fr** Sec. : Renée EL MELHEM Bât. Blaise PASCAL, 3e étage Tél : 04.72.43.80.46 Fax : 04.72.43.16.87 **infomaths@univ-lyon1.fr**	M. Luca ZAMBONI Bât. Braconnier 43 Boulevard du 11 novembre 1918 69 622 Villeurbanne CEDEX Tél : 04.26.23.45.52 **zamboni@maths.univ-lyon1.fr**
Matériaux	**MATÉRIAUX DE LYON** **http://ed34.universite-lyon.fr** Sec. : Marion COMBE Tél : 04.72.43.71.70 Fax : 04.72.43.87.12 Bât. Direction **ed.materiaux@insa-lyon.fr**	M. Jean-Yves BUFFIÈRE INSA de Lyon MATEIS - Bât. Saint-Exupéry 7 Avenue Jean CAPELLE 69 621 Villeurbanne CEDEX Tél : 04.72.43.71.70 Fax : 04.72.43.85.28 **jean-yves.buffiere@insa-lyon.fr**
MEGA	**MÉCANIQUE, ÉNERGÉTIQUE, GÉNIE CIVIL, ACOUSTIQUE** **http://edmega.universite-lyon.fr** Sec. : Marion COMBE Tél : 04.72.43.71.70 Fax : 04.72.43.87.12 Bât. Direction **mega@insa-lyon.fr**	M. Philippe BOISSE INSA de Lyon Laboratoire LAMCOS Bâtiment Jacquard 25 bis Avenue Jean CAPELLE 69 621 Villeurbanne CEDEX Tél : 04.72.43.71.70 Fax : 04.72.43.72.37 **philippe.boisse@insa-lyon.fr**
ScSo	**ScSo*** **http://ed483.univ-lyon2.fr** Sec. : Viviane POLSINELLI Brigitte DUBOIS INSA : J.Y. TOUSSAINT Tél : 04.78.69.72.76 **viviane.polsinelli@univ-lyon2.fr**	M. Christian MONTES Université Lyon 2 86 Rue Pasteur 69 365 Lyon CEDEX 07 **christian.montes@univ-lyon2.fr**

*ScSo : Histoire, Géographie, Aménagement, Urbanisme, Archéologie, Science politique, Sociologie, Anthropologie

Foreword / Avant-propos

This PhD thesis work is the result of a collaboration between the Contacts and Structures Mechanics Laboratory (LaMCoS) of INSA Lyon, the Energy and Materials Laboratory of ECAM Lyon (LabECAM), and the Renault Trucks company of the Volvo Group.

It is a CIFRE convention of the National Association of Research and Technology (ANRT) and is registered under the number 2014/0508.

Ces travaux de thèse sont le résultat d'une collaboration entre le laboratoire de Mécanique des Contacts et des Structures (LaMCoS) de l'INSA Lyon, le laboratoire d'Énergétique et des Matériaux de l'ECAM de Lyon (LabECAM), et la société Renault Trucks du Groupe Volvo.

Il s'agit d'une Convention Industrielle de Formation par la Recherche (CIFRE) mise en œuvre par l'Agence National pour la Recherche et la Technologie (ANRT). Elle est enregistrée sous le n°2014/0508.

Remerciements

Je souhaiterais remercier toutes les personnes qui ont contribué, de près ou de loin, à la réussite de ces travaux de thèse :

Mes directeurs de thèse, Fabrice VILLE et Christophe CHANGENET, pour m'avoir confié ce projet et m'avoir épaulé avec bienveillance et humour tout au long de la thèse.

Les membres du jury, Daniele DINI, Agnès FABRE et Jorge SEABRA, pour avoir accepté cette charge.

Mes encadrants industriels, Vincent BERIER et Denis BARDAY, pour m'avoir permis d'intégrer l'équipe Driveline et de découvrir le Groupe Volvo.

Toute l'équipe Driveline, et plus largement les personnes rencontrées au sein du Groupe Volvo, pour la belle expérience en entreprise et la bonne ambiance. Grâce à vous, j'ai beaucoup découvert : les ponts, évidemment ; les cellules d'essais moteur, la fonderie de Vénissieux, l'usine moteur, les pistes d'essais… ; mais aussi le laboratoire de matériaux, les différences culturelles au sein du groupe…

Tout le LaMCoS de l'INSA Lyon pour la découverte du travail en laboratoire, avec ses séminaires et ses moyens d'essais. Je remercie plus particulièrement Sophie De OLIVEIRA pour le soutien administratif et Jérôme CAVORET pour l'aide technique.

Le Pôle Energétique de l'ECAM Lyon, et plus largement le personnel ECAM, pour les bons moments professionnels mais aussi de convivialité passés sur la colline de Fourvière.

Tous les doctorants, d'ici ou d'ailleurs, pour avoir partagé les mêmes combats et surtout la bonne humeur, pour les beaux souvenirs qui resteront et ceux encore à venir.

Enfin, mes amis, ma famille et surtout mon compagnon pour m'avoir supportée pendant ces trois années de dur labeur.

Abstract

To fulfil customer demands, but also government regulations, the truck industry must decrease the fuel consumption and emissions of its vehicles. A key development is to improve the efficiency of the powertrain, which includes the axle. Until recently, optimisation of axle design has mainly concerned durability and noise aspects.

The aim of this study is then to characterise the efficiency of truck axles. As for most of the mechanical transmissions, power dissipation in axles is due to gear mesh, rolling element bearings, seals and oil churning. Formulae already exist to estimate these power losses at a global level, but they are not always adapted to axles. Indeed, the main component of axles is a spiral bevel or a hypoid gear set. The influence of these special gears on efficiency is investigated here: their shape drives oil churning losses, while their tooth geometry and their kinematics impact friction at gear mesh. Therefore, the meshing friction of the gear set is also evaluated thanks to a local approach. The influence of some gear parameters is studied.

However, power losses are influenced by temperature through oil viscosity. As previous experiments underline non-negligible temperature difference between components, it is necessary to consider local temperatures instead of a global oil temperature. Efficiency but also durability can be impacted by local hot spots. The thermal network method is used to model the thermal exchanges inside and outside the axle and to calculate temperature distribution. Usual efficiency tests on axles measure only global power loss and oil temperature: no evidence allows to confirm a power loss breakdown. Thus, a test campaign with temperature measurements is done and validates the model on local temperature calculation but also on estimation of component power losses. The model can be used at design stage for future development of axles.

Keywords: power losses, thermal network, thermal exchanges, axle, hypoid gear, gear friction

Résumé

Pour répondre au besoin des clients ainsi qu'aux réglementations gouvernementales, les constructeurs de camions doivent diminuer la consommation et les émissions de leurs véhicules. Une solution-clé est d'améliorer le rendement de la transmission du camion, dont le pont fait partie. Leur design n'a longtemps été optimisé qu'en fonction de critères de durabilité et de bruit.

L'objectif de ce travail est donc de caractériser le rendement des ponts de camion. La dissipation de puissance au sein du pont est causée par l'engrènement, les roulements, les joints et le barbotage. Des méthodes permettent d'estimer globalement ces pertes de puissance, mais elles ne sont pas forcément adaptées aux ponts. En effet, l'élément principal du pont est un engrenage spiro-conique ou hypoïde et son importance est étudiée : sa forme influe sur le barbotage, tandis que sa géométrie de denture et sa cinématique gouvernent le frottement à l'engrènement. Il semble ainsi important d'évaluer le frottement de ces couples coniques par une approche locale et d'étudier l'influence des paramètres de denture.

Cependant, les pertes de puissance dépendent de la température, via les propriétés de l'huile. Des expériences montrent un important écart de température entre les composants. Il faut donc considérer des températures locales plutôt qu'une température d'huile globale. Le rendement et la durabilité peuvent être impactés par des points chauds. La méthode des réseaux thermiques permet de modéliser les échanges thermiques du pont ainsi que la distribution de températures. Les tests classiques de rendement mesurent uniquement la perte globale et la température d'huile : rien ne permet de confirmer la répartition des pertes entre sources. Une campagne d'essais avec mesures de température est donc réalisée et valide le modèle pour le calcul des températures locales et pour l'estimation des pertes de chaque composant. Ce modèle peut alors être utilisé lors du design de futurs ponts.

Mots-clés : pertes de puissance, réseaux thermiques, échanges thermiques, pont, engrenage hypoïde, frottement à l'engrènement

Summary

Résumé étendu

Introduction

Alors que plus en plus de biens sont transportés à travers le monde, les poids-lourds jouent un rôle important dans le fret terrestre. Ils assurent notamment l'approvisionnement local en nourriture, médicaments, biens de consommation, carburant… En Europe, les poids-lourds doivent respecter la réglementation sur les émissions. Euro 0 remonte à 1990 et Euro VI, sa dernière version, date de fin 2013. Les constructeurs de camions ont ainsi peu à peu amélioré leur technologie en ce qui concerne les émissions de particules, de NOx, d'Hydrocarbures et de Monoxydes de carbone. Cependant, selon la Commission Européenne [1], les camions, les bus et les cars contribuent pour un quart aux émissions de CO2 dues au transport routier en Europe. Une réglementation spécifique au CO2 doit entrer en vigueur dans un futur proche.

Un moyen de réduire les émissions de particules et de CO2 est de diminuer la consommation de carburant. Au-delà des questions de réglementation, les clients demandent aussi des solutions de transport plus efficaces, principalement pour réduire les dépenses de carburant. Pour ce qui est d'améliorer le rendement, la transmission du véhicule est toujours un élément-clé de développement. Ainsi, il est important de déterminer exactement les pertes de puissance de la transmission pour pouvoir ensuite les réduire.

Cette étude s'intéresse au pont, qui est le dernier élément de la transmission du camion. Son principal composant est un engrenage spiro-conique ou hypoïde. Ces engrenages spéciaux permettent de

transmettre la puissance entre des arbres perpendiculaires, et ce avec une durée de vie et un bruit acceptables. La plupart des développements menés sur les ponts se sont justement focalisés sur les aspects de durabilité et de bruyance. Le rendement a longtemps été étudié de manière empirique uniquement. Le premier modèle de rendement d'un pont date de 2013 [2] et s'intéresse aux ponts de voiture. S'ils ont une architecture et un fonctionnement similaires, ils ont en revanche des conditions opératoires bien différentes. Cela peut être à l'origine de nouvelles problématiques.

Cependant, les modèles développés pour estimer le rendement des ponts se basent uniquement sur des approches isothermes : le pont est considéré à température d'huile. Cette hypothèse est pourtant remise en question par des essais [3] qui soulignent d'importants écarts de température entre les composants. Cela peut modifier les propriétés de l'huile et ainsi le rendement. De plus, les transmissions sont aujourd'hui plus compactes tandis que plus de chaleur est générée. Les questions de refroidissement et de durabilité doivent être gardées à l'esprit, car des défauts peuvent alors survenir sur les engrenages et les roulements à cause de l'apparition de points chauds. Le comportement thermique des composants et de l'huile doit donc être modélisé et analysé.

Finalement, l'objectif de cette étude est de développer un modèle thermomécanique d'un pont de camion. Une approche globale est utilisée pour considérer le système complet. Les pertes de puissance et les échanges thermiques sont estimés à l'aide de méthodes simples pour permettre un cycle de développement rapide et donc un usage lors de la phase de design. Le rendement du pont mais aussi la distribution de température sont obtenus.

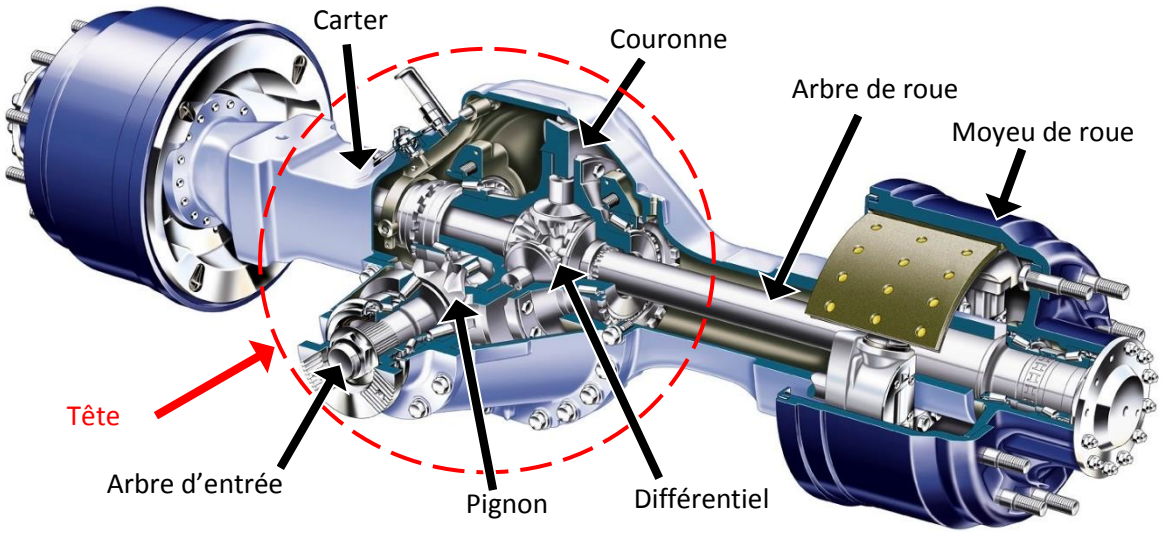

Figure 0.1: Les principaux éléments d'un pont de camion

Chapitre 1 – Bibliographie

Architecture d'un pont de camion

Le système mécanique étudié ici est un pont de camion, représenté sur la Figure 0.1. Le pont a trois rôles : i) transmettre la puissance de l'arbre de transmission aux arbres de roue (ces éléments sont

généralement perpendiculaire) ; ii) réaliser une dernière réduction de la vitesse ; iii) permettre au véhicule de tourner en évitant que les roues ne patinent grâce au différentiel. La réduction de vitesse est réalisée grâce à un engrenage spiro-conique, ou hypoïde s'il existe un décalage (offset) entre l'axe du pignon et celui de la couronne. Cet offset induit un pignon hypoïde plus gros que celui du spiro-conique pour une couronne de même taille : le pignon est donc plus résistant pour une garde au sol identique. L'hypoïde a aussi un meilleur rapport de conduite et est ainsi plus silencieux. Cependant, le glissement et la perte au contact sont plus importants pour l'hypoïde à cause de l'offset.

En plus du couple conique, la tête du pont comprend plusieurs roulements et le carter est partiellement rempli d'huile afin d'assurer la lubrification des éléments. Les ponts de camion et de voiture ont la même architecture, mais ceux de camion sont plus gros : la couronne a un plus grand diamètre, le volume d'huile est plus important ; mais la puissance transmise est aussi plus grande. Cela peut mener à des rendements similaires.

Rendement d'un pont

Les pertes de puissance du pont sont générées par certains composants. La principale source de frottement est le couple conique. La lubrification par bain d'huile de l'engrenage cause des pertes par barbotage. Les roulements produisent des pertes par frottement mais aussi par traînée. Enfin, les joints à lèvre génèrent du frottement par rotation.

Le rendement des ponts a d'abord été étudié grâce à des moyens expérimentaux. Une première procédure de laboratoire est proposée en 1979 par Hobson [4], qui évalue le rendement simplement, en mesurant couples et vitesses. En 1988, Winter et Wech [5] utilisent un banc d'essai pour engrenages hypoïdes en boucle fermée et testent divers paramètres. L'offset de l'hypoïde et les lubrifiants influent beaucoup le rendement sous charge, tandis que la précharge des roulements et le barbotage prédominent à haute vitesse. Plus récemment, Xu et al. [6] soulignent l'importance de la température d'huile. En ce qui concerne les approches théoriques, Kolekar et al. [2] établissent un modèle de rendement en 2013. Ils considèrent les différentes sources de pertes et évaluent le rendement pour différentes conditions. Kakavas et al. [7] ont récemment développé parallèlement les approches expérimentale et théorique. Chaque source de pertes est estimée sur un cycle routier et la perte globale est comparée avec succès à des mesures.

Les pertes par frottement au joint sont évaluées par des approches simples, comme celle de Simrit [8] qui est utilisée dans le rapport technique ISO/TR 14179-2 [9], celle de Linke [10], ou celle de Kettler [11]. Une comparaison en fonction de la température permet de choisir la formule de Simrit. Les pertes des roulements sont estimées selon les méthodes de Harris [12] ou de SKF [13]. Les résultats obtenus divergent cependant selon les conditions d'application et les deux méthodes seront testées dans le second chapitre sur le cas du pont. Les pertes par barbotage ont été beaucoup étudiées pour les engrenages cylindriques. Concernant les spiro-coniques et les hypoïdes, des formules génériques proposées dans les rapports techniques ISO/TR 14179-1 [14] et ISO/TR 14179-2 [9] peuvent être appliquées. Une formule spécifique a aussi été établie par Jeon [15] dans une étude sur les ponts automobiles. Ces trois formules donnent toutes des résultats différents et seront aussi testées dans le second chapitre. Enfin, le rendement des engrenages spiro-coniques ou hypoïdes peut être estimé d'après les formules de Buckingham [16], de Coleman [17], ou de Niemann et Winter dans l'ISO/TR

14179-2 [9]. Comme pour les cylindriques, le rendement des hypoïdes peut être exprimé en fonction du coefficient de frottement et d'un facteur géométrique. Une comparaison en fonction du couple révèle un comportement incohérent de la formule de Coleman. Les deux autres formules sont conservées pour questionner la pertinence d'une approche globale par la suite.

Comportement thermique d'un pont

La plupart des études sur les ponts s'intéressent uniquement aux pertes ([4]–[6], [18]) et travaillent toujours à température d'huile fixe. Les quelques études thermiques considèrent généralement le pont comme isotherme, à température de la cuve d'huile. C'est le cas de Kolekar et al. [2], mais aussi de Kakavas et al. [7]. Ils calculent ainsi une température d'huile globale et évaluent le rendement en fonction des conditions ambiantes sur un cycle routier. Ce type d'approche permet d'évaluer le rendement global du pont, mais ne peut pas confirmer la répartition des pertes entre les sources. Seule une mesure de la température des composants pourrait indiquer la prédominance d'une source.

Le comportement thermique du pont est étudié expérimentalement par Hurley [19] et Xu et al. [3] : la température est enregistrée en de nombreux points du pont. Pour différentes conditions opératoires, ils observent des écarts de température entre les composants, par exemple entre pignon et roulements. Il apparaît aussi que le pignon est plus chaud que l'huile, ce qui est important pour des questions de durabilité mais aussi pour le calcul du coefficient de frottement. Quelques-uns se sont intéressés spécifiquement au couple conique, comme Handschuh [20] ou Wang et al. [21]. Le premier observe expérimentalement l'influence de la charge et de la lubrification par jet sur la température de masse du pignon. Il constate également que le pied et la tête sont les parties les plus chaudes de la dent. Wang et al. montrent que la forme du contact influe sur la génération de chaleur par frottement. Un contact étendu produit ainsi moins de pertes localement.

Finalement, aucune étude n'a établi de modèle thermique d'un pont complet. Cela peut pourtant avoir une influence sur la température de masse des engrenages ou d'autres éléments. Cela permettrait également de connaître la répartition des pertes entre sources.

Chapitre 2 – Pertes de puissance du pont

Rendement du pont de camion

Un pont à simple réduction pour une application longue distance est étudié. Des essais de rendement sont menés sur ce pont à l'aide d'une méthode similaire à celle de Hobson [4]. Deux bancs sont utilisés : l'un permet de mesurer la perte sous charge et l'autre la perte à vide. Les couples et vitesses sont mesurés, ainsi que la température de la cuve d'huile, qui est maintenue à 80°C grâce à des ventilateurs. Trois paliers de puissance sont testés sur le premier banc et six paliers de vitesse sur le second banc. Les résultats obtenus, de l'ordre de quelques kilowatts de pertes, sont ensuite comparés aux calculs.

Les pertes indépendantes de la charge sont d'abord étudiées. Le frottement au joint est évalué selon la formule de Simrit et ne génère pas plus de 200 W de pertes. Les pertes dans les roulements sont estimées selon Harris et SKF. Pour les conditions sans charge, les deux méthodes donnent des résultats

similaires car certains roulements sont préchargés. En revanche, les résultats divergent sous charge. La méthode SKF prédit une perte plus importante que celle de Harris, or cela induit un très bon rendement du couple conique, ce qui n'est pas réaliste. Cette méthode est donc écartée. Les pertes par barbotage sont calculées selon les formules de Mauz et de Jeon et comparées pour les conditions sans charge. La formule de Mauz surestime complètement le barbotage tandis que la formule de Jeon le sous-estime. Une étude plu poussée sur ces pertes est donc menée juste après.

Etude du barbotage des engrenages hypoïdes

La formule de Jeon [15] a été développée pour le barbotage des engrenages hypoïdes dans les ponts automobiles. Cependant, son étude s'est basée sur deux engrenages de géométrie proche. Il est donc important d'analyser plus en détail l'influence des paramètres géométriques par de nouveaux essais. Le banc utilisé, représenté Figure 0.2, permet de tester un engrenage à la fois, de varier la vitesse et le sens de rotation et de contrôler la température du bain d'huile. Quatre géométries d'engrenage et deux de cône sont testées, ainsi que plusieurs huiles. Des essais sont établis afin de couvrir les plages de fonctionnement d'un pont de camion, en se basant sur des paramètres équivalents : la vitesse périphérique des engrenages, la viscosité et le niveau d'huile. La forme du carter du banc peut également être modifiée à l'aide de déflecteurs pour approcher celle d'un pont.

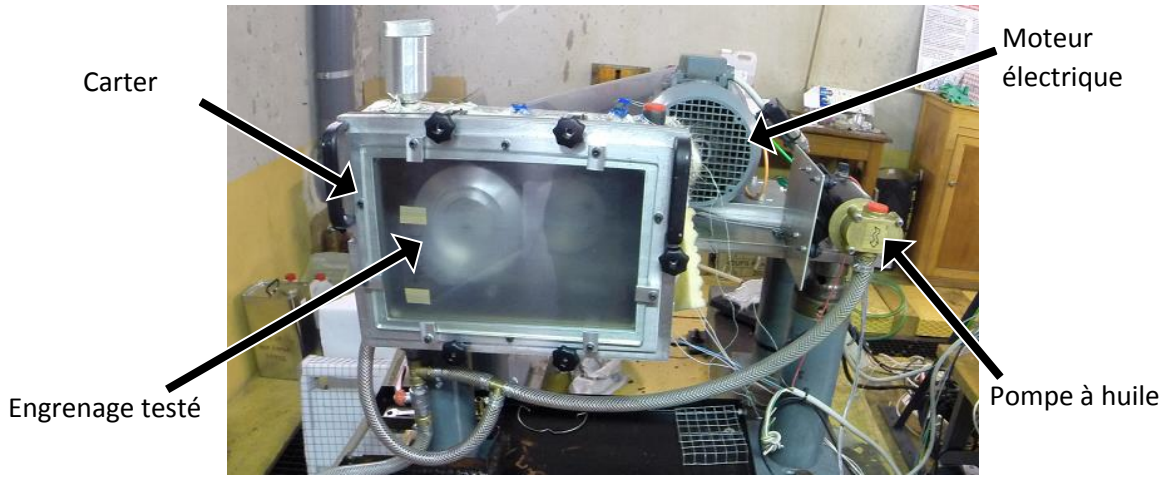

Figure 0.2: Banc d'essais pour mesurer les pertes par barbotage

Les essais menés permettent d'abord d'observer l'influence des conditions opératoires : vitesse de rotation Ω, ratio d'immersion h_{lub}/R_o et propriétés de l'huile. Les pertes par barbotage augmentent de manière importante avec la vitesse. Ces pertes augmentent également avec le niveau d'huile : le ratio d'immersion est retenu comme facteur influent. Les pertes diminuent lorsque la viscosité ν_{lub} baisse, mais elles restent constantes à faible viscosité (sous 30 cSt) : deux régimes d'écoulement semblent exister. L'influence de la densité ρ n'est pas observée ici, faute d'une différence significative de cette caractéristique entre les huiles utilisées. L'effet sur les pertes de la géométrie des engrenages est ensuite étudié : rayon extérieur R_o, largeur, largeur de denture, demi-angle et nombre de dents. Une comparaison entre un engrenage et un cône d'enveloppe extérieure identique permet de montrer que les dents ont peu d'influence sur les pertes par barbotage des spiro-coniques. Il apparaît ensuite que le diamètre extérieur est un paramètre plus influent que toutes les autres caractéristiques

géométriques testées ici. Les mesures sont finalement comparées aux calculs réalisés d'après les formules de Mauz et de Jeon : les résultats divergent. Des modifications sont donc nécessaires.

Amélioration de la formule de barbotage pour les ponts de camion

La formule de Jeon n'est pas cohérente avec les paramètres géométriques identifiés grâce aux essais, car elle utilise notamment la largeur : deux engrenages de même diamètre extérieur génèrent ainsi des pertes différentes. Une nouvelle formulation de la perte par barbotage d'un engrenage spiro-conique est proposée :

$$P_{churning} = \frac{1}{2}\,\rho\,\Omega^3\,{R_o}^3\,S_m\,C_m \tag{0.1}$$

La surface mouillée S_m considère l'enveloppe extérieure de l'engrenage. Une modification est aussi apportée au calcul du couple adimensionné de barbotage C_m afin de prendre en compte les deux régimes d'écoulement d'huile identifiés. Ceux-ci se distinguent grâce au nombre de Reynolds :

Pour Re $\leq$ 20 000 : $$C_m = 1.45\left(\frac{h_{lub}}{R_o}\right)^{0.15}\left(\frac{V_{lub}}{{R_o}^3}\right)^{-0.20} Re^{-0.25}\,Fr^{-0.53} \tag{0.2}$$

Pour Re $>$ 20 000 : $$C_m = 0.12\left(\frac{h_{lub}}{R_o}\right)^{0.15}\left(\frac{V_{lub}}{{R_o}^3}\right)^{-0.20} Fr^{-0.53} \tag{0.3}$$

Cette formule peut enfin être appliquée au pont de camion. D'après Jeon, un couple d'engrenages génère plus du double de la perte de la couronne seule, à cause d'un changement du flux d'huile. Afin de prendre ce phénomène en considération, le niveau d'huile est augmenté de 30% pour un couple conique. La Figure 0.3 présente les résultats obtenus, qui concordent bien avec les mesures.

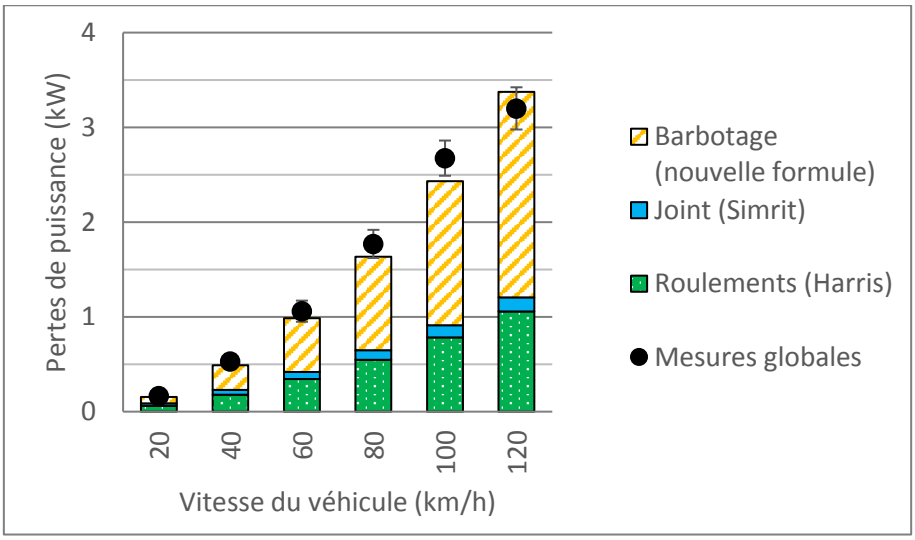

Figure 0.3: Comparaison des mesures et des calculs de pertes pour les conditions sans charge

Calcul des pertes dépendantes de la charge

Les pertes aux roulements ont déjà été évaluées et il reste donc à estimer les pertes par frottement à l'engrènement. Les deux formules, Buckingham et ISO, sont appliquées au couple conique du pont. Les résultats obtenus avec Buckingham surestiment beaucoup ces pertes, en partie à cause du calcul du

coefficient de frottement (estimé à environ 0,04 contre 0,02 pour l'ISO). L'ISO donne des résultats plus cohérents, comme illustré sur la Figure 0.4. Cependant les pertes sont sous-estimées à faible charge et surestimées à forte charge. Cela peut être dû à une mauvaise évaluation du contact hypoïde ou au calcul du coefficient de frottement, qui seront donc étudiés dans le chapitre suivant.

D'après la Figure 0.4, la principale source de pertes est le frottement à l'engrènement à fort couple et le barbotage à faible couple. Ce dernier est d'autant plus important que le niveau d'huile est élevé. En revanche, comme relevé par Kakavas [7], ce sont les roulements qui génèrent le plus de pertes pour une application voiture. Cela provient en fait d'une température de fonctionnement plus basse (40°C) et peut être reproduit sur le cas du camion.

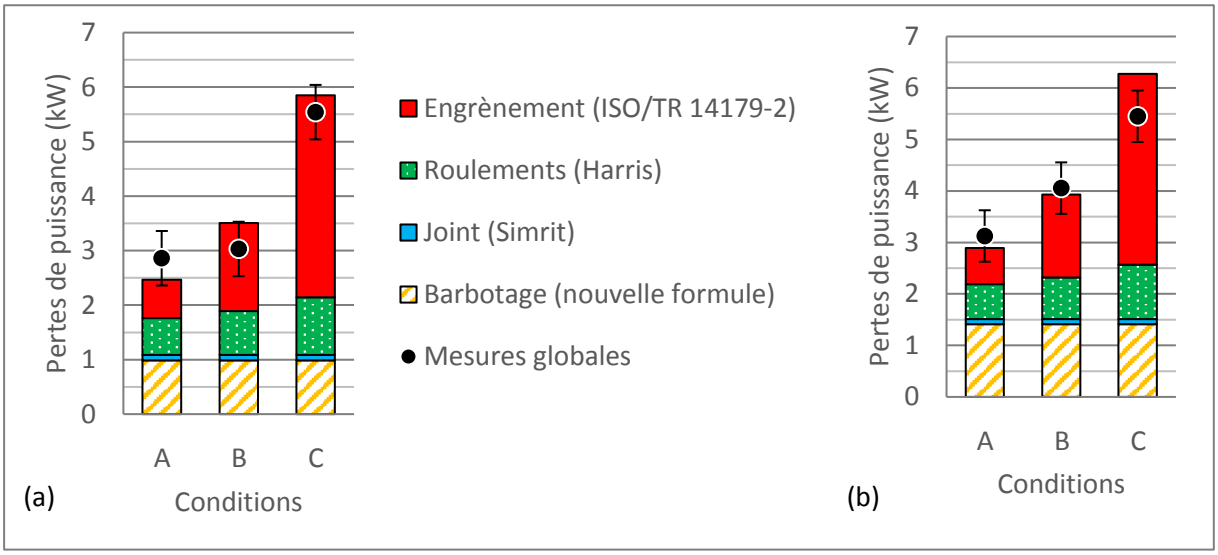

Figure 0.4: Comparaison des mesures sous charge et des calculs de pertes pour un niveau d'huile (a) normal et (b) élevé

Chapitre 3 – Frottement à l'engrènement des engrenages hypoïdes

Particularités des engrenages spiro-coniques et hypoïdes

Lors de la conception d'un engrenage hypoïde, les paramètres de base sont définis : diamètre primitif, angle de spirale, offset… Ce dernier est la caractéristique la plus spécifique des engrenages hypoïdes et implique un angle de spiral différent sur le pignon et la couronne. La fabrication de ces engrenages débute par le forgeage suivi du taillage. Sont ensuite réalisés des traitements thermiques (cémentation, trempe et revenu) et une opération de finition (rectification ou rodage). Deux méthodes de taillage sont possibles pour les engrenages spiro-coniques et hypoïdes :

- Le face-milling (FM) taille les dents une à une à l'aide d'une fraise de centre fixe. Les flancs obtenus sont des arcs de cercle. Le gros bout est plus haut que le petit bout.
- Le face-hobbing (FH) taille toutes les dents dans un même mouvement, car la fraise et l'engrenage généré tournent ensemble. Les flancs obtenus sont des épicycloïdes. Le petit et le gros bout sont de hauteur équivalente.

S'ajoute ensuite le choix du taillage avec ou sans génération, qui donnent un profil de denture et des

stries d'usinage différentes, comme illustré sur la Figure 0.5. La génération nécessite une machine plus sophistiquée mais donne un meilleur profil de denture. Le pignon est donc toujours généré, alors que la couronne est souvent taillée sans génération pour des raisons de production.

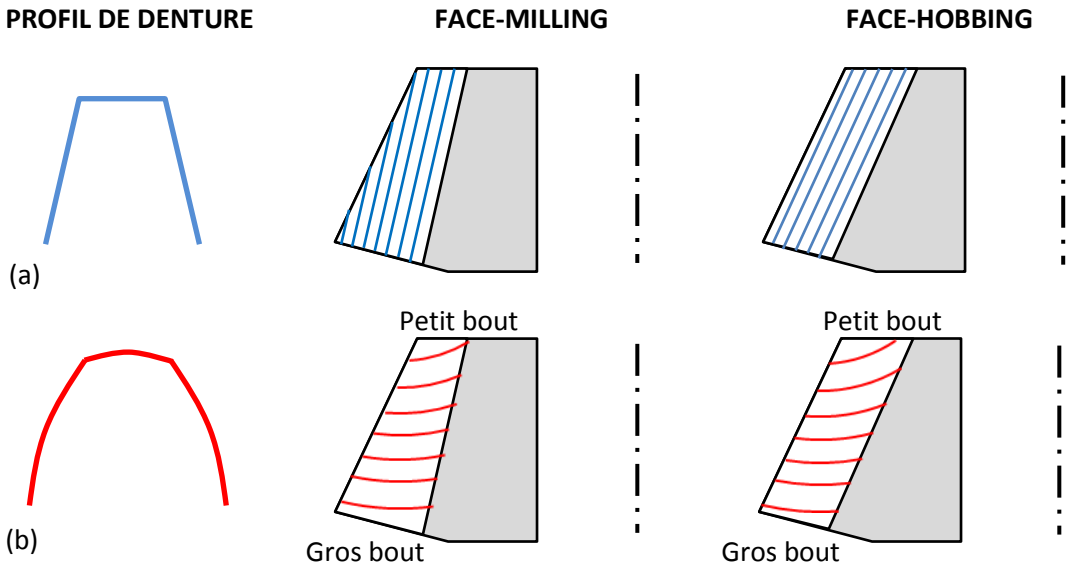

Figure 0.5: Profil de denture et stries d'usinage pour un taillage (a) sans et (b) avec génération

Afin de prendre en compte ces particularités géométriques, un logiciel de calcul de l'engrènement a été développé et validé par Barday [22]. La géométrie de la denture est établie en simulant le processus de fabrication, mais des mesures topographiques peuvent aussi être utilisées. Les modèles en Eléments Finis d'une dent du pignon et d'une de la couronne sont créés et une analyse tridimensionnelle est réalisée pour déterminer la flexion et le cisaillement sur ces deux dents.

L'engrènement des hypoïdes est théoriquement un contact linéaire. Cependant, la charge et les déformations en fonctionnement induisent plutôt un contact elliptique. Cette ellipse est généralement discrétisée en plusieurs contacts linéaires ([23], [24]). C'est aussi le cas du modèle de Barday qui détermine les lignes de contact potentiel et les discrétise en segments de longueur variable. Les conditions de contact varient d'une ligne de contact à une autre, mais également entre les segments au sein d'une même ligne : les vitesses de surface, la charge et le rayon de courbure évoluent et modifient la largeur de contact, l'épaisseur de film d'huile et la cinématique du contact. Cette dernière est étudiée à partir des vitesses de surface du pignon V_1 et de la couronne V_2. La vitesse de glissement V_s, la somme des vitesses de surface V_Σ et la vitesse d'entraînement V_e sont alors calculées :

$$V_s = V_1 - V_2 \tag{0.4}$$

$$V_\Sigma = V_1 + V_2 \tag{0.5}$$

$$V_e = \frac{V_\Sigma}{2} \tag{0.6}$$

En dehors du cône primitif, les vitesses de surface des engrenages spiro-coniques ont des valeurs et des directions différentes. Ces directions sont définies par l'angle d'orientation des vitesses δ et l'angle d'orientation de l'entraînement δ_e, comme illustré sur la Figure 0.6. Le glissement a lieu uniquement

le long de l'axe mineur de l'ellipse, comme pour les engrenages cylindriques. En revanche, il y a aussi du glissement selon l'axe majeur de l'ellipse sur les engrenages hypoïdes, à cause des angles de spirale différents. Cela induit également un glissement tout le long de l'engrènement.

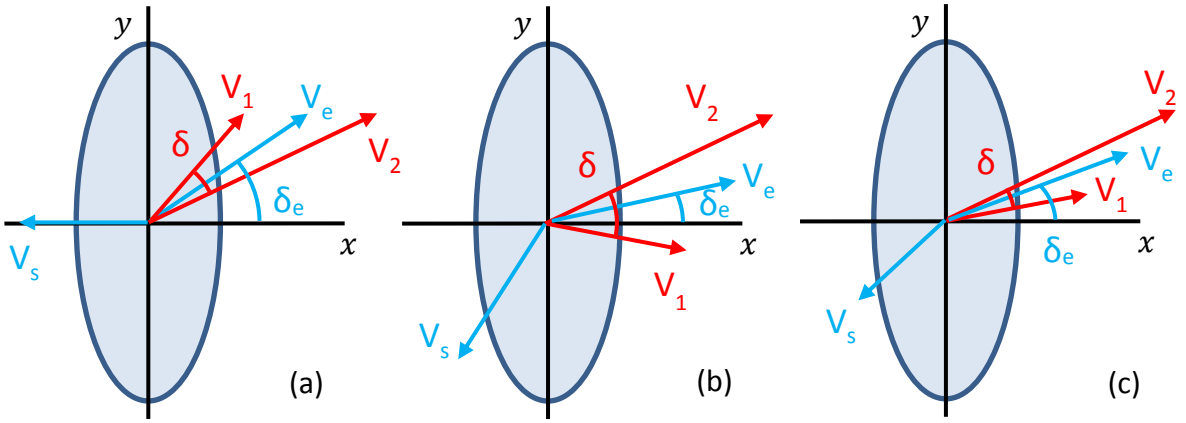

Figure 0.6: Exemples de vitesses dans le contact d'un engrenage (a) spiro-conique et (b)-(c) hypoïde

La vitesse d'entraînement au sein de l'ellipse est analysée selon les composantes transverse et longitudinale à la ligne de contact. Il apparaît que la composante longitudinale est constante, mais que la composante transverse varie le long de l'ellipse, provoquant une légère rotation.

Estimation des pertes

Une approche locale est utilisée pour évaluer le frottement à l'engrènement, en se basant sur les données fournies par le logiciel de Barday. Deux couples coniques sont étudiés : un hypoïde et un spiro-conique. Le coefficient de frottement est fixé à 0,05 et ne varie pas localement. Les conditions de contact le long de l'engrènement montrent que la vitesse de glissement s'annule presque au point primitif pour le spiro-conique, tandis que le glissement est permanent sur l'hypoïde. La perte de puissance est calculée sur chaque segment et sommée pour obtenir la perte d'une ligne de contact complète. La perte instantanée est ensuite déduite en fonction des paires de dent simultanément en contact, comme représenté sur la Figure 0.7. Plus la charge augmente et plus le recouvrement entre les dents est important, ce qui stabilise la perte le long du cycle. Le comportement est identique pour un couple spiro-conique et un couple hypoïde.

L'approche locale est comparée à l'approche globale utilisée dans l'ISO/TR 14179-2 [9] afin de discuter de la validité de cette dernière pour le calcul des pertes. Les résultats obtenus avec les deux méthodes présentent des tendances similaires. Cependant, l'approche globale surestime toujours les pertes, et d'autant plus pour le spiro-conique. Cela est dû à l'évaluation de la vitesse de glissement : l'ISO estime cette vitesse globalement, tandis que l'approche locale considère uniquement la zone en contact. Plus le contact est étendu, plus les deux méthodes concordent. D'une manière générale, l'ISO donnera toujours le cas le moins favorable. L'approche locale est maintenant appliquée aux conditions d'essais du Chapitre 2, avec les coefficients de frottement globaux calculés par l'ISO (A : 0,020 ; B : 0,023 ; C : 0,026). La comparaison avec les mesures sur la Figure 0.8 montre que l'approche locale est plus cohérente. L'utilisation d'un coefficient de frottement local pourrait encore améliorer sa précision.

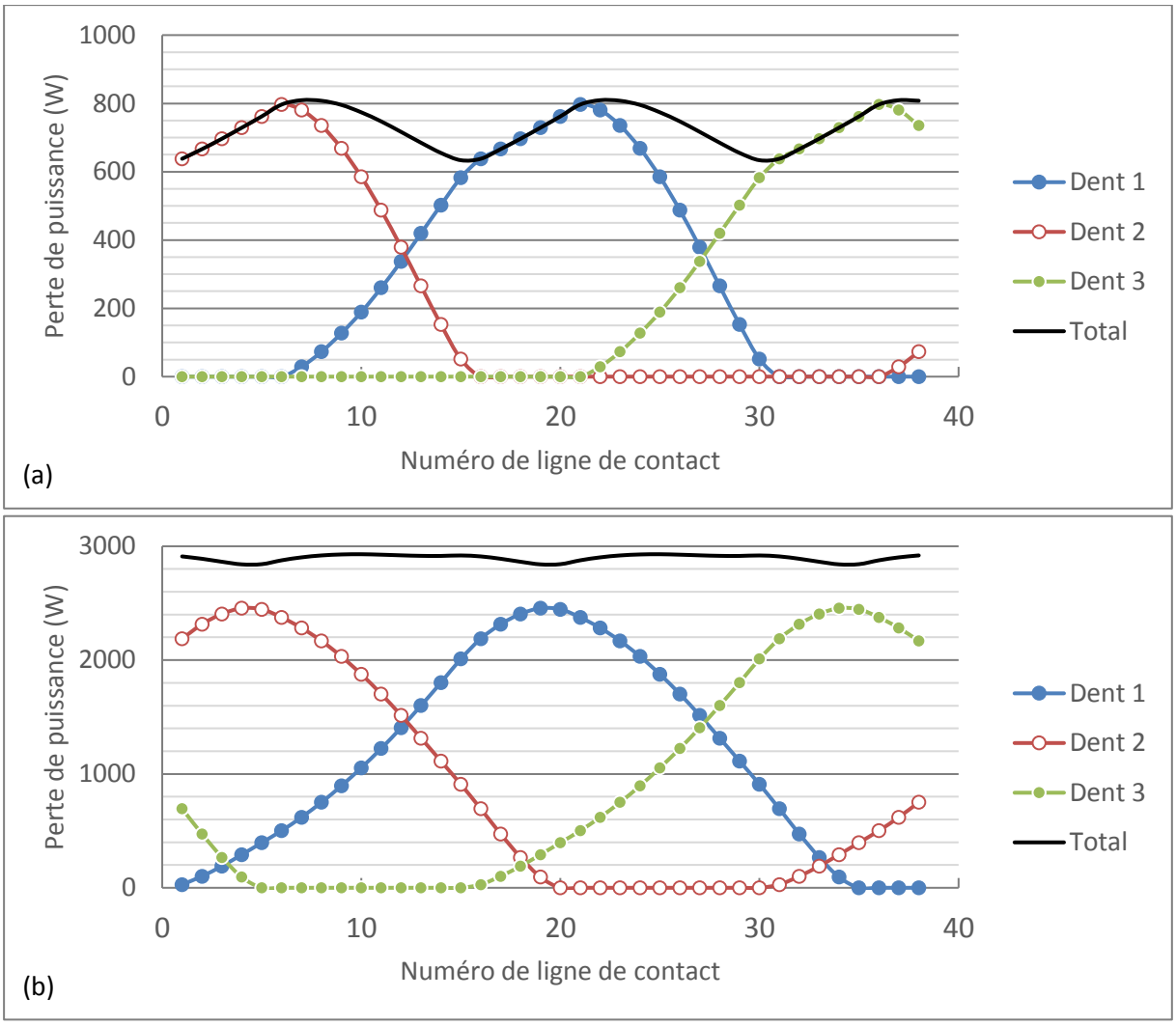

Figure 0.7: Perte par frottement le long d'un engrènement complet (1000 tr/min et (a) 280 N.m ou (b) 1120 N.m)

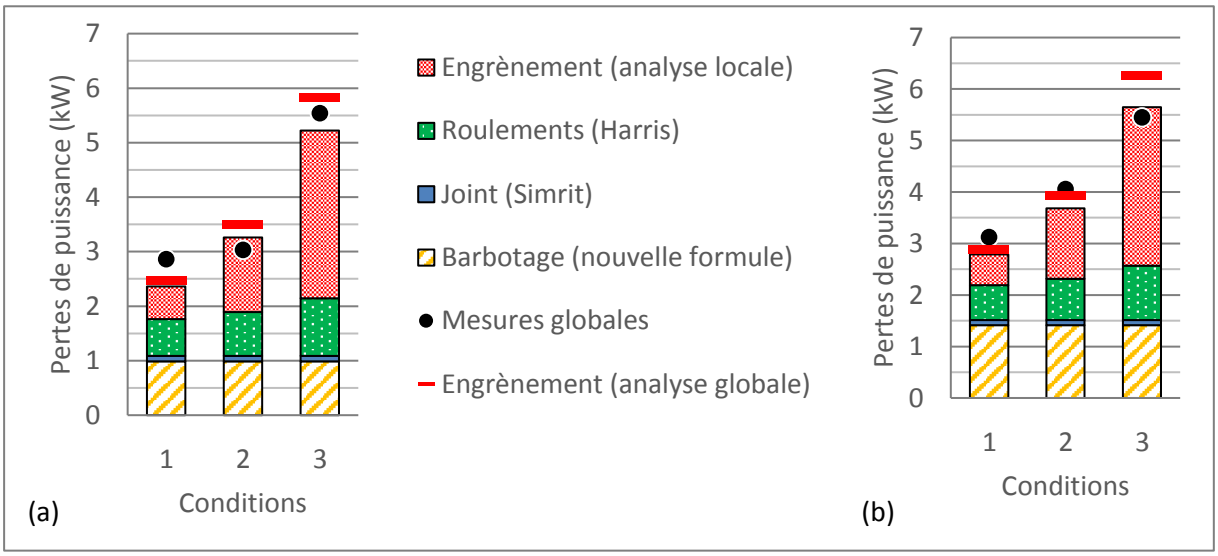

Figure 0.8: Comparaison des mesures et du calcul des pertes à l'engrènement avec les approches locale et globale pour un niveau d'huile (a) normal et (b) élevé

Coefficient de frottement

Le coefficient de frottement est un paramètre de premier ordre pour les pertes à l'engrènement. Lui-même est principalement influencé par la charge, les vitesses d'entraînement et de glissement, les propriétés de l'huile et la rugosité de surface. Ces paramètres définissent le contact élastohydrodynamique entre les dentures et les différents régimes de lubrification : lubrification limite, en film complet, ou mixte. Ce dernier régime, qui mêle frottements dus aux aspérités et au cisaillement fluide, est le plus courant dans les engrenages. Des formules évaluent le coefficient de frottement de manière à considérer les conditions locales de contact. La plupart se basent sur des mesures obtenues à l'aide de machines qui reproduisent les conditions de contact à l'engrènement. La formule de Benedict et Kelley [25] est fréquemment utilisée, bien qu'elle ne considère pas la rugosité de surface. Ce paramètre est bien intégré dans les formules proposées par Diab et al. [26] et par Xu [27].

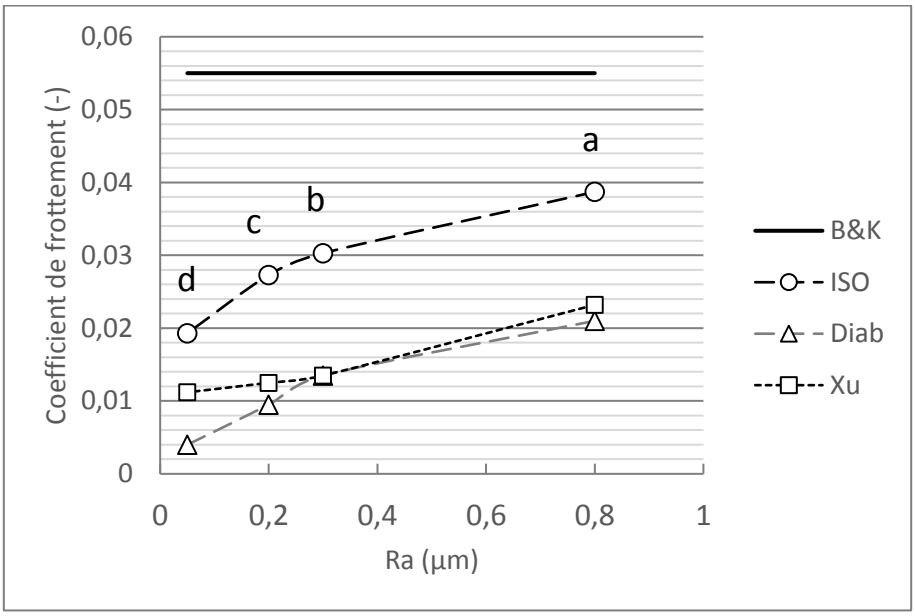

Figure 0.9: Coefficient de frottement moyen d'après plusieurs formules et pour différentes rugosités de surface (1000 tr/min, 1120 N.m, huile à 80°C)

L'influence de la rugosité de surface sur le coefficient de frottement est d'abord étudiée. La rugosité générale dépend surtout de la finition. Elle est caractérisée par la rugosité moyenne arithmétique du profil Ra et par la hauteur maximale du profil Rz. Diab et al. [26] montrent que le coefficient de frottement double si deux surfaces rugueuses sont utilisées plutôt que des lisses. Une moyenne du coefficient de frottement est calculée d'après les approches locales pour différentes finitions : rectification grossière (a), rectification fine (c) et superfinition (d). Une surface rodée à l'usage (b) sert de référence. Les résultats sont comparés au coefficient de frottement global calculé avec l'ISO sur la Figure 0.9. En plus de ne pas changer avec la rugosité, la formule de Benedict et Kelley prédit plus de pertes que toutes les autres estimations. Celles-ci donnent des tendances similaires : le coefficient de frottement est divisé par deux entre les conditions (a) et (d). Les pertes étant directement proportionnelles au coefficient de frottement, celles-ci sont également réduites. Cependant, la rugosité moyenne arithmétique donne seulement une approximation de la rugosité de surface et les stries d'usinage peuvent avoir un impact sur le coefficient de frottement. Contrairement au cas des engrenages cylindriques, les stries d'usinage des spiro-coniques et hypoïdes sont obliques par rapport

à la direction de roulement. Des profilométries optiques sont réalisées sur le pignon et la couronne : il apparaît que leurs surfaces ont des rugosités différentes. Des essais comme ceux effectués par Diab [26] permettraient de mieux caractériser le frottement de ce type de surface.

L'influence des angles d'orientation δ et δ_e sur le coefficient de frottement est enfin étudiée, car ils caractérisent les vitesses de surfaces et d'entraînement des spiro-coniques et des hypoïdes. La plupart des études menées sur ces angles d'orientation dans les contacts elliptiques s'intéressent uniquement à la lubrification élastohydrodynamique et à l'épaisseur de film de lubrifiant ([28]–[31]). Par des essais ou des modèles empiriques, il apparaît que l'amplitude et l'orientation de la vitesse d'entraînement modifient la formation du film. La diminution de l'épaisseur de film pourrait être causée par un plus grand taux de cisaillement dû à un frottement important. Cependant, aucune étude ne s'est penchée sur cet aspect. Carli et al. [32] étudient le frottement dans les contacts circulaires avec un film de lubrifiant anormal. Comme ces anomalies sont dues à une vitesse d'entraînement orientée, le modèle établi pourrait être transposé aux contacts elliptiques. Ce phénomène est aussi comparable à celui observé dans certains roulements, entre le collet du rouleau et la bague du roulement : un contact circulaire pivotant. Doki-Thonon [33] analyse le frottement dans ce contact, mais la similitude avec l'ellipse pivotante des hypoïdes n'est pas facile à valider.

Des essais préliminaires sont réalisés pour mesurer le coefficient de frottement en fonction des angles d'orientation. Deux positions sont testées (δ=0° et δ=10°), ainsi que différentes conditions de charge et de vitesse de surface. Le coefficient de frottement obtenu est toujours plus élevé pour δ=10°, d'autant plus que la vitesse de surface est faible. La charge a le même effet quel que soit l'angle. Ainsi, une modification de l'angle d'orientation modifie le coefficient de frottement et donc les pertes.

Chapitre 4 – Modèle thermique du pont

Modèle thermique du pont

Le modèle thermique se base sur les formules de pertes présentées dans les chapitres précédents et calcule également les échanges thermiques. Le carter est simplifié par un parallélépipède rectangle décomposé en trois parties : carter latéral, côté tête et côté cuve. Dans un premier temps, l'approche isotherme proposée par le rapport technique ISO/TR 14179-2 [9] est appliquée au pont de camion. La température du pont, qui correspond à celle de la cuve d'huile, est ainsi calculée en fonction des échanges thermiques avec l'environnement : rayonnement et convection forcée entre l'air et le carter, convection forcée avec l'huile. Il apparaît que la température calculée est plus basse que celle mesurée à cause d'une surestimation des échanges thermiques. Celle-ci peut être due à une mauvaise prise en compte par l'ISO du flux d'air autour du carter. Dans un second temps, la méthode des réseaux thermiques sert à modéliser le pont de camion. Basée sur une analogie électrique, elle reprend la loi d'Ohm pour lier l'écart de température ΔT au flux de chaleur Q par une résistance thermique R_{th} :

$$\Delta T = R_{th} \times Q \tag{0.7}$$

La chaleur générée par les pertes est injectée dans le réseau au nœud i correspondant. L'évolution de chaque température de nœud T_i est ensuite estimée selon la première loi de la thermodynamique :

$$M_i\, c_i\, \frac{dT_i}{dt} = Q_i + \sum_{j=1\ and\ j\neq i}^{nb} \frac{T_j - T_i}{R_{th}(i,j)} \qquad (0.8)$$

Ainsi, la température de chaque élément est utilisée plutôt qu'une température globale. Ce calcul transitoire est réalisé grâce à un algorithme. L'intégration numérique est faite avec la méthode de prédiction-correction d'Adams [34]. Les seules conditions limites du réseau sont la vitesse et la température de l'air environnant.

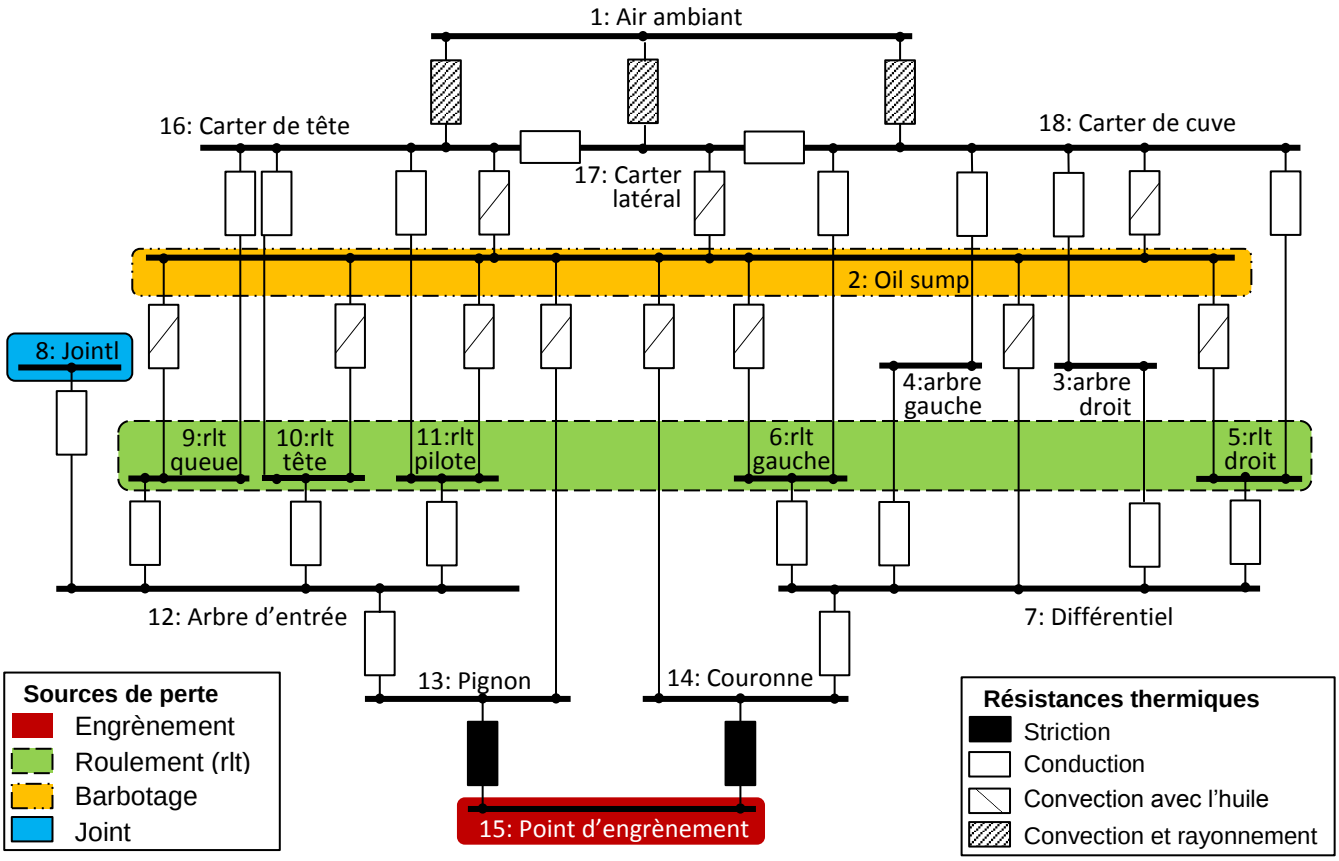

Figure 0.10: Réseau thermique du pont de camion

Le réseau thermique du pont est représenté sur la Figure 0.10 avec les sources de perte et les différentes résistances thermiques. Ces dernières établissent les échanges thermiques entre les nœuds :

1) La conduction a lieu entre les éléments en contact, comme un roulement avec son arbre, etc. ;
2) La convection et le rayonnent ont lieu entre l'environnement et le carter, qui est décomposé en plusieurs plaques pour considérer les différents flux d'air circulant autour ;
3) La convection entre l'huile et les engrenages en rotation est prise en compte car ces derniers sont lubrifiés par bain. La convection entre l'huile et le carter a aussi lieu ;
4) La striction contrôle l'échange entre les engrenages et leur point d'engrènement. La température du contact augmente beaucoup mais, comme la zone de contact est très petite comparée à la taille de l'engrenage, la température de masse est peu influencée.

Grâce à ces résistances, différents fonctionnements du camion sont modélisés. Si le véhicule roule, l'air environnant est en convection forcée avec le carter: le flux arrive côté tête et est considéré différemment selon les faces du carter. L'huile est aussi en convection forcée avec les éléments internes du pont, car les engrenages et les roulements sont en rotation. Si le véhicule est à l'arrêt, la convection est libre à l'intérieur et à l'extérieur.

Le réseau thermique obtient des résultats plus proches des mesures grâce aux flux distincts selon les faces du carter et à des formules plus adaptées aux échanges thermiques. Un autre intérêt du réseau thermique est de connaître les températures de masse des éléments du pont, sans nécessiter un modèle Eléments-Finis complexe. Le rapport technique ISO/TR 13989-2 [35] propose lui aussi de calculer la température de masse du couple conique, avec quelques spécificités : 1) Seul le couple d'engrenages et le lubrifiant sont pris en compte ; 2) La température d'huile est requise pour le calcul, cela implique une mesure de température, qui n'est en revanche pas nécessaire pour le réseau thermique ; 3) Seule une température globale du couple conique est calculée : il est considéré que le pignon et la couronne sont à la même température, alors que les mesures réalisées par Xu et al. [3] suggèrent le contraire. Des résultats similaires sont obtenus par les deux approches pour la température de masse de la couronne. En revanche, une différence importante est observée sur celle du pignon : le réseau thermique estime jusqu'à 10°C supplémentaires, ce qui peut être critique pour du grippage. Le pignon est plus chaud que la couronne, ce qui est en accord avec les mesures de Xu et al. [3]. Cela s'explique par un nombre de cycles et une inertie différents, mais aussi par un échange plus important entre l'huile et la couronne, ce qui la refroidit mieux. De plus, les roulements de l'arbre d'entrée, proches du pignon, sont très chauds.

Investigations sur le comportement thermique du pont

Le réseau thermique du pont doit être validé à l'aide d'une campagne d'essais spécifiques. En effet, les précédentes mesures ne sont pas suffisantes car seule la température d'huile était enregistrée. De nouveaux essais sont donc réalisés : des bancs similaires à ceux du Chapitre 2 sont utilisés et une dizaine de thermocouples sont placés en différents points du pont (huile, roulements, carter, environnement). Trois paliers de puissance (0 kW, 60 kW, 120 kW) avec chacun deux vitesses de fonctionnement sont réalisés, ainsi qu'une phase de refroidissement. Une ventilation constante est maintenue durant la totalité des essais pour caractériser la convection forcée avec l'air.

Des résultats en termes de perte globale du pont et de températures des composants sont obtenus. Les pertes de puissance évoluent comme attendu : elles augmentent avec la vitesse et le niveau d'huile. Il faut noter que la température d'huile est basse (<60°C), ce qui favorise le rendement du couple conique tout en augmentant les pertes des roulements. Concernant la température des composants, les différentes zones du carter sont à des températures différentes, ce qui soutient une décomposition du carter en plusieurs éléments. Les roulements de l'arbre d'entrée sont plus chauds que l'huile, tandis que les roulements du différentiel sont plus froids. Ceci est principalement dû à la faible vitesse de rotation des arbres de roue.

Grâce aux essais, il est possible de valider les échanges thermiques et les pertes de puissance. Il s'agit d'abord d'estimer correctement les échanges avec l'environnement, car ils conditionnent tout le reste, températures et pertes. La phase de refroidissement permet de caractériser la convection forcée avec

l'air. Le modèle obtient une décroissance en température similaire aux essais pour l'huile et le carter de tête. Les autres phases peuvent ensuite être étudiées : le palier sans charge (0 kW) et ceux sous charge (60 kW, 120 kW). L'évolution des températures a la même tendance d'après le modèle et les mesures. Les températures stabilisées calculées selon le modèle sont proches des mesures, comme le montre la Figure 0.11 pour les roulements et la Figure 0.12 pour l'huile. Les pertes sont bien estimées aussi par le modèle, comme présenté sur la Figure 0.13. Un second pont avec un couple spiro-conique est testé et modélisé. Les résultats obtenus sont cohérents : le modèle peut servir d'outil de design.

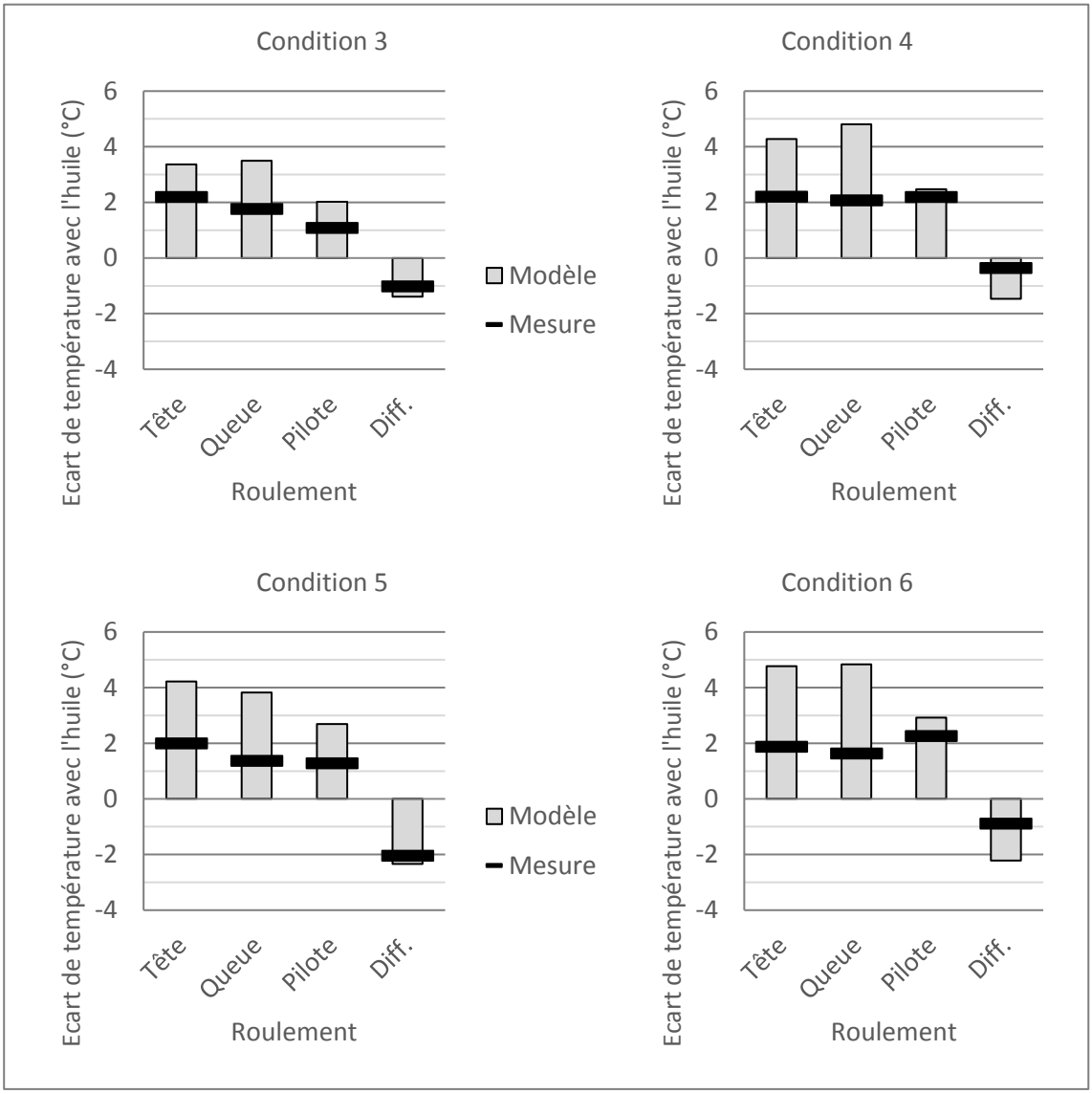

Figure 0.11: Température des roulements comparée à l'huile d'après les mesures et le modèle

Exploitation du modèle

Le modèle thermomécanique est maintenant utilisé pour analyser l'influence de certains paramètres sur les pertes et les températures de masse. Ainsi, un lubrifiant plus fluide induit une température de masse des engrenages plus basse mais pas forcément un meilleur rendement de pont. Une surface de denture plus lisse est un avantage à la fois en termes de pertes à l'engrènement et de température de

masse des engrenages. Enfin, augmenter le flux d'air autour du pont diminue les températures mais augmente les pertes. Ce dernier cas souligne le fait que les pertes et les températures n'augmentent de pair que si les échanges thermiques sont maintenus identiques.

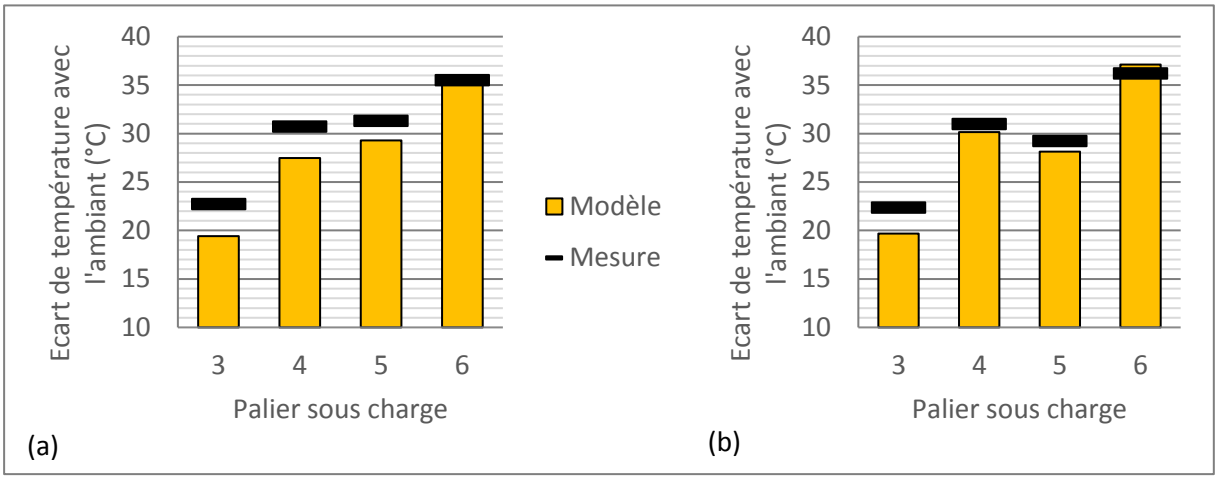

Figure 0.12: Température d'huile comparée à l'ambiant d'après les mesures et le modèle pour un niveau d'huile (a) normal et (b) élevé

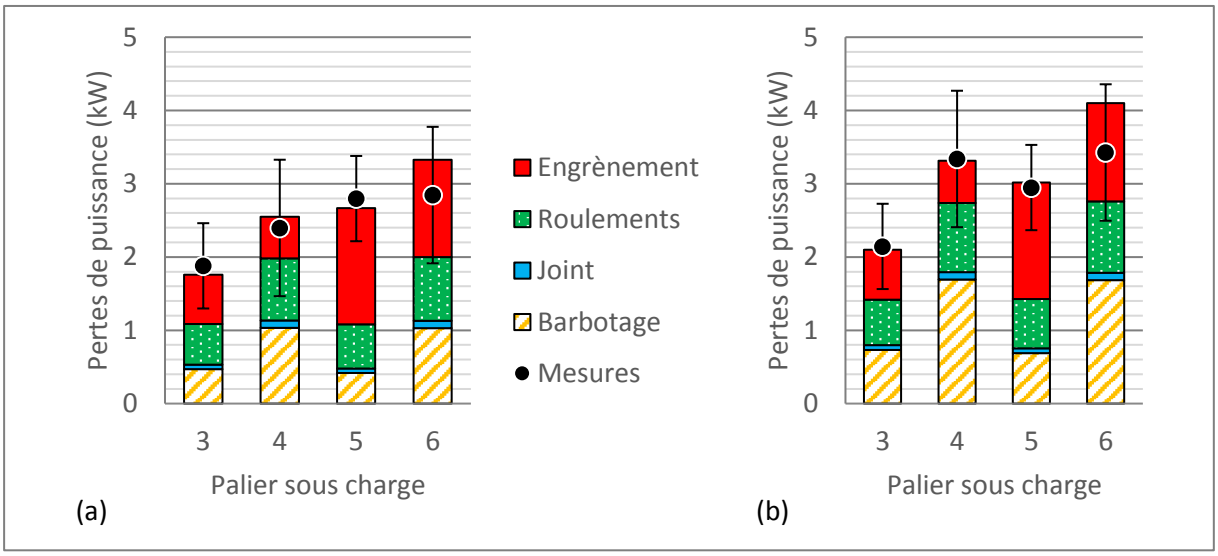

Figure 0.13: Comparaison des pertes de puissance mesurées et calculées pour un niveau d'huile (a) normal et (b) élevé

Conclusion

La consommation de carburant et les émissions des camions doivent être diminuées, notamment en améliorant le rendement de la transmission et donc du pont. Ainsi, cette étude s'attache à caractériser le rendement des ponts de camion grâce à un modèle thermomécanique. Celui-ci estime à la fois les pertes de puissance et les échanges thermiques par une approche globale du système. Une approche locale est aussi utilisée pour analyser le frottement à l'engrènement des engrenages hypoïdes.

Le premier chapitre décrit le pont de camion et son couple conique : hypoïde ou spiro-conique. La plupart des études concernant les ponts de voiture, les différences avec ceux des camions sont présentées, car elles influencent les pertes même si le rendement reste comparable. La littérature s'intéressa d'abord au rendement du pont par le biais d'expériences, puis par des études théoriques, et identifia ainsi des paramètres influents (conditions opératoires, macro- et micro-géométrie des engrenages). Des modèles existent pour chaque source de perte mais ils ne sont pas toujours cohérents entre eux. Le comportement thermique du pont fut principalement étudié par des approches isothermes. Or, des essais montrent des écarts de température entre composants [3]. Cela peut engendrer des problèmes de refroidissement et de durabilité, mais aussi modifier les pertes via la viscosité d'huile. Connaître les températures des composants permet aussi de valider la répartition des pertes entre les différentes sources.

Le second chapitre s'attache à estimer le rendement du pont de camion. Des essais sont réalisés pour évaluer les pertes dépendantes et indépendantes de la charge. Les pertes sont ensuite calculées d'après les formules issues de la littérature et une méthode est sélectionnée pour chaque source de pertes. Pour le frottement du joint, la formule de Simrit est choisie. Pour les roulements, il apparaît que la formule de SKF surestime la perte sous charge ; des résultats plus cohérents sont obtenus avec la formule de Harris qui est conservé pour la suite. Pour le frottement à l'engrènement, l'estimation fournie par l'ISO/TR 14179-2 donne une bonne tendance, mais une étude plus poussée est envisagée. Pour le barbotage, les solutions de Mauz et Jeon donnent des résultats irréalistes. Le barbotage des spiro-coniques et des hypoïdes est donc étudié plus en détails grâce à un banc spécifique. Des essais sont réalisés sur plusieurs cônes et engrenages spiro-coniques pour différentes huiles et conditions opératoires. Les résultats montrent l'influence de conditions opératoires (vitesse, ratio d'immersion, viscosité d'huile), mais aussi d'un paramètre géométrique (diamètre extérieur). En revanche, les dents ont peu d'impact sur le barbotage. Un nouveau modèle basé sur celui de Jeon est proposé pour prendre en compte les paramètres identifiés, ainsi que les deux régimes d'écoulement. Grâce à cette formule, l'estimation des pertes du pont est plus cohérente avec les mesures.

Le troisième chapitre s'intéresse à la principale source de pertes du pont de camion : le frottement à l'engrènement des hypoïdes. Les paramètres géométriques de ces engrenages particuliers sont déterminés par les choix de conception et de fabrication. Ils sont pris en compte dans le modèle développé par Barday [22], qui discrétise le contact elliptique de l'engrènement en plusieurs contacts linéaires. La cinématique des engrenages hypoïdes est différente de celle des autres engrenages : les vitesses et le glissement ne suivent pas les axes de l'ellipse de contact et ils peuvent varier en son sein. Le frottement à l'engrènement est étudié sur deux couples coniques (un spiro-conique et un hypoïde), suivant une approche locale basée sur les données du logiciel de Barday. Les conditions de contact et la perte sont analysées le long de l'engrènement. Une comparaison est ensuite réalisée avec l'approche globale de l'ISO pour en discuter la validité. Cette dernière surestime toujours les pertes à cause de l'estimation de la vitesse de glissement. L'approche locale utilisée avec un coefficient de frottement global obtient ainsi des résultats plus proches des mesures. Un coefficient de frottement local pourrait cependant donner des résultats plus précis. Les formules pour le calculer se basent généralement sur les mêmes paramètres : la charge, les vitesses d'entraînement et de glissement, la viscosité d'huile et la rugosité de surface. Deux paramètres sont analysés : la rugosité de surface et les vitesses définies par les angles d'orientation. Leur influence sur le coefficient de frottement est importante et ils doivent donc être considérés pour les questions de rendement.

Le quatrième chapitre présente le modèle thermique du pont, basé sur la méthode des réseaux thermiques. Les échanges thermiques entre les éléments du pont sont contrôlés par des résistances thermiques (conduction, convection, rayonnement). Les pertes sont estimées d'après les formules vues précédemment et la chaleur générée est injectée au nœud-source correspondant. Les pertes et les températures sont calculées grâce à un algorithme permettant d'obtenir des résultats en régime permanent ou transitoire. Le réseau thermique apparaît comme plus fiable, que ce soit par rapport à l'ISO/TR 14179-2 [9] pour les échanges thermiques avec l'environnement ou par rapport à l'ISO/TR 13989-2 [35] pour le calcul des températures de masse du couple conique. Une campagne d'essais sert à valider le modèle thermomécanique du pont en mesurant la température en de nombreux points de celui-ci. Les résultats montrent des écarts de température entre les éléments. La comparaison avec le modèle est cohérente pour les différentes conditions opératoires : les températures et les pertes calculées sont représentatives. Un autre pont est testé et modélisé et des résultats probants sont obtenus : le modèle thermomécanique peut servir d'outil de design. L'influence de paramètres comme le lubrifiant, la rugosité de surface des dentures et le flux d'air autour du carter est étudiée.

Finalement, le modèle thermomécanique du pont développé dans cette étude permet d'obtenir son rendement et la distribution de températures. En ce qui concerne les applications industrielles pour le Groupe Volvo, cet outil peut être utilisé lors du design pour d'une part optimiser le rendement du pont, la durabilité et la bruyance pouvant être aussi prises en compte grâce un logiciel préexistant. D'autre part, les défauts dus aux points chauds sur les roulements ou les engrenages peuvent être étudiés. En parallèle de cette étude, un modèle a également été établi sur les trains planétaires [36]. En le couplant avec le modèle de pont, il serait possible d'étudier les ponts à double réduction.

Des résultats expérimentaux doivent encore être analysés. En effet, deux ponts supplémentaires ont été testés lors des essais thermiques pour étudier d'autres paramètres : la méthode de taillage (face-hobbing et face-milling) et le ratio (4,625 et 2,643). Ces résultats d'essais sont importants afin de valider la cohérence du modèle pour des paramètres spécifiques.

La complexité du frottement dans les engrenages spiro-coniques et hypoïdes a été relevée. Les stries d'usinage sont obliques par rapport à la direction de roulement, or cela a un impact sur le coefficient de frottement [26]. De plus, le pignon et la couronne présentent des rugosités de surface différentes. Des essais sur machine bi-disque permettraient de caractériser leur coefficient de frottement. Cependant, sur cette machine, les directions de roulement des deux disques sont identiques, tandis que ce n'est pas le cas sur les spiro-coniques et les hypoïdes. Cette configuration particulière est reproduite sur certains bancs ([29], [30]), mais seule l'épaisseur de film est étudiée. Les essais préliminaires du Chapitre 3 montrent l'influence de l'angle d'orientation sur le coefficient de frottement. Il serait intéressant d'aller plus loin, en caractérisant plus précisément l'impact de cet angle et en testant également des éprouvettes rugueuses, comme sur la machine bi-disque.

Enfin, les roulements peuvent aussi être pointés. Ils sont actuellement considérés comme des éléments isothermes. Le modèle pourrait être affiné en décomposant les roulements en plusieurs éléments, afin de prendre en compte l'écart de température entre les bagues extérieure et intérieure. Cela permettrait une étude plus précise des défauts de roulement ou de l'expansion des bagues.

Nomenclature

Symbol	Meaning	Unit
A_0	Apparent contact area	m²
A_{air}	Ventilated housing area	m²
A_c	Actual average contact area	m²
A_{ca}	External housing area	m²
A_g	Arrangement constant, $A_g = 0.2$	-
A_i	Surface of plate i	m²
A_{oil}	Internal housing area	m²
a	Thermal diffusivity of oil	m²/s
B	Bearing inner ring width	mm
b	Gear width	m
b_c	Contact half-width	mm
b_t	Tooth width	mm
b_{tooth}	Gear tooth width	m
b_0	Reference value of gear tooth width, $b_0 = 10$ mm = 0.01 m	m
$C_{churning}$	Churning torque	N.m
C_m	Dimensionless churning torque	-
$C_{m\,exp}$	Experimental dimensionless churning torque	-
C_{sp}	Splash oil factor	-
C_1, C_2, C_3	Factors	-
c_i	Specific heat of element i	J/kg.K
D	Gear outside diameter	mm
d_M	REB mean diameter	mm
d_s	Seal counter diameter	mm
d_{sh}	Shaft diameter	mm
dl	Variable length of segment	mm
$\overrightarrow{dN^1_{2_{IJ}}}$	Elementary normal effort between pinion and crown gear	N
$\overrightarrow{dT^1_{2_{IJ}}}$	Elementary tangent friction effort between pinion and crown gear	N
E_{hypoid}	Hypoid gear efficiency	-
E_{spur}	Spur gear efficiency	-
F	Tooth normal force	N
F_D	Viscosity factor depending on temperature	-
F_a	Bearing axial load	N
F_n	Tooth normal load	N
F_r	Bearing radial load	N
F_w	Total face width of gear	mm
Fr	Froud number	-

f_0	Factor depending on type of bearing and method of lubrication	-
f_1	Factor depending on load and bearing design	-
f_g	Gear dip factor, $0 \leq f_g \leq 1$	-
G_{rr}, G_{sl}	Variable depending on bearing type, dimension and load	-
g	Standard gravity, $g = 9.81$	m/s²
H_{tooth}	Tooth height	m
H_v	Geometrical factor for spur and helical gears	-
H_v^{hypoid}	Geometrical factor for hypoid gears	-
h_c	Height of contact point above the lowest point of immersing gear	mm
h_{conv}	Heat transfer coefficient of convection with air	W/(m²K)
h_{e0}	Reference value of immersion depth, $h_{e0} = 10$ mm	mm
$h_{e1,e2}$	Tip circle immersion depth with oil level stationary	mm
$h_{e,max}$	Maximum tip circle immersion depth with oil level stationary	mm
h_i	Heat transfer coefficient	W/(m²K)
h_{lub}	Immersion depth of gear	m
h_{lub}/R_o	Immersion ratio	-
h_{oil}	Heat transfer coefficient of convection with oil	W/(m²K)
h_{rad}	Heat transfer coefficient of radiation	W/(m²K)
K_{roll}	Constant related to roller bearing	-
$K_{S1,S2}$	Constant depending on seal type and bearing type and size	-
k	Lubricant thermal conductivity	W/(m.K)
L	Characteristic dimension	m
l_h	Hydraulic length, $l_h = 4\,A_G/U_M$	mm
l_x	Flow length	m
M	Applied torque on gear	N.m
M_{SKF}	Bearing loss torque according to SKF formulation	N.mm
M_{b0}	No-load bearing loss torque	N.m
M_{b1}	Load bearing loss torque	N.m
M_{drag}	Bearing frictional moment of drag torque, churning, splashing…	N.mm
M_i	Mass of element i	kg
M_{in}	Input torque	N.m
M_{max}	Maximum gear torque	N.m
M_{out}	Output torque	N.m
M_{rr}	Bearing rolling frictional moment	N.mm
M_{seal}	Bearing seal friction moment	N.mm
M_{sl}	Bearing sliding frictional moment	N.mm
m_t	Transverse tooth module	-
Nu	Nusselt number	-
n	Rotational speed	rpm
nb	Number of thermal network nodes	-
$P_{bearing\ drag}$	Bearing drag power losses	W
$P_{bearing\ friction}$	Bearing friction power losses	W
$P_{churning}$	Oil churning power losses	W
$P_{churning}^{measured}$	Measured oil churning power losses	W
P_{gear}	Gear mesh friction power losses	W
P_h	Maximum Hertzian pressure	GPa

P_{hypoid}	Hypoid gear mesh friction power losses	W
P_i	Power loss along a complete contact line i	W
P_{in}	Input power of the axle	W
P_{load}	Load dependent losses	W
P_{loss}	Global power losses	W
$P_{no\ load}$	Load independent losses	W
P_{out}	Output power of the axle	W
P_{seal}	Seal power losses	W
P_{sides}	Churning losses of gear faces	kW
P_{tooth}	Churning losses of gear tooth	kW
P_1	Equivalent bearing load	N
Pr	Prandtl	-
p_{moy}	Mean contact pressure	Pa
Q	Heat flow	W
Q_i	Heat flow injected at node i	W
q	Evacuated heat quantity for a tooth face per width unit	W
R	Effective radius of curvature	m
R_{eq}	Equivalent radius of curvature	mm
R_f	Roughness factor	-
R_o	Outer radius of gear	m
R_p	Gear pitch radius	m
R_{proj}	Thermal resistance of oil projection	K/W
$R_{striction}$	Thermal resistance of striction	K/W
R_{th}	Thermal resistance	K/W
$R_{th}(i,j)$	Thermal resistance between elements i and j	K/W
Ra	Arithmetic average roughness	µm
Re	Reynolds number	-
Re'	Modified Reynolds number	-
Rz	Profile maximum height	µm
S_m	Immersed surface area	m²
SR	Slide-to-Roll Ratio	-
T_{air}	Air temperature	K
T_{ca}	Housing temperature	K
T_i, T_j	Temperature of elements i and j	K
T_{oil}	Oil temperature	K
T_{wall}	Housing wall temperature	K
t	Time	s
U	Overall heat transfer coefficient	W/(m²K)
V	Air flow velocity	m/s
$\overrightarrow{V_2^1}(M_{ij})$	Local velocity vector of sliding between pinion and gear teeth	m/s
V_1, V_2	Pinion and crown gear surface velocity	m/s
V_e	Entrainment velocity	m/s
V_{lub}	Oil volume	m³
$V_{r\,i}$	Mean surface velocity of gear i	m/s
V_s	Sliding velocity	m/s
$V_{s\,in}$	Sliding velocity	in/s

V_Σ	Sum of surface velocities	m/s
$V_{\Sigma\,\mathrm{in}}$	Sum of surface velocities	in/s
V_M	Variable function of oil level	-
v_{gm}	Mean sliding speed	m/s
v_t	Tangential speed	m/s
v_{t0}	Reference tangential speed, $v_{t0} = 10$ m/s	m/s
v_Σ	Resultant sum velocity	m/s
W_{lb}	Load by unit of length	lb/in
X_L	Lubricant factor	-
X_S	Lubrication factor	-
X_{mp}	Contact factor	-
Z	Gear teeth number	-
α_{oil}	Oil-side heat transfer coefficient	W/(m²K)
α_{conv}	Convection heat transfer coefficient	W/(m²K)
α_{rad}	Radiation heat transfer coefficient	W/(m²K)
β	Generated helix angle	°
β_s	Exponent depending on seal and bearing type	-
$\gamma_{1,2,3,4,5}$	Coefficients	-
ΔT	Temperature difference	K
δ	Velocity orientation angle	°
δ_e	Entrainment orientation angle	°
ϵ	Housing emissivity	-
$\overrightarrow{\epsilon_{ij}}$	Local orientation vector	-
η^*	Temperature ratio	-
η_{oil}	Lubricant dynamic viscosity at operating temperature	mPa.s
θ	Temperature	°C
θ_M	Gear bulk temperature	°C
θ_{flaint}	Mean flash temperature	K
θ_{oil}	Lubricating oil temperature	°C
θ_{proj}	Centrifugal projection angle	rad
μ	Friction coefficient	-
μ_{ij}	Local friction coefficient	-
μ_m	Mean friction coefficient	-
μ_{sl}	Sliding friction coefficient	-
ν_{air}	Kinematic viscosity of air	mm²/s
ν_{lub}	Kinematic viscosity of lubricant at operating temperature	mm²/s
ν_{40}	Oil kinematic viscosity at 40°C	mm²/s
ρ	Fluid density	-
σ	Stefan-Boltzman constant, $\sigma = 5.67 \times 10^{-8}$	W/(m²K⁴)
τ_{dry}	Shear stress due to dry friction	Pa
τ_{fluid}	Shear stress due to fluid friction	Pa
ϕ	Pressure angle	°
ϕ_{ish}	Inlet shear heating reduction factor	-
ϕ_{rs}	Kinematic replenishment/starvation reduction factor	-
$\phi_{spiral\ bevel}$	Spiral bevel gear loss factor	-
ϕ_{worm}	Worm gear loss factor	-

φ	Angle associated to the immersed surface of the gear	°
φ_{max}	Immersion angle of the gear	°
χ	Thermal effusivity of oil, $\chi = \sqrt{k\ \rho\ c}$ N/m.s$^{1/2}$.°C	N/m.s$^{1/2}$.°C
Ψ	Dimensionless number for oil projection	-
ψ_G	Gear mean spiral angle	°
ψ_P	Pinion mean spiral angle	°
Ω	Rotational speed	rad/s

Introduction

More and more goods are transported worldwide to ensure growth and economic development. Road is the most important mode of transportation for inland freight. This notably provides local supply of food, medicine, consumer goods, fuel, mail… Heavy duty vehicles like trucks play an important role in this delivery.

In Europe, heavy duty vehicles have to fulfil a regulation concerning emissions: Euro 0 dates from 1990 and the last version (Euro VI) was implemented end 2013. Truck manufacturers have then gradually improved their technology regarding emissions of particulates, NOx, HydroCarbons and Carbon Monoxide. Nevertheless, according to the European Commission, “trucks, buses and coaches produce about a quarter of CO_2 emissions from road transport in the EU and around 5% of the EU’s total greenhouse gas emissions – a greater share than international aviation or shipping” [1]. A specific CO2 regulation should be enforced in a near future.

One way to decrease emissions of particulates and CO2 is to improve fuel consumption: less fuel used means less oxides produced. Besides regulation perspectives, customers also ask for more efficient solutions of transport, mainly to decrease operating costs. Among efficiency improvements, the vehicle powertrain is still a key development for the truck industry: the engine is the source of power and the driveline must transmit it to the wheels. It is therefore important to determine precisely the power losses of the driveline in order to decrease them.

The present study focuses on the axle, which is the last part of the truck driveline. Its main component is a gear set: a spiral bevel or a hypoid one. This type of gear is special as it transmits power between

perpendicular shafts. It is used in power transmissions not only for automotive but also for aerospace applications. Most of the developments done on axles have centred on durability and noise aspects. For a long time, efficiency has been studied only through empirical approach. The first model for axle efficiency dates from 2013 [2] and studies automotive axles. These are similar in structure and working to truck axles, but operate in quite different conditions. This may bring in new issues.

Nevertheless, models developed for axle efficiency use only isothermal approaches: axle is considered at oil sump temperature. This hypothesis is however refuted by the experiments of Xu et al. [3] that highlight noticeable temperature differences between components. This can influence lubricant viscosity and so efficiency. Moreover, heat is still generated while systems tend toward higher compactness. Cooling and durability issues must then be kept in mind, as local hot spots can be created: gears and rolling element bearings can be subject to failure. The thermal behaviour of components and oil must be modelled and analysed.

Finally, the present study aims to develop a thermo-mechanical model for truck axles. A global approach is used to take into account the whole system. Power losses and thermal exchanges are then estimated thanks to simple models in order to allow a fast increment and to be used at design stage. Axle efficiency and temperature distribution are thus obtained.

The first chapter describes the truck drive axle and defines its power losses. Literature is reviewed regarding axle efficiency and thermal behaviour. As most of the studies concern car and medium duty axles, differences with truck axles are highlighted. Different methods to calculate power losses for mechanical transmissions in general are summarized there.

The second chapter attempts to estimate power losses of truck axles. Experiments are conducted to measure the efficiency of a specific axle. Power losses are then calculated according to the different methods and compared to each other's and to test results. The aim is to determine if a simplified analytical approach suffices to estimate axle efficiency. Churning losses are then studied more thoroughly. As experimental data concern only oil temperature and global power loss, estimation of global power loss is validated but not the power loss breakdown.

The third chapter focuses on the major power loss source of truck axles: gear mesh friction. The gear set of an axle is a spiral bevel or a hypoid one, mainly for durability reasons. However, there is more sliding at the meshing of hypoid gears and so more friction, due to the offset between pinion and crown gear. As kinematic and friction aspects of hypoid gears are not well understood, they are investigated in this part. Manufacturing process is also considered from cutting to finishing, as this induces gear characteristics, like macro- and micro-geometry. Regarding power loss estimation, global and local approaches are compared. Finally, formulae for friction coefficient calculation are reviewed and some influential parameters are studied.

The last chapter refers to the model of axle thermal behaviour. Due to power losses, heat is produced at different point of the system. This can induce local hot spots and modify oil properties. Efficiency and durability can be influenced. A thermo-mechanical model is then developed thanks to the thermal network method. This model and an isothermal one are compared regarding thermal exchanges and temperature evaluation. The selected model is validated against specific measurements of global power loss and temperature of several components. Influential parameters are finally investigated.

1. Literature review

1. Introduction

This first chapter is a review of previous works on axles regarding both efficiency and thermal behaviour. The aim is to have a basis of theoretical and experimental studies in order to drive the development of a global thermo-mechanical approach of the axle. Indeed, the use of simple models is a key to address efficiency issue at design stage, as this allows for a fast increment.

The chapter begins with a description of the truck drive axle and its specificities. As most of the studies concern car and medium duty axles, it is important to underline the differences. Axle efficiency is then presented thanks to a definition of power loss sources. Previous efficiency tests and models on axles are reviewed and each power loss contribution is detailed with general calculation methods. The thermal behaviour is finally investigated through testing results and global models from the literature.

2. Drive axle architecture

The mechanical system studied here is a truck drive axle, which is part of the truck driveline. This component, presented on Figure 1.1, has three main roles: i) to transmit power from the drive train to the wheel shafts (both parts are usually perpendicular); ii) to make a final speed reduction; iii) to allow the vehicle to turn without wheel slippage, thanks to the differential.

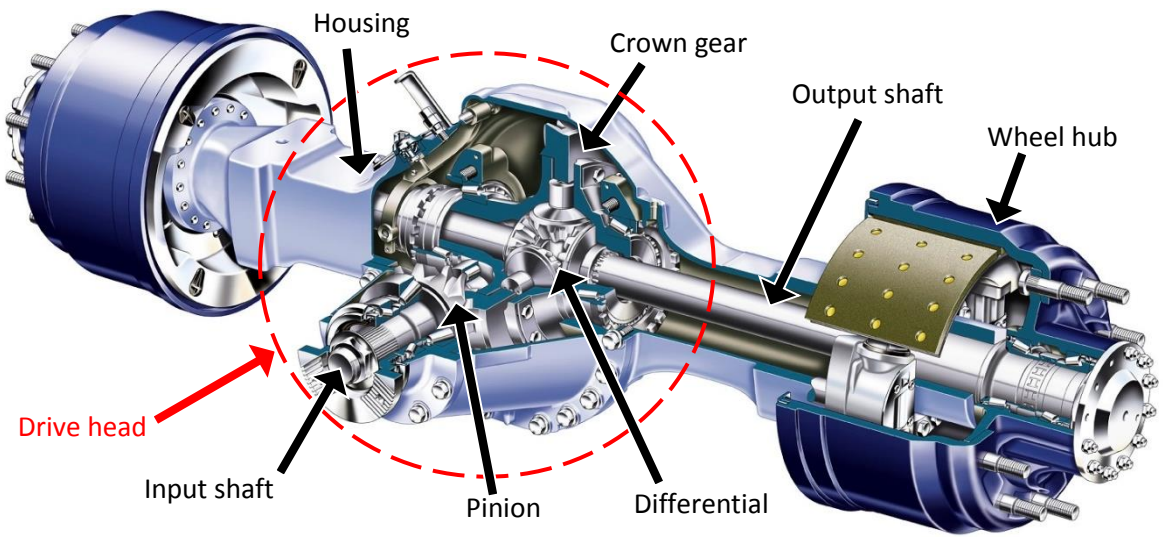

Figure 1.1: Main elements of a truck drive axle

On a truck, there could be one to four drive axles depending on vehicle use. An example of a truck with three drive axles is presented on Figure 1.2: as this vehicle is for severe construction application, it needs to have all wheels driven. Subsequently, only the drive axle is considered in this study and is simply called an axle.

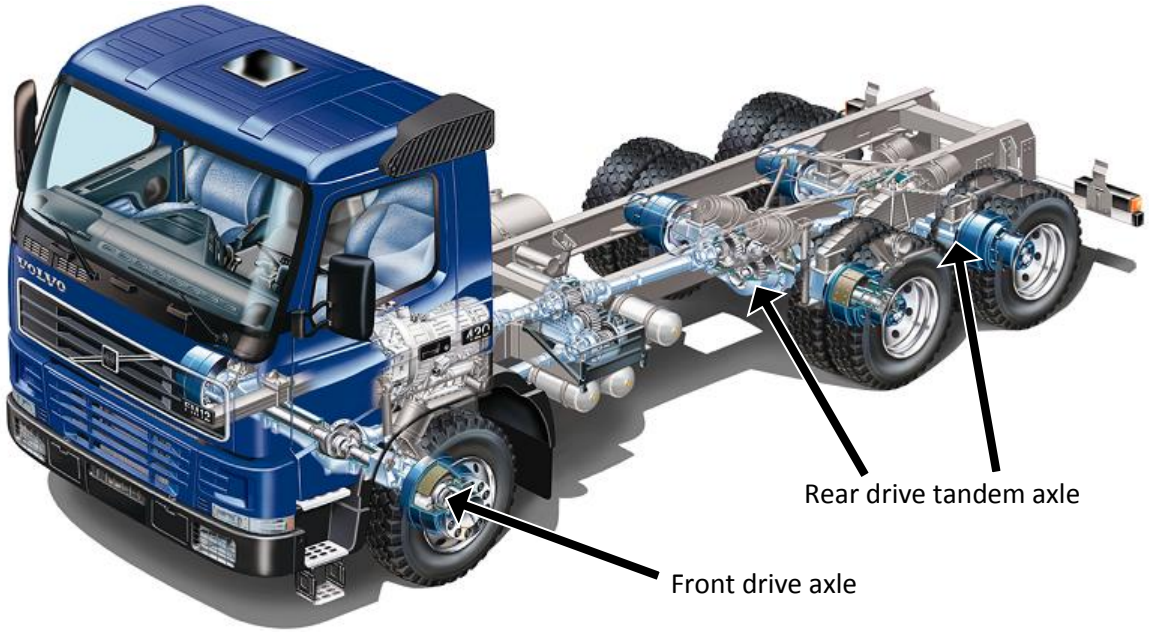

Figure 1.2: An all-wheel drive truck (6x6)

Single reduction axles ensure speed reduction with the gear set only. This gear set is a spiral bevel or a hypoid one, as presented on Figure 1.3. The main difference is the offset between pinion and crown gear axis, which is null for the spiral bevel gear. Thanks to this offset, it is possible to position the propeller shaft lower, which is helpful in terms of architecture. Moreover, this induces a bigger hypoid pinion gear than the spiral bevel one for a crown gear of the same size; pinion is so more durable, notably regarding tooth bending resistance, and ground clearance is kept. The hypoid gear has also a

better contact ratio and is then quieter. However, there is more sliding at hypoid gear mesh due to pinion offset.

An amboid gear has inversely an offset above pinion axis (or negative offset). This is an unusual case for axles but is interesting for architecture aspects. It is not studied here.

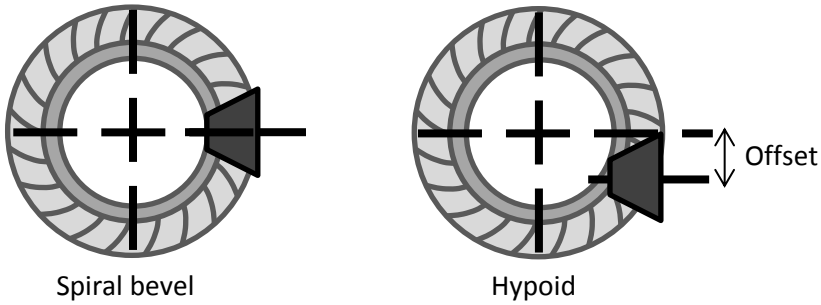

Figure 1.3: Architecture of spiral bevel and hypoid gear set

For hub reduction axles, a second reduction occurs in wheel hubs. This allows to transmit higher torques and is used for severe applications.

In addition to the gear set, the drive head is composed of several rolling element bearings, which are highlighted on Figure 1.4 by dashed frames in green. There are two tapered roller bearings supporting the differential and at least two others on the input shaft. An additional cylindrical roller bearing can reinforce the input shaft on some axles.

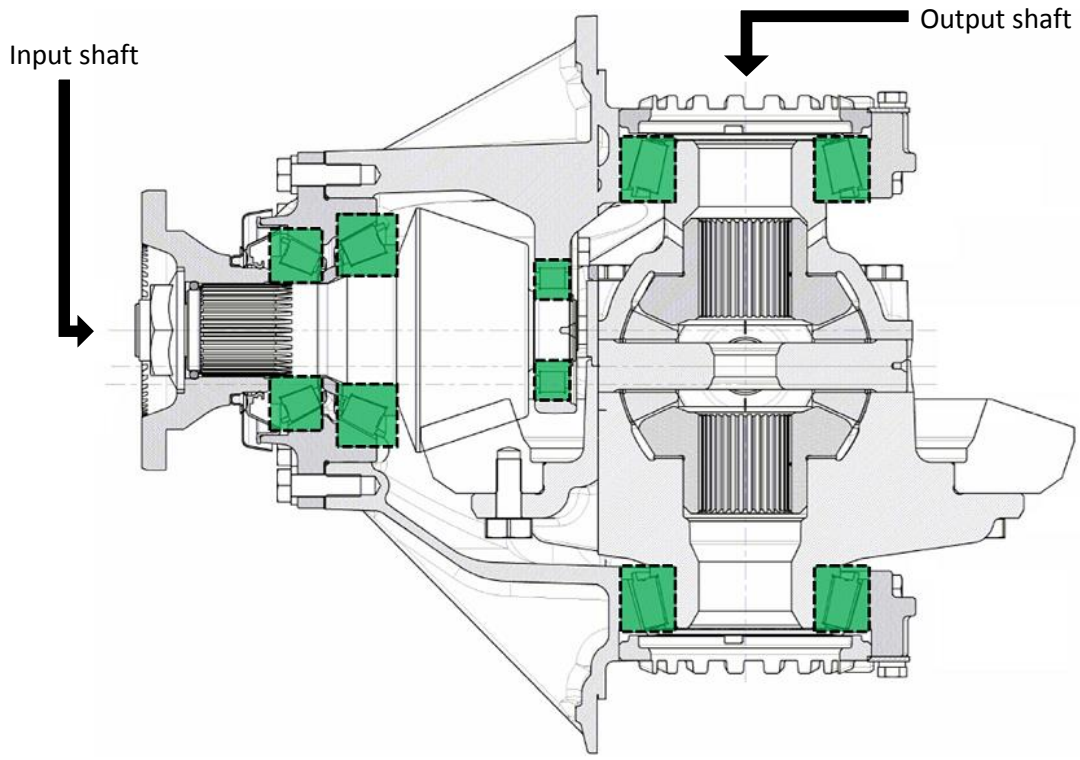

Figure 1.4: Example of a drive head architecture

The axle housing is partially filled with oil. This ensures the dip lubrication of gear set and differential bearings. Input shaft bearings are splash lubricated thanks to the crown gear or dip lubricated depending on oil level and axle installation angle.

Automobile and truck axles have the same architecture, but truck ones are larger: crown wheel has a larger diameter, oil sump volume is more important; but the power transmitted is also higher. However, this may lead to comparable efficiency. For information only, some figures are displayed in Table 1.1 regarding light, medium and heavy duty axles. Light duty axles are for car application. Medium duty axles are for distribution trucks while heavy duty ones are for long haul and construction trucks.

Table 1.1: Representative figures for axles depending on application and duty

	Car application [1]	**Truck application** [2]	
	Light duty	**Medium duty**	**Heavy duty**
Ratio	2 to 3.5	2 to 6	2 to 10
Input speed (rpm)	1000 to 6000	500 to 1500	500 to 2000
Input power (kW)	20 to 150	20 to 200	60 to 400
Crown wheel size (mm)	200 to 250	300 to 450	300 to 500
Oil volume (L)	1 to 4	7 to 18	12 to 28

3. Axle efficiency

3.1. Drive axle power losses

The axle generates power losses: some of its components are source of dissipation. The main source of friction is the gear set, especially for a hypoid one, as sliding is more important. Dip lubrication of the gear set generates non-negligible oil churning losses. Rolling element bearings induce losses due to friction between rolling elements and races and also due to dip lubrication, or at least splash lubrication. The seals generate friction between lip and rotating shaft.

The efficiency is simply defined as the ratio between output and input power:

$$\text{Efficiency} = \frac{P_{out}}{P_{in}} \tag{1.1}$$

If the gear set is considered as having no transmission error, this is equivalent to:

$$\text{Efficiency} = \frac{1}{ratio}\frac{M_{out}}{M_{in}} \tag{1.2}$$

where M_{out} and M_{in} are the output and input torques, and $ratio$ is the axle ratio.

[1] Based on publications [4], [6], [7], [15], [37]
[2] Based on Volvo Group data [69]

3.2. Experimental and theoretical investigations

Axle efficiency study started through experimental means. A first laboratory procedure was proposed in 1979 by Hobson [4]. He considered different testing methods to evaluate efficiency: measurement of heat rejection, axle temperature rise, balance beam method, and torque and speed measurements. The two thermal approaches were eliminated as they require a long time for stabilisation. Finally, the torque and speed measurements solution was selected to quantify power losses due to its reduced complexity and its advantages over the balance beam method. A complete test map is then defined, but also a standard test to allow a first approach, as represented on Figure 1.5. This standard test is based on US conditions with an oil temperature at 66°C. The rated torque is calculated according to the Gross Combination Weight (GCW) of the vehicle.

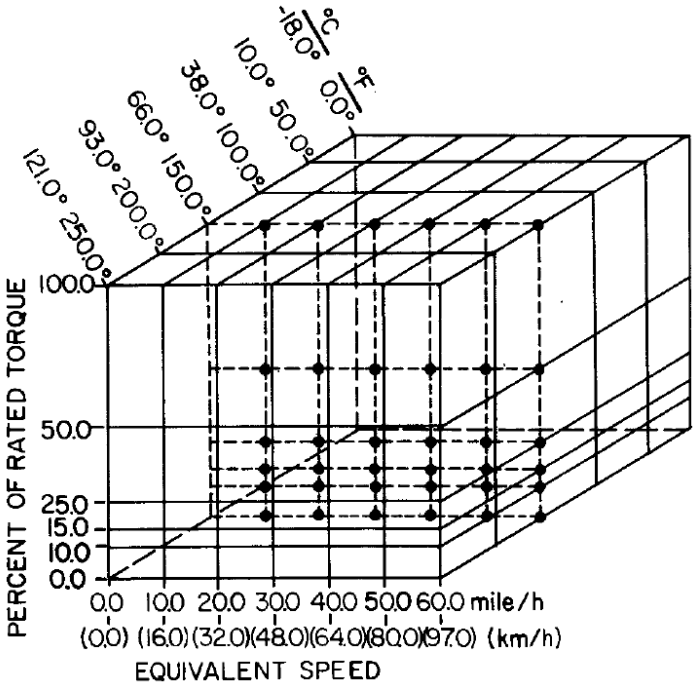

Figure 1.5: Matrix of potential data points (standard test indicated by dashed grid) [4]

In 1988, Winter and Wech [5] worked with a back-to-back test rig for hypoid gears, combining four axles and operating under car conditions. They investigated various factors as gear geometry, operating conditions, lubricant… Hypoid offset and lubricant appear to have a big influence on axle efficiency, power losses increasing with higher offset. This is mostly true under heavy load as gear friction is the major source, whereas bearing preload, dip lubrication and sliding seals predominate at high speed. More recently in 2012, Xu et al. [6] performed tests on a car axle to study the influence of bearing preload, oil volume and temperature. Oil temperature is considered as the first influencing parameter. Bearing preload comes in second position and last oil volume. Nevertheless, it is important to note that oil quantity inside a car axle is limited: here, volume varies between 1.5L and 3.5L. Moreover, operating temperature depends mostly on the heat generated by power losses: if a lubricant generates less losses at a same temperature level, then temperature will decrease slightly and so the efficiency. There could finally be no gain.

Concerning theoretical studies on axles, Kolekar et al. [2] established an efficiency model in 2013. Their quasi-static formula considers the different power loss sources and is coupled to a transient thermal analysis for calculating oil temperature. They estimated the total power loss for two lubricants on various simulated cycles and showed that the lubricant choice depending on drive application is a key in terms of efficiency. Formulae used in this study are analysed in detail in Part 3.3. Mohammadpour et al. [18] focused on hypoid gears in axles with a multi-body dynamics model using an EHL contact. They investigated the gear pair efficiency and its link with Noise Vibration Harshness refinement. They underlined that this NVH refinement is a better indicator of the transmission efficiency than an efficiency measurement or calculation on a drive cycle. Indeed, a drive cycle is generally established for specific road conditions.

Kakavas et al. [7] recently developed both experimental and model approaches on axle efficiency. Each source of power losses is evaluated on a complete drive cycle for cars, the NEDC (New European Drive Cycle). Then, the global power loss is calculated and compared to measurements, obtaining good agreement. Figure 1.6 presents the simulated power loss for each source of dissipation. When the vehicle accelerates, high torque is applied: gear friction and bearing losses are predominant; when speed is stabilised and so torque is lower, gear friction drops. For this type of drive cycle and according to these calculations, the major contribution is apparently due to bearings, up to almost the total power loss.

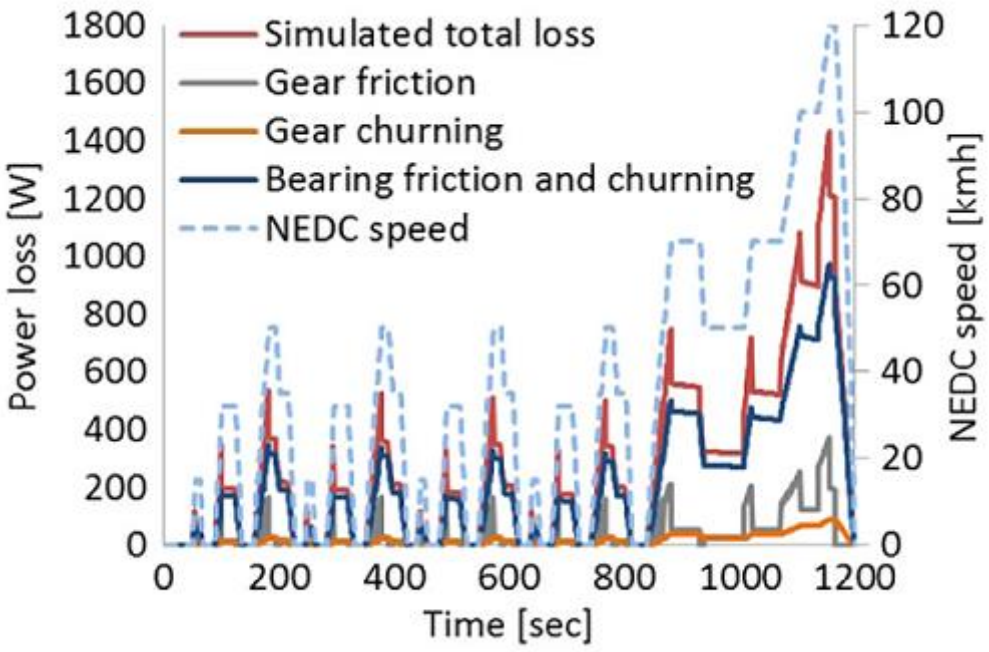

Figure 1.6: Breakdown of estimated axle loss over the NEDC [7]

Takaki et al. [37] evaluated power losses in car axles, mainly on churning, bearing and meshing friction. According to their measurements presented on Figure 1.7, more than 50% of friction losses are due to hypoid gear meshing. This observation is in contradiction to the study of Kakavas et al., as torque and speed inputs are at the same level; however, the operating temperature is not specified by Takaki et al., while it is quite low (25°C to 40°C) for Kakavas et al.. Takaki et al. then focused on gear mesh friction. They proceeded to an analysis on gear parameters such as spiral angle, offset, face width, ease off…

and defined a solution to increase efficiency without losing on durability and noise characteristics. As Winter and Wech [5], they concluded that a smaller offset but also a smaller spiral angle generates lower friction; for durability aspects, this can be balanced with a larger face width. On the opposite, ease off and surface modifications appear to have almost no influence on hypoid efficiency.

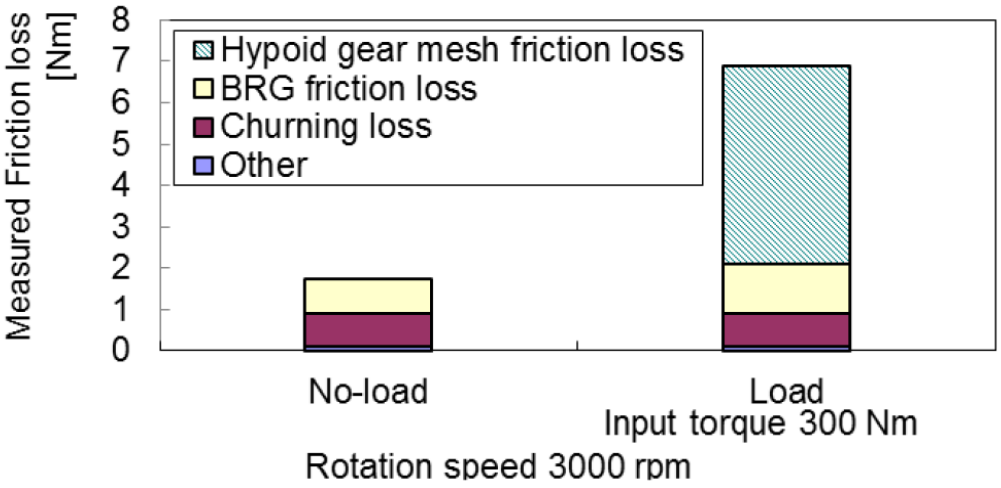

Figure 1.7: Breakdown of loss torque on experiments of Takaki et al. [37]

3.3. General power loss calculations

The power losses generated in the axle and described previously are separated in load-dependent and load-independent losses [38]:

$$P_{loss} = P_{load} + P_{no\ load} \tag{1.3}$$

With:

$$P_{load} = P_{gear} + P_{bearing\ friction} \tag{1.4}$$

$$P_{no\ load} = P_{bearing\ drag} + P_{churning} + P_{seal} \tag{1.5}$$

These power loss sources have been thoroughly studied for various systems, and standards notably exist, but not specifically for axles. They are detailed hereafter. Since the axle works at low speeds, up to an order of 2000 rpm on input side, load-dependent losses have a major impact [26]. Thus, great attention is paid to friction losses at gear mesh but also in rolling element bearings.

3.3.1. Shaft seal friction

Seal power loss results of the friction between seal lip and rotating shaft. This is no major contribution for power losses in axles as shown by the experimental results of Takaki et al. [37] on Figure 1.7. This is explained by the low rotational speeds of the system. Simple approaches are thus summarized, as the one proposed by Simrit [8] which is used in the ISO/TR 14179-2 [9], or by Linke [10] and by Kettler [11] who are taking the temperature into account.

Freudenberg-Simrit formula defines shaft seal friction losses as:

$$P_{seal} = 7.69 \times 10^{-6} \, {d_{sh}}^2 \, n \tag{1.6}$$

where d_{sh} is the shaft diameter (mm) and n the rotational speed (rpm).

Kettler formula is close to Simrit one, but it takes the temperature influence on oil viscosity by means of a coefficient F_D:

$$P_{seal} = 7{,}9163 \times 10^{-6} \, F_D \, {\mathrm{d}_{sh}}^2 \, n \tag{1.7}$$

Linke proposed another type of formula:

$$P_{seal} = [145 - 1.6 \times \theta + 350 \times \log\log(\nu_{40} + 0.8)] \times 10^{-7} \, {d_{sh}}^2 \, n \tag{1.8}$$

where θ is the temperature (°C), and ν_{40} is the oil kinematic viscosity at 40°C (mm²/s).

A comparison between Simrit and Linke models[3] is performed for a 75W-90 lubricant at 80°C (ν_{40} =120mm²/s), which is typical for a European long haul truck application on highway. Results are represented on Figure 1.8: losses increase with speed for both solutions but Linke gives a higher estimation than Simrit. The amount of seal losses is still negligible regarding the global power losses of the axle that are up to several kilowatts. As a matter of fact, they are often neglected ([2], [7]). However, when considering load-independent losses only, seal losses can contribute.

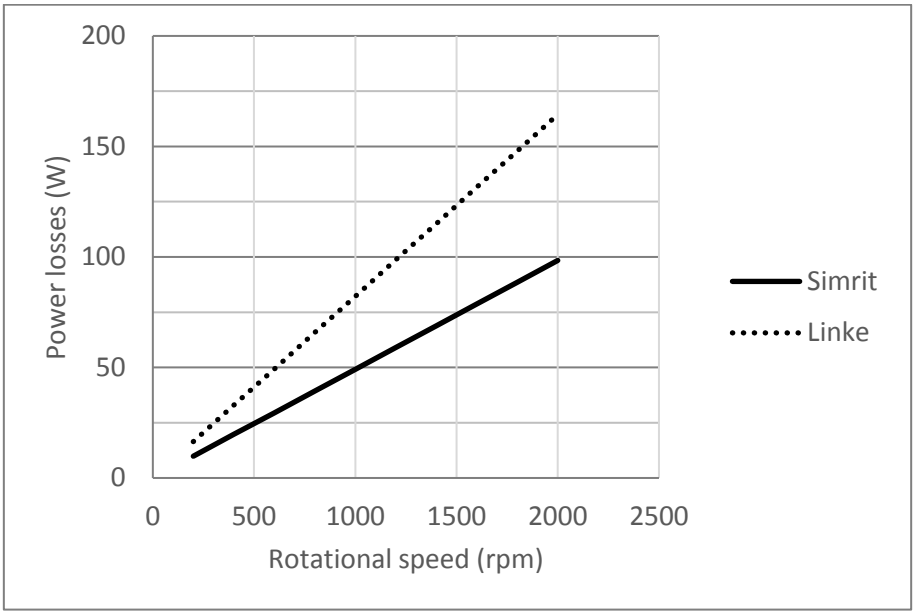

Figure 1.8: Comparison of seal power losses for Simrit and Linke formulae (d_{sh} = 80 mm)

No discrimination between formulae can be done based on speed comparison. Results according to temperature are then plotted on Figure 1.9. A less viscous oil is also tested in this case (ν_{40} =40mm²/s). When temperature increases, the estimation according to Linke formula comes close to zero. This is

[3] As the work from Kettler [11] is not accessible, the definition of coefficient F_D is not known and no comparison with Kettler formula can be held.

even more pronounced for a less viscous lubricant. As application boundaries are not clear for Linke formula, this can lead to incoherent results. It is then discarded for this study.

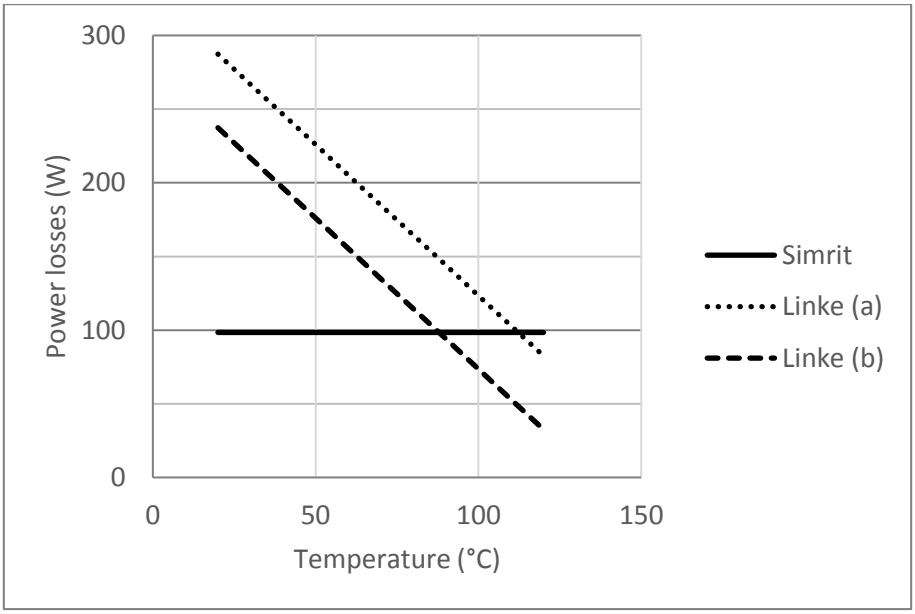

Figure 1.9: Temperature comparison of seal power losses for Simrit and Linke formulae with (a) viscous oil (ν_{40} =120mm²/s) and (b) fluid oil (ν_{40} =40mm²/s)

3.3.2. Rolling Element Bearing drag and friction

Rolling Element Bearings (REB) generate friction losses as their rolling elements are rolling and sliding on raceways and also drag losses due to the lubricant. These power losses are defined as:

$$P_{bearing\ drag} + P_{bearing\ friction} = (M_{b0} + M_{b1})\ \frac{\pi\ n}{30} \tag{1.9}$$

where M_{b0} is the no-load bearing loss torque or drag torque (N.m), M_{b1} the load bearing loss torque or friction torque (N.m), and n is the rotational speed (rpm).

Harris [12] established well-known formulae for these torque losses. Typically, for tapered or cylindrical roller bearings, loss torques are:

$$M_{b0} = 1.6\ f_0\ {d_M}^3 \times 10^{-8} \qquad \text{for } \nu_{lub}\ n < 2000\ \text{mm}^2/\text{s.min} \tag{1.10}$$

$$M_{b0} = f_0\ (\nu_{lub}\ n)^{2/3}\ {d_M}^3 \times 10^{-10} \qquad \text{for } \nu_{lub}\ n \geq 2000\ \text{mm}^2/\text{s.min} \tag{1.11}$$

$$M_{b1} = f_1\ P_1\ d_M \times 10^{-3} \tag{1.12}$$

where f_0 and f_1 are factors depending respectively on bearing and lubrication types, and on bearing design and load, ν_{lub} is the lubricant kinematic viscosity (mm²/s), d_M is the bearing mean diameter (mm) and P_1 is the equivalent bearing load (N). For the ISO technical report 14179-2 [9], Eschmann based his formulae on Harris work to calculate friction and drag forces.

SKF Group [13] developed his own numerical formula, using a total frictional moment:

$$M_{SKF} = \phi_{ish}\phi_{rs}\mathrm{M_{rr}} + M_{sl} + M_{seal} + M_{drag} \tag{1.13}$$

M_{rr} is the rolling frictional moment (N.mm) and M_{sl} is the sliding frictional moment (N.mm), defined as:

$$\mathrm{M_{rr}} = G_{rr}(\nu_{lub}\, n)^{0.6} \tag{1.14}$$

$$M_{sl} = G_{sl}\, \mu_{sl} \tag{1.15}$$

where G_{rr} and G_{sl} are variables depending on bearing type, dimension and load, and μ_{sl} is a sliding friction coefficient. M_{rr} and M_{sl} are thus load dependent moments.

M_{seal} is the seal friction moment (N.mm) and M_{drag} is the frictional moment of drag torque, churning, splashing… (N.mm) defined as:

$$M_{seal} = K_{S1}\, {d_s}^{\beta_s} + K_{S2} \tag{1.16}$$

$$M_{drag} = 10 \times V_M\, K_{roll}\, B\, {d_M}^4\, n^2 \tag{1.17}$$

where K_{S1} and K_{S2} are constant depending on seal type and bearing type and size, d_s is the seal counter diameter (mm), β_s is an exponent depending on seal and bearing type, V_M is a variable function of oil level, K_{roll} is a constant related to roller bearing, and B is the bearing inner ring width (mm).

Finally, these moments can be categorised in the same manner as for Harris formula, depending on load or on rotational speed:

$$M_{b0} = \left(M_{seal} + M_{drag}\right) \times 10^{-3} \tag{1.18}$$

$$M_{b1} = (\phi_{ish}\phi_{rs}\mathrm{M_{rr}} + M_{sl}) \times 10^{-3} \tag{1.19}$$

ϕ_{ish} and ϕ_{rs} are factors to take into account the effects of respectively shear heating and starvation. Kakavas et al. [7] and Kolekar et al. [2], refer to SKF approach in their work.

An analysis is conducted for both Harris and SKF formulae, considering a tapered roller bearing with a mean diameter of 110 mm. This bearing is located on the input shaft of the axle. Losses are calculated under load ($F_r = 7000$ N and $F_a = 15000$ N) for speed increasing from 200 to 2000 rpm and lubricant at 80°C. Figure 1.10 displays the results. A great discrepancy between Harris and SKF is observed: with increasing speed, power losses according to SKF are doubled compared to Harris estimations.

An important fact in this configuration is that axial load is predominant on radial load, conducting to a particular equivalent load on the bearing. If axial load is virtually decreased, the ratio is inversed: the results obtained in this configuration are plotted on Figure 1.11. The two models are then more coherent.

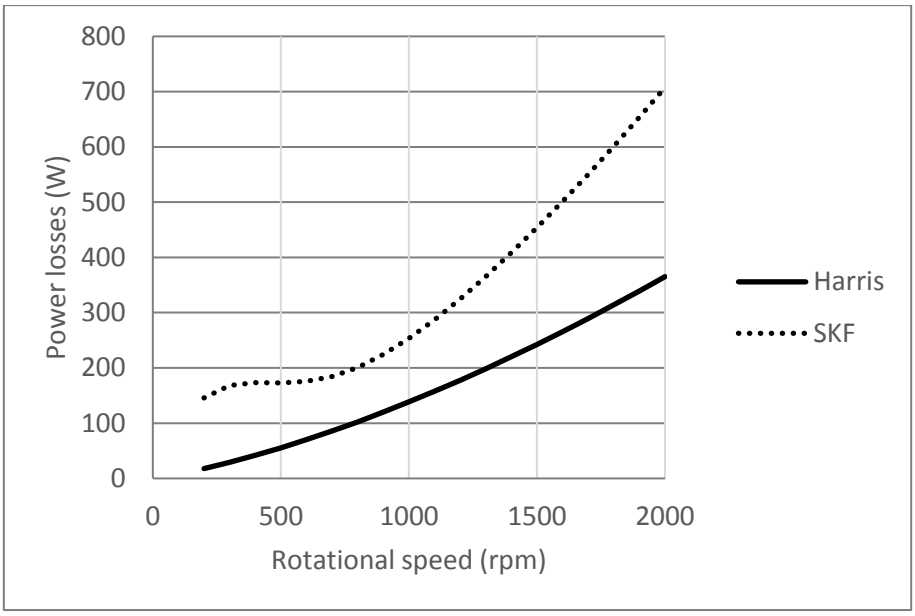

Figure 1.10: REB power losses according to Harris and SKF formulae

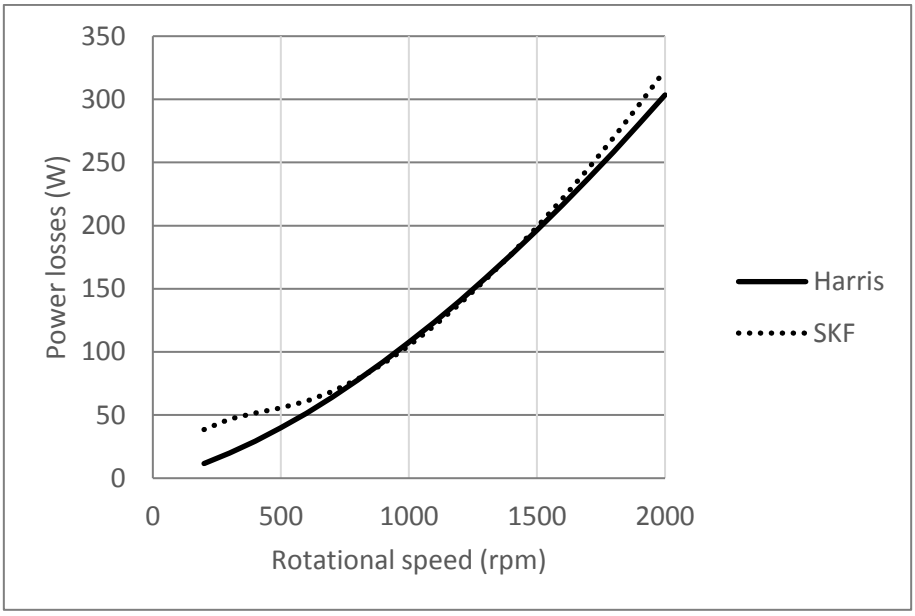

Figure 1.11: REB power losses according to Harris and SKF formulae considering a different load share

In order to understand the difference between both formulae, losses are decomposed into their different contributions: no-load losses and load losses. Breakdown of the results is plotted on Figure 1.12. Concerning SKF, Figure 1.12 (a) highlights the big contribution of load losses in comparison to no-load losses when speed is over 1000 rpm. On Figure 1.12 (b), Harris solution presents a relative equilibrium between friction and drag; the drag becomes predominant with speed, which seems coherent.

The discrepancy observed between Harris and SKF models under specific conditions raises the question of the application domain validity. Indeed, it seems that SKF formula overestimates load losses when the rolling element bearing is loaded mainly radially.

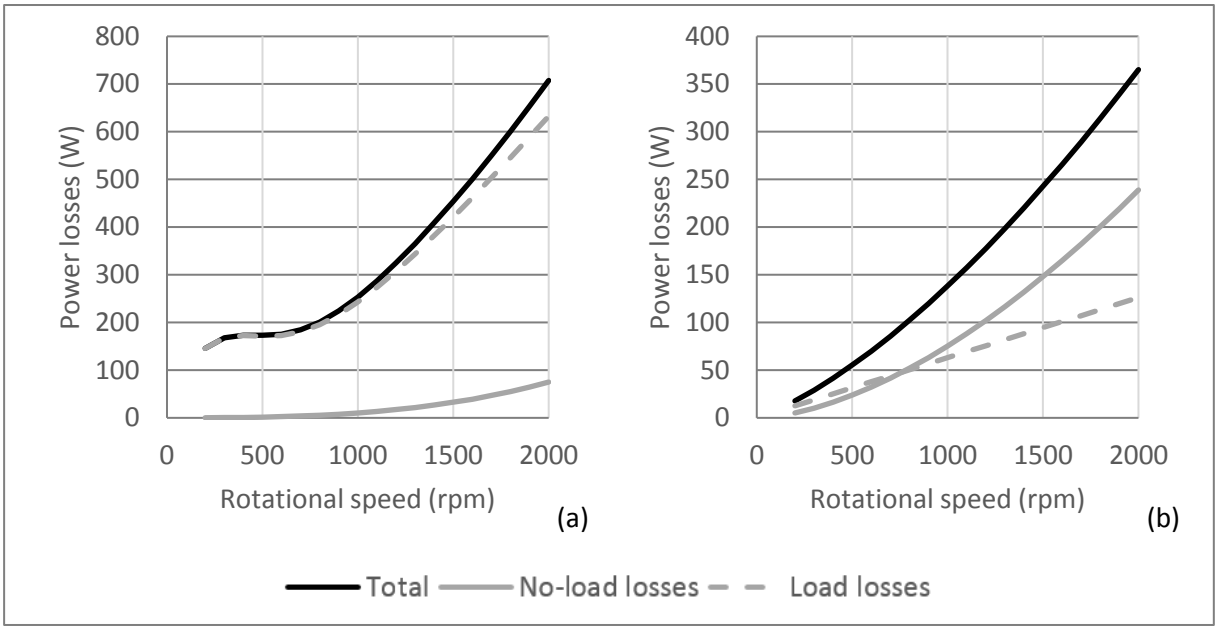

Figure 1.12: Comparison of no-load and load losses for (a) SKF formula and (b) Harris formula

In tapered roller bearings, contacts occur between roller ends and ring flanges, due to axial load. The shape and size of this contact depend on bearing design and operating conditions. But it is generally a large contact, which generates friction. As Harris formulae are empirically determined, this phenomena is taken into account. SKF model is a numerical approach and it does not explicitly consider this loss.

Nevertheless, further investigations on the complete bearing set of the axle are held in the second chapter.

3.3.3. Oil churning

The aim of gear lubrication is to ensure both contact durability and heat evacuation. As gear peripheral speeds are rather low in truck applications, dip lubrication is used for the gear set. This induces oil churning: oil is moved by the gears, splashed inside the housing, and trapped between the mating gear teeth.

Investigations on churning started with experiments on smooth plane discs by Daily and Nece [39]. Luke and Olver [40] proceeded to a wide experimental study on dip-lubricated spur gears in order to understand the discrepancy between the formulae proposed previously by Boness (1989), Terekhov (1991) and Höhn (1996). Changenet et al. [41] described the existence of distinct flow regimes: at low speeds, diameter is the major influential parameter on churning losses; at higher speeds, face width has more importance. Daily and Nece [39], and more recently Changenet and Velex [42], investigated the influence of axial and radial clearances thanks to deflectors and flanges. According to these various studies on spur gears, it appears that the main factors influencing churning losses are: rotational speed, gear diameter and casing.

Few studies have been conducted on churning losses of spiral bevel and hypoid gears. However, two ISO technical reports (14179-1 [14] and 14179-2 [9]) propose a formula to calculate these losses, whatever the gear.

ISO/TR 14179-1 decomposes churning losses as the sum of the ones associated with gear faces P_{sides} (kW) and the ones of tooth surfaces P_{tooth} (kW). For gear faces, it is defined as:

$$P_{sides} = \frac{1.474 \times f_g \, \nu_{lub} \, n^3 \, D^{5.7}}{A_g \times 10^{26}} \tag{1.20}$$

where f_g is a gear dip factor ($0 \leq f_g \leq 1$), ν_{lub} is the kinematic viscosity of oil at operating temperature(mm²/s), n is the rotational speed (rpm), D is the gear outside diameter (mm), and A_g is the arrangement constant (=0,2). For tooth surfaces, it is:

$$P_{tooth} = \frac{7.37 \times f_g \, \nu_{lub} \, n^3 \, D^{4.7} \, F_w \left(\frac{R_f}{\sqrt{tan\,\beta}} \right)}{A_g \times 10^{26}} \tag{1.21}$$

where F_w is the total face width (mm), and β is the generated helix angle (°) (if $\beta < 10°$ then consider $\beta = 10°$). R_f is a roughness factor which is defined as:

$$R_f = 7.93 - \frac{4.648}{m_t} \tag{1.22}$$

where m_t is the transverse tooth module.

The ISO technical report 14179-2 calculates the churning losses according to Mauz formula:

$$P_{churning} = C_{sp} \, C_1 \exp\left(C_2 \left(\frac{v_t}{v_{t0}} \right) \right) \Omega \tag{1.23}$$

where C_{sp} is a splash oil factor, C_1 and C_2 are factors depending on tooth width and immersion depth, v_t is the tangential speed (m/s), v_{t0} is the reference tangential speed (=10 m/s), and Ω is the gear angular velocity (rad/s). The various factors are defined as:

$$C_{sp} = \left(\frac{4 \, h_{e,max}}{3 \, h_c} \right)^{1.5} \frac{2 \, h_c}{l_h} \tag{1.24}$$

$$C_1 = 0.063 \left(\frac{h_{e1} + h_{e2}}{h_{e0}} \right) + 0.0128 \left(\frac{b_{tooth}}{b_0} \right)^3 \tag{1.25}$$

$$C_2 = \frac{h_{e1} + h_{e2}}{80 \, h_{e0}} + 0.2 \tag{1.26}$$

where $h_{e1,e2}$ are the tip circle immersion depths of both gear and $h_{e,max}$ the maximum one (mm), h_{e0} is the reference value of immersion depth (mm), h_c is the height of point of contact (mm), l_h is the hydraulic length (mm), b_{tooth} is the tooth width (m), and b_0 its reference value (=0.01 m).

Figure 1.13 illustrates the various immersions considered. An interesting choice of this formula is not to take into account the lubricant viscosity.

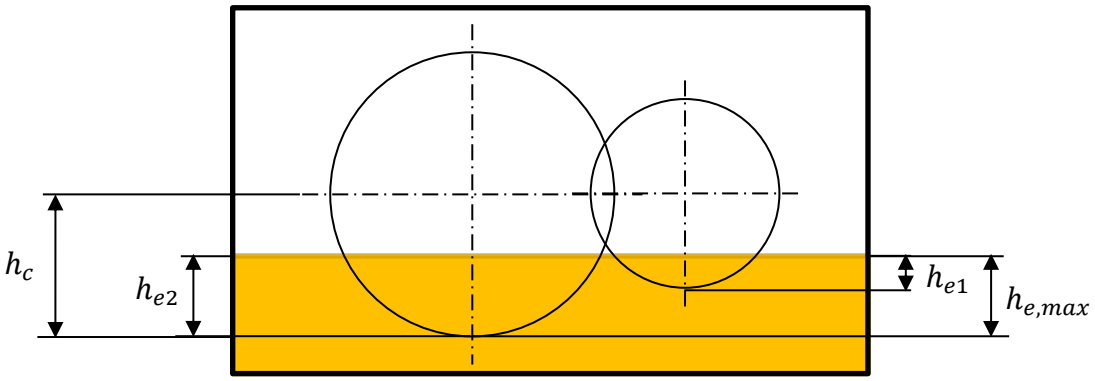

Figure 1.13: Splash oil factor according to Mauz [9]

In his work on an automotive axle, Jeon [15] studied churning losses for hypoid gears and established a specific relationship:

$$P_{churning} = \frac{1}{2}\,\rho\,\Omega^3\,b\,{R_p}^2\,S_m\,C_m \tag{1.27}$$

where ρ is the lubricant density, Ω is the gear angular velocity (rad/s), b is the gear width (m), R_p is the gear pitch radius (m), S_m is the gear immersed surface area (m²). C_m is the dimensionless drag torque, defined as:

$$C_m = 2.19\left(\frac{h_{lub}}{R_p}\right)^{0.15}\left(\frac{V_{lub}}{{R_p}^3}\right)^{-0.20} Re^{-0.25}\,Fr^{-0.53} \tag{1.28}$$

where h_{lub} is the gear immersion depth (m), V_{lub} is the oil sump volume (m³), Re is the Reynolds number, and Fr is the Froud number.

Jeon proposed a second formula of the dimensionless drag torque to consider an air-oil mix around gears:

$$C_m = 10\left(\frac{h_{lub}}{R_p}\right)^{0.18}\left(\frac{V_{lub}}{{R_p}^3}\right)^{-0.22} Re^{-0.42}\,Fr^{-0.45}\left(\frac{\nu_{lub}}{\nu_{air}}\right)^{-0.18} \tag{1.29}$$

where ν_{lub} and ν_{air} are respectively lubricant and air kinematic viscosity (mm²/s). Kakavas et al. [7] used this last formula.

Calculations are made according to ISO technical reports and Jeon formulae for a spiral bevel gear pair. The diameter of the crown wheel is 157 mm. Equation (1.28) is used for calculations according to Jeon. The results for speed increasing from 200 to 2000 rpm are presented on Figure 1.14. The three methods give different estimations of churning losses, which can be more than doubled. Each solution is then tested on the axle case in the second chapter.

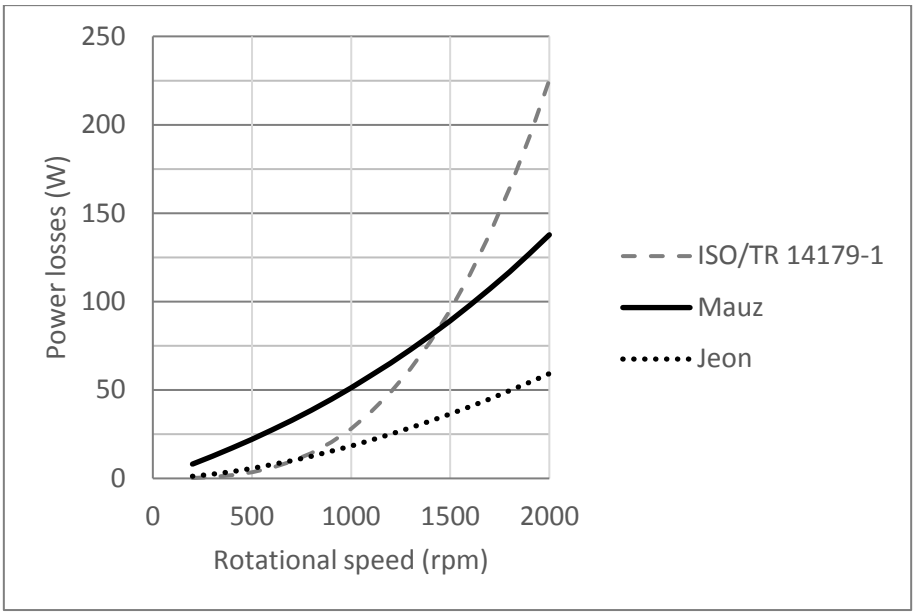

Figure 1.14: Comparison between Jeon and ISO technical report formulae for churning losses

Kolekar et al. [2] used Equations (1.27) and (1.28) proposed by Jeon, and combined it with Changenet and Velex approach for a gear pair [43]. Indeed, contrary to Mauz formula, Equation (1.27) is valid for a single gear only; the gear pair is considered by adding both contributions. Changenet and Velex [43] investigated the churning losses of a meshing spur gear, especially by testing different rotation directions as represented on Figure 1.15. They showed that the addition of the two individual contributions is realistic for a clockwise rotation, but not for a counter-clockwise rotation, which generates higher losses.

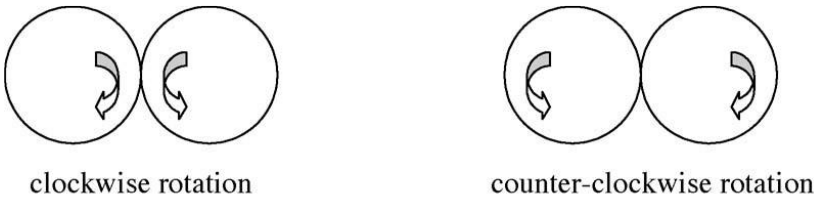

Figure 1.15: Definition of rotation directions [43]

The gear set of a rear axle rotates clockwise when the vehicle is going forward. Thus, according to the solution of Changenet and Velex, the contribution of pinion and crown gear should just be added. However, for a meshed gear pair, Jeon [15] measured a greater increase of churning losses: this can be due to oil trapping between gear teeth or to a modification of the oil flow around the crown gear, as observed by Jeon. The power loss of the pair is then bigger than the addition of each gear contribution.

3.3.4. Hypoid gear mesh friction

The hypoid gear set is the main component of the drive axle and it can be also the main source of friction. Due to pinion offset, sliding occurs all along the contact line. This induces an efficiency of

roughly 96% to 98% [24]. The gear mesh friction loss is commonly described as the product of friction coefficient, load or applied pressure, and relative velocity between gear teeth surfaces.

The efficiency of the hypoid gear set was studied by Buckingham [16], who considers the hypoid as a combination between a spiral bevel gear and a worm gear. In 1949, he expressed its efficiency as:

$$E_{hypoid} = \frac{1}{1 + \phi_{spiral\ bevel} + \phi_{worm}} \tag{1.30}$$

where $\phi_{spiral\ bevel}$ is the friction loss factor of spiral bevel gear taking into account the conjugate gear tooth action, and ϕ_{worm} is the friction loss factor of worm gear considering the sliding velocities. Details of the formula are given in Annex 1.A. However, Buckingham does not use directly the sliding velocity in his formula; he determines a friction coefficient depending on sliding velocity value.

In 1975, Coleman [17] proposed another formula of the hypoid efficiency:

$$E_{hypoid} = \frac{100}{1 + \sqrt{M_{max}/M}\left(0.01 + \mu\ \sec\phi\ \sqrt{(\tan\psi_P - \tan\psi_G)^2 + 0.0225}\right)} \tag{1.31}$$

where M and M_{max} are respectively the applied and maximum gear torque (N.m), ϕ is the pressure angle (°), and ψ_P and ψ_G are pinion and gear mean spiral angle (°). The friction coefficient μ ranges from 0.01 to 0.12 depending on lubricant and tooth surface, but is generally equal to 0.05. According to this formula, the efficiency can be improved by reducing pressure and spiral angles or by increasing operating load.

ISO/TR 14179-2 [9] uses the work of Niemann and Winter (1983) to determine hypoid friction loss. An equivalent helical gear substitutes for the hypoid one for gear mesh calculation. Hypoid friction power loss is defined as:

$$P_{hypoid} = F_n\ v_{gm}\ \mu_m \tag{1.32}$$

where F_n is the tooth normal load (N), v_{gm} is the mean sliding speed (m/s), and μ_m is the mean friction coefficient. Details of the formula are also given in Annex 1.A.

These three analytical formulae (Buckingham, Coleman and ISO/TR 14179-2) present different structures. To hold a comparison, an analogy to spur and helical gears efficiency is proposed: according to Velex and Ville [44], classical efficiency formulae for spur and helical gears given by Buckingham (1949) or Niemann and Winter (1989) can be expressed as:

$$E_{spur} = 1 - \mu\ H_v \tag{1.33}$$

where H_v is a factor depending on spur or helical gear geometry. This means that load and speed can have an influence only through friction coefficient and that efficiency depends only on gear geometry if friction coefficient is kept constant. Concerning hypoid efficiency, the ISO technical report formula can be expressed with a similar structure:

$$E_{hypoid} = 1 - \frac{P_{hypoid}}{P_{in}} = 1 - \mu_m\ H_v^{hypoid} \tag{1.34}$$

where H_v^{hypoid} is a factor depending on hypoid gear geometry. This is less evident for the two other formulae.

A comparison is then conducted on hypoid efficiency formulae with friction coefficient at 0.05, as proposed by Coleman. Efficiency is calculated for an input torque increasing from 200 N.m to 2000 N.m. Main characteristics of the hypoid gear pair considered are given in Table 1.2.

Table 1.2: Gear set characteristics

	Pinion	Crown gear
Number of teeth	8	37
Outer diameter (mm)	134.6	428
Face angle (°)	15.18	74.57
Pressure angle (°)	21.35	/
Spiral angle (°)	45	34.42
Offset (mm)	35	/

Results are plotted on Figure 1.16 and are valid whatever the speed. Buckingham and ISO/TR 14179-2 formulae give a constant efficiency, while Coleman formula increases with load. This variation of efficiency with load is not in agreement with the previous analysis, as the friction coefficient is fixed. Coleman formula is then discarded.

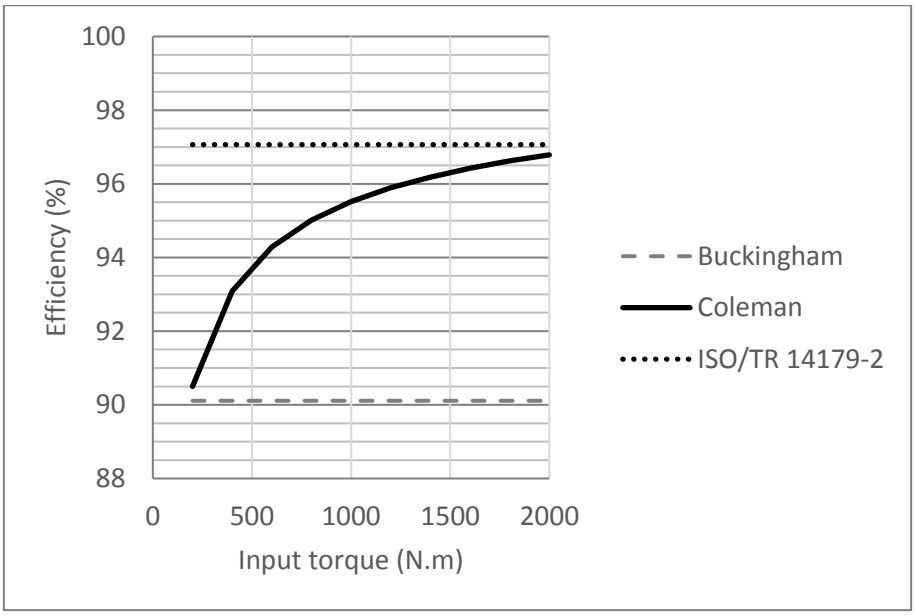

Figure 1.16: Hypoid gear efficiency according to Buckingham, Coleman and ISO/TR 14179-2 formulae (fixed friction coefficient = 0.05)

Although their behaviour is similar, Buckingham and ISO technical report formulae show great discrepancy. This can be explain by the fixed friction coefficient: for Buckingham, it should rely only on sliding velocity, while load, oil viscosity and surface roughness also have an influence for ISO technical report.

Kakavas et al. [7] and Kolekar et al. [2] used an approach similar to the ISO technical report or to Buckingham with average values too.

Besides these analytical formulae of the gear efficiency, some discretisation approaches of the contact friction are researched. Xu and Kahraman [45] developed a method using a hypoid gear contact analysis model and a gear pair mechanical efficiency formula. They also proposed a friction coefficient calculation based on an elastohydrodynamic lubrication model. They identified surface roughness amplitude and lubricant temperature as influential parameters of efficiency. Kolivand et al. [24] improved this previous work, notably by taking into account surface asperities for the friction coefficient calculations.

Takaki et al. [37] evaluates the hypoid efficiency by calculating friction loss at each meshing point along the contact path based on real tooth geometry.

In a first time, analytical formulae (Buckingham and ISO/TR 14179-2) are used for hypoid gear loss estimation in the second chapter. The appropriateness of this global approach is then questioned.

4. Axle thermal behaviour

The power loss sources reviewed in the previous part generate heat at different points of the system. In order to establish a thermo-mechanical model of the axle, it is necessary to know more precisely the thermal exchanges with the environment but also inside the axle. This allows to determine not only the oil temperature, but also the operating temperature of each component. Indeed, this information is important to predict bearing and gear failures, like scoring [20], pitting, or even scuffing. It seems also rather imprecise to calculate the gear set bulk temperature considering only oil temperature and gears operating condition [35], ignoring the global system around it. Previous work has already shown some limitations for this kind of method: for example, the position of jet lubrication is not taken into account while influencing bulk temperature [46].

4.1. Thermal behaviour of the complete axle

Most of axle studies focus only on power losses ([4]–[6], [18]). Operating conditions are thus all under control. Among them, oil sump temperature is set up to a target value. For those who deal with thermal aspects, a common hypothesis is to consider the axle as an isothermal system at oil sump temperature. Indeed, Kolekar et al. [2] developed a simple thermal model of the axle, where the whole axle is at oil sump temperature. This temperature is calculated, as forced convection between air and axle occurs. On-road cycles are thus simulated and the efficiency is evaluated depending on environmental conditions. Kakavas et al. [7] adopted a similar approach in order to work on the NEDC complete drive cycle. The calculated oil temperature is in good agreement with the measured one.

This kind of approach may be sufficient to estimate the global efficiency; but at the same time, component temperatures are an indicator of the power loss share between the different sources. For example, no experimental evidence confirms the breakdown presented on Figure 1.6 by Kakavas et al.

If the real power loss split is unknown, it can be difficult to know which component should be improved.

Some have investigated the thermal behaviour of the axle using experimental means: Hurley [19] and Xu et al. [3] recorded the temperature at multiple points on axle parts. For various operating conditions, they observed the temperature difference between components: for example on Figure 1.17, pinion tooth (sensors P1-P2) are hotter than input shaft bearing inner races (sensors P3-P4 and P6-P7). This information helps to estimate that the amount of power losses generated by the gear mesh is bigger than the one of the bearings for the tested conditions.

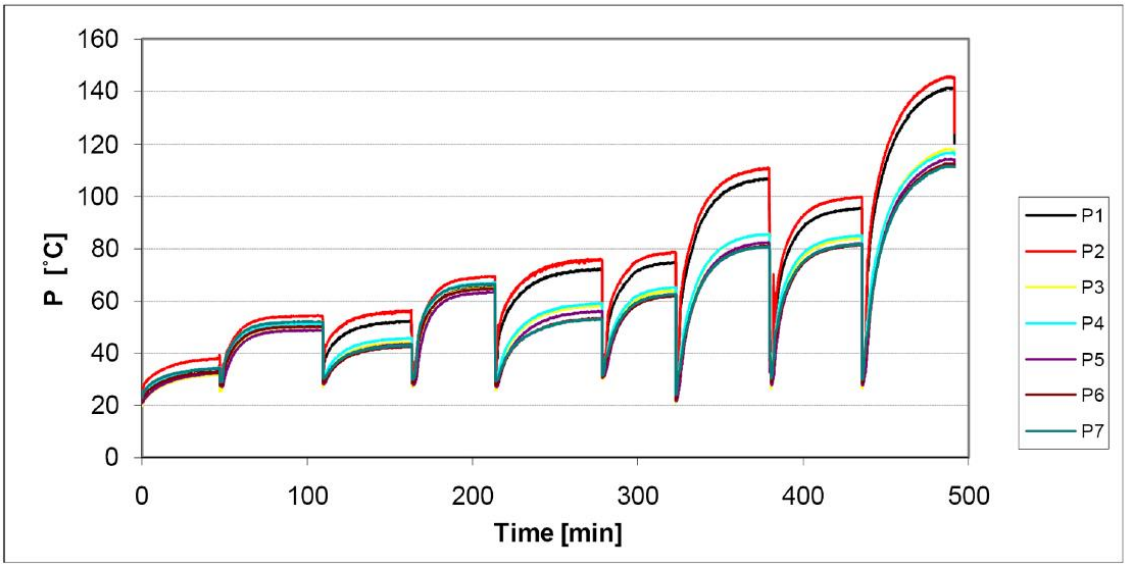

Figure 1.17: Pinion temperature variations in the nine point loaded test with 45 mph simulated winds speed [3]

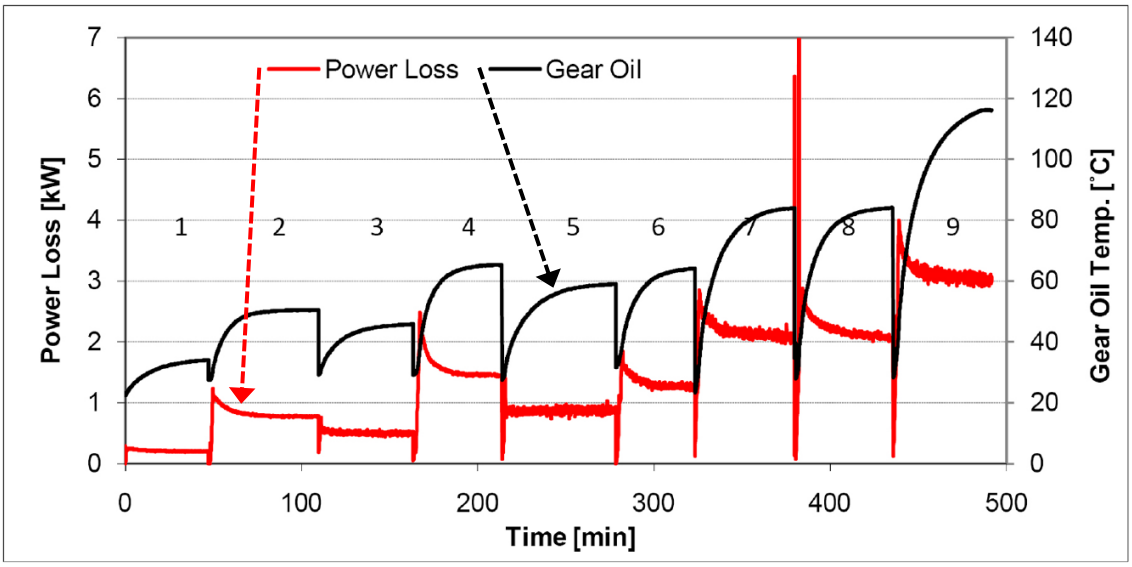

Figure 1.18: Power loss and gear oil temperature in the nine point loaded test with 45 mph simulated wind speed [3]

On Figure 1.18, the power loss decreases during each load step, as oil temperature increases and oil becomes less viscous. Another interesting point is to compare oil temperature presented on Figure 1.18 to pinion temperature of Figure 1.17 for the same test. It appears clearly that gear bulk temperature is higher than oil temperature, up to 30°C. It is then important to choose the correct temperature for durability issues, but also for the friction coefficient calculation. A local approach on the gear set can be investigated to address these issues.

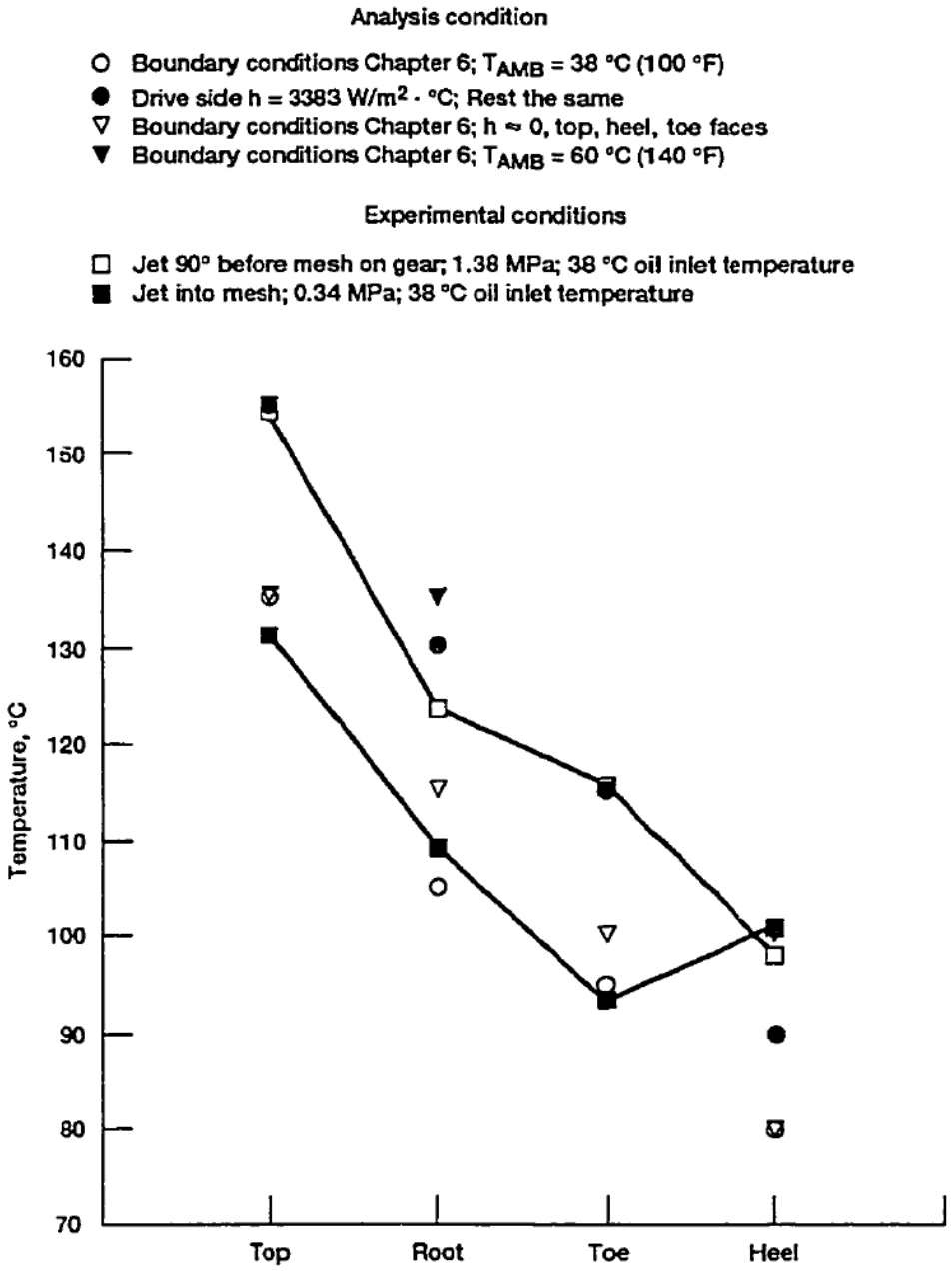

Figure 1.19: Comparison of bulk measurements from thermocouples to time averaged boundary condition analytical results [20]

4.2. Thermal behaviour of the gear set

Some have focused specifically on the gear set, as Handschuh [20] or Wang et al. [21].

Handschuh conducted both experimental and modelling approaches for aerospace applications. He notably measured the pinion bulk temperature and observed a great influence of load and lubrication jet position. He also developed a thermal model of one tooth, representative of a complete gear: a three-dimensional Finite Element model of the tooth allows to consider the heat flux along active profile; at each time step, a new Hertzian contact is activated. Figure 1.19 exposed analytical and experimental results on bulk temperatures and showed that top and root are the hottest part of the tooth.

Wang et al. proposed a Finite Element model of a gear pair to calculate the heat generated by meshing friction, considering a constant friction coefficient ($\mu = 0.05$). For computational time saving, a transient thermal analysis of one tooth is then used with its heat accumulating with cycles. Thanks to this model, a comparative study is made for three different contact patterns as showed on Figure 1.20. For an identical friction coefficient, the most tilted and extended contact (case 3) has a reduced frictional heat generation. Thus, as this induces fewer losses, they also addressed the efficiency issue.

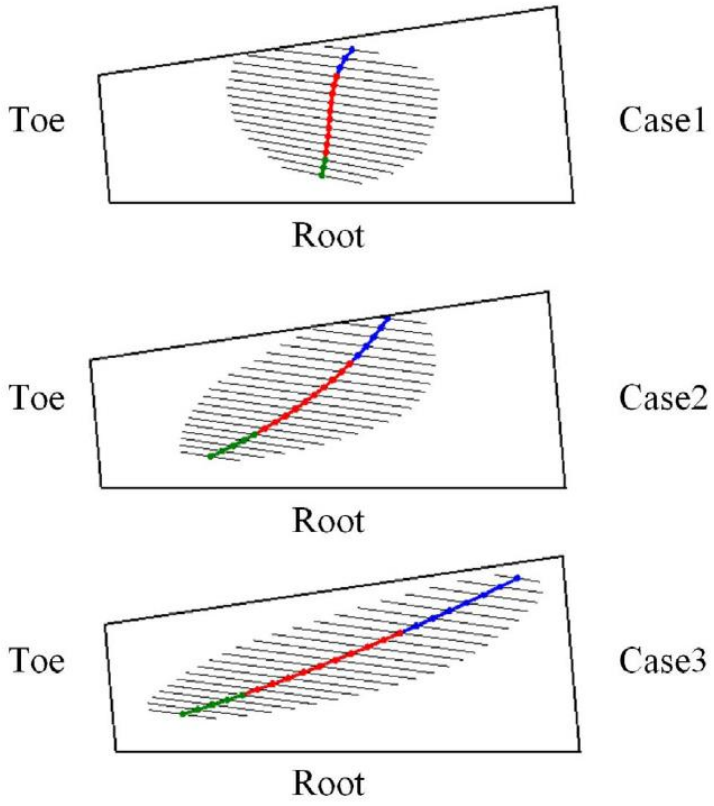

Figure 1.20: Tooth contact patterns for different pinion machine-setting parameters [21]

On both study, the heat flux is equally divided between the mating gears.

It is not specified how the global system can influence on local temperature of the gear mesh contact. Nevertheless it seems important to consider the axle as a whole, with components at different

temperatures exchanging between them. Finally, no present study has developed a model to obtain these components temperature.

5. Conclusion

The truck drive axle was first presented with its main components and specificities. The most important part is the gear set, which is a spiral bevel or a hypoid one. The literature mainly presents studies on automotive and light to medium duty axles. These are similar in structure and working to heavy duty axles, but their operating conditions and dimensions are different. This may result in new issues.

The power loss sources of the axle were identified: shaft seal friction, rolling element bearing drag and friction, oil churning and gear mesh friction. Previous studies evaluated globally or separately these power losses by experimental or theoretical means. Influential parameters are highlighted through these investigations: operating conditions, such as lubricant temperature, rotational speed, load…; gear macro-geometry parameters, like hypoid offset, spiral angle, face width, diameter, ease-off… and micro-geometry parameters, like surface roughness.

Nevertheless, these proposed power loss models do not always agree with each other. Depending on application and operating conditions, great discrepancies can be observed between estimations. Some of the models used by Kolekar et al. [2] or Kakavas et al. [7] are under question. Appropriate formulae should be selected for the truck axle case, after specific comparisons held in the next chapter.

The thermal behaviour of the axle was investigated thanks to isothermal approaches and for efficiency purposes. This has some limitations, as the estimated power loss breakdown cannot be validated with only oil temperature. Some thorough testing campaigns underline the temperature difference between components like gears and bearings, suggesting power loss amount. Oil sump temperature appears not to be the correct parameter for durability and friction aspects. Specific local thermal models were developed for the spiral bevel gear set to address both durability and efficiency issues, and support the importance of contact pattern.

However, no detailed thermal model for axles has been developed yet to compute both efficiency and temperatures. Thus, the aim of this work is to develop a thermo-mechanical model of the axle.

2. Axle power losses

1. Introduction

The first chapter has underlined that different relationships can be used to estimate the power loss sources of a truck axle. This one aims to analyse if simplified analytical approaches, as the one presented in ISO/TR 14179-2 [9], are suitable to quantify the efficiency of such gear unit. As a first approach, the efficiency of a specific axle is estimated through experiments and compared to various theoretical formulae.

2. Truck axle efficiency

2.1. Considered drive axle

This study focuses on a single reduction axle for a long haul application. The major part of interest is the drive head. The technical drawing of Figure 2.1 helps to locate the main studied components:

- Pinion gear (A) and crown gear (B)
- Rolling Element Bearings (1) to (5)
- Seal (6)

Although it is also represented on Figure 2.1, the differential is considered unused, as if the truck was running along a straight line. Then, it does not generate any power loss.

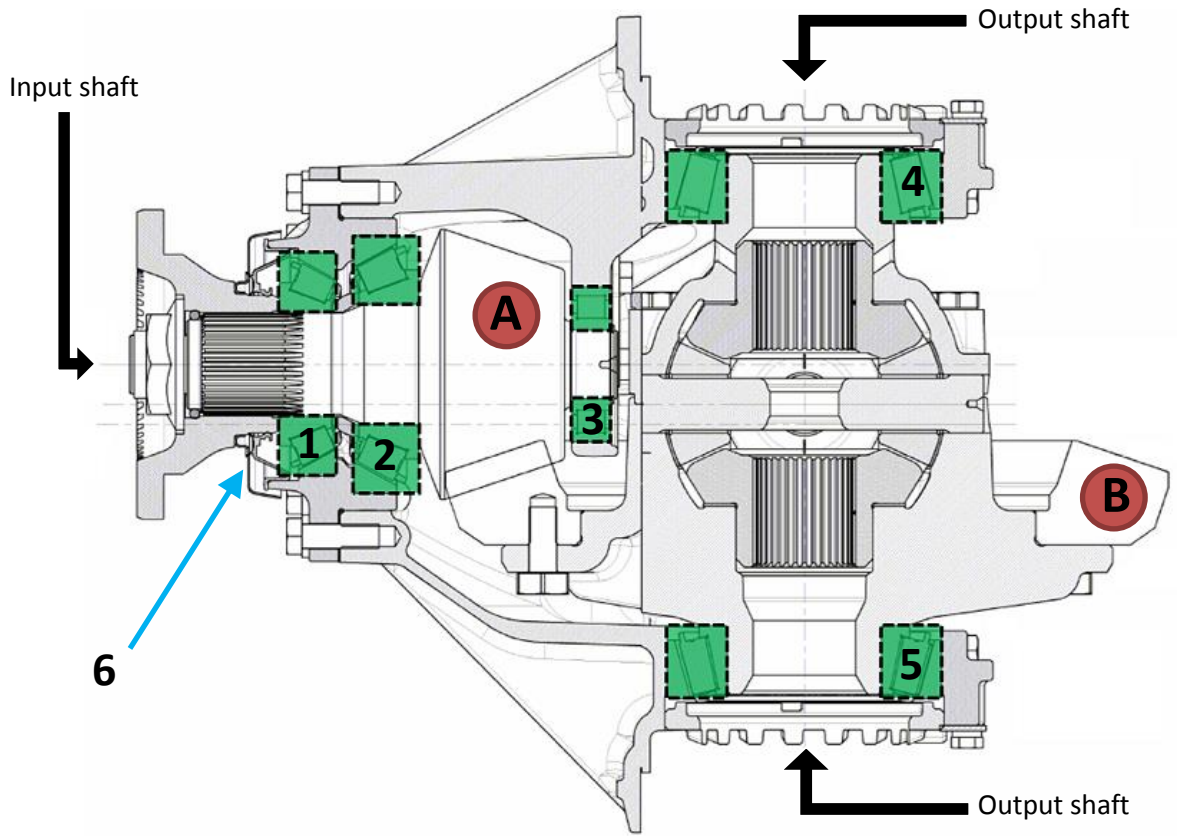

Figure 2.1: Location of main components on drive head technical drawing

The gear set is an hypoid one and its characteristics are given in Table 2.1. The main features of the bearings are listed in Table 2.2. The seal is a one lip seal with a shaft diameter of 80 mm.

The axle housing is partially filled with oil: the normal fill corresponds to 14L.

2.2. Efficiency tests

Tests were conducted in order to measure the efficiency of the considered axle, using a similar procedure than Hobson's one [4]. Two types of tests were conducted: with and without an applied input torque.

For tests with an applied load, the bench described on Figure 2.2 (a) was used. It allows for measurement of input and output torques and rotational speeds. Two types of dynamometers are used: torque range is of 3kN.m on the input shaft and 5kN.m on each output with an accuracy of +/- 1.5N.m.

For tests without an applied load, the bench described on Figure 2.2 (b) was used. The output shafts and the wheel hubs are dismantled and so just remains the drive head of the axle. Only the input torque and rotational speed are measured. The torque range of the dynamometer is of 500N.m with an accuracy of +/-0.15N.m.

Table 2.1: Axle gear set characteristics

	Pinion (A)	Crown gear (B)
Number of teeth	8	37
Outer diameter (mm)	134.6	428
Width (mm)	85	62
Face width (mm)	74.4	63
Face angle (°)	15.18	74.57
Pressure angle (°)	21.35	/
Spiral angle (°)	45	34.42
Hand of spiral	LH	RH
Offset (mm)	35	/

Table 2.2: Rolling Element Bearings characteristics

	Tail REB (1)	Head REB (2)	Pilot REB (3)	Differential REB (4) and (5)
Bearing designation	31312	31314	NJK308	32218F
Roller type	tapered	tapered	cylindrical	tapered
Inner diameter (mm)	60	70	40	90
Outer diameter (mm)	130	150	90	160
Width (mm)	33.5	38	23	42.5
Preload (kN)	20	0	0	4 / 0

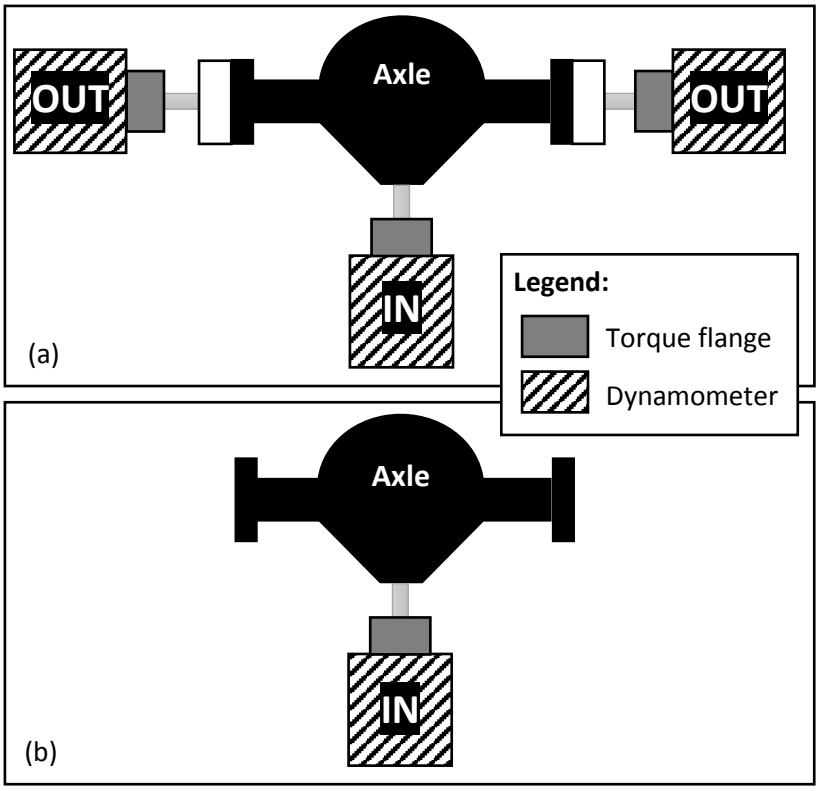

Figure 2.2: Test bench set-up for (a) load dependent test and (b) no load test

On both benches, oil temperature in the sump is monitored and maintained at 80°C by the use of fans. Characteristics of the oil used for the tests are presented in Table 2.3.

The brand-new axle is run-in in order to obtain stabilised power losses. For a typical condition under load (120kW), the variation of power losses between two break-in cycles must be lower than 200W in order to consider that the running-in procedure is achieved.

During load-dependent losses tests, the three conditions presented on Table 2.4 are reproduced. Condition B is a typical highway condition for long haul trucks in Europe. For each of these conditions, two different oil levels are considered: a normal and a high one, respectively corresponding to 14L and 20L of oil volume.

Table 2.3: Oil characteristics

Kinematic viscosity @ 40°C (cSt)	120
Kinematic viscosity @ 100°C (cSt)	15.9
Viscosity Index	140
Density @ 15°C	0.860
Oil type	Synthetic

Table 2.4: Conditions of load-dependent losses tests

Condition	**A**	**B**	**C**
Vehicle speed (km/h)	80		
Power input (kW)	60	120	240

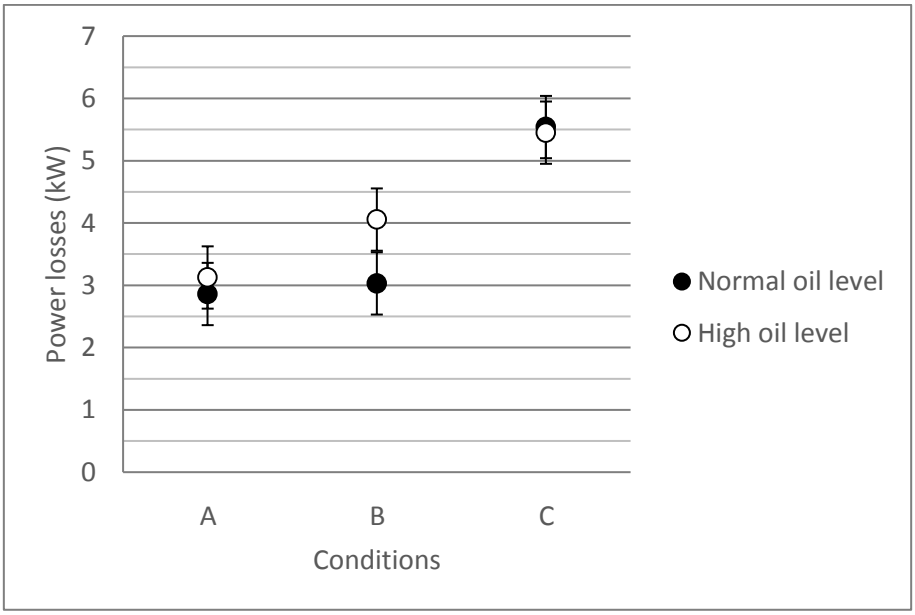

Figure 2.3: Measurement results for load test conditions and two different oil levels

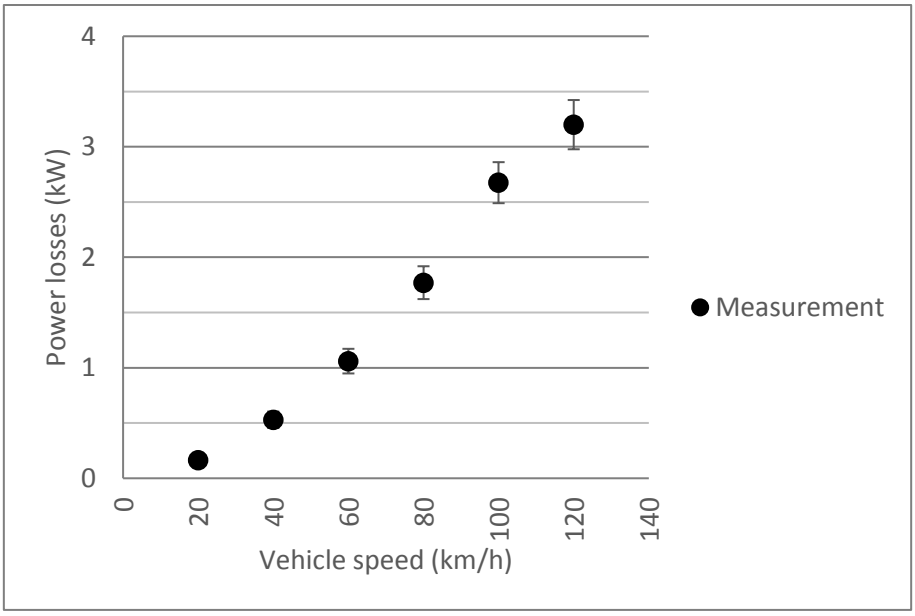

Figure 2.4: Measurement results for load-independent losses test conditions

Load-independent losses tests consist of successive speed conditions corresponding to the vehicle speed from 20km/h to 120km/h with steps of 20km/h. No torque is transmitted during these tests. Only the resisting torque is measured.

The results of these tests are plotted on Figure 2.3 and Figure 2.4. According to the tests under load, the efficiency of this axle ranges from 94% to 98% depending on conditions. A higher oil level induces more power losses, except under high torque where losses are at the same level.

These experimental results are compared to calculations in the next part.

2.3. Calculations of load-independent losses

In the previous chapter, the load-independent sources of dissipation were identified as:

- Shaft seal friction
- Rolling Element Bearing drag and friction (friction is considered as there is preload on some REBs)
- Oil churning

These power losses are now evaluated by using theoretical approaches presented in the literature and compared to the experimental results [47]. To this end, the whole system is assumed to be isothermal at oil sump temperature, which is equal to 80°C.

2.3.1. Input shaft seal friction

The equation proposed by Simrit [9] is used. This is the reference for ISO/TR 14179-2 [9] and appears to be the most robust formula for seal loss calculation. As presented on Figure 2.5, seal power losses are smaller than 200 W. This is not a major source of dissipation when compared to the axle power losses, especially under load conditions (Figure 2.3).

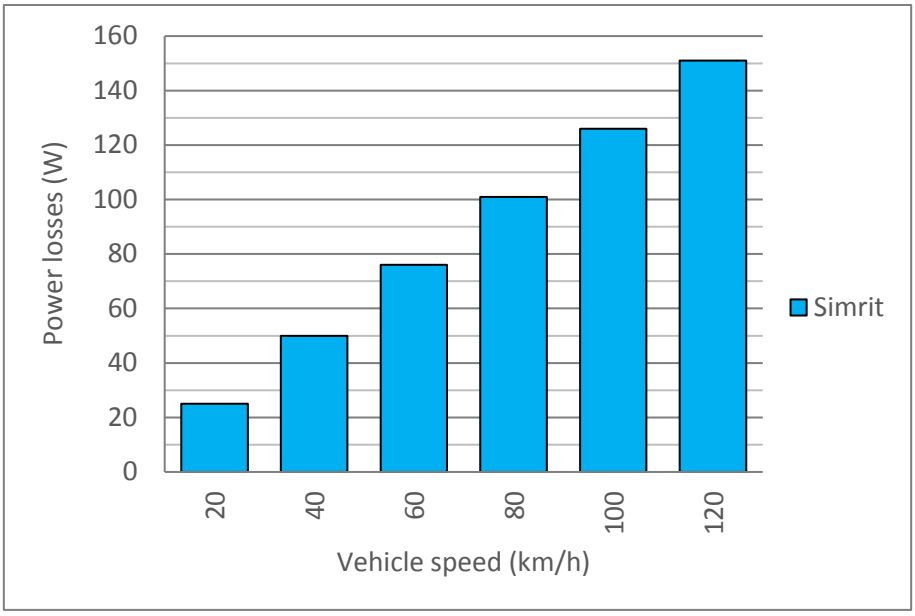

Figure 2.5: Seal friction losses according to Simrit formula

2.3.2. Rolling Element Bearing drag and friction

Concerning the Rolling Element Bearing losses, a comparison between Harris and SKF formulae is performed for every test conditions. Factors used for Harris formula are presented in Table 2.5. Results are plotted on Figure 2.6. As some bearings have a preload, the losses of no-load test conditions are the drag ones but also a part of bearing friction ones. For no-load test conditions (Figure 2.6 (a)), the two models give close results. Nevertheless, for the load test conditions (Figure 2.6 (b)), estimations given by SKF formula equal almost the double of Harris formula results.

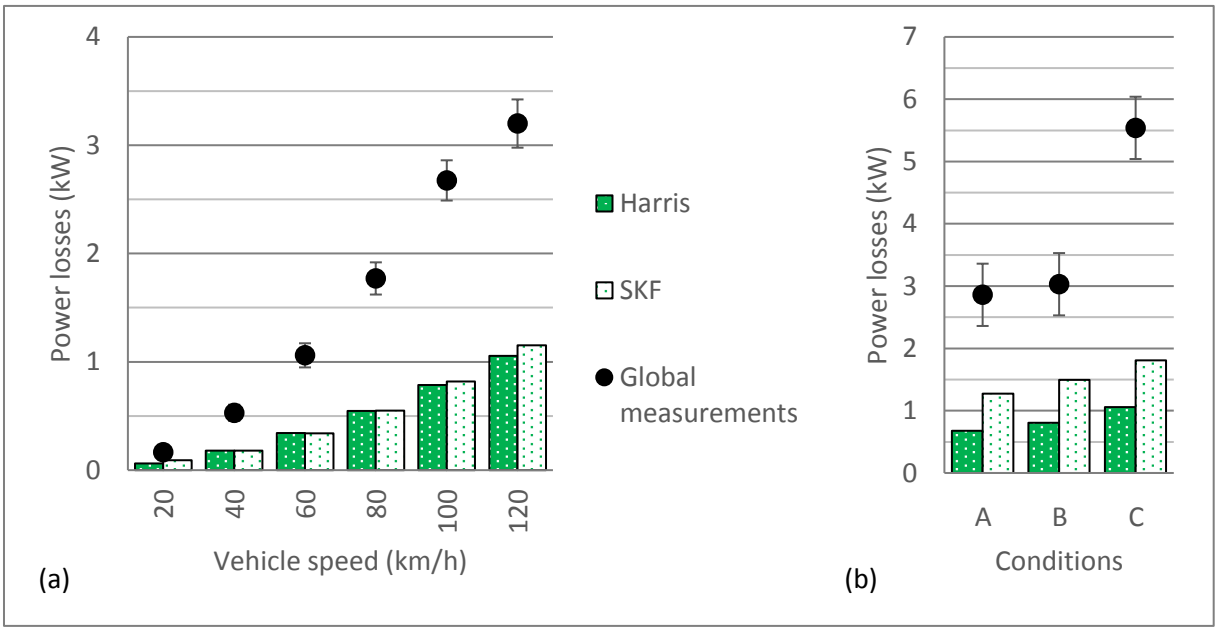

Figure 2.6: Comparison between total power loss measurement and REB loss calculation results according to Harris and SKF formulae for (a) no-load test conditions and (b) load test conditions

Table 2.5: Factors used for Harris formula

	Tail REB	Head REB	Pilot REB	Differential REB
f_0	3	3	5	8
f_1	0.0004	0.0004	0.00055	0.0004

Measurements of the global power loss are also represented on Figure 2.6 to give an order of magnitude of the power loss source contribution.

In order to discriminate among the solutions, a comparison is made between experimental and calculation results for different tests. The no-load test at 80 km/h is used as a reference: under these conditions, the estimated bearing losses are around 550 W for both models. As rotational speed, oil level and temperature are the same for the loaded cases, the load-independent losses should be identical. This includes:

- 550 W of REBs losses (calculated)
- 100 W of seal friction (calculated in Part 2.3.1)
- 1100 W of oil churning (deduced from Figure 2.6)

For the loaded cases, the load losses are added:

- REBs losses increase, depending on load and model (calculated)
- Gear mesh friction

The efficiency of the gear mesh is then deduced for both Harris and SKF models and presented on Figure 2.7. According to SKF formula, hypoid gear mesh efficiency is close to or over 99%. This is unlikely, as the hypoid efficiency is more around 96-98% [24]. Thus, SKF formula gives unrealistic results and is not adapted for this case. For Harris model, the evaluated efficiency ranges approximately from 98% to 99%. Although this is still a good efficiency, Harris model calculates more coherent results. It is kept for the continuation.

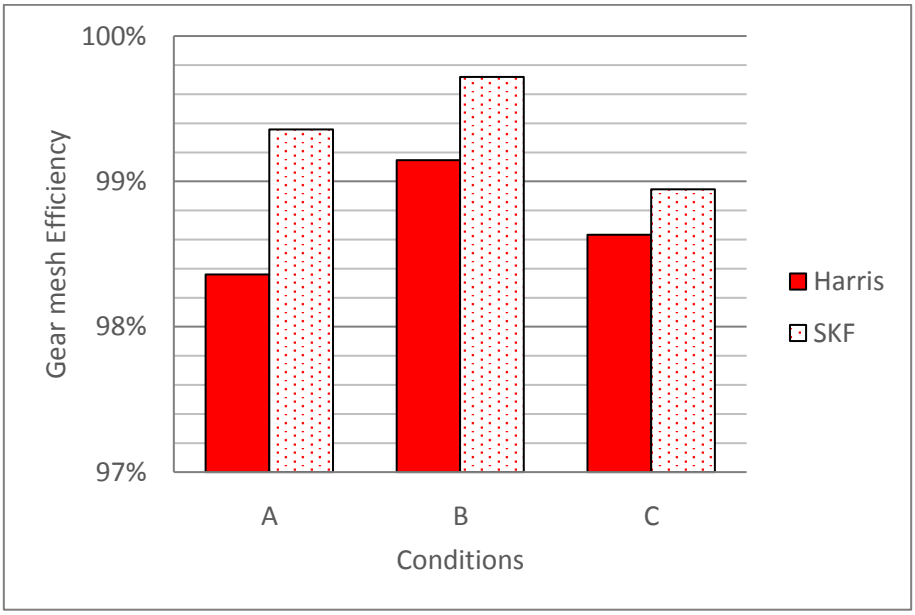

Figure 2.7: Deduction of gear mesh efficiency from Harris and SKF bearing loss formulae

2.3.3. Oil churning

Mauz and Jeon formulae are compared for oil churning losses. As these are pure load-independent losses, only the no-load test conditions are considered; calculation results are presented on Figure 2.8.

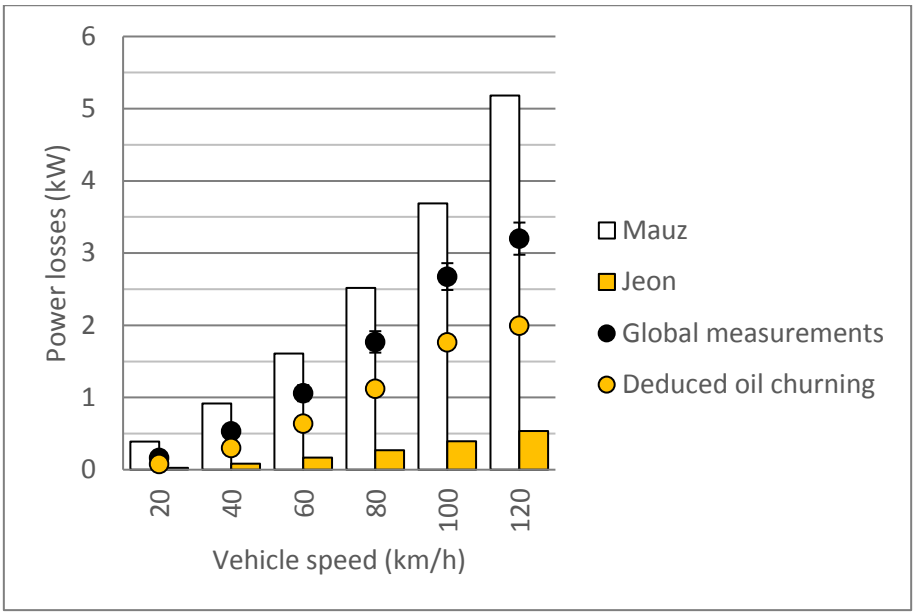

Figure 2.8: Comparison between global measurements (no-load tests), deduced churning loss and churning loss calculation results according to Mauz and Jeon formulae

It appears clearly that Mauz formula overestimates the power losses, as calculated churning losses represent on their own more than the measured load-independent losses. On the contrary, the estimation given by Jeon formula is too low when compared to experimental measurements and to the deduced oil churning losses. Indeed, at 80 km/h, the churning losses are around 1 kW whereas Jeon gives 270 W. Both models are not adapted to this case. Thus, a further study is required on oil churning losses and is conducted in the next part of this chapter.

3. Investigations on oil churning losses of hypoid gears

As underlined in the first chapter, the literature is rather limited concerning oil churning of hypoid and spiral bevel gears in general. Moreover, as shown in the previous part, Mauz and Jeon formulae seem unsuitable for the truck axle application. However, Jeon worked specifically on an automotive axle, which is similar to a truck axle. A closer observation of his work is then made. The established relationship for oil churning of spiral bevel gears is:

$$P_{churning} = \frac{1}{2}\,\rho\,\Omega^3\,b\,{R_p}^2\,S_m\,C_m \tag{2.1}$$

where ρ is the lubricant density, Ω is the gear angular velocity (rad/s), b is the gear width (m), R_p is the gear pitch radius (m), S_m is the gear immersed surface area (m²), and C_m is the dimensionless drag torque. This formula is based on the main geometrical features of the gear: width, pitch radius, immersed area… However, Jeon has tested only two geometries and their pitch diameters are close

(respectively 210 mm and 220 mm). It seems important to proceed to a broader study of the spiral bevel gears geometry influence on churning losses.

3.1. Test rig

A specific test rig is used in order to study oil churning losses. The test set-up is fully described by Changenet and Velex [42] and is represented on Figure 2.9. Hereafter are summarised the major information concerning the rig.

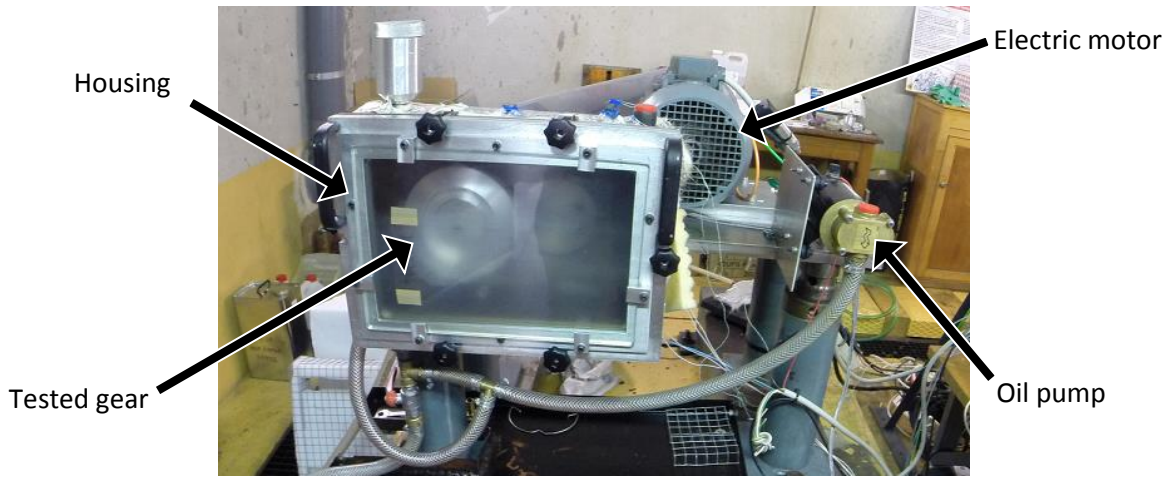

Figure 2.9: Oil churning test rig

An electric motor drives the tested gear via a belt. The test rig allows for measurement of churning torque and gear rotational speed. The torque sensor has a range of 2 N.m with an accuracy of +/- 0.002 N.m, while the speed ranges from 0 to 7000 rpm. A pump allows for modification of the oil level; heating covers and thermocouples manage the oil temperature. During tests, the oil flow can be observed through the Plexiglas face of the housing. The housing case itself measures 400 x 275 x 93 mm; this allows to avoid wall effects on oil flow. The addition of deflectors is possible as illustrated on Figure 2.10: this allows for changing housing shape.

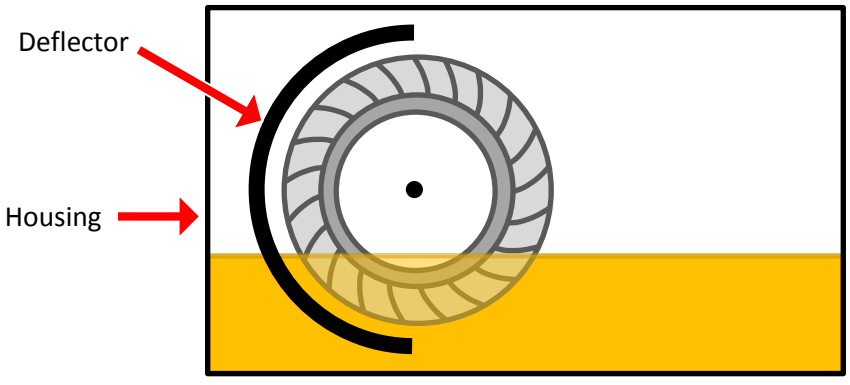

Figure 2.10: Deflector modifies housing shape

The tested gear is supported by ball bearings, as presented on Figure 2.11. Their power loss contribution is removed from the total power losses to consider only oil churning losses.

Only a single spiral bevel gear can be tested, the gear couple configuration being exclusively available for cylindrical gears. Four different spiral bevel gears are used to study the influence of various geometrical parameters. Two smooth cones are also tested to observe the effect of gear teeth. Their characteristics are described in Table 2.6.

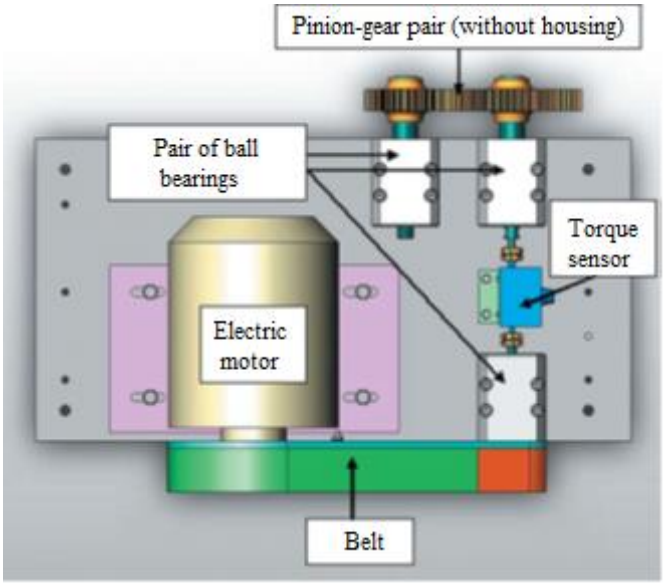

Figure 2.11: Oil churning test rig scheme (cylindrical gear pair configuration)

Table 2.6: Tested gears characteristics

	Gear 1	Gear 2	Gear 3	Gear 4	Cone 1	Cone 2
Number of teeth	41	37	41	37	/	/
Outer diameter (mm)	157	130	188	154	157	160
Width (mm)	22	27	30	30	22	27
Face width (mm)	27	24,5	32	27,5	27	24,5
Face angle (°)	72,4	58,1	72,4	58,1	72,4	58,1
Pressure angle (°)	20	20	20	20	/	/
Spiral angle (°)	35	35	35	35	/	/
Hand of spiral	LH	LH	LH	LH	/	/

It can be noticed that the outer diameter is used here instead of the pitch diameter. The outer diameter is also representative of the gear general shape, as represented on Figure 2.12, and easy to know. By the way, outer diameters and pitch diameters are almost similar on Jeon's tested gears (respectively 213.2 and 210 mm for the first crown gear, and 222 and 220 mm for the second).

Various oils are available to investigate the influence of oil properties. Their characteristics are gathered in Table 2.7.

Table 2.7: Tested oils characteristics

	Oil A	Oil B	Oil C	Oil D
Kinematic viscosity @ 40°C (cSt)	220	35	45.1	120
Kinematic viscosity @ 100°C (cSt)	19	7.5	7.7	15.9
Density @ 15°C	0.895	0.870	0.885	0.860
Oil type	Mineral	Mineral	Mineral	Synthetic

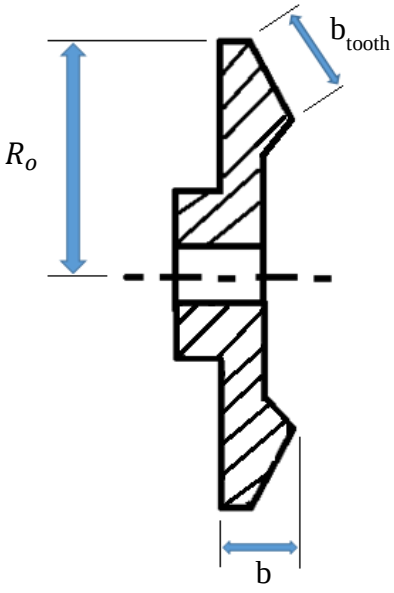

Figure 2.12: Definition of the gear main geometrical parameters

3.2. Truck axle application

In this study, a general approach of churning losses of spiral bevel and hypoid gears is made. Additionally to this, the truck axle application is also investigated. In order to use the test bench results for this case, some operating conditions must be covered during experiments. A similitude approach is then used: equivalent parameters are peripheral speed, oil viscosity and immersion. An immersion ratio h_{lub}/R_o is defined as the ratio between the immersion depth h_{lub} and the gear outer radius R_o, as illustrated on Figure 2.13.

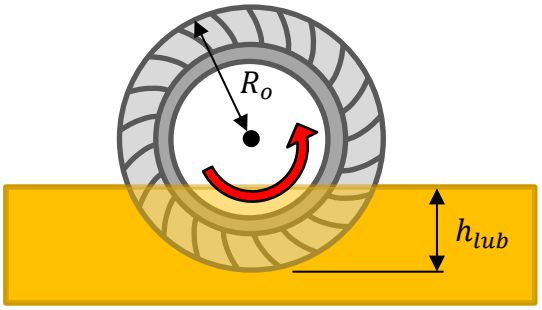

Figure 2.13: Definition of the immersion ratio

Tested gears are left handed, whereas the truck axle crown gear is right handed. An opposite direction of rotation is then used to obtain the same behaviour.

Considering the axle crown gear, peripheral speeds presented in Table 2.8 range from 2.5 to 12.4 m/s. They are quite low as the truck tyres have a big radius (0.48 m in this case). Pinion gear has slightly higher peripheral speeds (from 3.6 to 18 m/s). Indeed, due to offset, hypoid pinion gear has a bigger diameter than the spiral bevel one for the same crown gear size. The tested gears experience the same peripheral speeds (from 6.8 to 19.7 m/s), except for very low speeds as the motor drive is not stable under 800 rpm. It is important to notice that a single reduction axle is considered here; in the case of a double reduction axle, the main speed reduction takes place in the wheel hubs and the gear set thus rotates at higher speeds.

Table 2.8: Peripheral speeds on truck application and on test rig

TRUCK APPLICATION	Vehicle speed (km/h)	20	50	80	100
Peripheral speed (m/s)	Crown gear	2.5	6.2	9.9	12.4
	Pinion gear	3.6	9.0	14.4	18.0

TEST RIG	Input speed (rpm)	1000	1500	2000
Peripheral speed (m/s)	Gear 1	8.2	12.3	16.4
	Gear 2	6.8	10.2	13.6
	Gear 3	9.8	14.8	19.7
	Gear 4	8.1	12.1	16.1

Tested oil D is a typical drivetrain lubricant and is the same as the one used for previous axle tests of the study. The oil temperature range considered here evolves from 20°C to 100°C, which corresponds to a viscosity of 352 cSt to 16 cSt.

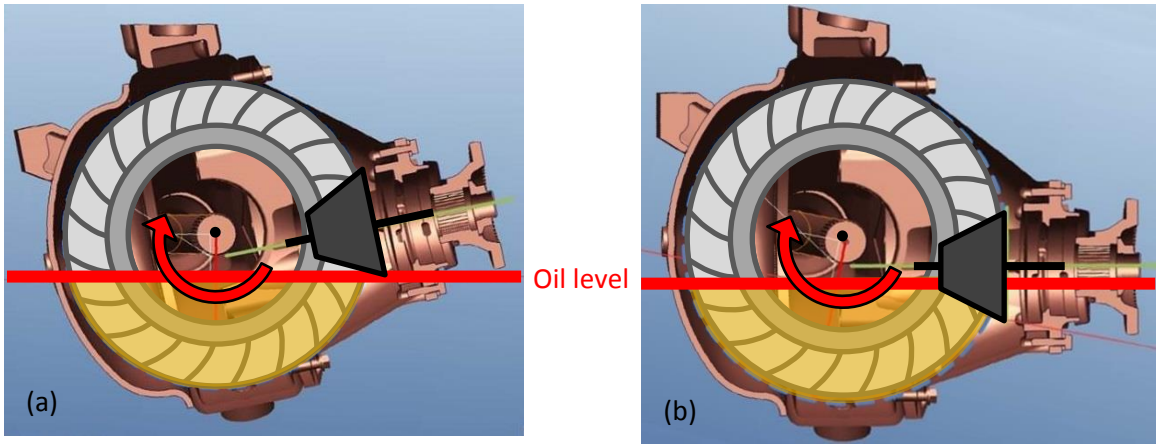

Figure 2.14: Immersion of crown and pinion gears in an axle (a) with inclination and (b) without inclination

Concerning oil immersion, the rolling element bearings of the differential are small in comparison to the crown gear and their lubrication must be ensured thanks to a sufficient oil level. Thus, the crown gear is highly immersed: the static immersion ratio ranges from 0.7 to 0.9. However, oil level decreases

during axle operation due to oil splashing. The maximum dynamic immersion ratio used during experiments is then 0.6.

The immersion of the pinion is harder to reproduce since the axle is generally tilted when mounted on a truck, as illustrated on Figure 2.14. Nevertheless, for practical reasons, most of the tests on axles were done with no inclination. This leads to a relatively important immersion of the pinion.

Figure 2.14 also highlights the housing shape of an axle. The circular casing possibly leads to particular oil flows, as observed by Jeon [15] on Figure 2.15: with speed, the oil is moved away along the housing and so the immersion level decreases a lot.

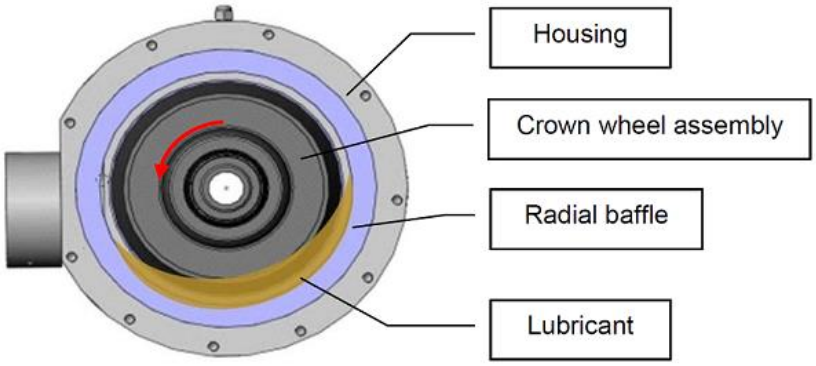

Figure 2.15: Behaviour of free surface of lubricant inside the extension housing while the ring gear was rotating forward [15]

However, rotational speeds in automotive axle are higher and so peripheral speeds, even if the crown gear diameter is smaller. Truck speeds can be insufficient to generate these phenomena. As the test rig housing is a parallelepiped, use of deflectors allows for changing both the distance between tested gear and wall and the wall shape, as presented on Figure 2.10, while keeping the same oil volume.

3.3. Experimental results

All the results obtained during the study are sum-up in Annex 2.A.

The influence of operating conditions on churning losses is investigated. Tests are performed on every gear geometry with various rotational speeds, immersion levels and oil properties (density and viscosity).

For each tested gear, churning losses are measured with an increasing speed, from 1000 to 2000 rpm. The other operating conditions (immersion, oil properties) are kept constant. Results for oil C at 40°C and an immersion ratio of 0.5 are plotted on Figure 2.16. Churning losses increases greatly with the rotational speed: the proportionality is to the power 1.7.

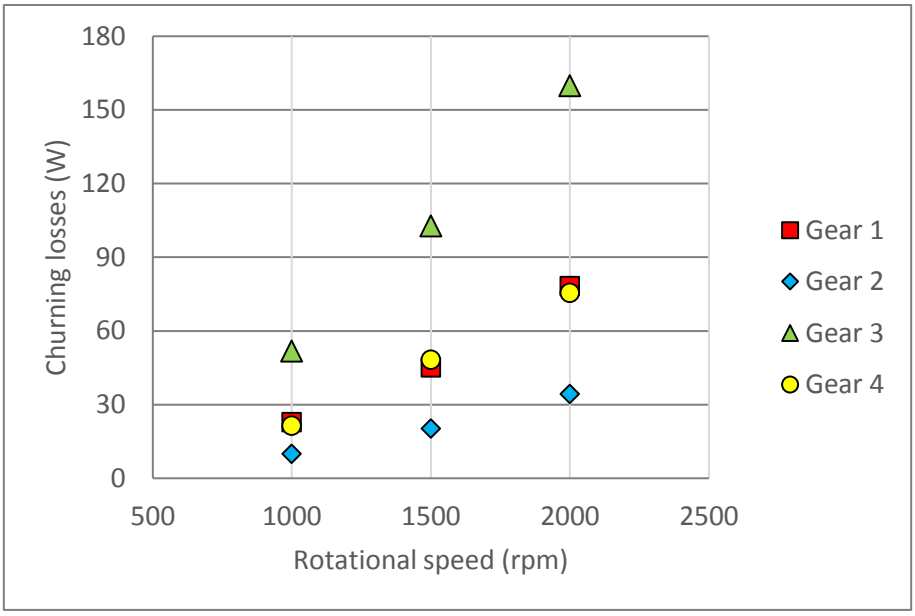

Figure 2.16: Influence of rotational speed on churning losses (oil C, h_{lub}/R_o=0.5, 40°C)

Another series of tests is done to observe the effect of immersion on losses. Measurements are performed at various immersion levels. Figure 2.17 presents the results at 2000 rpm and for oil C at 40°C. It shows that the immersion ratio is a parameter of first order on churning losses.

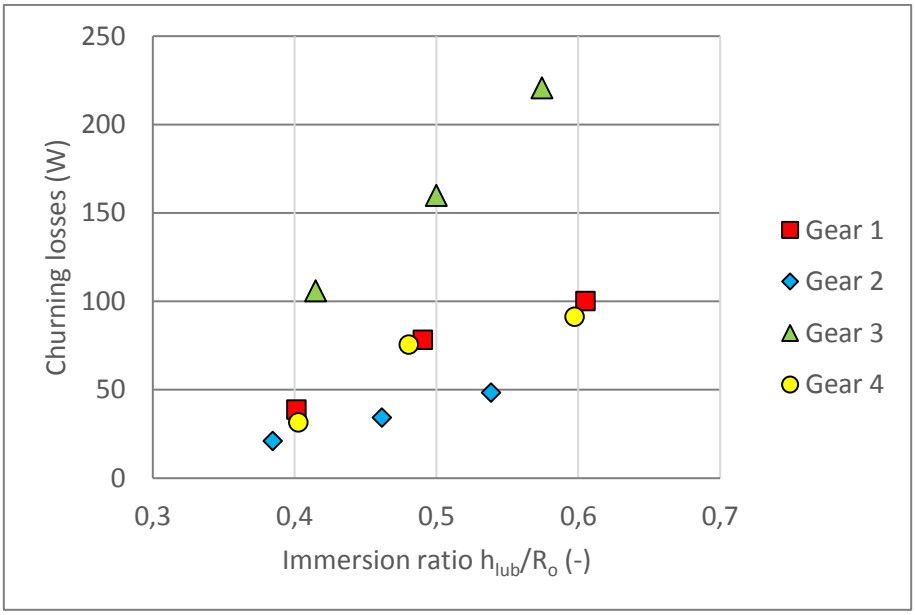

Figure 2.17: Influence of immersion on churning losses (oil C, 2000 rpm, 40°C)

Concerning the influence of oil properties, a comparison of different oils is made on Figure 2.18. Churning losses clearly increase with oil viscosity. At low viscosity (under 30 cSt), losses remain constant. This phenomena was not observed by Jeon: in his experiments, viscosity of the lubricant is over 30 cSt. Changenet et al. [41] have already underlined this behaviour for cylindrical gears. Measurement results are similar for the various oils and no influence of oil densities is observed, because this characteristic is close for all tested oils.

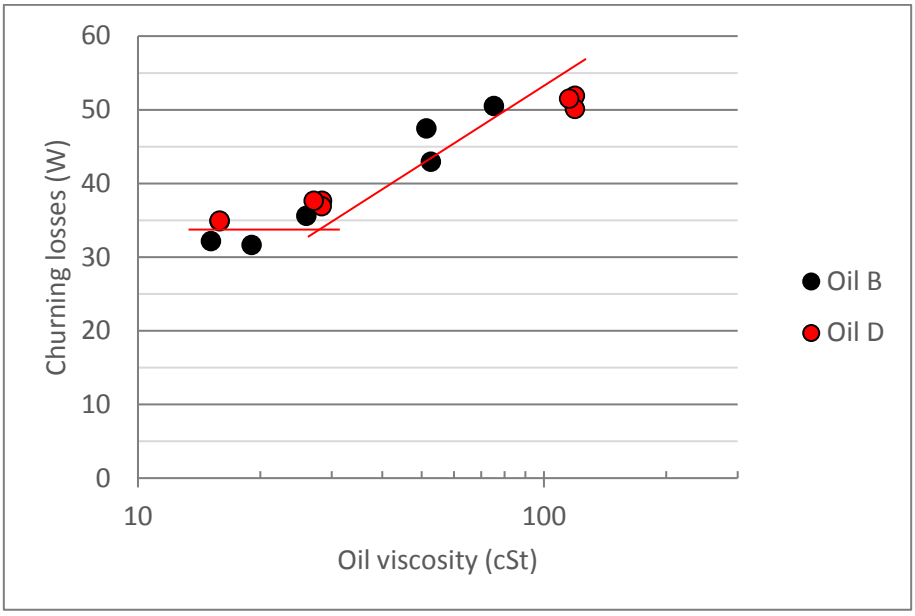

Figure 2.18: Influence of oil properties (viscosity and density) on churning losses (1000 rpm, gear 3, h_{lub}/R_o= 0.46)

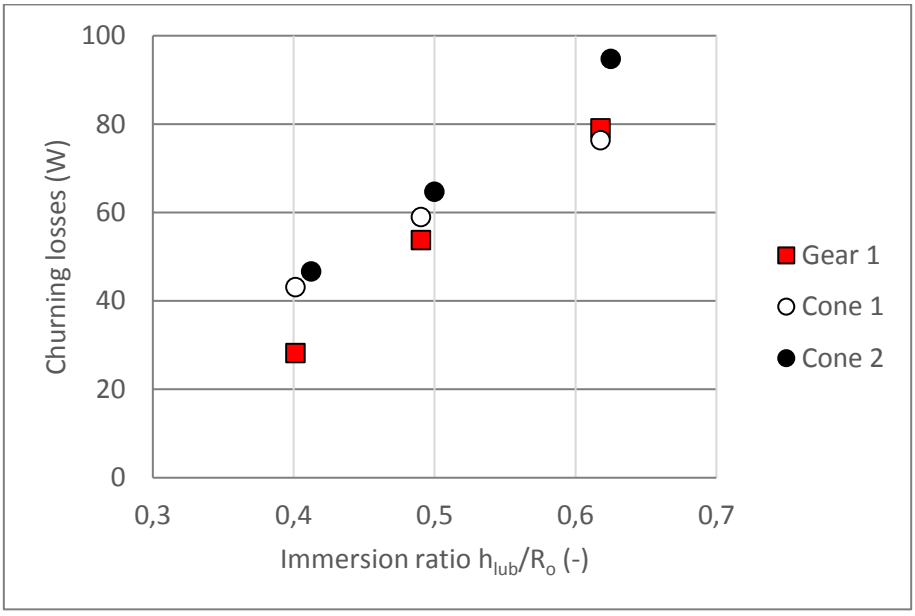

Figure 2.19: Comparison between churning losses for gear 1 and cones 1 and 2 (oil D, 1500 rpm, 40°C)

In a second time, the focus is put on the effect of gear geometrical parameters: outer diameter, width, face width, face angle, and number of teeth. Comparison between the various tested gears is made.

Gear 1 and cone 1 have the same geometry, apart from the presence of teeth, as indicated in Table 2.6. Their respective churning losses are plotted on Figure 2.19 for different immersions. The same tendencies are observed, so teeth have limited influence on churning losses.

Gear 1 and gear 4 display the same power loss behaviour, according to rotational speed on Figure 2.16 or to oil immersion on Figure 2.17. However, these gears have different geometrical parameters: number of teeth, face angle, width… while they have similar outer diameter. As well, Figure 2.19 presents comparable results for cone 1 and cone 2. These cones also have close outer diameter but dissimilar face width, face angle and width. In conclusion, the gear outer diameter is a geometrical parameter of first order for churning losses compared to other ones. For a bigger outer diameter (gear 3), higher churning losses are experienced; conversely, there are less losses for a smaller outer diameter (gear 2).

3.4. Comparison with existing calculation methods

Some comparisons of measured power losses with those predicted from the existing relationships are done. According to ISO/TR 14179-1, churning losses are proportional to Ω^3 which is not in accordance with experiments (proportional to $\Omega^{1.7}$). Because of this divergence, ISO/TR 14179-1 is disregarded in the following analyses. Figure 2.20 presents churning losses generated by gear 3 as a function of speed. This figure highlights discrepancy with ISO/TR 14179-2 (Mauz) and Jeon formulae, even if results are closer to experimental results than ISO/TR 14179-1.

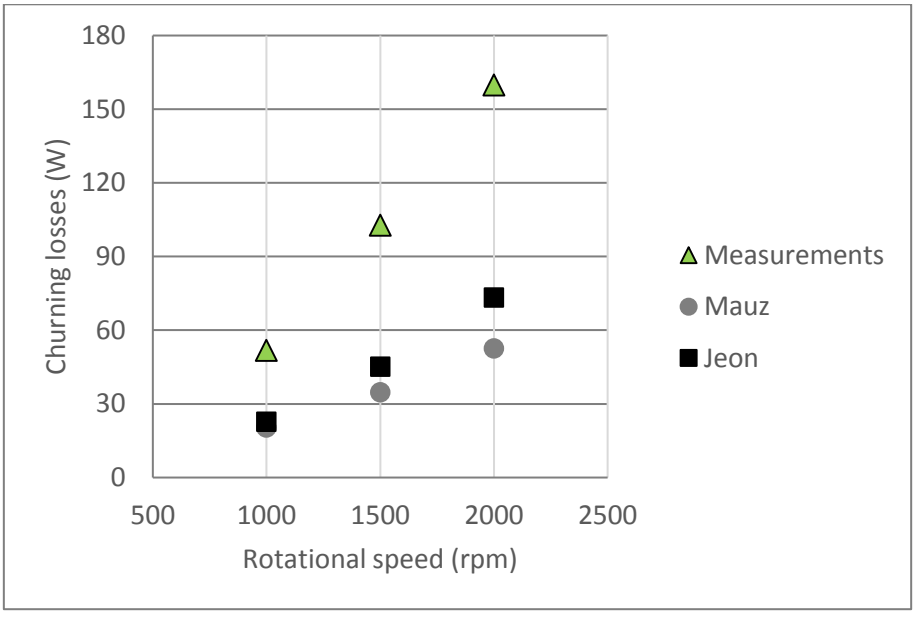

Figure 2.20: Influence of speed on measured and calculated churning losses (oil C, gear 3, h_{lub}/R_o=0.5)

It appears also on Figure 2.20 that Mauz and Jeon laws have a similar behaviour. This is quite surprising as Mauz formula is established for a parallelepiped housing close to the test rig one, while a circular housing is studied by Jeon. A better accordance of Mauz formula was expected for the test rig case.

Moreover, for the axle application analysed on Figure 2.8, Mauz and Jeon laws estimate really different results. Jeon formula still underestimates losses, while Mauz formula overestimates them. It seems that Mauz formula is deeply influenced by the housing size and shape, leading to this divergence.

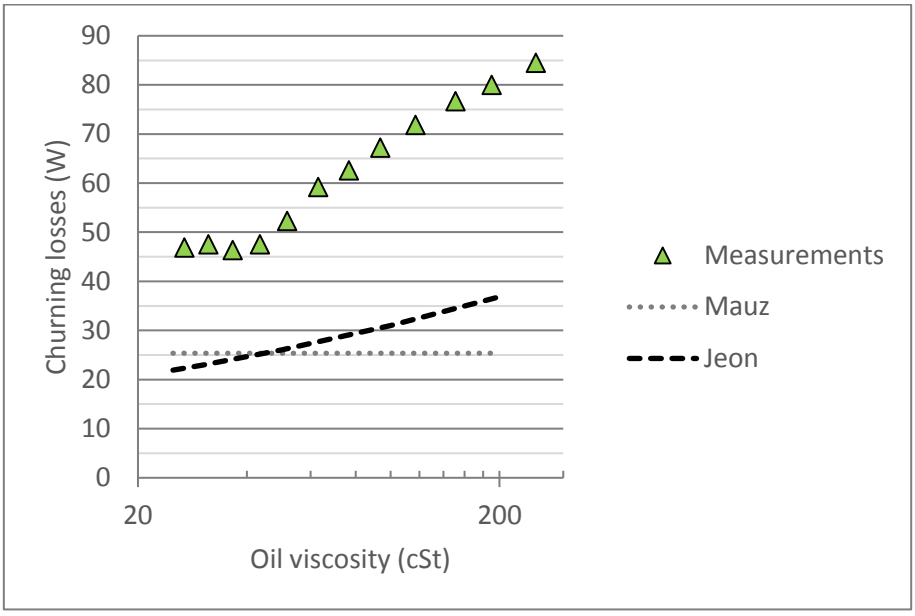

Figure 2.21: Influence of oil viscosity on measured and calculated churning losses (oil D, 1000 rpm, gear 3, h_{lub}/R_o=0.57)

Another comparison, associated with the influence of oil properties, is given in Figure 2.21. As it has been underlined, two flow regimes clearly emerge from measurements whereas calculation methods are based on a single regime: the churning losses always decrease with viscosity according to Jeon's approach and it remains constant by using the relationships of Mauz.

The discrepancy observed between measurements and existing formulae implies modifications.

4. Improvement of oil churning formula for truck axles

4.1. Specifications for spiral bevel and hypoid gears

According to the gear geometry study of the previous part, gear teeth have no influence on churning losses. This induces a similar immersed surface area for both gears and cones. Calculation of this surface is detailed by Laruelle et al. [48] and reported in Annex 2.B: it considers an envelope geometry of the gear.

Using formula (2.1) and test measurements, an experimental dimensionless churning torque C_m is calculated as:

$$C_{m\,exp} = \frac{2}{\rho\,\Omega^3\,b\,{R_p}^2\,S_m}\,P_{churning}^{measured} \tag{2.2}$$

It is plotted on Figure 2.22 (a). Gear 1 and gear 4 obtain different results.

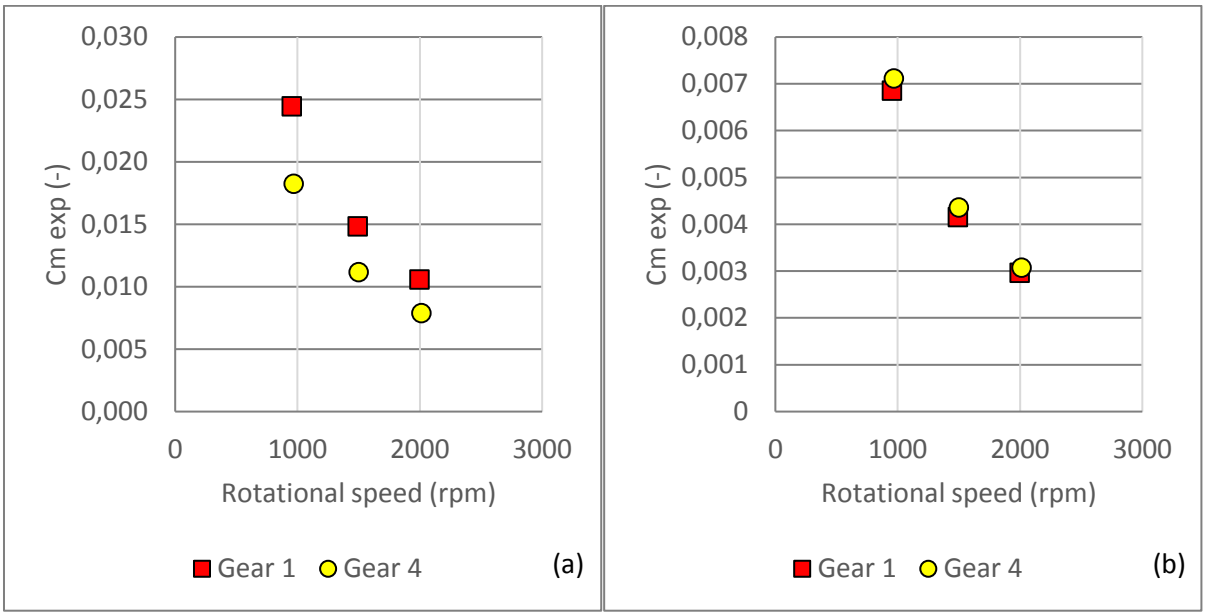

Figure 2.22: Experimental dimensionless churning torque according to (a) Equation (2.1) and (b) Equation (2.4) (oil B, 70°C, h_{lub}/R_o=0.5)

However, they have similar radius, which is the only geometrical feature included in the expression of C_m according to Jeon:

$$C_m = 2.19\left(\frac{h_{lub}}{R_p}\right)^{0.15}\left(\frac{V_{lub}}{{R_p}^3}\right)^{-0.20} Re^{-0.25}\,Fr^{-0.53} \tag{2.3}$$

where h_{lub} is the gear immersion depth (m), V_{lub} is the volume of oil sump (m^3), Re is the Reynolds number, and Fr is the Froud number. This discrepancy implies a modification, whether of the dimensionless churning torque or of the churning power loss formula, to be in agreement with dimensionless analysis. Experimental results underline that gear width has a limited influence on churning losses, contrary to gear outer diameter. Formula (2.1) is then modified to the following equation:

$$P_{churning} = \frac{1}{2}\,\rho\,\Omega^3\,{R_o}^3\,S_m\,C_m \tag{2.4}$$

where R_o is the gear outer radius (m). Using this new formula, a better concordance is observed on Figure 2.22 (b) for gear 1 and gear 4 in terms of dimensionless churning torque.

Gear width and teeth are identified as non-influential parameters for dimensional analysis. Churning torque still depends on one gear geometrical parameter (outer radius), dynamic parameters

(rotational speed, gravity), fluid parameters (viscosity, density), and oil sump geometrical parameters (oil volume, immersion level):

$$C_{churning} = fct[R_o, \Omega, g, \nu_{lub}, \rho, V_{lub}, h_{lub}] \tag{2.5}$$

For dimensional analysis, these seven parameters can be expressed by fundamental unities: length, time and mass. According to Buckingham π theorem [49], three principal parameters R_o, Ω, and ρ are selected and four dimensionless parameters can be constituted to define the dimensionless churning torque:

$$C_m = fct\left[Re, Fr, {h_{lub}}/{R_o}, {V_{lub}}/{{R_o}^3}\right] \tag{2.6}$$

with Reynolds and Froude numbers defined as follows:

$$Re = \frac{\Omega\, {R_o}^2}{\nu_{lub}} \tag{2.7}$$

$$Fr = \frac{\Omega^2\, R_o}{g} \tag{2.8}$$

where ν_{lub} is the oil kinematic viscosity (mm²/s).

According to the various tests presented in previous part, the dimensionless churning torque is now analysed and compared with Jeon approach:

$$C_m = \gamma_1 \left(\frac{h_{lub}}{R_o}\right)^{\gamma_2} \left(\frac{V_{lub}}{{R_o}^3}\right)^{\gamma_3} Re^{\gamma_4}\, Fr^{\gamma_5} \tag{2.9}$$

Evolution of C_m is first studied regarding Reynolds number. Speed is thus kept constant in order to have no variation on Froude number.

Figure 2.23 shows the existence of two oil flow regimes, with a transition around a Reynolds of 20 000. For the regime bellow the transition, torque decreases with the Reynolds number as found by Jeon: γ_4 equals -0.25. The second regime is not described by Jeon, as it is out of his scope of tests in terms of oil viscosity. The Reynolds number, and so viscous forces, have no more influence for this regime and γ_4 is null.

The influence of Froude number is isolated through tests where only the rotational speed varies as the ones given in Figure 2.16. The constant γ_5 is then deduced: a value of -0.53 is found which is in agreement with Jeon's formula.

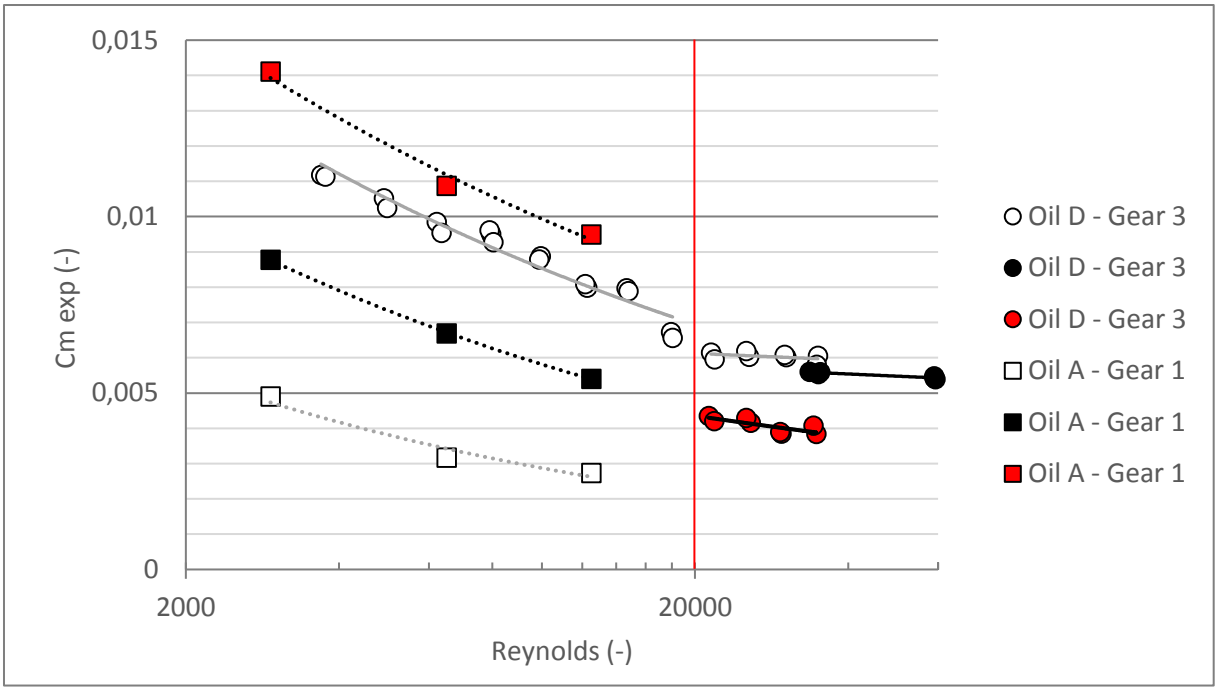

Figure 2.23: Two flow regimes of churning depending on Reynolds number

Concerning oil immersion and volume, the test bench shape is far from the axle one. Tests with and without deflector that modifies the housing shape are performed for different oil levels. In order to characterise the influence of oil immersion on churning, the immersion ratio is isolated from the experimental dimensionless churning torque formula according to Equation (2.9):

$$\frac{C_{m\,exp}}{\left(\frac{V_{lub}}{{R_o}^3}\right)^{-0.20} Re^{-0.25}\,Fr^{-0.53}} = \gamma_1 \left(\frac{h_{lub}}{R_o}\right)^{\gamma_2} \tag{2.10}$$

This expression is used as ordinate on Figure 2.24 for both housing configurations.

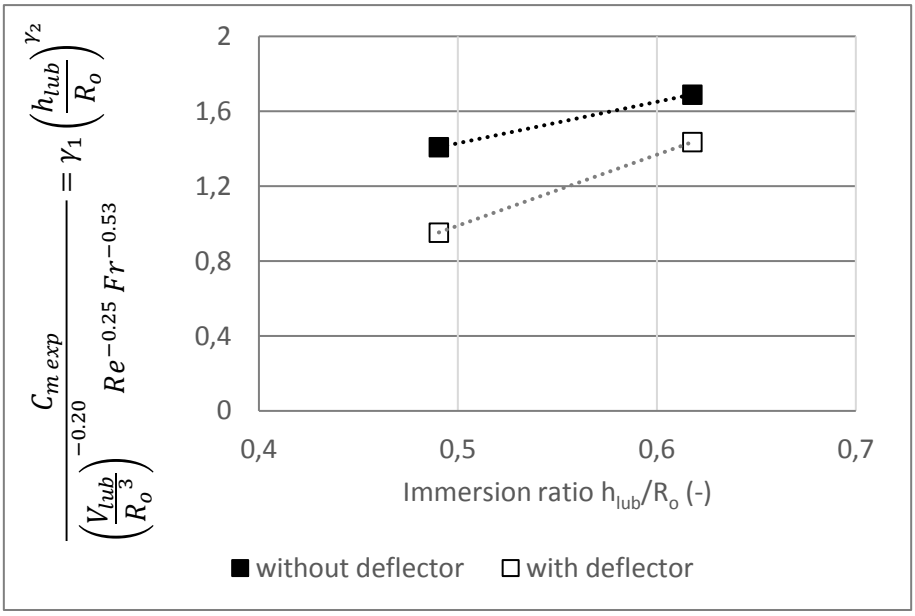

Figure 2.24: Housing influence on churning (Gear 1, 2000 rpm, oil D, 40°C)

This highlights that oil immersion influence changes notably with housing shape. This induces different coefficients γ_2 depending on the housing. As Jeon experiments are closer to the truck axle case, coefficients γ_2 and γ_3 are kept as 0.15 and -0.20.

However, Figure 2.25 highlights discrepancy between test results and Jeon theoretical formula. This can be induced by the different approaches adopted. Indeed, no comparison could be performed between gear immersed surface areas defined by Jeon and Laruelle; also, the dimensionless experimental data depend on gear radius but not on gear width as proposed by Jeon.

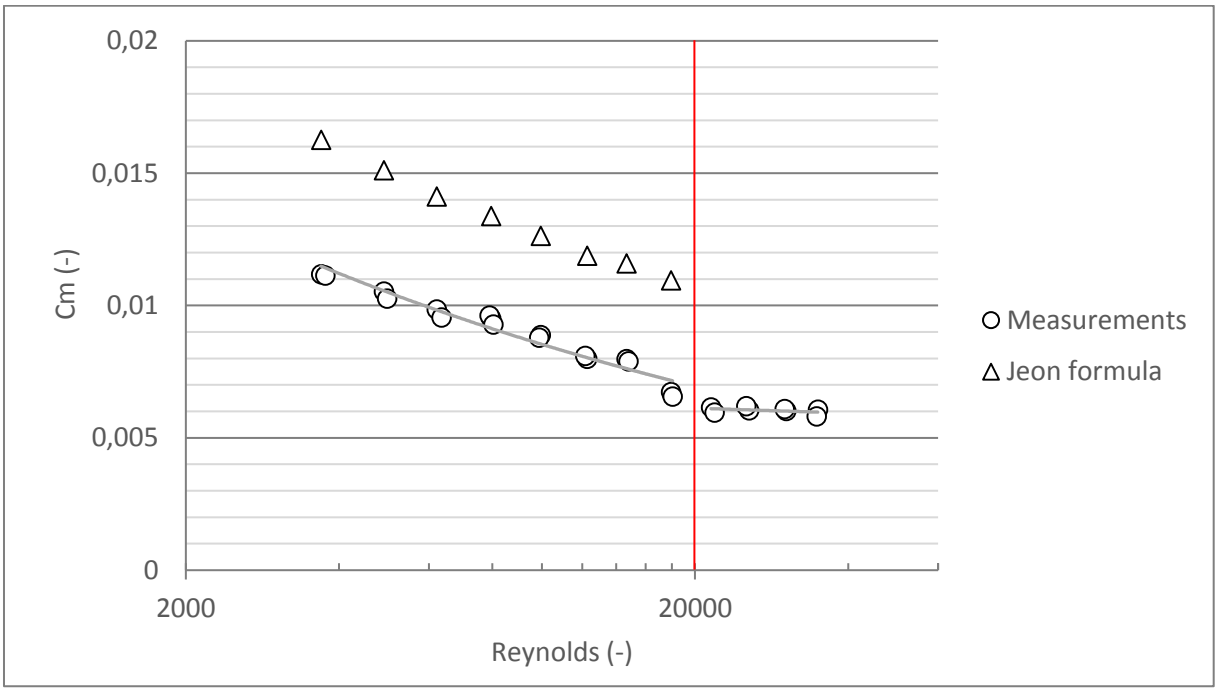

Figure 2.25: Comparison between measurements and Jeon theoretical formula

Therefore, a modification of the coefficient γ_1 is needed. A comparison is thus made between a test performed by Jeon and the test presented on Figure 2.25 in order to check experimental coherence. An identical immersion ratio of 0.6 and the same rotational speed of 1000 rpm are selected. A good agreement between Jeon data and measurements is shown on Figure 2.26. This allows the definition of a corrected γ_1.

Finally, two different flow regimes are defined to calculate C_m for the truck application:

for Re $\leq$ 20 000 :

$$C_m = 1.45 \left(\frac{h_{lub}}{R_o}\right)^{0.15} \left(\frac{V_{lub}}{{R_o}^3}\right)^{-0.20} Re^{-0.25}\, Fr^{-0.53} \tag{2.11}$$

for Re $>$ 20 000 :

$$C_m = 0.12 \left(\frac{h_{lub}}{R_o}\right)^{0.15} \left(\frac{V_{lub}}{{R_o}^3}\right)^{-0.20} Fr^{-0.53} \tag{2.12}$$

Results for this new formula are presented on Figure 2.26 and are in agreement with test results.

This equation is valid for a single spiral bevel gear surrounded by a close housing and must be applied to both pinion and crown gears.

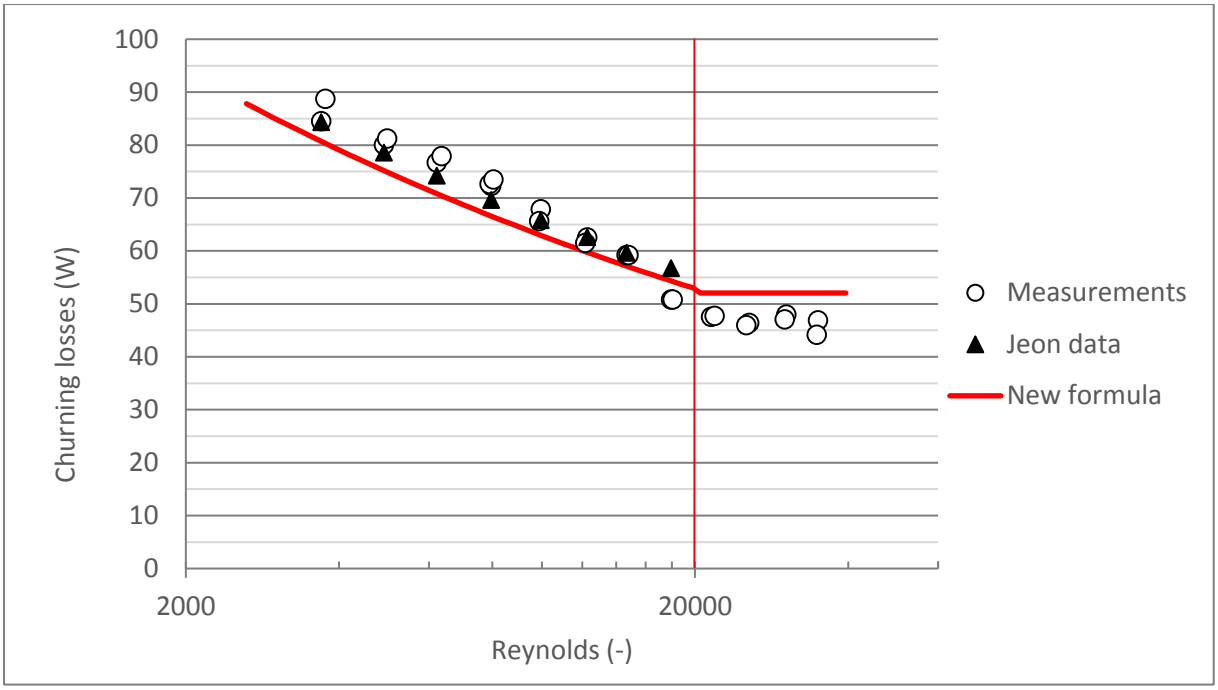

Figure 2.26: Comparison between experimental results and the new formula for churning losses

4.2. Application to the power loss model for truck axles

The new churning loss relationship is applied to the axle case. Results are compared to measurements and Jeon original formula on Figure 2.27.

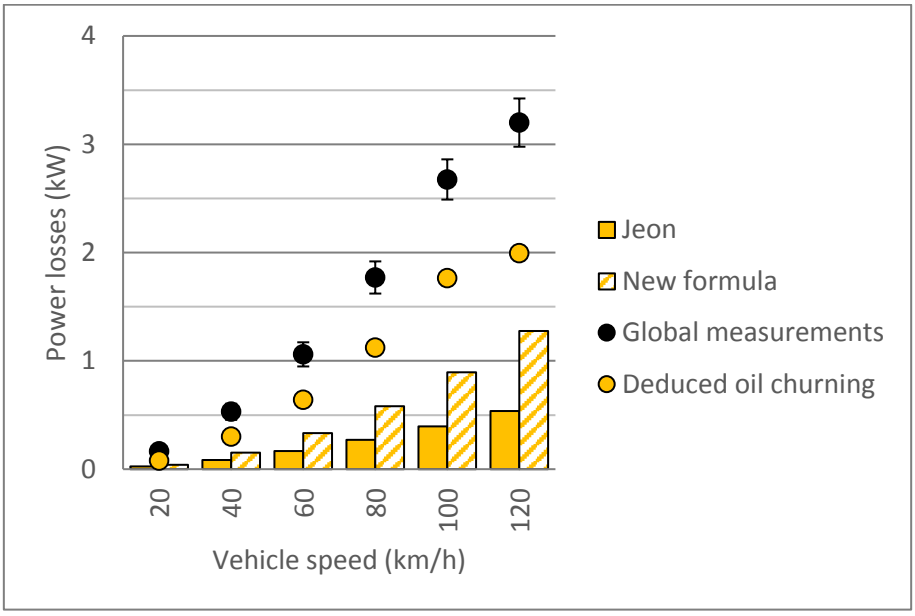

Figure 2.27: Comparison between no-load measurements, deduced oil churning values and oil churning calculations according to Jeon formula and new formula

The newly estimated churning losses are higher than the ones calculated according to Jeon formula. However, churning losses are still underestimated. It is important to highlight that calculated churning losses of pinion gear are low compared to crown gear ones. Indeed, its immersion surface is smaller.

As explained in the first chapter, a meshed hypoid gear pair generates more losses than the addition of each gear contribution. According to Jeon [15], the churning losses of a complete gear set can be more than doubled when compared to that of crown gear alone. Figure 2.28 illustrates this assumption for the axle case. The new formula shows good agreement with test results.

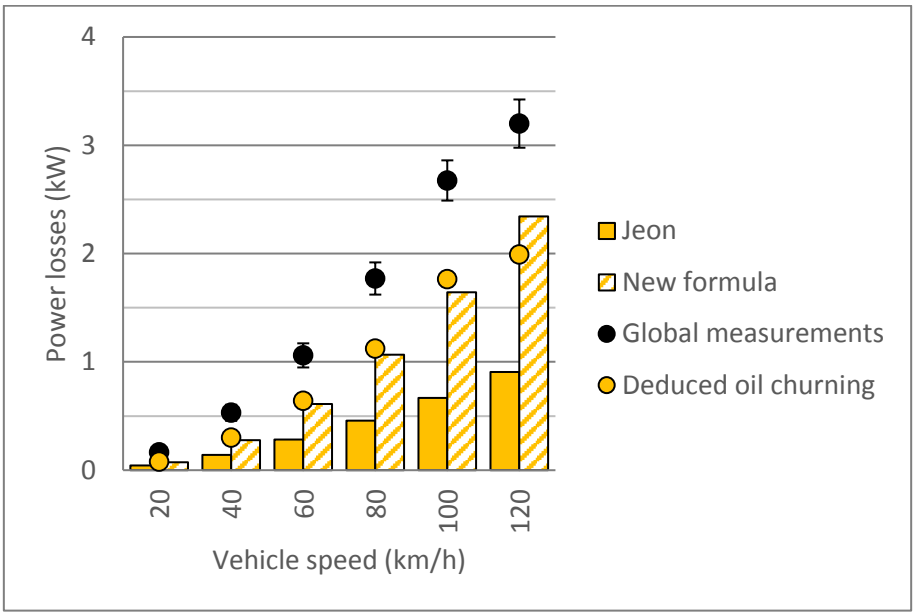

Figure 2.28: Increase of the churning losses for a complete gear set

Jeon has observed a modification of the oil flow due to pinion presence. To take this phenomenon into account, the immersion level is modified for the churning loss calculation in order to obtain similar power loss amount. Finally, the immersion level is increased by 30% for the meshed gear pair.

Thanks to this new churning loss relationship, more coherent results are obtained with the no-load measurements, as presented on Figure 2.29.

5. Calculations of load-dependent losses

As load-independent losses are now well estimated, a new focus is made on load losses:

- Rolling Element Bearing friction
- Hypoid gear mesh friction

Bearing friction losses were already studied in Part 2.3.2 with the bearing drag losses. Then, hypoid gear mesh friction is investigated hereafter according to analytical formulae of the literature, still with an isothermal system at 80°C. Figure 2.30 gives an order of hypoid gear mesh friction losses deduced from the previous calculations. This highlights a possible error on measurement B at normal oil level: the trend is really different between both oil levels.

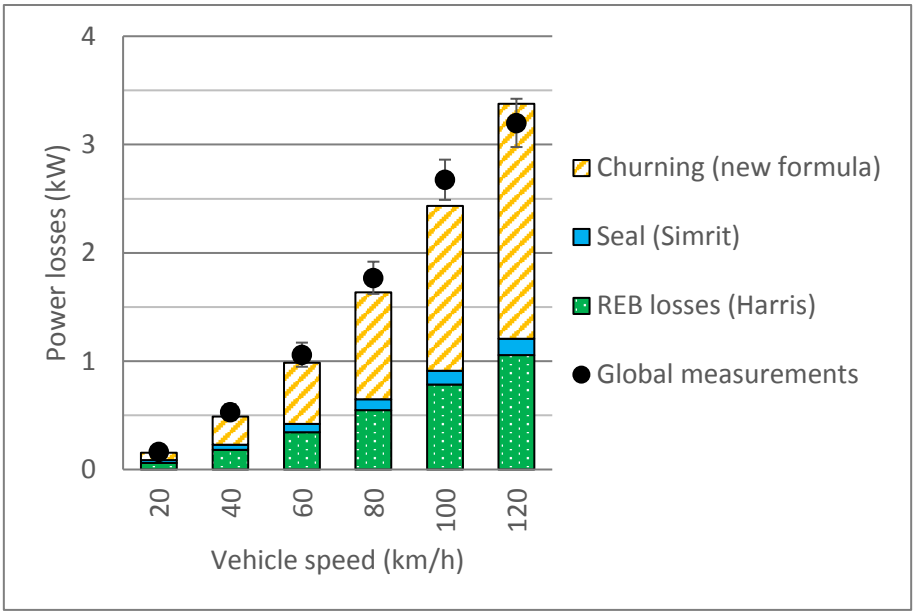

Figure 2.29: Comparison between no-load measurement and standard calculation (with the new churning formula)

5.1. Hypoid gear mesh friction

A first approach of hypoid losses is exposed here by comparing ISO/TR 14179-2 [9] and Buckingham [16] formulae. The friction coefficient is determined according to the different methods: for Buckingham, a chart allows to identify it according to sliding velocity, while it is calculated with a formula specified in Annex 1.A for the ISO technical report. For ISO formula, factor $X_L = 0.8$ as the oil used is a polyalfaolefin (other characteristics are reported in Table 2.3).

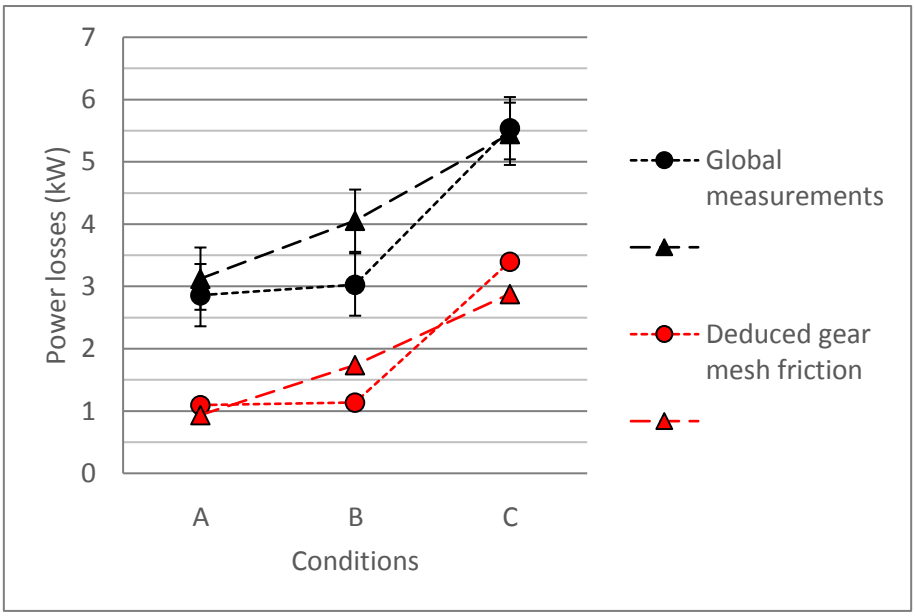

Figure 2.30: Deduced gear mesh friction for load test conditions with (..o..) normal oil level and (-Δ-) high oil level

Results are plotted on Figure 2.31 and compared with the gear friction loss deduced from measurements. It appears clearly that Buckingham formula greatly overestimates the losses. The ISO technical report formula is in good agreement with the deduced gear friction losses. This is coherent with the observation made in the previous chapter: for an identical friction coefficient, Buckingham formula is more pessimistic than the ISO. Moreover, the friction coefficient estimated according to Buckingham is higher (0.035 for spiral bevel part and 0.042 for worm part) than the ISO (from 0.020 to 0.026 depending on load).

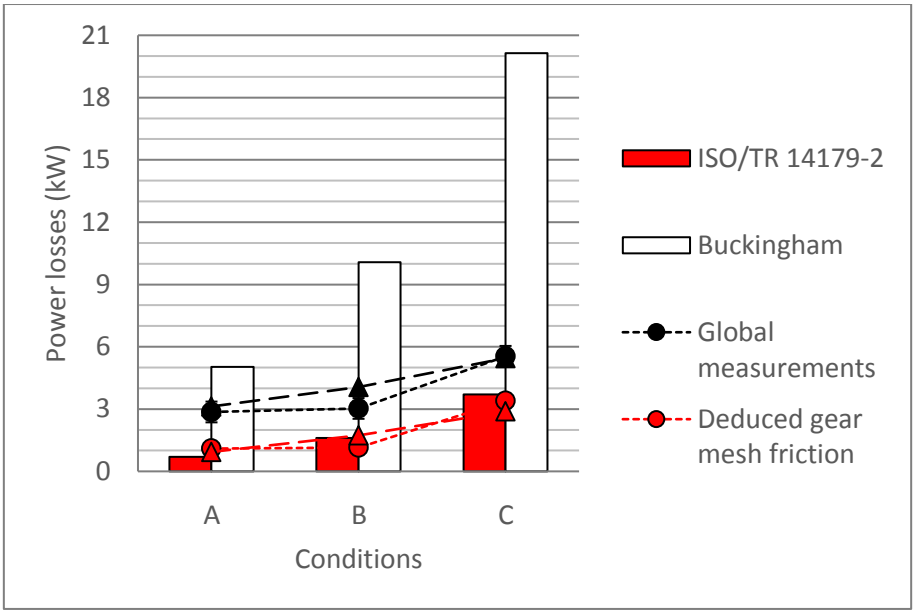

Figure 2.31: Comparison of estimated gear friction power losses according to ISO and Buckingham and measurements with (..o..) normal oil level and (-Δ-) high oil level

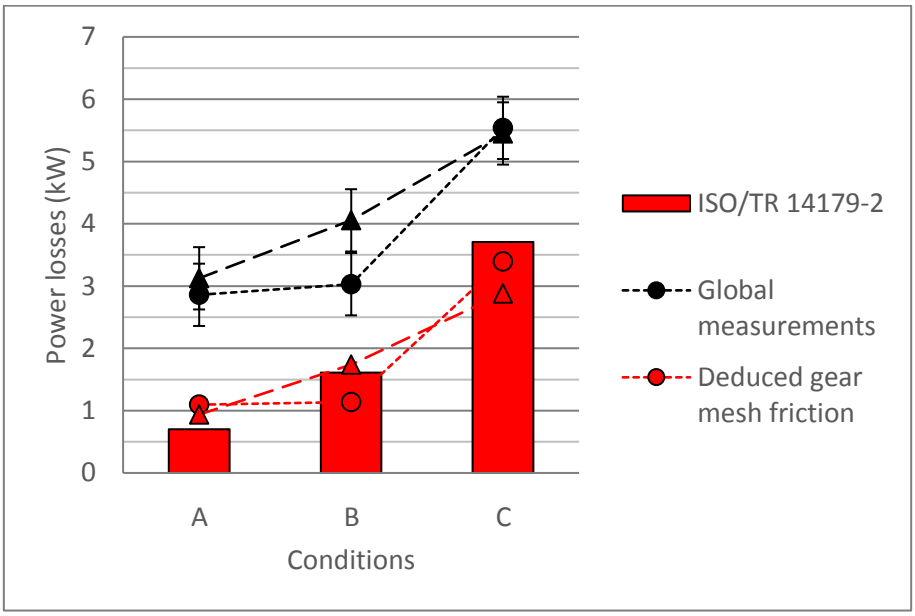

Figure 2.32: Analyse of results with ISO technical report formula and measurements with (..o..) normal oil level and (-Δ-) high oil level

Figure 2.32 allows for a better comparison between ISO/TR 14179-2 and measurements. Gear mesh friction appears to be overestimated under high load and underestimated under low load. This can be due to a misevaluation of the hypoid gear mesh contact or of the friction coefficient. A more thorough study is conducted in the next chapter to address these issues.

5.2. Influence of oil level and temperature

As far as tests with an applied load are concerned, the global power loss of the axle is presented and compared with measurements on Figure 2.33 for two oil levels. The friction coefficient used for the calculation of the gear mesh losses is calculated according to ISO/TR 14179-2.

There is a good agreement between experimental data and calculations. The major power loss source varies with operating conditions: gear mesh losses are predominant at high torque; churning losses have more importance at low torque. An increase of churning losses participation is observed between normal and high oil level (respectively Figure 2.33 (a) and (b)): oil churning contribution varies with the rise of gears immersed area. Seal losses are negligible as forecasted, since the total amount of power losses is in kW.

It can be noticed again that the gear friction power loss model has some limits. The friction of hypoid gears is very specific and so a dedicated friction model must be used and validated with experiments in order to calculate accurately gear mesh losses. Both kinematic and friction aspects are addressed in the next chapter. Nevertheless, the power loss estimation presented here is satisfactory. Moreover, the calculation is noteworthy simpler and faster than with a complete elastohydrodynamic lubrication model.

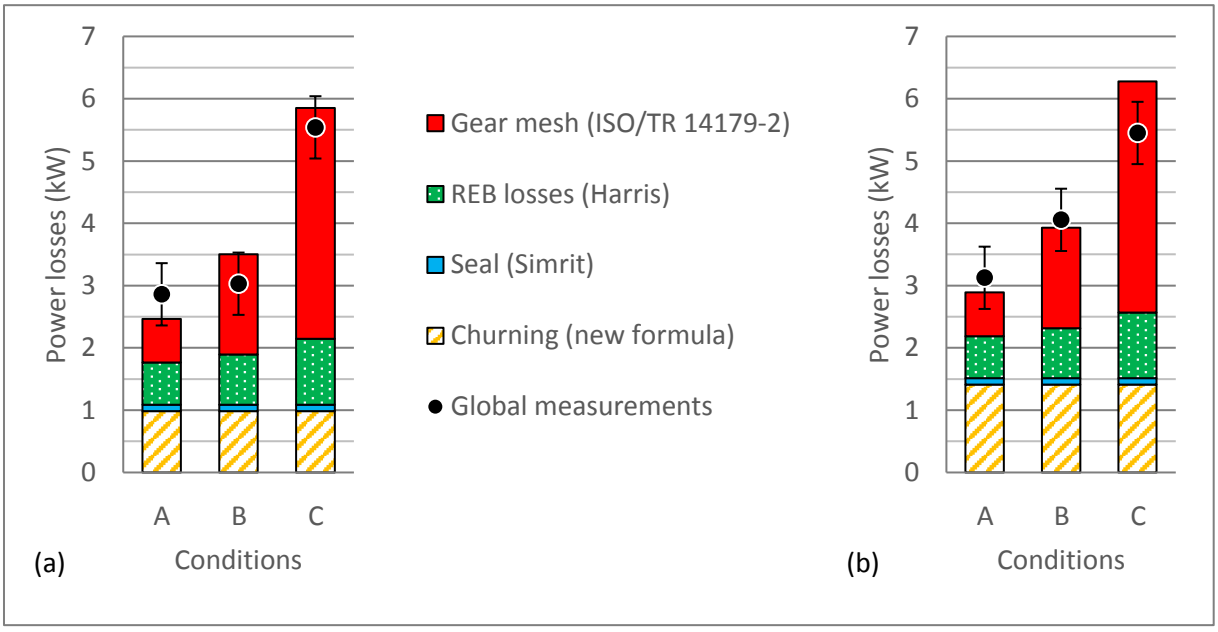

Figure 2.33: Comparison of load measurements with analytical calculations for (a) normal oil level and (b) high oil level

It can be underlined that Kakavas [7] presents a different power loss breakdown: rolling-element bearing losses (both drag and friction) are the major contribution. Nevertheless, he uses a urban drive

cycle, the New European Drive Cycle (NEDC), which means that the input torque is moderate and the axle remains relatively cool, as suggested by Kolekar [2]. Indeed, during the cycle, the oil sump temperature varies between 20 and 40°C, which is really lower than the 80°C measured on long haul truck axles. In order to quantify oil temperature influence on power losses split, some calculations were conducted. Figure 2.34 shows a higher loss contribution of bearings when lubricant temperature is lower, which is in agreement with Kakavas observations.

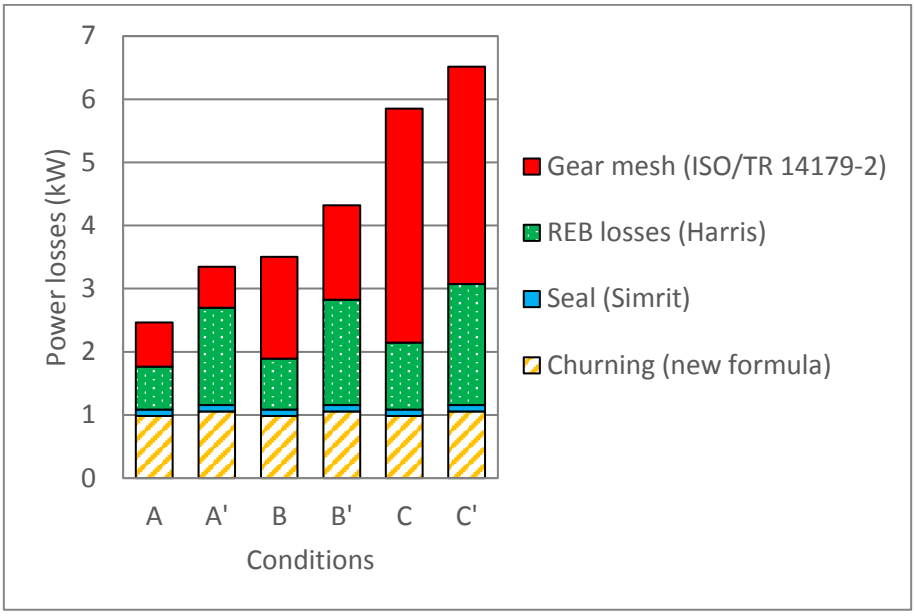

Figure 2.34: Calculation results for oil temperature at 80°C (A, B, C) and at 40°C (A', B', C')

Moreover, it can be noticed that gear friction coefficient would also be modified by temperature, as it changes for cylindrical gears [26].

6. Conclusion

Truck axle efficiency was investigated through tests and calculations. Global power losses were measured for both loaded and unloaded conditions in order to evaluate load-dependent and load-independent losses. Each source of dissipation was then estimated separately according to the different formulae presented in the first chapter. For shaft seal friction, the formula of Simrit is kept. For Rolling Element Bearings losses, it appears that SKF formula overestimates the losses under load; more coherent results are obtained with Harris formula, which is used subsequently. For hypoid gear mesh friction, the estimation according to the ISO/TR 14179-2 formula gives a good trend, but a more thorough study is required to improve it. For oil churning, both Mauz and Jeon solutions gives unrealistic results; investigations are then conducted on churning losses of spiral bevel and hypoid gears.

Experiments were performed on a specific test bench with various spiral bevel gears and cones. Different oils and operating conditions were also tested. Results highlight the influence of some operating conditions like speed, immersion ratio and oil viscosity, but also of a main gear geometrical

parameter which is the outer diameter. By contrast, it appears that gear teeth have little influence on churning losses. Discrepancies are observed when comparing these test results with Mauz and Jeon formulae. An improvement of the existing formula given by Jeon is then proposed to take a better account of the identified influential parameters. This new model considers two different regimes depending on Reynolds number and also the greater contribution due to meshing gear pair.

Thanks to this new formula, power loss estimation for the truck axle case is in better agreement with test results.

3. Hypoid gear mesh friction

1. Introduction

The second chapter has highlighted that gear mesh friction is the major power loss source of the axle for truck conditions. Nevertheless, kinematic and friction aspects in hypoid gears are particular and not well understood. Thus, it seems important to lead a more thorough investigation.

The axle gear pair is generally a hypoid one, because of contact ratio and durability aspects. But this design increases the sliding velocity at the contact and consequently the friction. According to the literature ([5], [37]), this source of dissipation depends notably on the offset, which modifies also the spiral angle. The spiral bevel design is also considered, as it is a hypoid gear without offset.

In a first part, the specificities of spiral bevel and hypoid gears are exposed. Geometrical characteristics are induced by the gear cutting process and the basic gear parameters chosen (ratio, offset). Gear mesh contact and its characteristics are described. Gear surface kinematics and its influence on oil film formation are investigated.

In a second part, the power loss due to the gear mesh is estimated for a given value of friction coefficient and according to different approaches: a global one and a local one. Indeed, the ISO/TR 14179-2 proposes an estimation at a global level, considering the gear mesh as a whole. There are generally several teeth in contact at the same time, each with different loads and sliding speeds. A calculation at contact level should be more realistic. A comparison between both approaches is used to discuss validity of the global one.

Finally, friction coefficient was identified as a major parameter of gear mesh friction loss. Different friction coefficient formulae are then reviewed and potentially influential parameters are highlighted and analysed.

2. Specificities of spiral bevel and hypoid gears

2.1. Macro-geometrical aspects

To design a hypoid gear, basic parameters are defined: pitch diameter, spiral angle, offset, tooth proportions… Pinion offset is the most distinctive parameter of hypoid gears. A higher offset allows a bigger pinion and so increases load capacity. Nevertheless this also increases power losses due to higher sliding velocities. Höhn et al. [50] also observed a faster and bigger growth of micro pitting area on tooth flanks when increasing offset.

Contrary to spiral bevel gears and due to offset, hypoid gears do not have a pitch diameter proportional to the number of teeth. Gear teeth are asymmetrical: pressure angle is different on concave and convex sides of the teeth. Moreover, spiral angle is different on pinion and crown gear. On spiral bevel gears, spiral angle is the same for both gear pair members.

Once main parameters are defined, a fabrication process must be chosen. The two main gear cutting methods for spiral bevel and hypoid gears are face-milling and face-hobbing:

- Face-milling (FM) process cuts teeth one by one, as the cutter head rotates around a fixed centre. Created flanks are thus circular arcs.
- Face-hobbing (FH) process cuts all the teeth in a same movement, as the cutter head and the generating gear rotate together. Created flanks are thus extended epicycloids.

These cutting processes are illustrated on Figure 3.1 and detailed by Kolivand [51].

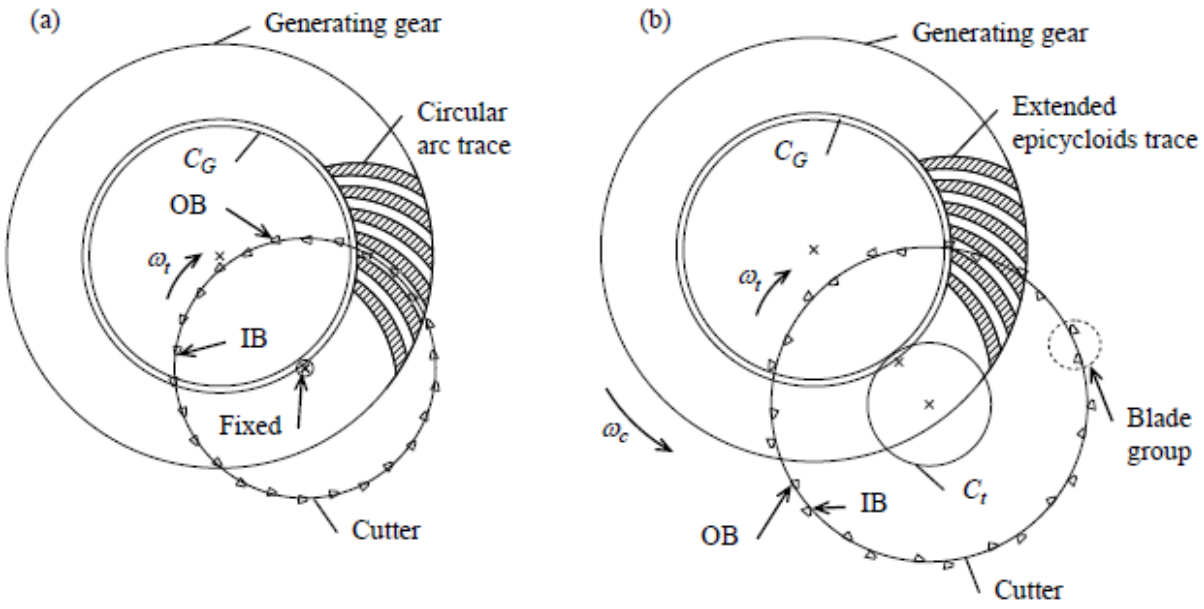

Figure 3.1: (a) Face-milling and (b) face-hobbing cutting processes [51]

This also have an impact on tooth height: a face-milled gear tooth has a higher heel than the toe, while a face-hobbed one has a heel and a toe of same height as represented on Figure 3.2.

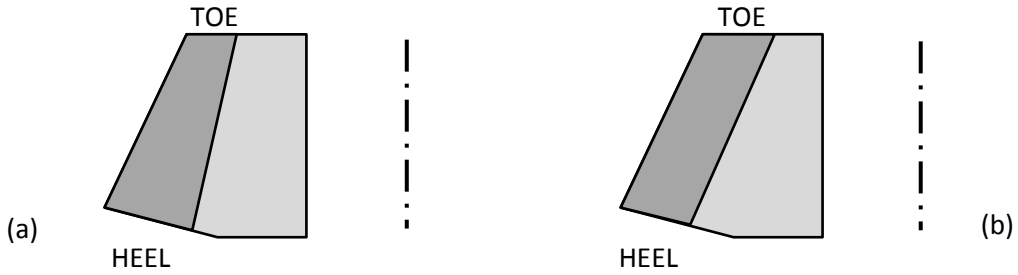

Figure 3.2: (a) Face-milled and (b) face-hobbed gear tooth

On another level, because of Formate® and Generate processes, tooth profile and cutting grooves are not the same, as represented on Figure 3.3 and Figure 3.4. Indeed, gear blank is fixed (FM) or rotates with cutter head (FH) for Formate® process, while Generate process uses an additional rotation between gear blank and cradle axis. This then requires a more sophisticated machine.

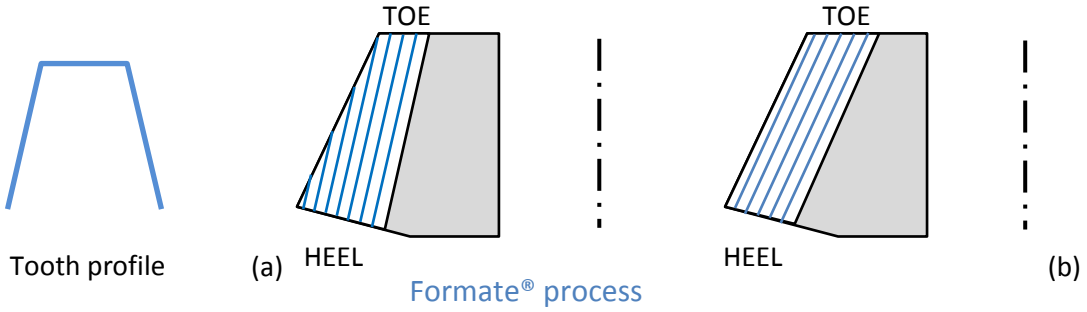

Figure 3.3: Formate® tooth profile and cutting grooves for (a) face-milled and (b) face-hobbed process

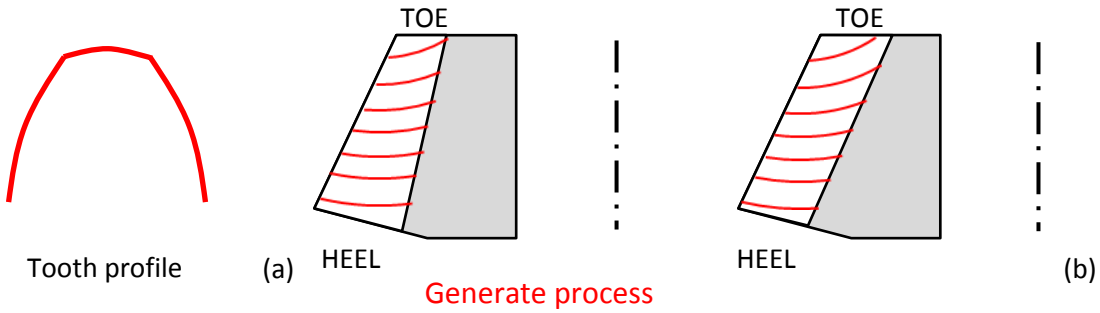

Figure 3.4: Generate tooth profile and cutting grooves for (a) face-milled and (b) face-hobbed process

The pinion is always Generate to ensure a good tooth profile. The crown wheel is generally Formate® for production reasons, but sometimes also Generate. As for spur and helical gears, tooth corrections can also be applied to hypoid gears: crowning on profile and/or on length, root and tip relief… Various ease-off are thus obtained.

The whole manufacturing process of axle hypoid gears is presented on Figure 3.5. It begins with gear

forging and cutting. Some thermochemical treatments are then performed: gear is case-carburised, quenched and tempered. Depending on cutting process, different finishing operations are done: grinding or lapping. Grinding shapes slightly tooth surfaces and helps to remove heat-treatment distortion, tooth by tooth. Lapping polishes tooth surfaces thanks to an abrasive paste.

Some optional operations can be performed after this process, like shot-peening to improve bending resistance. A manganese phosphating coating is sometimes applied, but only on one gear pair member. Phosphating is generally used for rusting problems and must prevent scuffing in early life of gear. According to Chen et al. [52], this also improves pitting fatigue life when applied on only one gear of the pair due to the creation of oil reservoirs in tooth surface.

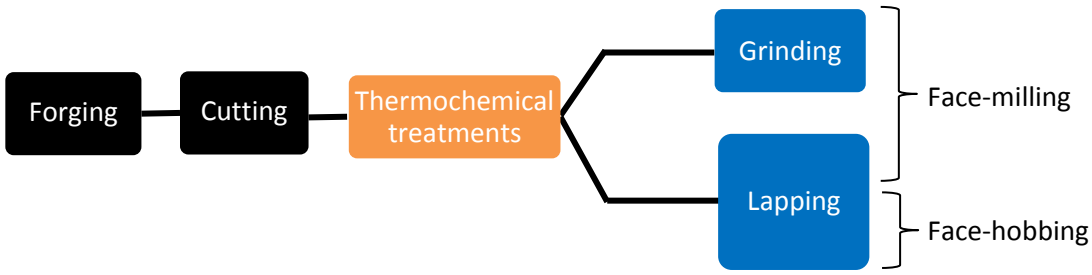

Figure 3.5: Typical manufacturing process for axle hypoid gears

It seems important to take into account all these specificities when designing a hypoid gear. Hypoid gear teeth are generally modelled thanks to Finite Elements for geometry and mechanical aspects ([23], [24], [53]–[55]). This allows notably for performing a Tooth Contact Analysis (TCA). The analytical approach is more rarely adopted: an equivalent helical gear approximates the hypoid one ([50], [56]). Moreover, Höhn et al. [50] validated this approximation by comparison with a Finite Element analysis.

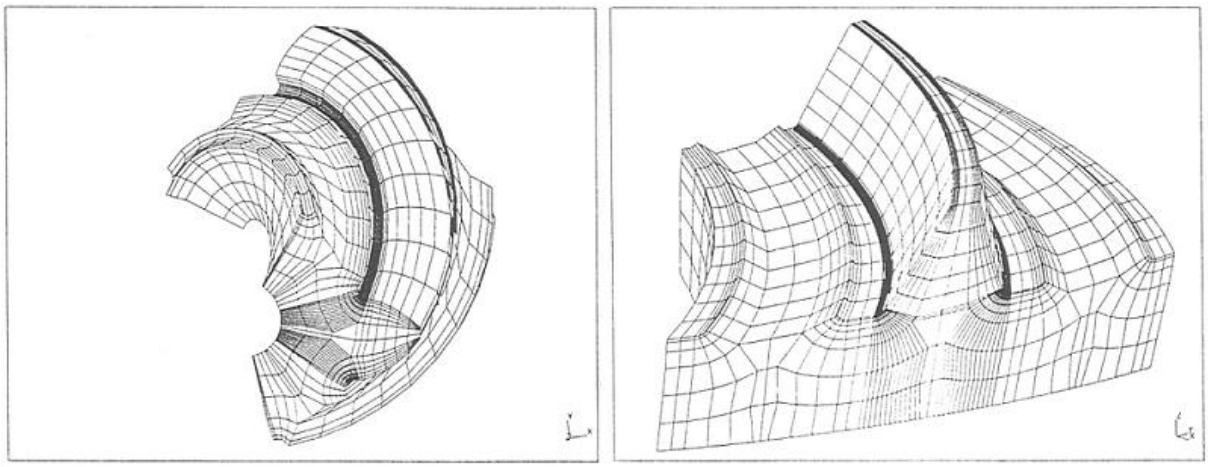

Figure 3.6: Finite Element model of a gear set using Barday software [22]

A meshing calculation software was developed and validated by Barday [22] at Renault VI (now part of Volvo Group). The gear surface geometry is generated according to a manufacturing process simulation. Finite Element models of one tooth of pinion and crown are then created as illustrated on Figure 3.6. A three-dimensional analysis of the gear set is conducted to determine bending and shear deformation before any gear meshing is considered.

This model was first developed for durability aspects. Through Transmission Error calculations, noise emission issue was also addressed [57]. It can indeed consider the ease-off topography or even a 3D measurement surface topography of an existing gear, allowing accurate estimations.

2.2. Contact aspects

A hypoid gear set is unique as pinion and crown are paired. To obtain a good contact pattern, the optimal mounting distance of gear set is checked thanks to the use of paint on teeth. Typical shape of this contact pattern is approximately a parallelogram, as illustrated on Figure 3.7. Höhn et al. [50] noticed that the angles of this parallelogram depend on hypoid offset. For spiral bevel gears, this becomes a rectangle.

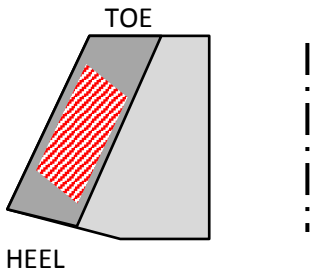

Figure 3.7: Representation of a typical contact pattern for a hypoid gear set

The contact pattern spreads with increasing load, as underlined on Figure 3.8.

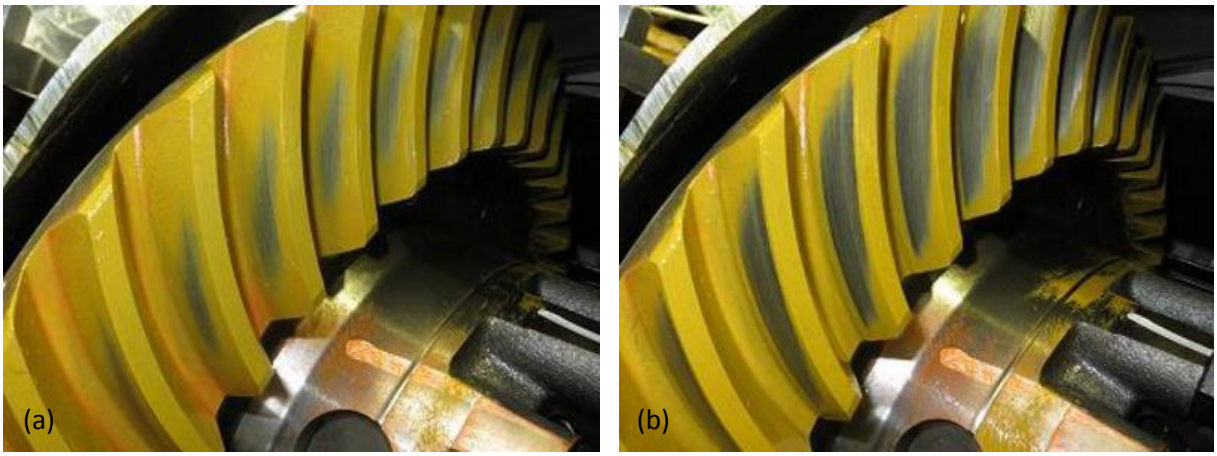

Figure 3.8: Contact pattern spread is highlighted thanks to yellow paint for (a) low loaded case and (b) more loaded case

The hypoid gear mesh is theoretically a line contact. However, in operation, this is more an elliptical contact due to load and deformations. Many authors discretised the ellipse in several line contacts (Xu et al. [23], Kolivand et al. [24]). The elliptical contact is generally used to consider contact area and elastohydrodynamic lubrication (Karagiannis et al. [53], Mohammadpour et al. [54]). Hertz contact theory is presented in Annex 3.A for both line and elliptical contacts.

Potential line of contact are determined with the model of Barday. As illustrated on Figure 3.9, each

line is discretised with segments of variable length dl: both ends of the lines are discretised more finely than line centre. Depending on operating conditions, some segments experience a load and are represented by rectangles on Figure 3.9. A line contact is used on each of them: contact half-width b_c (mm) is calculated according to Equation (3.15) of Annex 3.A.

Even if an elliptical contact is not considered through this method, an estimation of the ellipse can be done according to lengths dl and half-widths b_c. An example of contact ellipse is plotted in red dashes on Figure 3.9.

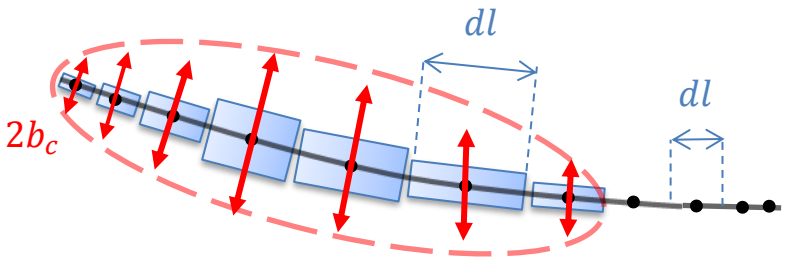

Figure 3.9: Discretisation of a potential line of contact and representation of a contact ellipse

Figure 3.10 shows an example of contact line analysis obtained thanks to Barday software. The contact centre is highlighted all along its path through gear mesh. On this illustration, three teeth pairs are potentially in contact at the same time (depending on load), at the three numbered positions.

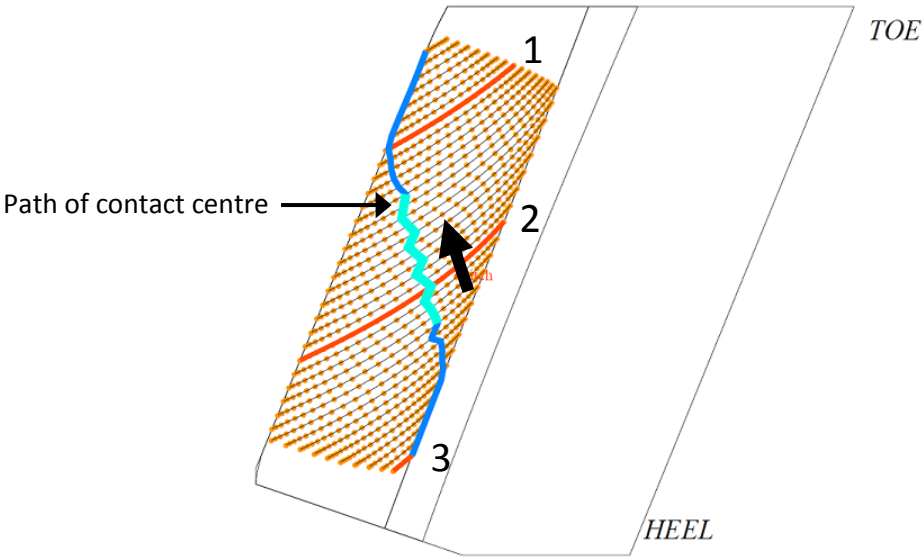

Figure 3.10: Pinion contact lines obtained by using Barday software

Between two lines of contact, there are naturally different contact conditions. But it is also the case along a contact line itself: surface velocities, load and radius of curvature are varying and thus modifying contact width, oil film thickness and contact kinematics.

On another level, because of Generate and Formate® processes, the angle between cutting lines and contact lines can also change along contact path.

2.3. Kinematic aspects

To evaluate friction at gear mesh, sliding between surfaces in contact must be known. Classically, sliding velocity V_s, sum of surface velocities V_Σ and entrainment velocity V_e (m/s) are defined as:

$$V_s = V_1 - V_2 \tag{3.1}$$

$$V_\Sigma = V_1 + V_2 \tag{3.2}$$

$$V_e = \frac{V_\Sigma}{2} \tag{3.3}$$

where V_1 and V_2 are respectively pinion and gear surface velocities (m/s).

Considering spiral bevel gears, pinion and crown surface velocities are identical in terms of value and direction on pitch cone only. Elsewhere, due to their conical shape and to spiral angle, their surface velocities differ in value and direction. This induces a velocity orientation angle δ between surface velocities and an entrainment orientation angle δ_e between entrainment velocity and ellipse axis x, as represented on Figure 3.11. Sliding occurs only along ellipse minor axis, as for spur and helical gears. On hypoid gears, spiral angles of contacting surfaces are different between pinion and gear due to offset. This generates sliding in longitudinal direction to contact line as well. Figure 3.11 illustrates these various cases. Höhn et al. [50] analysed that sliding transverse component along hypoid tooth profile is similar to helical gears. The difference in sliding conditions between hypoid and helical gears comes from the longitudinal component, which induces higher sliding velocities and more friction.

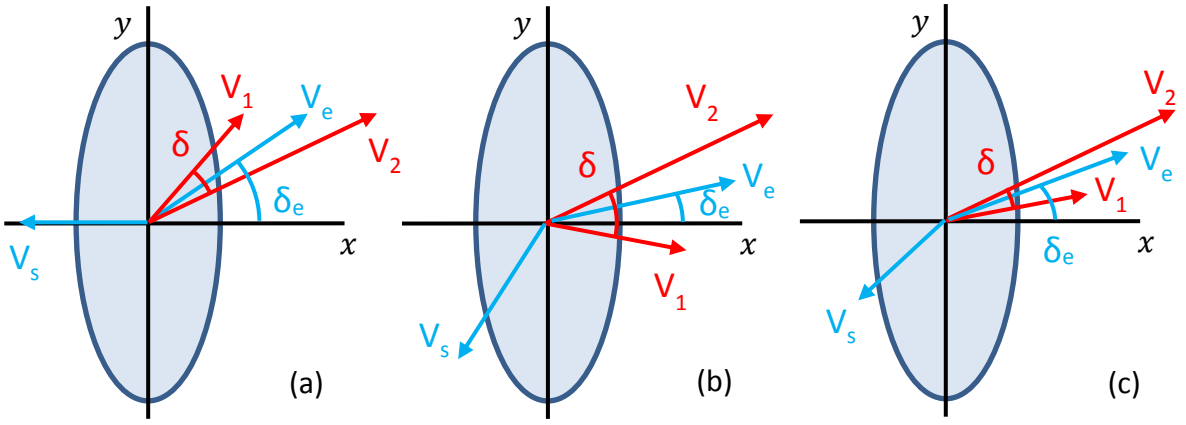

Figure 3.11: Examples of contact velocities for (a) spiral bevel gear and (b)-(c) hypoid gear

Buckingham [16] defines the pitch surfaces of hypoid gears as hyperboloids of revolution. Their contacting circles touch at pitch point but do not rotate in the same plane or in planes at right angles to each other, due to offset. This induces sliding even at pitch point.

Surface velocities vary along contact line, as represented on Figure 3.12: value and direction change. Kinematics inside contact ellipse of hypoid gears is then quite particular.

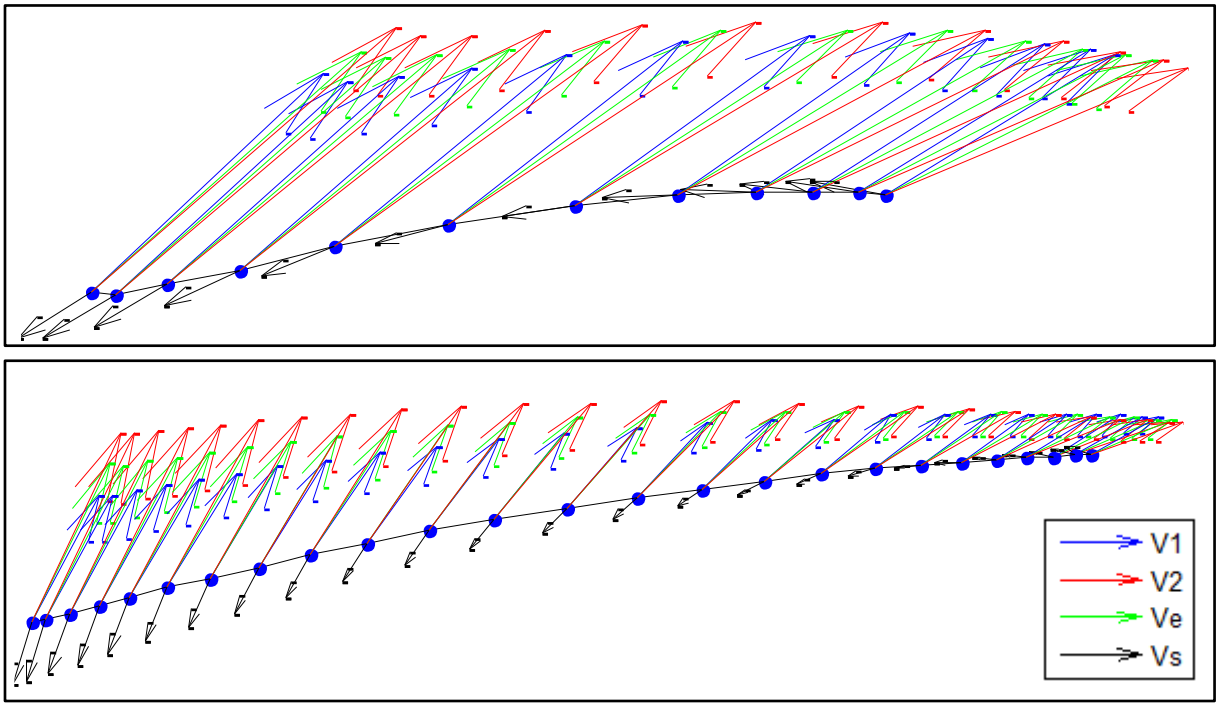

Figure 3.12: General view of velocities for two different lines of contact in tooth tangent plane

For analysis purpose, the entrainment speed V_e is decomposed into two components: one transverse to contact line $V_{e,x}$ and one longitudinal to contact line $V_{e,y}$. A mean entrainment speed is defined in each direction, giving general displacements of the contact ellipse. Figure 3.13 illustrates entrainment velocities of contact ellipse. The longitudinal component of entrainment velocity seems constant. Concerning the transverse component, it changes all along the ellipse, inducing a slight rotation.

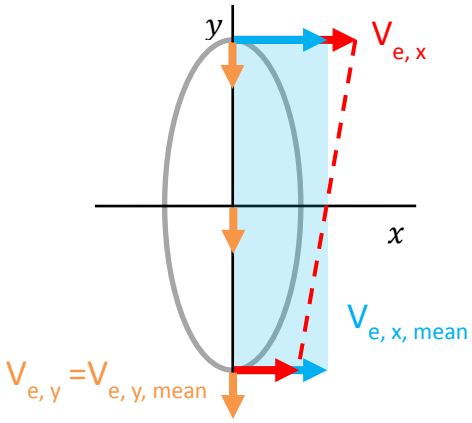

Figure 3.13: Ellipse entrainment velocities

3. Power loss estimation

Gear mesh appears to be the major power loss source in the truck axle case. In Chapter 2, this dissipation was finally evaluated according to ISO/TR 14179-2. These calculations are based on an equivalent helical gear, which is determined according to hypoid gear characteristics, as presented in Annex 1.A. This is an approximation and cannot take into account all the specificities of hypoid gears presented in the previous part.

Therefore, the validity of this friction power loss law is discussed. A local approach based on Barday software results is presented to estimate gear mesh losses. A comparison is then conducted between both approaches, with a fixed friction coefficient.

3.1. Local approach

From a purely mechanical point of view, gear mesh friction loss is due to tangent friction effort and sliding velocity between surfaces. Tangent friction effort is generated by the normal effort applied at contact and is in the direction opposite to sliding velocity.

As potential contact lines are discretised, each segment is represented by its centre M_{ij}, with i the contact line number and j the segment number. Figure 3.14 illustrates this local contact and the related forces and velocities. A tangent friction effort $\overrightarrow{dT^1_{2_{ij}}}$ (N) is then locally defined as:

$$\overrightarrow{dT^1_{2_{ij}}} = \mu_{ij} \left\| \overrightarrow{dN^1_{2_{ij}}} \right\| \overrightarrow{\epsilon_{ij}} \tag{3.4}$$

where μ_{ij} is the local friction coefficient, $\overrightarrow{dN^1_{2_{ij}}}$ is the elementary normal effort (N) and $\overrightarrow{\epsilon_{ij}}$ is the local orientation vector, which is:

$$\overrightarrow{\epsilon_{ij}} = \frac{\overrightarrow{V^1_2}(M_{ij})}{\left\| \overrightarrow{V^1_2}(M_{ij}) \right\|} \tag{3.5}$$

where $\overrightarrow{V^1_2}(M_{ij})$ is the velocity vector of sliding between pinion and gear teeth.

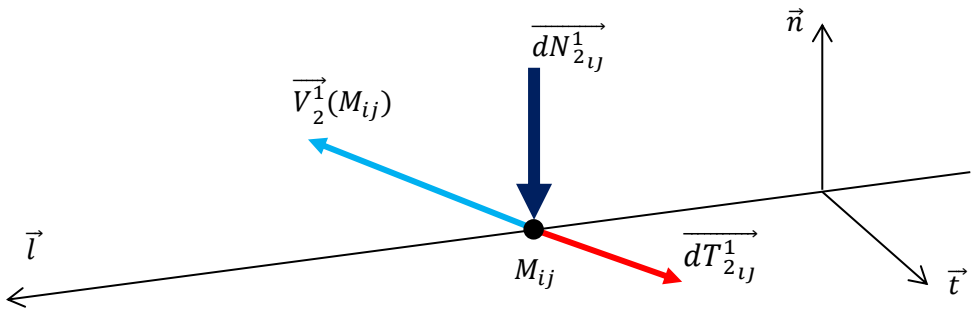

Figure 3.14: Forces and velocities at local contact

The power loss along a complete contact line i (W) is:

$$P_i = \sum_j \overrightarrow{V_2^1}(M_{ij}) \cdot \overrightarrow{dT_{2_{ij}}^1} \tag{3.6}$$

Finally, the instantaneous power loss of the hypoid gear pair is calculated according to the simultaneous teeth pairs in contact.

Results obtained thanks to this method are exposed hereafter. Two different gear sets are considered: a hypoid one (gear set A) and a spiral bevel one (gear set B). They have the same ratio and their characteristics are listed in Table 3.1. For these examples, a fixed friction coefficient of 0.05 is used on each point: no local friction coefficient is calculated.

Table 3.1: Characteristics of gear sets

	Gear set A		**Gear set B**	
	Pinion	**Crown gear**	**Pinion**	**Crown gear**
Number of teeth	8	37	8	37
Outer diameter (mm)	134.6	428	135.5	478
Width (mm)	85	62	77.7	60.7
Face width (mm)	74.4	63	75.5	75.5
Face angle (°)	15.11	74.34	16.42	79.33
Pressure angle (°)	21.21	/	20	/
Spiral angle (°)	45	34.25	38	38
Hand of spiral	LH	RH	LH	RH
Offset (mm)	35	/	0	/

First, contact conditions are studied on only one teeth pair contact among the simultaneous ones for a complete mesh cycle. For each successive contact line, total normal force and mean sliding velocity of the contact are calculated. Figure 3.16 presents these values for gear set A and Figure 3.17 for gear set B for various input torques.

As torque increases, normal force variations are smoother: the contact is more spread along mesh cycle and there is more overlap between teeth contact. Mean sliding velocity of the contact changes slightly as contact length increases with load. Indeed, contact shape is modified by load as illustrated on Figure 3.15.

The hypoid gear set A has a permanent sliding all along the gear mesh cycle (>1m/s), while it is close to pure rolling for spiral bevel gear set B around pitch point (<0.2m/s). This is due to hypoid offset.

Figure 3.15 highlights the difference of contact pattern between hypoid and spiral bevel gears: parallelogram for hypoid, and close to rectangle for spiral bevel. The contact zone increases similarly with load for both gears. However, it is less spread along tooth width for the considered spiral bevel gear design.

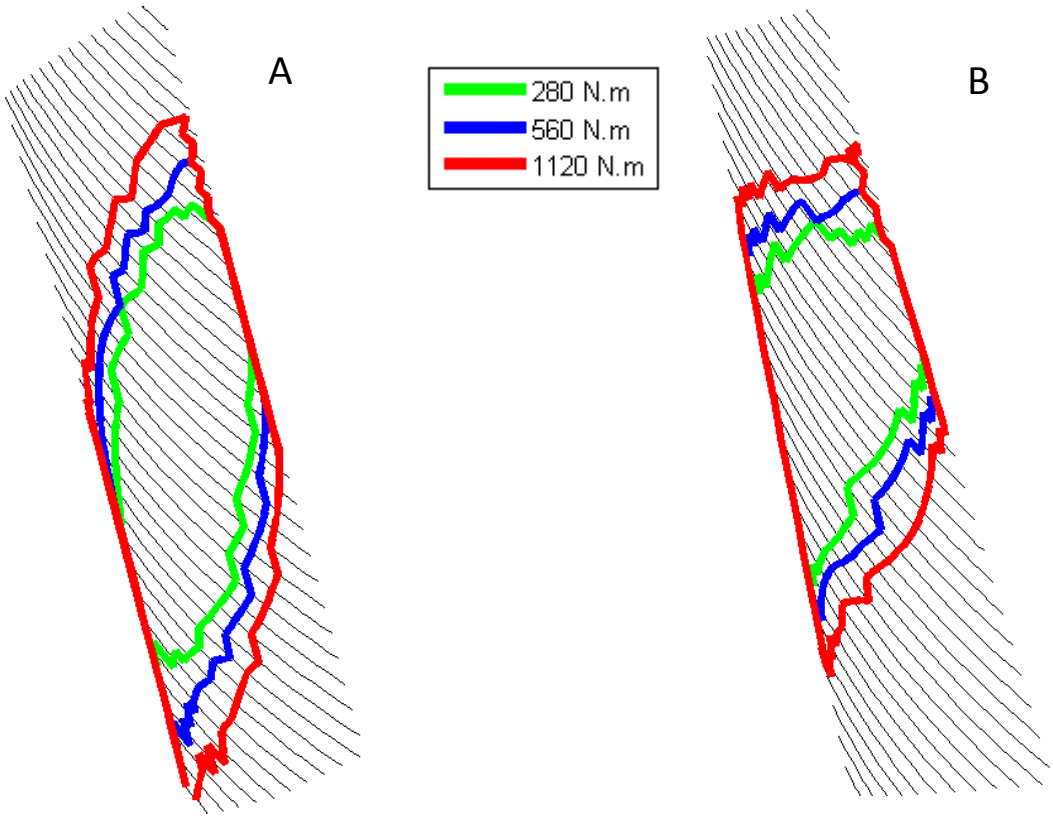

Figure 3.15: Contact pattern for different input torques on gear set A and gear set B

Power loss is then calculated over a complete mesh cycle for each engaged teeth pair. The total power loss of gear mesh is deduced at any time. Typical results obtained are plotted on Figure 3.18 for gear set A. As load and overlap increase, power loss is stabilised through mesh cycle. A similar behaviour is presented on Figure 3.19 for gear set B. It is nevertheless more wavering due to its restrained contact pattern.

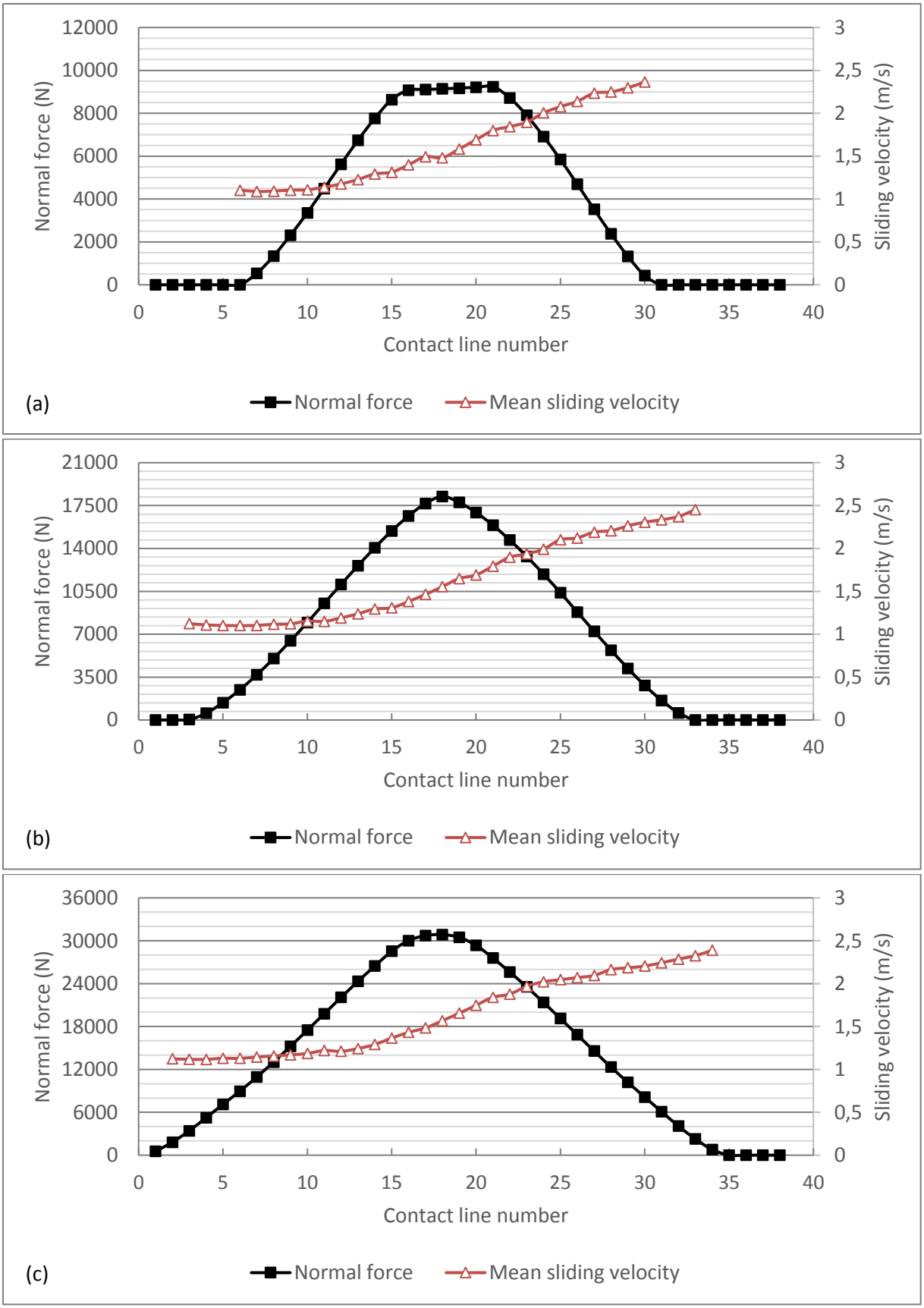

Figure 3.16: Contact conditions of gear set A on one contact line along a complete gear mesh cycle for an input speed of 1000 rpm and different input torques: (a) 280 N.m, (b) 560 N.m and (c) 1120 N.m

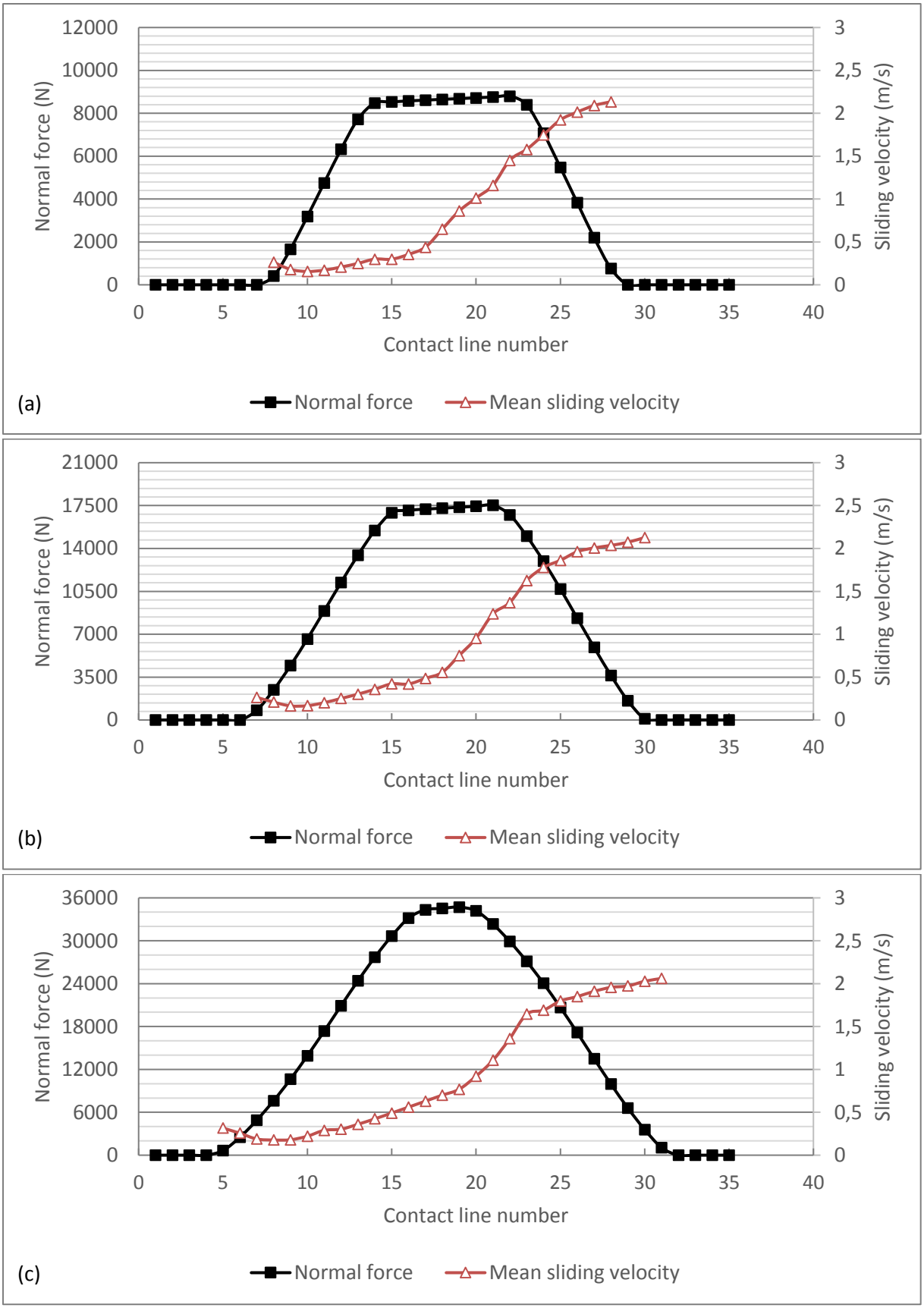

Figure 3.17: Contact conditions of gear set B on one contact line along a complete gear mesh cycle for an input speed of 1000 rpm and different input torques: (a) 280 N.m, (b) 560 N.m and (c) 1120 N.m

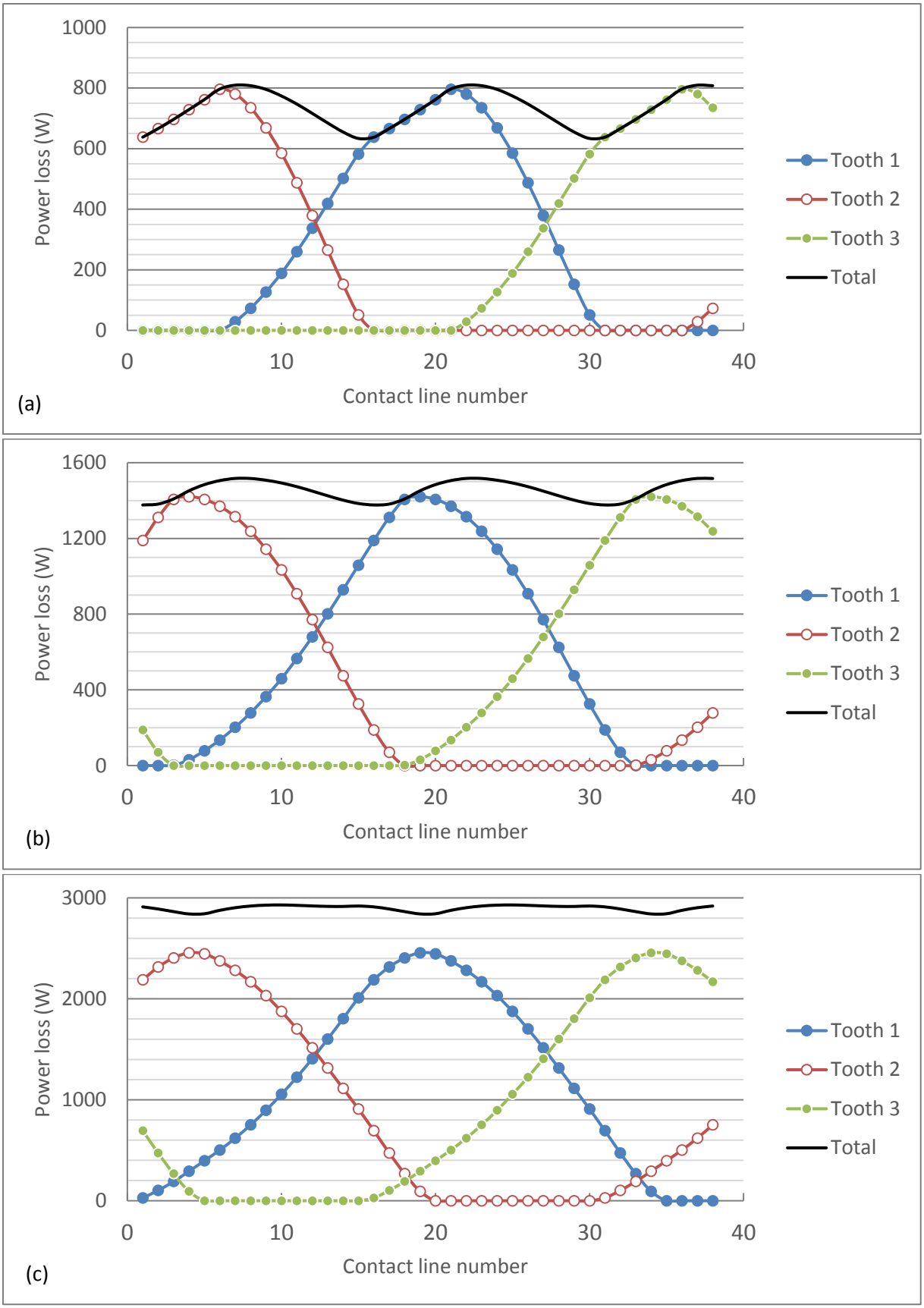

Figure 3.18: Gear friction power loss along a complete gear mesh cycle of gear set A for an input speed of 1000 rpm and different input torques: (a) 280 N.m, (b) 560 N.m and (c) 1120 N.m

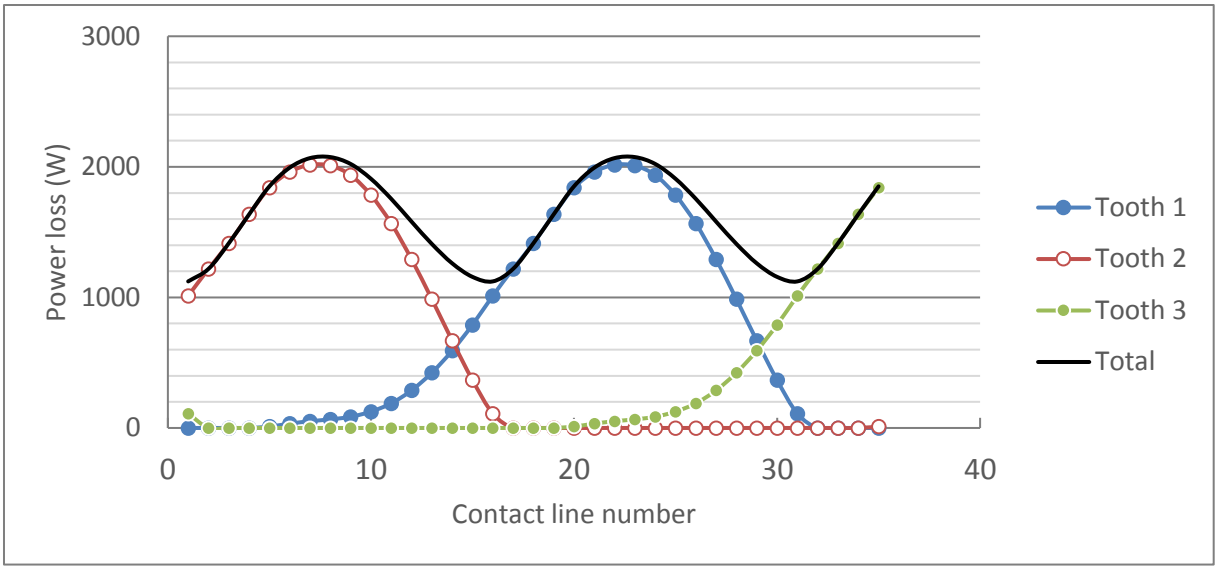

Figure 3.19: Gear friction power loss along a complete gear mesh cycle of gear set B for an input speed of 1000 rpm and an input torque of 1120 N.m

3.2. Comparison between global and local approaches

The ISO/TR 14179-2 [9] is used in Chapter 2 for the calculation of gear mesh power loss at a global level. To discuss the validity of this approximation, a comparison is made here with the local approach presented in the previous section.

For this purpose, the two gear sets described in Table 3.1 are again considered. Gear mesh friction loss is estimated for each gear set at various input torques and speeds. As in the previous section, a fixed friction coefficient of 0.05 is used to compare both approaches. For local approach, the instantaneous power loss is averaged on a complete meshing and is considered as the gear mesh global power loss (Local approach #1). Results are plotted on Figure 3.20 for gear set A and on Figure 3.21 for gear set B.

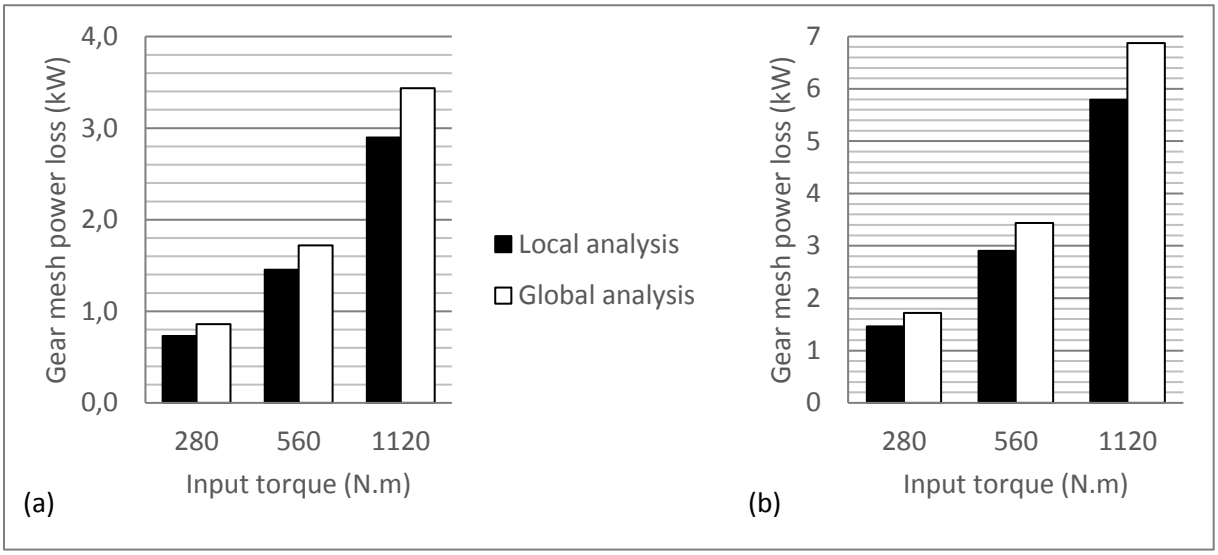

Figure 3.20: Comparison of power loss estimation according to local and global approaches for gear set A at an input speed of (a) 1000 rpm and (b) 2000 rpm

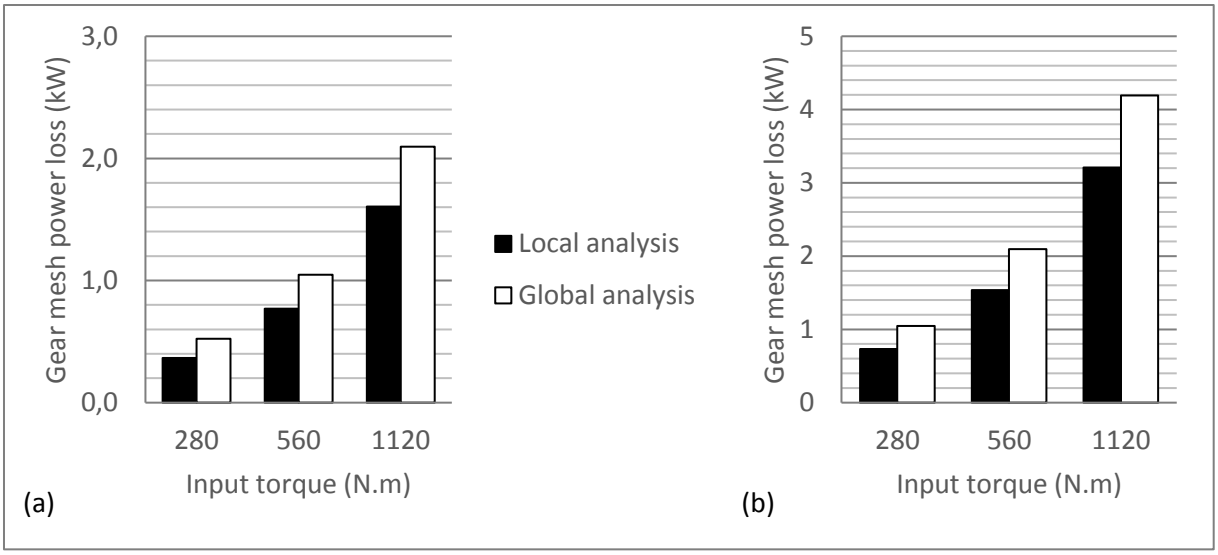

Figure 3.21: Comparison of power loss estimation according to local and global approaches for gear set B at an input speed of (a) 1000 rpm and (b) 2000 rpm

Both estimations give similar trends and results for each gear set: sliding velocity is directly proportionnal to input speed, so gear mesh power losses are almost doubled between the two speed conditions. Global approach always overestimates gear mesh power losses and it seems to be more pronounced for gear set B. Table 3.2 presents the difference between both estimations in terms of power loss. For gear set A, the difference is quite stable at roughly 18%. For gear set B, the difference is more important (over 30%) but decreases with higher torque.

Table 3.2: Estimation difference between local and global approaches

Input torque (N.m)		**280**	**560**	**1120**
Power loss difference (%)	**Gear set A**	17.7	18.3	18.7
	Gear set B	42.8	36.4	30.5

In order to compare both methods more precisely, mean values are calculated for the local approach (Local approach #2):

- Mean normal force: for each contact line, the total normal force is calculated and summed for the simultaneous teeth in contact; a mean over the complete meshing is then computed.
- Mean sliding velocity: for each contact line, a mean sliding velocity is calculated and averaged for the simultaneous teeth in contact; a mean over the complete meshing is then computed.

A mean gear mesh power loss is finally calculated, as for global approach:

$$P_{hypoid} = F_n \, v_{gm} \, \mu_m \tag{3.7}$$

where F_n is the tooth normal load (N), v_{gm} is the mean sliding speed (m/s), and μ_m is the mean friction coefficient (here, still 0.05).

Difference between estimations of local approach #1 and #2 is less than 3%. The mean values calculated for local approach #2 are thus accurate and representative of local approach: they can be

compared with the mean values of global approach.

Concerning mean normal force, global approach underestimates it by maximum 2% and this gap decreases with increasing torque. The mismatch between local and global methods is thus mainly due to sliding velocity estimation. A comparison is made between these two sliding velocity estimations in Table 3.3 and shows an overestimation up to almost 50% on sliding speed at low input torque. Indeed, local approach considers sliding velocity only in contact zone, which depends on contact pattern and so on torque. This difference is particularly marked for gear set B, as its contact pattern is rather small in comparison to gear set A as presented on Figure 3.15. If sliding velocity is considered on complete contact lines, local mean sliding velocity is increased and difference drops under 5% for gear set B.

Table 3.3: Difference of mean sliding velocity between local and global approaches

Input torque (N.m)		280	560	1120
Sliding velocity difference (%)	Gear set A	19.2	15.5	16.9
	Gear set B	48.0	38.2	33.3

Thus, with higher torque and wider contact pattern, local and global approaches should give identical results. However, this is an ideal case as contact pattern is rarely spread over the whole tooth. Global approach allows to obtain an approximation of gear mesh power loss, but will always give a worst case scenario, mainly due to sliding velocity overestimation.

In Chapter 2, it appears that ISO formula overestimates gear mesh friction under high load and underestimates it under low load. The same test cases are considered with local approach. Global friction coefficients are calculated according to ISO technical report: 0.020 for condition A, 0.023 for condition B and 0.026 for condition C. Figure 3.22 presents the comparison of both global and local approaches with measurements.

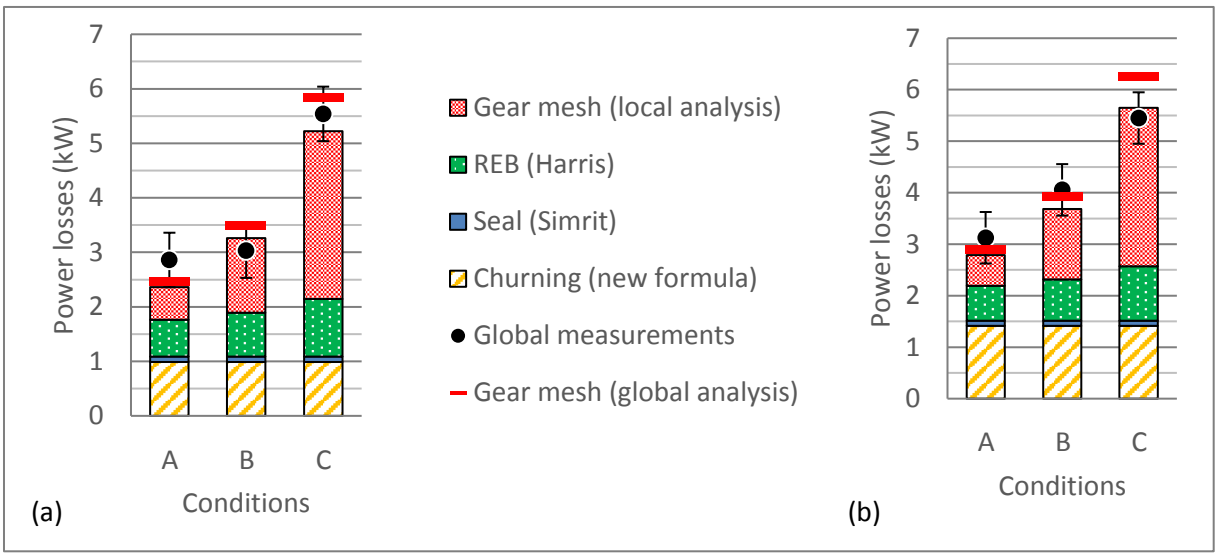

Figure 3.22: Comparison for gear set A between measurements and gear friction power loss according to local and global approaches with (a) normal oil level and (b) high oil level

A better agreement is obtained with local approach. However for both methods, power loss is underestimated at low load. This can be due to friction coefficient misevaluation, as it is identical in each approach. Moreover, for local approach, it is possible to calculate a local friction coefficient. This is investigated in the next section.

4. Friction coefficient

Friction coefficient is a first order parameter for gear mesh power loss. It is mainly influenced by load, entrainment and sliding velocities, oil properties, and surface roughness. As seen in Chapter 2 with Buckingham formula, its calculation is very important for the accuracy of gear mesh friction estimation: overestimation of power loss is directly linked to a high friction coefficient. Several friction coefficient formulae exist and depend on one to multiple parameters among the ones listed previously. They are reviewed in the next part. Results then vary from a formula to another. According to Buckingham [16], friction coefficient varies from 0.03 to 0.07 for a spiral bevel gear and from 0.03 to 0.2 for a hypoid gear, while according to Coleman [17], it ranges from 0.01 to 0.12 for hypoid gears in general.

Parameters influencing friction coefficient are characterising the elastohydrodynamic (EHD) contact between gear teeth. This contact is defined by the presence of a lubricant film and by the non-conforming surface geometry which induces a small contact area and high contact pressures.

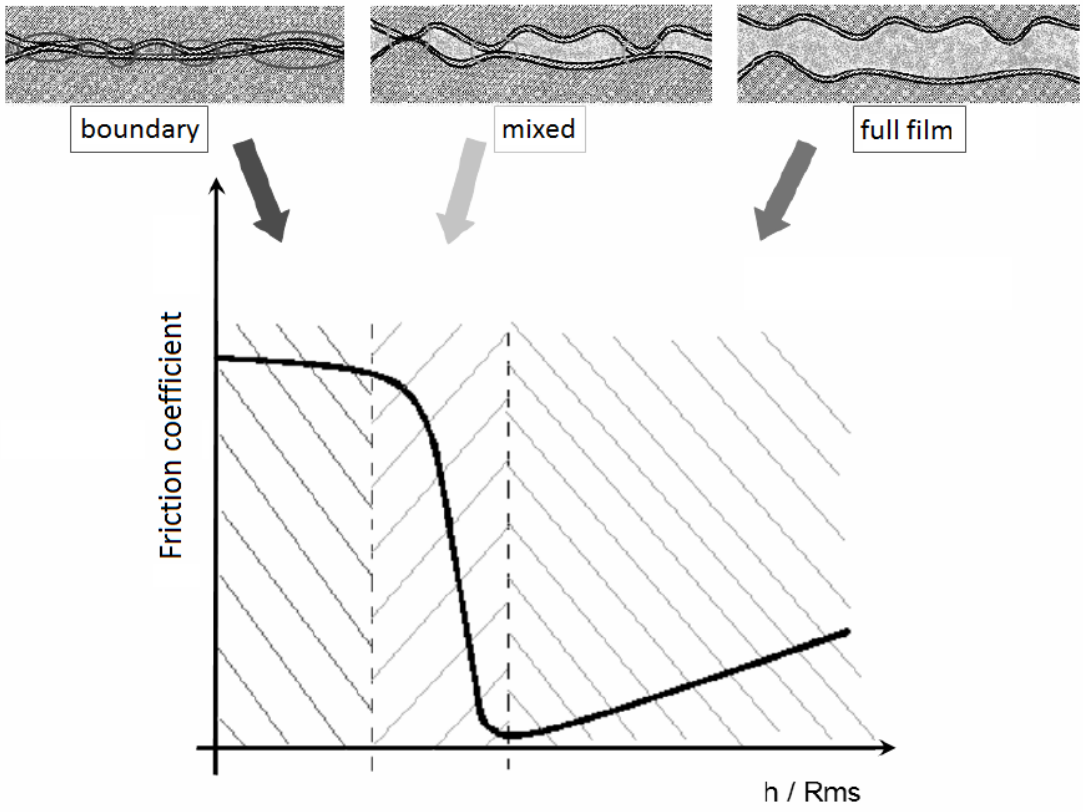

Figure 3.23: Stribeck curve - Friction coefficient evolution depending on lubrication regime [58]

Different regimes of lubrication are distinguished depending on the thickness of the lubricant film regarding surface roughness, as represented on Figure 3.23:

- Boundary lubrication: the two surfaces are in contact due to asperities and friction coefficient is influenced by additive properties;
- Full film lubrication: lubricant film separates completely the two surfaces and friction coefficient depends on lubricant properties only;
- Mixed lubrication: friction happens through asperity contacts and lubricant film shearing at the same time.

This last regime is the most common in gear mesh applications due to gear surface roughness and high sliding encountered notably at meshing beginning and end.

Different friction coefficient formulae are reviewed just hereafter to understand how these parameters can be taken into account. Some parameters are then analysed regarding hypoid gears to lead to potential efficiency improvements.

4.1. Friction coefficient formulae

Previously in this chapter, friction coefficient formula proposed in ISO technical report 14179-2 [9] was used. As already mentioned, this is a mean friction coefficient:

$$\mu_m = 0.048 \left(\frac{F/b_t}{v_\Sigma \, R_{eq}} \right)^{0.2} \eta_{oil}{}^{-0.05} \, Ra^{0.25} \, X_L \tag{3.8}$$

where F is the tooth normal force (N), b_t is the tooth width (mm), v_Σ is the resultant sum velocity (m/s), R_{eq} is the equivalent radius of curvature (mm), η_{oil} is the lubricant dynamic viscosity at operating temperature (mPa.s), Ra is the arithmetic average roughness (µm) and X_L is a lubricant factor. Some parameters are determined differently depending on gear type, as equivalent gears are used for calculation of complex gear pairs. Details are given in Annex 3.B.

Despites good results shown at the end of previous section, this formula does not allow to consider local conditions along contact lines and gear mesh. It is then interesting to review local approaches for friction coefficient calculation. Concerning lubricated contacts, most of friction coefficient formulae are empirical. They are based on data from experiments conducted on EHD simulators like twin-disc machines that reproduce gear teeth contact conditions. A formula frequently used is the one of Benedict and Kelley [25]:

$$\mu = 0.0127 \log_{10} \left(\frac{3.17 \times 10^8 \, W_{lb}}{\eta_{oil} \, V_{s\,in} \, V_{\sum in}{}^2} \right) \tag{3.9}$$

where W_{lb} is the load by unit of length (lb/in), η_{oil} is the lubricant dynamic viscosity (mPa.s), $V_{s\,in}$ is the sliding velocity (in/s) and $V_{\sum in}$ is the sum of surface velocities (in/s). This formula displays several important parameters influencing friction coefficient, but surface roughness is not considered. Moreover, it appears that this formula is valid only for high slide-to-roll ratio (20% to 50%) as the experiments were conducted for these conditions. Non negligible discrepancies are then obtained out of these boundaries [26].

Diab et al. [26] developed a formula based on Greenwood-Tripp theory (1971) completed by Mikic (1974) and on many traction curves:

$$\mu = \frac{1}{p_{moy}}\left[\frac{A_c}{A_0}\cdot\tau_{dry} + \left(1-\frac{A_c}{A_0}\right)\cdot\tau_{fluid}\right] \tag{3.10}$$

where p_{moy} is the mean contact pressure (Pa), A_c and A_0 are respectively the actual average contact area and the apparent contact area (m²), τ_{dry} and τ_{fluid} are respectively the shear stress due to dry friction and to fluid friction (Pa). Here, roughness is considered through contact areas. The contribution of asperities contact and of fluid shearing are considered separately. Details are given in Annex 3.B.

Xu and Kahraman [45] established an accurate elastohydrodynamic lubrication (EHL) analysis. A multiple linear regression of a large number of these analyses was done to obtain a formula that can be used directly:

$$\mu = e^{f(SR,P_h,\eta_{oil},Ra)}\ {P_h}^{b_2}\ |SR|^{b_3}\ {V_e}^{b_6}\ {\eta_{oil}}^{b_7} R^{b_8} \tag{3.11}$$

where SR is the Slide-to-Roll Ratio, P_h is the maximum Hertzian pressure (GPa), η_{oil} is the dynamic viscosity at oil inlet (mPa.s), Ra is the surface roughness (µm), V_e is the entraining velocity (m/s) and R is the effective radius of curvature (m). Details are given in Annex 3.B. This formula takes into account many important parameters influencing friction coefficient and has the advantage to be quite simple to use.

Xu [27], and after him Kolivand et al. [24], used only transverse sliding for friction coefficient calculation, arguing that longitudinal sliding is multiple times smaller than transverse sliding. However, as illustrated on Figure 3.12, it may not be always the case: longitudinal sliding is sometime higher than transverse one. For this reason, it seems more reliable to consider the whole sliding. Moreover, it has not been clarified if longitudinal sliding has a particular influence on friction coefficient or not.

4.2. Influence of parameters on friction coefficient

A recurrent parameter in friction coefficient formulae is the surface roughness. In the section 2 of this chapter, it was shown that hypoid gears surface roughness is due to specific gear cutting, surface treatment and finishing. A second particularity of hypoid gears are the orientation angles. As this influences entrainment and sliding velocity, it seems worth to study.

These two potentially influential parameters are then discussed here [59].

4.2.1. Surface roughness

As underlined by Diab et al. [26], surface roughness is important in two ways:

- the overall roughness of surface, which is characterised by the arithmetic average roughness Ra and by the profile maximum height Rz and depends mainly on surface finishing;
- the grooves orientation in surface roughness, which are due to surface machining during cutting and finishing process.

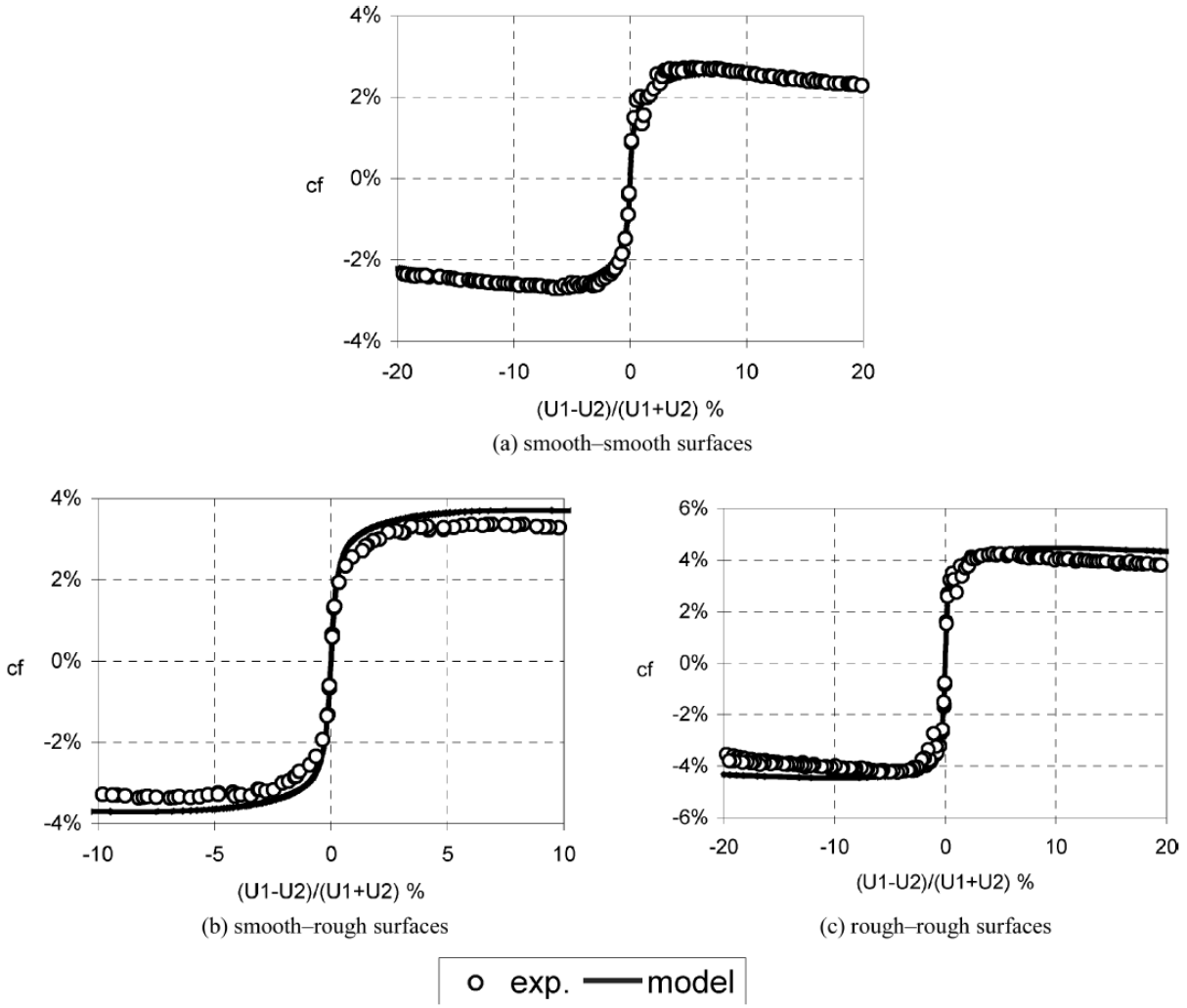

Figure 3.24: Example of traction curves – Influence of roughness (TVEP, 1.2GPa, 9,425m/s, 80°C). (a) Smooth-smooth surfaces; (b) smooth-rough surfaces; and (c) rough-rough surfaces. [26]

The effect of the overall roughness is illustrated on Figure 3.24: friction coefficient is doubled if two rough surfaces are used instead of two smooth surfaces.

Concerning overall roughness, surface finishing of hypoid gears can be made with different methods, as explained in section 2.1. Different roughness are then obtained, as presented in Table 3.4. The reference is a gear surface after running-in. According to Stadtfeld [60], machining grooves are first reduced during running-in phase and roughness is decreased too (Ra < 0.5 µm). It is then advantageous to proceed to a fine grinding after running-in in order to obtain quickly a slightly better surface finish.

Table 3.4: Gear surface roughness after various surface finishing

Condition	Surface finishing	Ra (µm)	Rz (µm)
a	Grinding (medium)	> 0.8	> 3
b	Reference	0.2 – 0.3	1.5 – 2.5
c	Lapping, grinding (fine)	0.2	3 – 4
d	Superfinishing	0.05 – 0.1	1 – 2

Based on the arithmetic average roughness Ra, mean friction coefficient is calculated according to formulae (3.8), (3.9), (3.10), and (3.11). For ISO technical report formula, global approach is still used. For each local formula, friction coefficient is calculated based on data used for the local approach presented in section 3.1 and is then averaged over meshing. Operating conditions are: gear set A, input torque of 1120 N.m, input speed of 1000 rpm and lubricant temperature of 80°C. Results are presented in Figure 3.25.

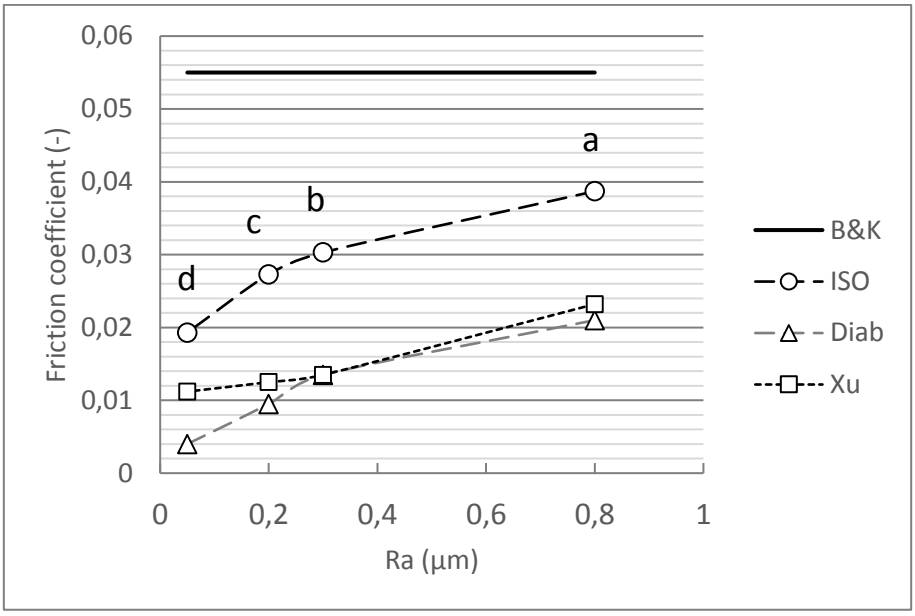

Figure 3.25: Mean friction coefficient according to several formulae for different surface roughness

As it does not take into account surface roughness, Benedict & Kelley formula gives always the same result. Moreover, it seems overestimated regarding other values. This suggests that tests were done on test samples with a high surface roughness. Diab [26] also underlined that grooves orientation of their test samples were directed differently from reality, which could lead to wrong results.

Concerning other formulae, friction coefficient is divided at least by two between condition (a) and (d), where surface roughness is much decreased. This is in line with Diab observations. However, some discrepancies are observed between methods: on one hand, Xu and Diab formulae predict a lower friction coefficient when compared to ISO; on the other hand, Diab and ISO formulae have a similar behaviour, with a steep decrease of friction coefficient at low roughness.

According to ISO formula, gear mesh power losses are proportional to the friction coefficient. Then, it does not vary linearly with surface roughness. Friction formula from ISO is used as a reference to give an example here. An improvement from surface roughness condition (a) to condition (b) (Ra varies from 0.8 µm to 0.3 µm) decreases gear friction losses by roughly 20%. An improvement from surface roughness condition (b) to condition (d) (Ra varies from 0.3 µm to 0.05 µm) decreases it by more than 30%. However, the improvement estimation is slightly different from a formula to another.

Arithmetic average roughness gives an approximation of surface roughness influence on friction coefficient. However, grooves orientation possibly has some impact as well. For spur gears, grooves are perpendicular to the rolling direction. In the case of spiral bevel and hypoid gears, contact lines are

inclined regarding tooth tip and foot, while grooves orientation depends on cutting method, as presented in sections 2.1 and 2.2. An angle between cutting and contact lines exists and can also change along contact path.

Footprints were taken on crown gear and pinion in order to study their surface roughness on a 3D optical profilometer. Figure 3.27 gives a global view of roughness topography: parallel striations are visible on both specimens but appears more clearly on crown gear. On pinion tooth surface, it is interesting to note the presence of many remaining cavities, due to phosphating.

In order to characterise these grooves, profiles of surface roughness along tooth height are presented on Figure 3.26. A periodicity of roughly 500 µm is observed on both specimens and grooves depth is mainly between 1 and 3 µm. The resultant Ra is around 0.3 µm for crown and pinion, but Rz is 2.4 µm for crown and 1.6 µm for pinion.

Thanks to surface texture analysis, it appears that pinion and crown gear tooth surfaces are different. As surface roughness influences friction coefficient and so power losses, it is important to take it into account. Friction coefficient formulae are generally limited to one roughness parameter which is not always representative of surface texture. Some tests must be done to characterise the friction of these types of surface, like the ones conducted by Diab [26].

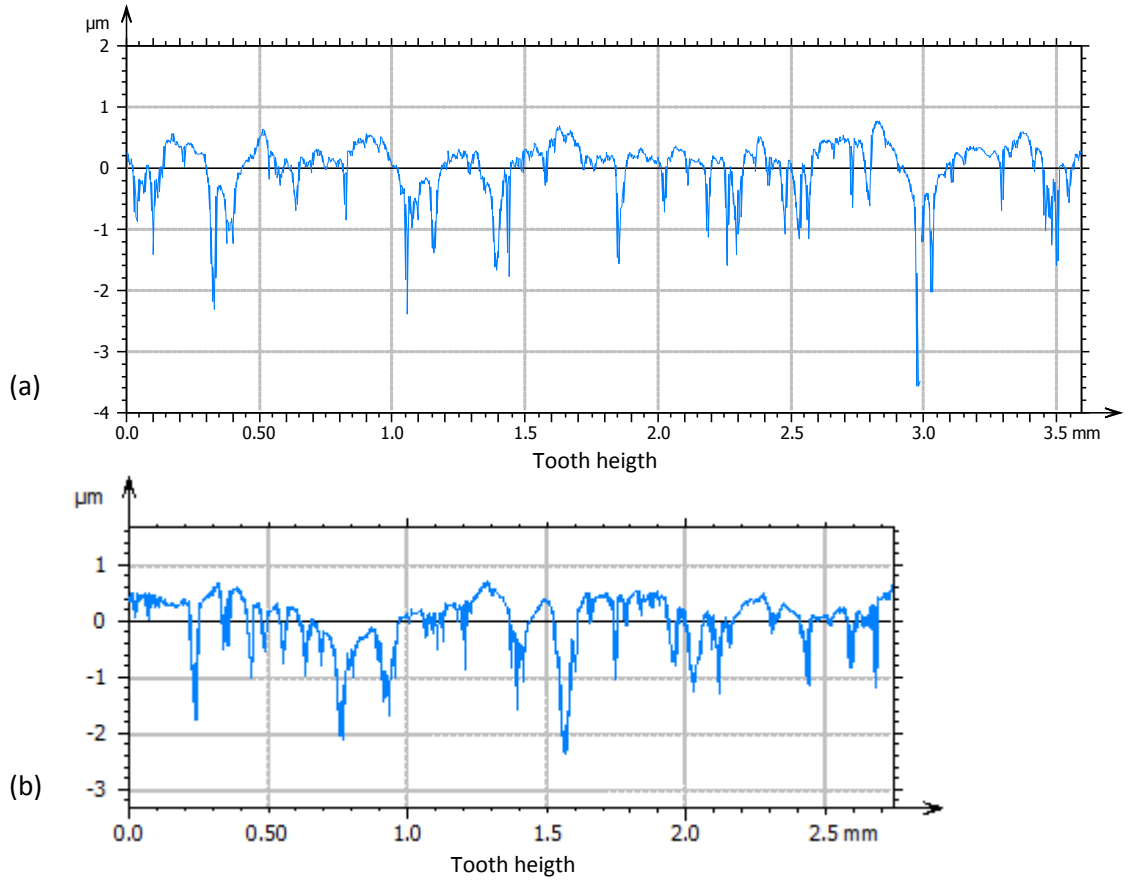

Figure 3.26: Tooth surface roughness profile of (a) crown gear and (b) pinion

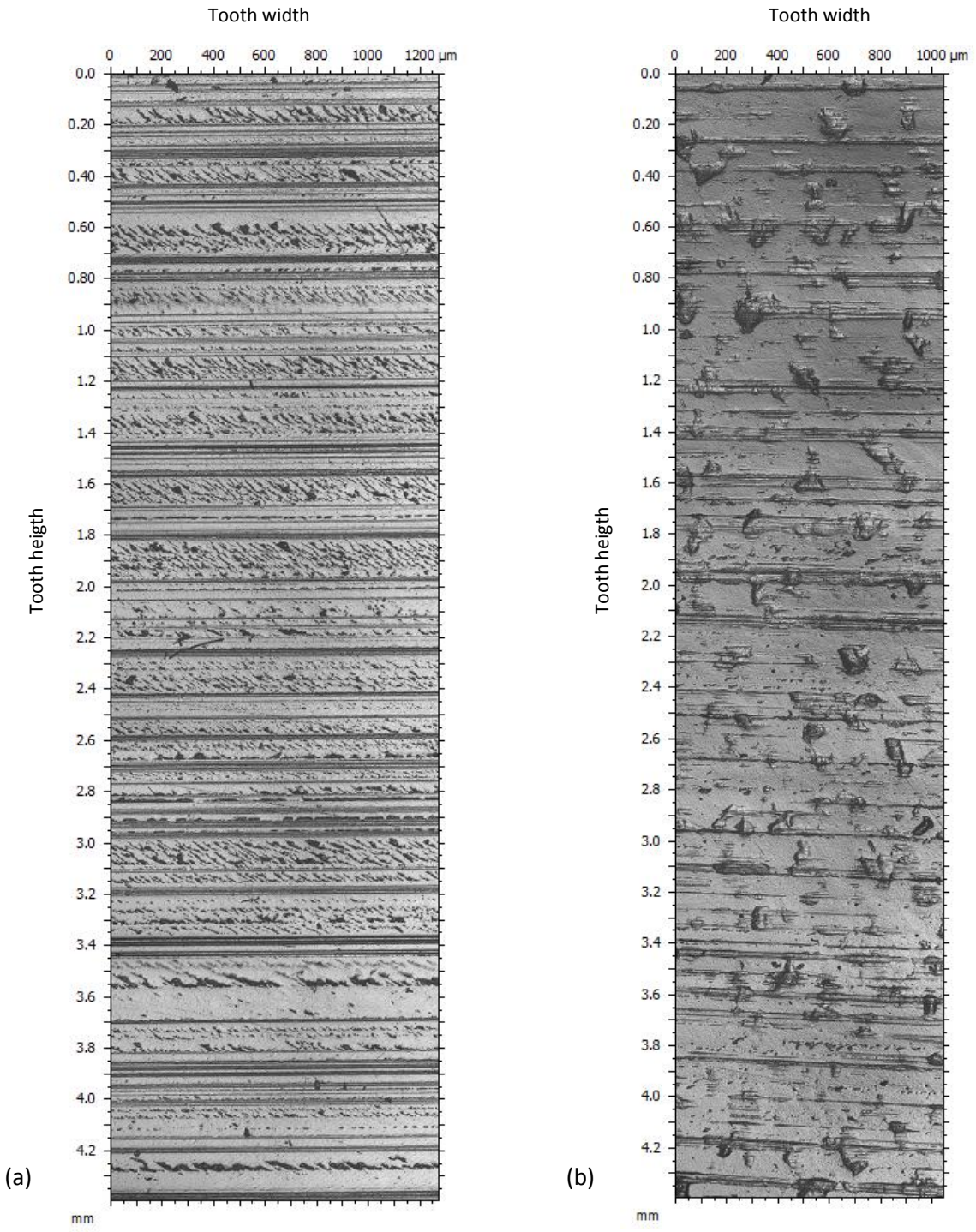

Figure 3.27: View of tooth surface roughness of (a) crown gear and (b) pinion

4.2.2. Orientation angles

As explained in section 2.3, surface and entrainment velocities of spiral bevel and hypoid gears are not along contact ellipse axis. Their directions are characterised by orientation angles: a velocity orientation angle δ between pinion and gear surface velocities and an entrainment orientation angle δ_e between entrainment velocity and contact ellipse axis x.

This phenomena was already reported in the literature. Many studies were conducted to investigate the effect of δ_e on elliptical contacts. However, an elastohydrodynamic lubrication (EHL) approach is generally used: contact lubrication and estimation of lubricant film thickness are the main point of investigation. Chittenden et al. [28] (1985) established empirical equations to determine minimum and central film thickness in elliptical contacts with entrainment angle. They observed a decrease in film thickness minimum when δ_e increases, while central film thickness can stay constant or decrease. Omasta et al. [29] (2012) investigated experimentally the impact of the velocity orientation angle δ and of the angle between entrainment and sliding velocities in circular EHL contacts. They observed variations in terms of film thickness distribution depending on angles: wedge, asymmetry, dimple formation... It appears also that sliding orientation has an influence. Stahl et al. [30] (2013) developed a steady-state isothermal EHL model and validated it with experimental results for circular contacts on a twin-disc machine with an orientable disc ($0° < \delta < 60°$). A comparison is then held for elliptical contacts with a roller-on-disc tribometer on which roller can be oriented ($0° < \delta < 45°$). A good agreement is observed between simulated and measured results and major conclusion is: sum velocity (so entrainment velocity as well) magnitude and orientation is the main parameter for EHL film formation. Finally, Pu et al. [31] developed a mixed EHL model to investigate the impact of δ_e on pressure and film thickness in elliptical contacts. This allows to extend the observation of Chittenden et al. to moderate and heavy loading cases: minimum film thickness also decreases with increasing δ_e, but central film thickness decreases and then increases again. A great difference is also noticed between both film thicknesses.

All these studies focus only on lubricant film thickness for elastohydrodynamic perspectives. Film thickness reduction could be due to heat generated by a higher shear rate and then a higher friction. However, no study address the friction coefficient issue for this type of contact. Carli et al. [32] did not work on contacts with orientation angles but on contact with anomalous film shapes. They proposed a friction coefficient evaluation in the EHL analysis and compared it with experimental results thanks to friction force measurements. Newtonian model overestimates the friction coefficient but a good agreement is obtained with Eyring model using an Eyring shear pressure τ_0 between 3 and 5 MPa. As unusual film shapes are obtain when entrainment speed is inclined, this model could be worth of interest.

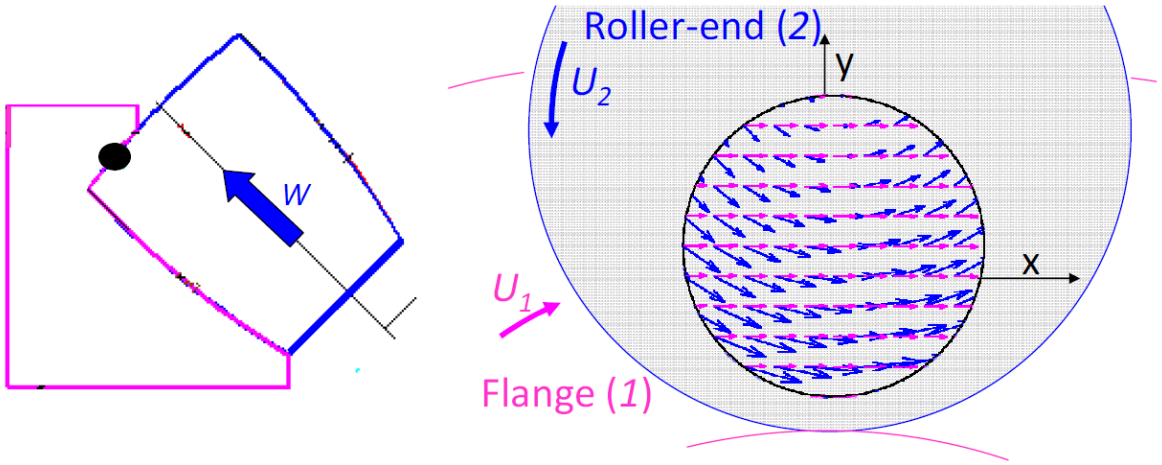

Figure 3.28: Flange design for spherical roller thrust bearing and schematic representation of the spin kinematics [33]

This phenomena can also be compared to the one observed in rolling element bearings supporting axial load, like spherical roller thrust bearings. As represented on Figure 3.28, a particular contact occurs between rib roller-end and flange: a spinning circular contact. Doki-Thonon [33] addressed this problematic of spinning, which is different from rolling-sliding kinematics and is due to rotational components of velocity fields. As in studies presented just before, asymmetry and reduction of film thickness were observed. Doki-Thonon also investigated experimentally the friction coefficient and split it into two components: along axis x, friction coefficient is similar but lower than for classical rolling-sliding contact; along axis y, it is almost null (<0.01).

This may be close to the hypoid kinematics observed on the global ellipse in section 2.3: a rotation of the ellipse entrainment velocity exists. However, it is hard to validate the similitude.

Thanks to the local approach of section 3.1, the two orientation angles δ and δ_e are estimated for gear set A (hypoid) and gear set B (spiral bevel). Their values are presented in Table 3.5. The angle between surface velocities decrease with increasing speed, while entrainment angle is more stable.

Table 3.5: Velocity and entrainment orientation angles for gear sets A and B

	Gear set A						Gear set B					
Input speed (rpm)	**δ (°)**			**δe (°)**			**δ (°)**			**δe (°)**		
	min	**mean**	**max**	**min**	**mean**	**max**	**min**	**mean**	**max**	**min**	**mean**	**max**
500	0	6	23	21	43	76	0	11	15	16	33	68
1000	0	4	14	22	41	70	0	6	10	19	35	65
1500	0	3	10	22	41	68	0	5	7	21	37	64
2000	0	2	8	22	41	67	0	4	6	21	37	64

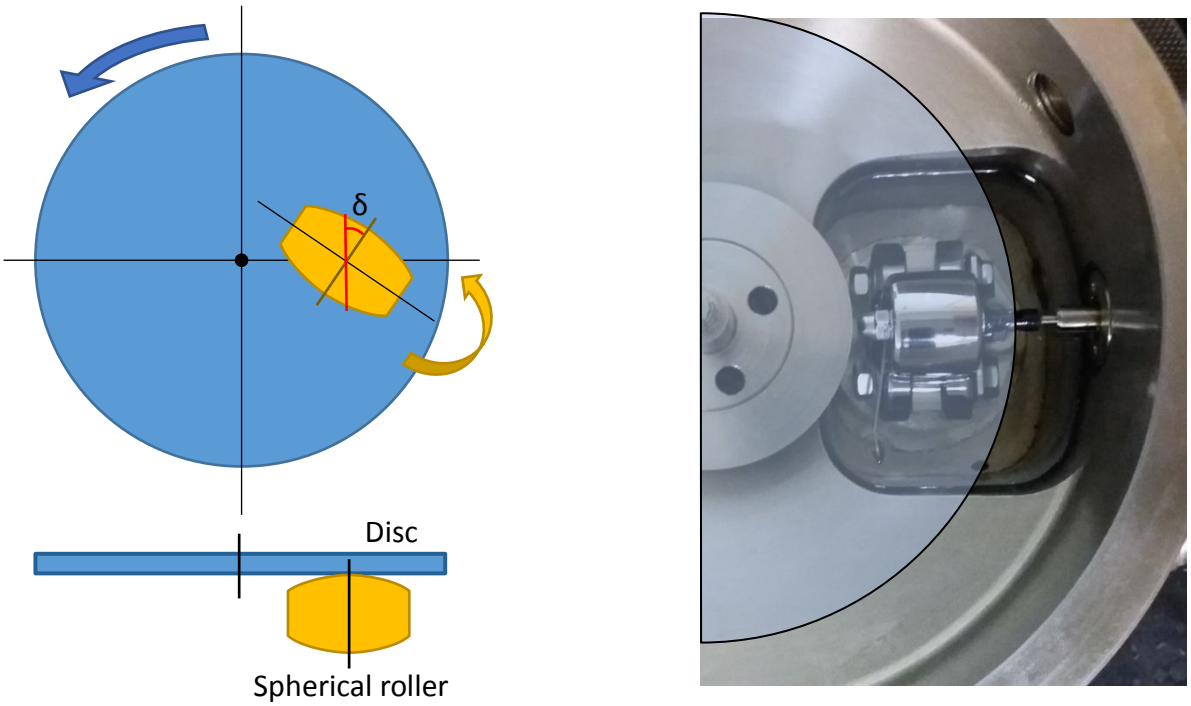

Figure 3.29: Ultra thin film measurement system with a swivelling carriage

Preliminary tests are conducted on an EHL-machine on which traction measurements can also be performed: the Ultra-Thin-Film Measurement System of PCS. A roller-on-disc contact is used to reproduce the hypoid elliptical contact. A swivelling carriage is manufactured to investigate the influence of angle δ on friction coefficient. The test set-up is presented on Figure 3.29. The different positions are secured by a blocking pin.

Experiments are done at two different positions: the normal one (δ=0°) and a rotated one (δ=10°). For both positions, various conditions are tested on roller surface velocity (0.5m/s, 1m/s) and on load (15N, 20N). Measurements are presented on Figure 3.30. For each condition, traction coefficient is higher for $\delta = 10°$. For an identical Slide to Roll ratio, this phenomena is more pronounced when roller surface velocity is low (U1=0.5m/s): friction coefficient is almost doubled. On the contrary, load has the same influence whatever the angle.

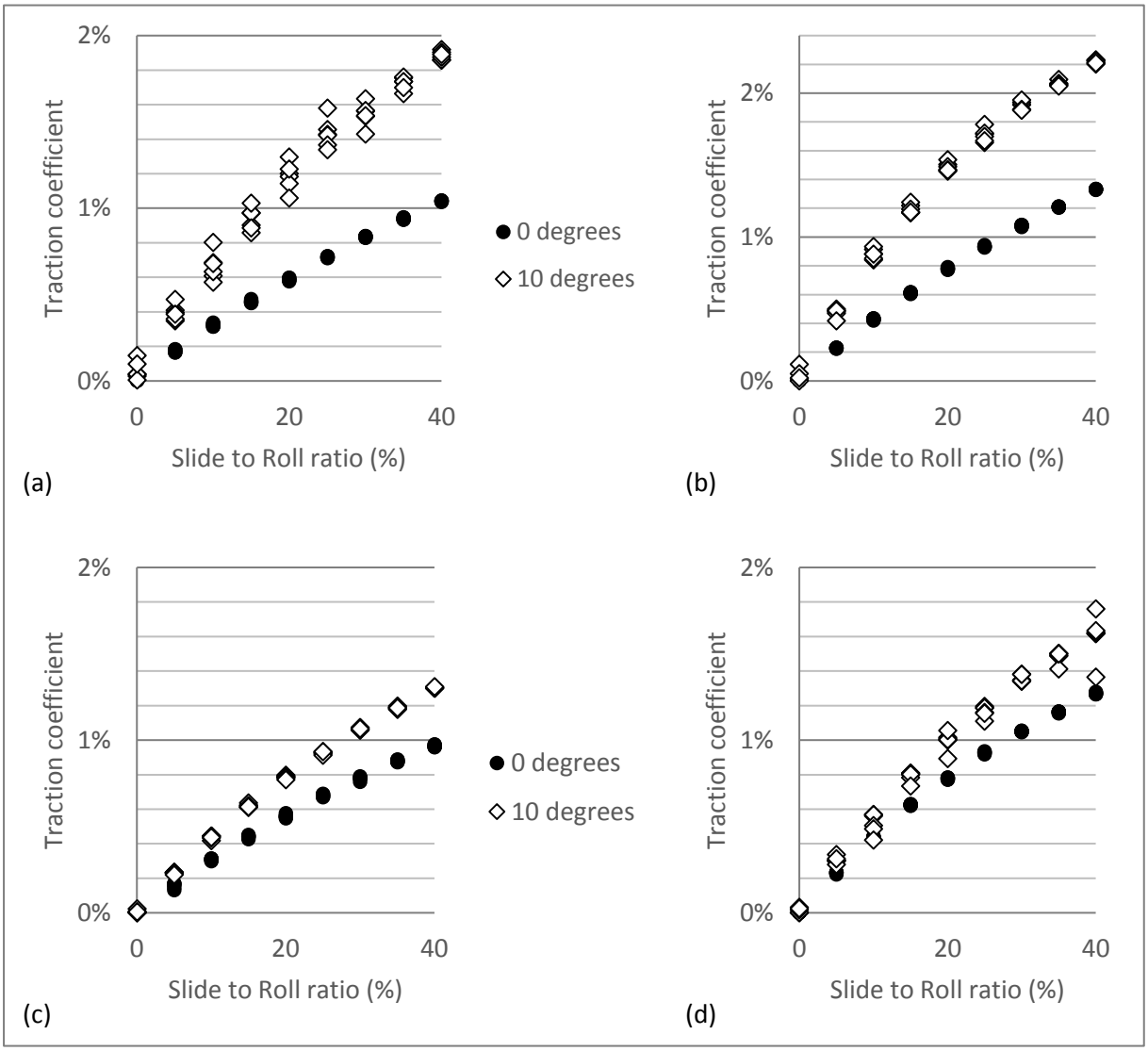

Figure 3.30: Traction coefficient measurements at δ=0° and δ=10° for (a) U1=0.5m/s and Load=15N, (b) U1=0.5m/s and Load=20N, (c) U1=1m/s and Load=15N and (d) U1=1m/s and Load=20N

As friction coefficient is directly linked to gear mesh power losses, the modification of the orientation angle can have a great influence on power losses.

5. Conclusion

The specificities of spiral bevel and hypoid gears were presented: geometrical parameters stem from design choices, cutting process, thermomechanical treatment and surface finishing. A model developed by Barday [22] allows to take most of these parameters into account. Considering gear mesh, gears are paired in order to have a well spread and centred pattern. This pattern results from the successive elliptical contacts occurring along contact path. For modelling purposes, each successive contact is discretised in several line contacts: contact conditions (load, velocities, surface curvature…) are calculated thanks to Barday software. The kinematic of these gears is also particular. Due to conical shape and spiral angle, surface velocities are not oriented along axis of contact ellipse, neither are they aligned together: a velocity entrainment angle δ defines the angle between surface velocities; an entrainment angle δ_e defines the angle between entrainment velocity and x-axis. Moreover, for hypoid gears, due to offset, sliding is not only along x-axis, a longitudinal component also exists. Finally, considering contact ellipse from a global perspective, it appears that a rotation occurs due to a variation of entrainment velocity along y-axis.

Power loss estimation of gear mesh is then investigated. A local approach based on data from Barday software is used to analyse contact conditions (load, sliding velocity) and power loss along contact path. Two gear sets are compared: a hypoid and a spiral bevel one. A decrease of sliding velocity is observed on spiral bevel gear around pitch point, while a permanent sliding is observed on the hypoid gear due to offset. As hypoid gears are special, a comparison is made between ISO global approach and local approach to discuss validity of ISO approximation. Global approach appears to always overestimate the power loss, due to sliding velocity estimation: indeed, sliding velocity varies a lot along contact line and local approach considers the sliding only on the part of the line really in contact. Thus, for higher loads, a better agreement is expected. In our case, ISO technical report estimation obtains more coherent results for the hypoid gear than the spiral bevel one. Finally, local approach is more accurate to evaluate gear mesh power loss. However, friction coefficient estimation is still a point of improvement and can be calculated locally.

For comparison purposes, the same friction coefficient was used for global and local approaches. However, local approach offers the possibility to use local friction coefficients, which can be more accurate. As it has a great influence on gear mesh friction loss, the friction coefficient estimation is reviewed through different formulae. Similar parameters are used in most of these equations: load, entrainment and sliding velocities, oil viscosity, and surface roughness. In the case of hypoid gears, two specific parameters were selected: surface roughness and velocities that are influenced by orientation angles. Surface roughness depends mainly on cutting process and on surface finishing. It is characterised by an overall roughness (defined by Ra and Rz) and by machining grooves orientation. The influence of overall roughness is studied thanks to the friction coefficient formulae that were presented. A decrease of friction coefficient, and so of gear mesh power losses, is observed for smoother surfaces. Concerning grooves orientation, surface roughness of a hypoid gear pair was analysed to obtain more detailed on actual contact conditions. Friction tests must be performed to characterise friction coefficient for these particular surfaces. Last, orientation angles influence was considered. Literature only focused on elastohydrodynamic aspects with film thickness analysis. The closest phenomena is the one observed at the contact between rib roller-end and flange in some rolling element bearings. The magnitude of these angles were evaluated for a hypoid gear and some

preliminary tests were performed to evaluate the influence of δ on friction coefficient. For δ=10°, friction coefficient can be doubled for low surface velocity. This induces a great increase of gear mesh power losses too.

4. Thermal model of the axle

1. Introduction

Previous chapters were dedicated to the estimation of power losses, especially of hypoid gear mesh ones. The different dissipation sources generate heat at distinct points of the system, inducing local hot spots. This can influence the efficiency due to oil properties that change with temperature and can even lead to cooling and durability issues. Bearing and gear failures can happen, like scoring, pitting, or even scuffing.

In order to correctly predict these phenomena, it is important to know the real operating temperature of each component, which is generally different from oil sump temperature. However, most of the thermal investigations on axles were done through isothermal models: the whole axle is considered at oil sump temperature. Even for efficiency applications, this has some limitations: correct estimations of global power loss and oil temperature do not validate power loss breakdown between sources.

Thus, a thermo-mechanical model is developed here to obtain both efficiency and temperatures. It is then necessary to understand more precisely the thermal exchanges inside the axle and with its surrounding environment.

At first, two approaches of the thermal model are presented: an isothermal one and a thermal network one. A comparison is then conducted according to power loss measurements and calculations exposed in Chapter 2 and 3.

The literature showed that the axle is not isothermal [3] and thermal network method is an appropriate tool to calculate the different bulk temperatures. An ISO technical report computes gear bulk

temperatures in order to prevent durability issues. Both methods are discussed.

A test campaign is made to investigate the thermal behaviour of the axle. After a description of experiments and their results, a comparison with thermal network is done. This finally allows for exploitation of the thermo-mechanical model: the influence of parameters is investigated.

2. Thermal model of the axle

A thermal modelling of the axle presented in Chapter 2 is developed. An isothermal approach is first used and is compared with the thermal network approach for a stabilised condition. It is important to notice that the formulations described in Chapter 2 and Chapter 3 are used to calculate the power losses for both thermal approaches: seal friction with Simrit, rolling element bearing losses with Harris, churning losses according to the new formula of Chapter 2 and gear mesh friction according to local approach of Chapter 3 with ISO/TR 14179-2 for friction coefficient calculation.

2.1. Additional data for axle thermal behaviour

There is no cooling system, apart from the air flow due to ventilation, and no foundation. There is only suspension brackets and shaft connections which are far from axle drive head. Thus, heat conduction through input and output shafts is neglected. Therefore, it is assumed that only the housing is dissipating the heat generated by the axle.

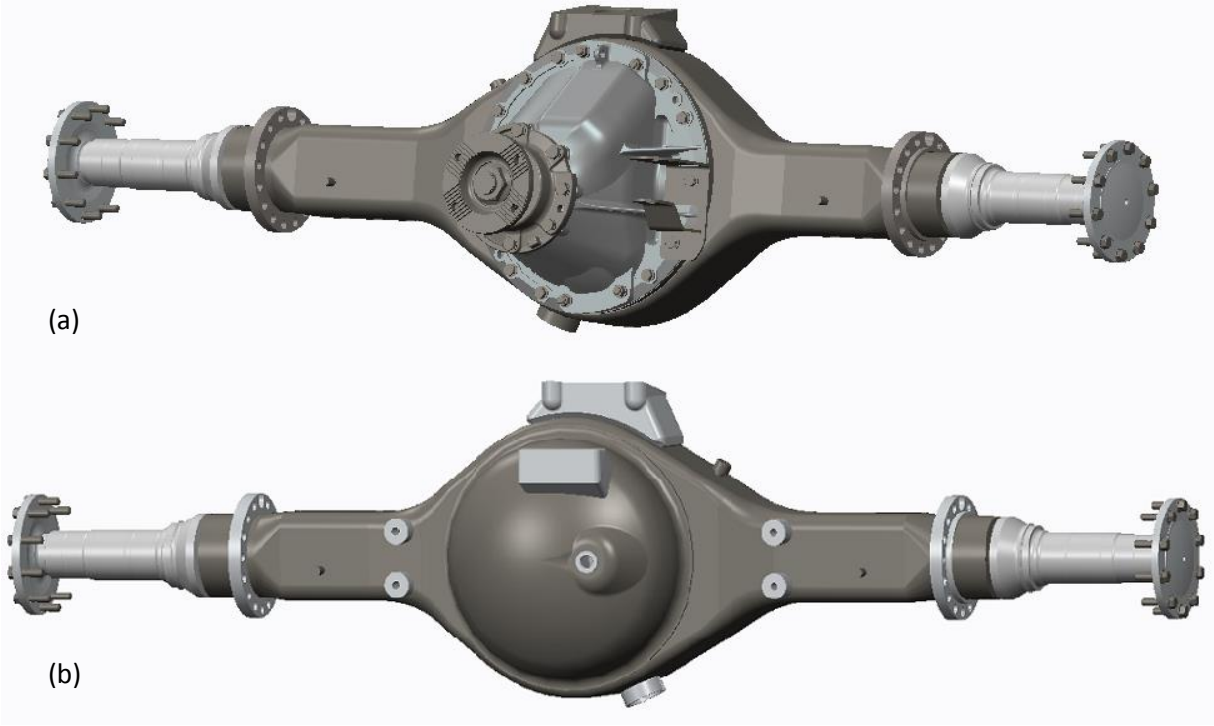

Figure 4.1: 3D-model of axle housing from (a) drive head side and (b) oil sump side

The axle housing is made of cast iron and weighs roughly 300 kg. It is modelled as a rectangular parallelepiped. The real housing shape is more complex, as represented on Figure 4.1.

To have a good representativeness, the external surface is evaluated according to the 3D-model. Dimensions of the parallelepiped represented on Figure 4.2 are then selected to have the closest approximation depending on surfaces.

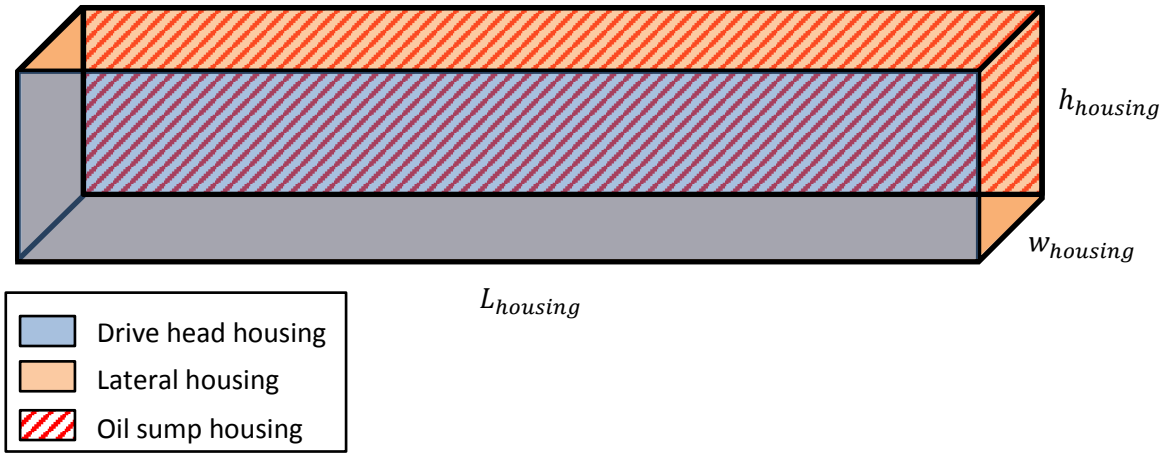

Figure 4.2: Parallelepiped representation of axle housing

Length $L_{housing} = 1450$ mm, width $w_{housing} = 110$ mm and height $h_{housing} = 350$ mm give surfaces reported in Table 4.1. Despite the parallelepiped approximation cannot reflect the bigger surface of drive head housing when compared to oil sump housing, total surface presents a good agreement.

Table 4.1: Housing surfaces according to 3D-model and parallelepiped approximation (A_{ca})

	Surface (mm²)		
	3D-model	**Parallelepiped**	**Difference**
Drive head housing	583,231	507,500	-13.0%
Oil sump housing	442,410	507,500	14.7%
Lateral housing	382,892	396,000	3.4%
Total	1,408,533	1,411,000	0.2%

2.2. Isothermal approach

The ISO technical report [9] proposes a simple heat balance with the environment for a steady state case. Details of this method are given in Annex 4.A. The whole axle is considered as a single unit at oil sump temperature. Knowing the global power loss of the axle and the environment conditions, oil temperature is calculated according to ISO/TR 14179-2. Temperature difference between oil and ambient air is defined as:

$$(T_{oil} - T_{air}) = \frac{1}{U\ A_{ca}} Q \tag{4.1}$$

where U is the heat transmission coefficient (W/(m²K)), A_{ca} is the external housing surface (m²), and Q is the heat generated by the axle (W). U is an overall coefficient which includes convection with the

oil, and convection and radiation with the surrounding environment. As suggested in the technical report, the heat conduction through the housing can be neglected for metallic housings.

$$\frac{1}{U} = \frac{1}{\alpha_{oil}} \frac{A_{ca}}{A_{oil}} + \frac{1}{\alpha_{conv} + \alpha_{rad}} \tag{4.2}$$

where α_{oil}, α_{con} and α_{rad} are respectively the heat transfer coefficient due to oil, convection with air and radiation (W/(m²K)), and A_{oil} is the internal housing area (m²).

$$\alpha_{oil} = 200 \text{ W/(m²K)} \tag{4.3}$$

$$\alpha_{rad} = 0.23 \times 10^{-6} \, \varepsilon \left(\frac{T_{wall} + T_{air}}{2} \right)^3 \tag{4.4}$$

where ε is the housing emissivity and T_{wall} is the housing wall temperature (K). In the case of forced convection with air, the heat transfer coefficient of convection becomes:

$$\alpha_{conv} = \left(\frac{0.0086 \, (Re')^{0.64}}{l_x} \right) \frac{A_{air}}{A_{ca}} \, \eta^* \tag{4.5}$$

where Re' is a modified Reynolds number, l_x is the flow length (m), A_{air} is the ventilated housing area (m²) and η^* is a temperature ratio.

A steady state case with running axle and constant air flow is considered. Convection with ambient air is then forced. Operating conditions reproduce efficiency tests presented in Chapter 2. Air flow velocity for each condition is given in Table 4.2.

Table 4.2: Air flow velocity during efficiency tests

Oil level	**Normal**			**High**		
Condition	**A**	**B**	**C**	**A**	**B**	**C**
Air flow velocity (m/s)	3	5	14	4	7	16

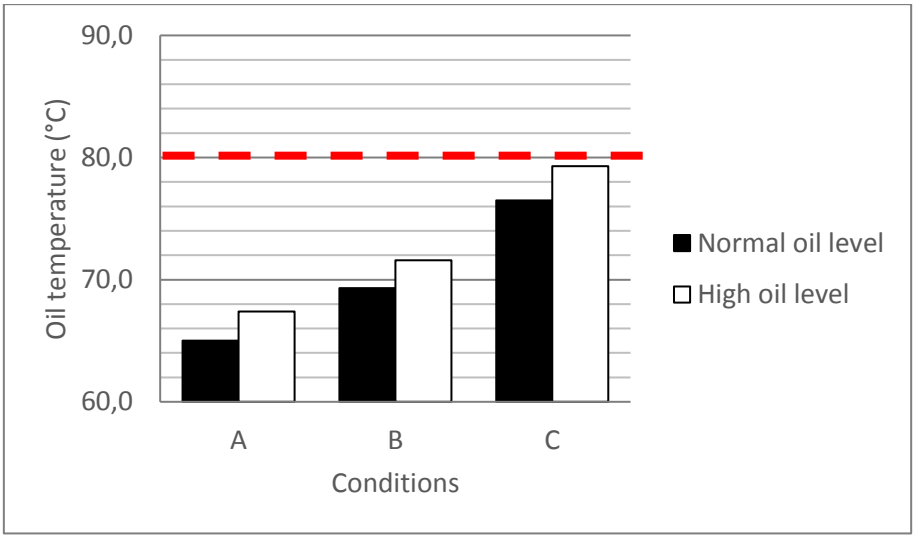

Figure 4.3: Oil temperature obtained with the standard formulation for air convection

The oil sump temperature obtained with this formulation is presented on Figure 4.3 and compared with oil temperature during the tests (80°C).

Thermal exchanges are overestimated, as already reported by Bendzulla et al. [61]. Figure 4.4 shows that the value of the overall coefficient U is conditioned by convection and radiation exchanges with the air.

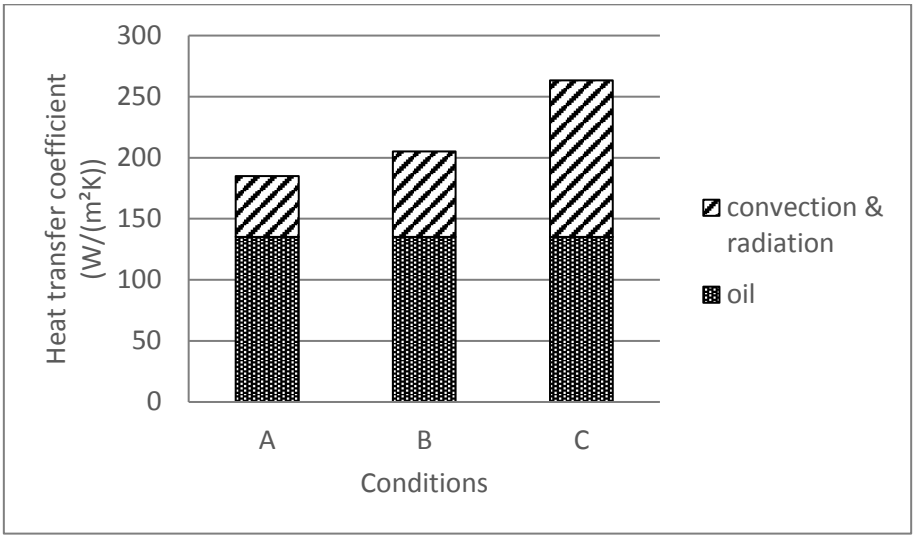

Figure 4.4: Heat transfer contributions for the isothermal approach

The assumption of a one part housing is not representative of the real conditions. Indeed, the air flow is not the same on every sides of the housing. This can induce less convection with the air and should be taken into account.

2.3. Thermal network approach

A more detailed model of the axle is developed to obtain a better estimation of the thermal behaviour. Figure 4.5 presents the considered components for this model, which are the main parts, such as gears, bearings, shafts and seal. Only housing and oil are missing on this illustration. The differential is still considered unused and does not generate any power loss. However, its thermal inertia is taken into account.

This system is then modelled using the thermal network method, which is explained in detail in Annex 4.B.

2.3.1. Method principle

Thermal network method is based on an electrical analogy with Ohm's law:

$$\Delta T = R_{th} \times Q \tag{4.6}$$

where ΔT is the temperature difference (K), R_{th} is the thermal resistance (K/W) and Q the heat flow (W).

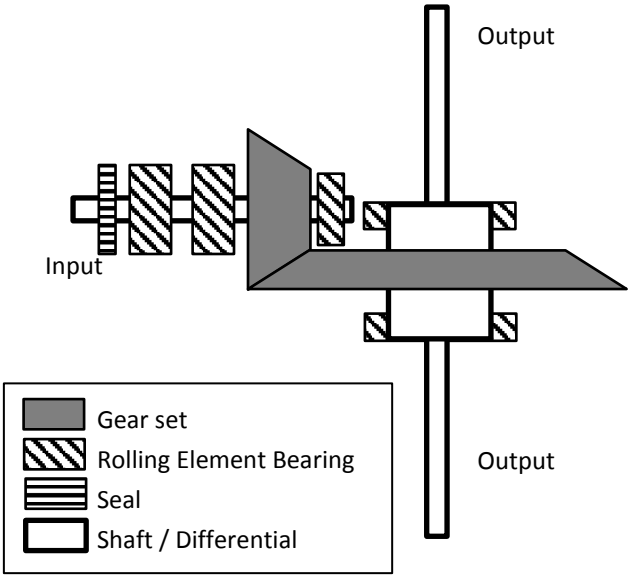

Figure 4.5: Modelled components of the axle

The heat generated by the various power losses is injected in the network at the corresponding node. The evolution of each node temperature is then estimated according to the first law of thermodynamics. The internal energy of an element of the system varies due to its own power dissipation and to heat exchanges with other elements of the system:

$$M_i \, c_i \, \frac{dT_i}{dt} = Q_i + \sum_{j=1 \; and \; j \neq i}^{nb} \frac{T_j - T_i}{R_{th}(i,j)} \tag{4.7}$$

where M_i is the mass of element i (kg), c_i is its specific heat (J/kg.K), T_i and T_j are the temperature of elements i and j (K), t is the time (s), Q_i is the heat flow injected at node i (W), $R_{th}(i,j)$ is the thermal resistance between elements i and j (K/W) and nb is the number of thermal network nodes.

This transient calculation is performed according to the algorithm described on Figure 4.6. The numerical integration is performed with Adams predictor-corrector method [34].

It is noteworthy that local oil temperatures are used instead of a global oil temperature. Also, the only input data of the thermal network are its boundary conditions: air speed and temperature.

2.3.2. Thermal network of a truck axle

Concerning the truck axle model, considered components are listed in Table 4.3 and the thermal network is represented on Figure 4.7. The power loss sources studied in Chapter 2 are used in the network: seal friction (node n°8), rolling element bearing drag and friction (nodes n°5, 6, 9, 10, 11), oil churning (node n°2) and gear mesh friction (node n°15). The housing is divided in three parts according to Figure 4.2: drive head housing, sump housing and lateral housing (nodes n°16, 17, 18).

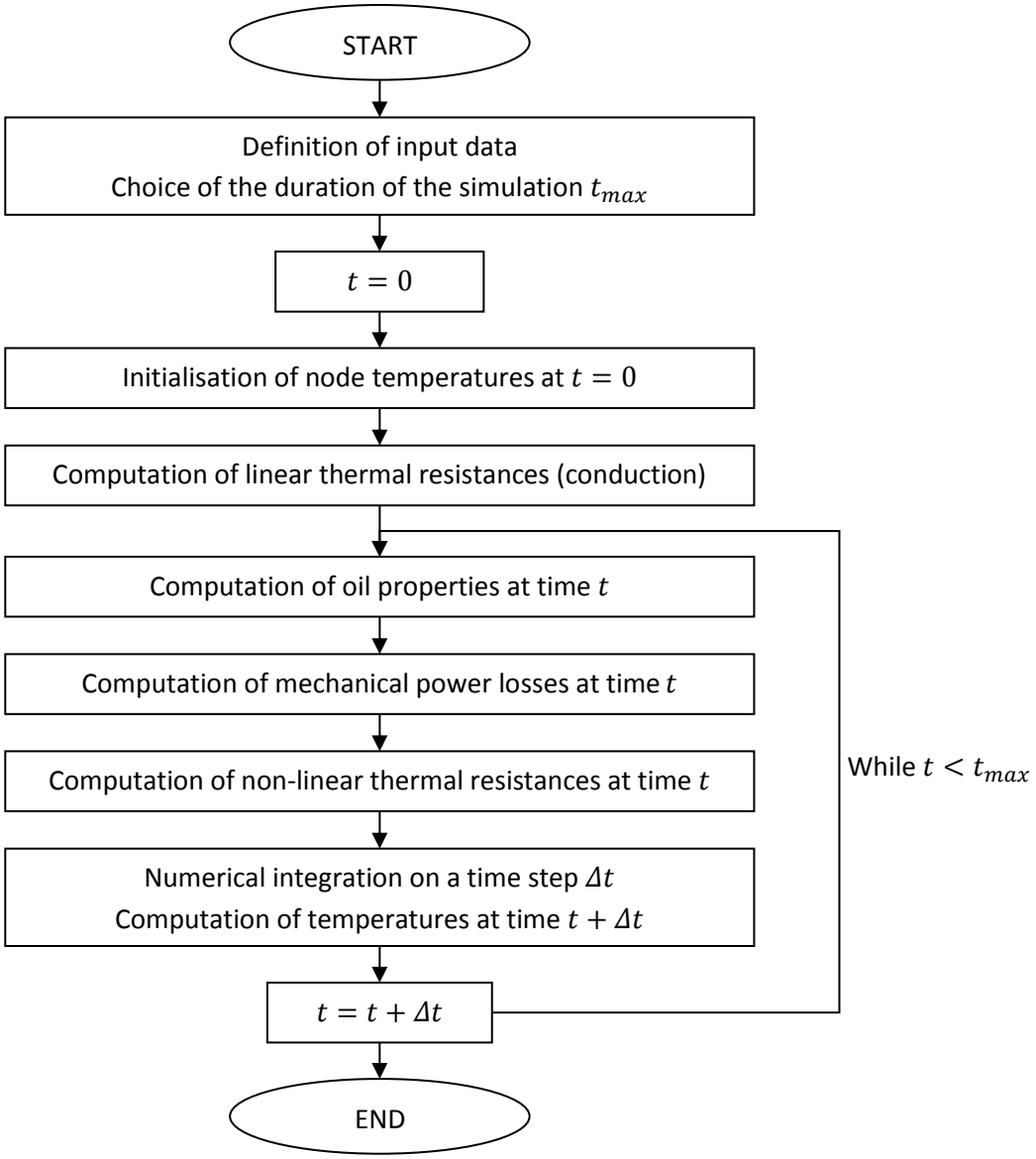

Figure 4.6: Algorithm for transient calculation

Table 4.3: List of thermal network elements for the truck axle model

Node number	Axle component
1	Ambient air
2	Oil sump
3	Right shaft
4	Left shaft
5	Right REB
6	Left REB
7	Differential
8	Seal
9	Tail REB

Node number	Axle component
10	Head REB
11	Pilot REB
12	Input shaft
13	Pinion
14	Crown gear
15	Contact point (gear mesh)
16	Drive head housing
17	Lateral housing
18	Sump housing

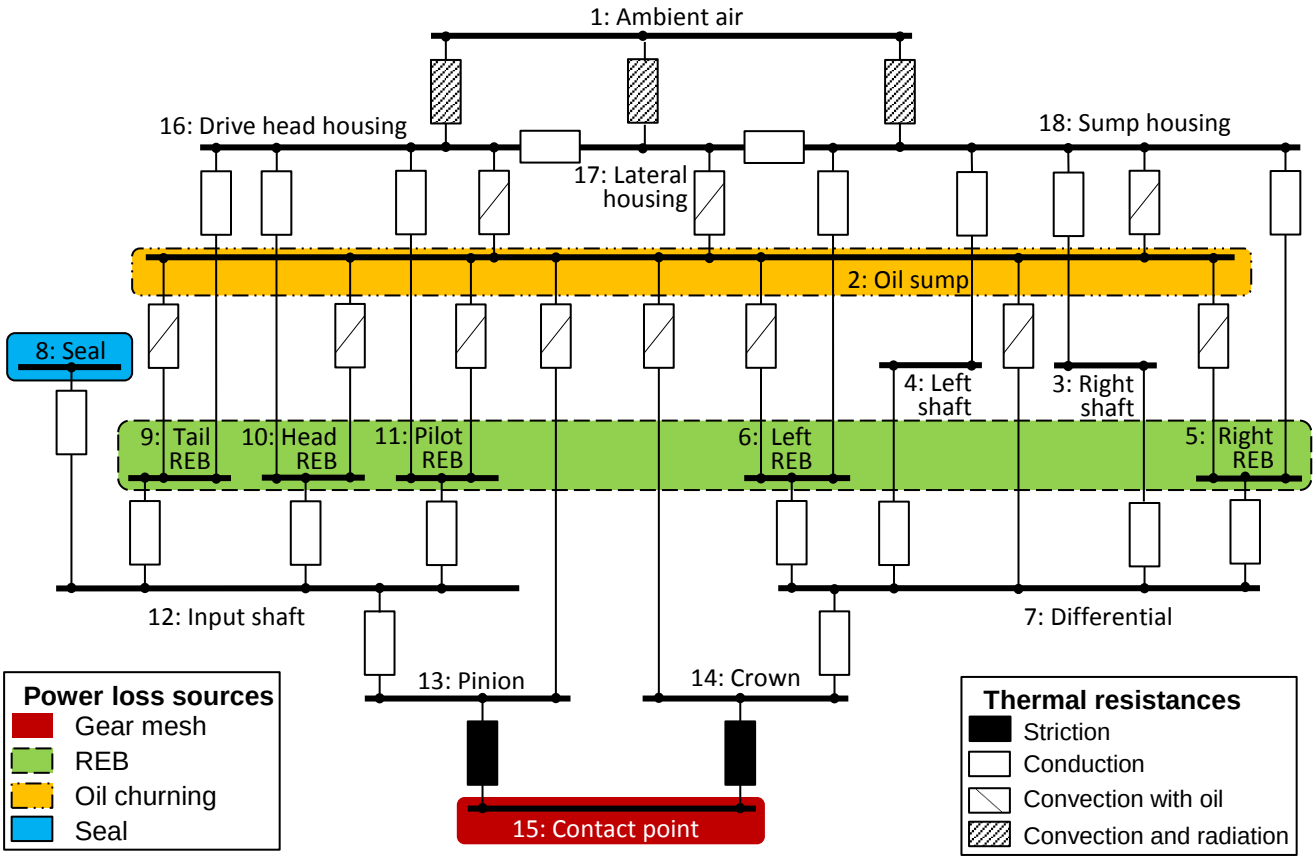

Figure 4.7: Thermal network of the axle

Different truck operating cases can be modelled and combined:

- **Concerning the environment surrounding the axle:**

If the vehicle is running, an air flow around the axle is considered, as illustrated on Figure 4.8. Forced convection occurs on drive head and lateral housings: a normal air flow cools the drive head housing and a tangential air flow cools the lateral housing. As it is on the opposite side, sump housing does not experienced the same air flow. However, it is not free convection either, as air goes around the housing. A tangential forced air flow is then also used on this side, as represented on Figure 4.8 (b).

If the vehicle is stopped, no air flow is taken into account (wind is neglected). Free air convection takes place on every parts of the housing.

On test bench, fans can be used to generate an air flow and to cool the axle. They are located on the axle sump side, contrary to the reality on truck where air flow comes from drive head side. However, the model can be easily modified to consider one case or the other: on Figure 4.8 (b), numbers 1 and 3 must be inverted.

❖ **Concerning the axle itself:**

If the vehicle is running, gears and rolling element bearings in the axle are rotating and oil is splashed. Forced convection between oil and lubricated components happens. Power losses are also generated depending on operating conditions.

If the vehicle is stopped, the axle is also not working. Free convection with oil occurs.

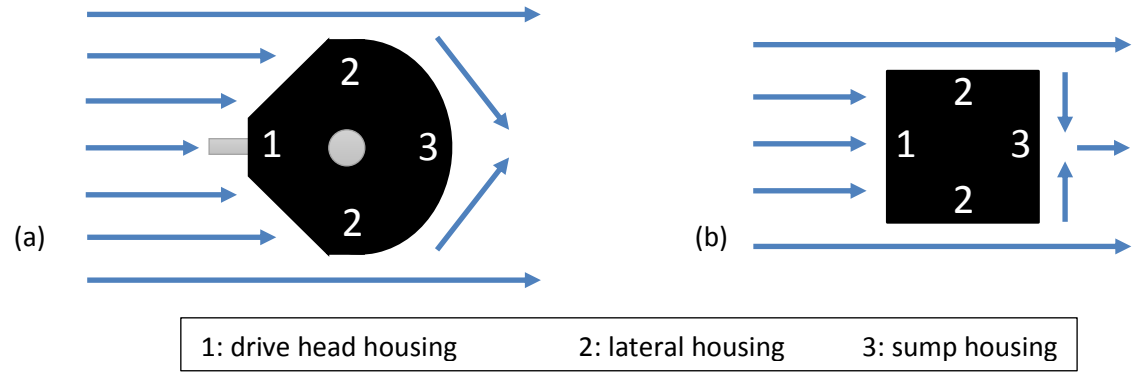

Figure 4.8: Air flow around (a) real axle and (b) modelled axle

2.3.3. Thermal resistances

Different kinds of thermal resistances manage the heat transfers between the nodes. Their complete descriptions and formulae are given in Annex 4.B. Simple geometrical shapes are used to model the components, like plates, cylinders or discs ([34], [62]). Here is a sum-up of thermal exchanges considered:

1) Conduction happens between several elements in contact, like bearings with shafts or housing, gears with their shaft, etc.;
2) Convection and radiation occur between environment and housing, which is decomposed in a set of flat plates to consider the different air flows around it;
3) Convection between oil and running gears is considered as the gears are dip lubricated; Convection between oil and housing also occurs;
4) Striction controls the exchange between gears and their meshing point. The contact temperature increases a lot but, as the contact zone is really small in comparison to gear size, the bulk temperature is then not much influenced.

A focus is made here on the case where the vehicle is running. Some thermal resistances are detailed hereafter to give a better understanding of the thermal behaviour of the system (for more details or for other thermal resistances, see Annex 4.B).

As the housing is decomposed in a set of flat plates, a global thermal resistance is calculated for each type of housing thermal exchange (convection with air or oil and radiation):

$$R_{th\ housing} = \frac{1}{\sum h_i\ A_i} \tag{4.8}$$

where h_i is the heat transmission coefficient of plate i (W/(m²K)) and A_i is the surface of plate i (m²).

- **Radiation and forced convection between housing and ambient air:** $R_{th}(1,16), R_{th}(1,17), R_{th}(1,18)$

The radiation coefficient is determined from the Stefan-Boltzmann law [63]:

$$h_{rad} = \epsilon\, \sigma \left({T_{ca}}^2 + {T_{air}}^2\right)(T_{ca} + T_{air}) \tag{4.9}$$

where ϵ is the material emissivity, σ is the Stefan-Boltzmann constant (5.67×10^{-8} W/(m²K⁴)), T_{ca} and T_{air} are respectively housing and ambient air temperatures (K).

The forced convection coefficient is defined according to formulae of Winter et al. [64]. For this thermal exchange, the distinction is made between surfaces normal and tangential to the air flow. For surfaces normal to the flow:

$$h_{conv} = 5.6 \cdot L^{-0.34} \cdot V^{0.66} \tag{4.10}$$

For surfaces tangential to the flow:

$$h_{conv} = 7.6 \cdot L^{-0.37} \cdot V^{0.63} \tag{4.11}$$

where L is the characteristic length (m) and V is the air flow velocity (m/s). For the particular case of forced convection with a surface normal to the flow, the characteristic length is: $L = {A}/{P}$ with A the normal surface area (m²) and P its perimeter (m).

- **Forced convection between oil and housing:** $R_{th}(2,16), R_{th}(2,17), R_{th}(2,18)$

For convection with oil, Holman [63] defines the different heat transfers with:

$$h_{oil} = \frac{Nu\, k}{L} \tag{4.12}$$

where Nu is the Nusselt number, k is the lubricant thermal conductivity (W/m.K) and L is the characteristic dimension (m). For forced convection inside the oil bath, a flow is generated by running gears. Nusselt number is then:

$$if\ Re < 5 \cdot 10^5, \qquad Nu = 0.664 \sqrt{Re}\ \ Pr^{1/3} \tag{4.13}$$

$$else\ \ Nu = \ Pr^{1/3}\ (0.037\ (Re^{0.8}) - 850) \tag{4.14}$$

where Pr is the Prandtl number. For Reynolds calculation, the fluid velocity to take into account is due to running gears.

Oil is also projected on housing walls due to gears rotation. For this oil trickling along non-immersed surfaces, the oil displacement is due to gravity.

❖ **Forced convection between oil and gears:**
$R_{th}(2,13), R_{th}(2,14)$

When gears are rotating, forced convection with oil occurs on gear flanks and teeth. Convection on gear flanks is considered as for housing. Convection with gear teeth takes place in a particular way: centrifugal projection of oil along gear teeth flanks evacuates the major amount of heat.

Oil projection is notably characterised by the angle of rotation where the gear projects oil. For dip lubricated gears, this angle θ_{proj} begins at gear teeth emergence from oil and ends at gear mesh point, as illustrated on Figure 4.9. Projection duration is also important and is defined as: t= θ_{proj}/Ω .

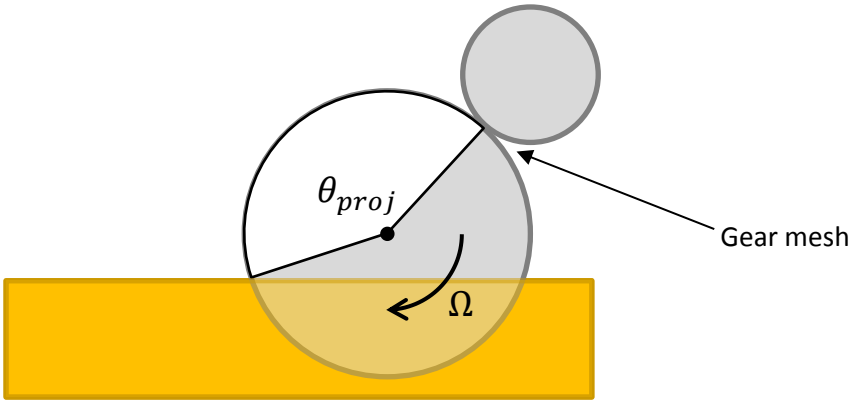

Figure 4.9: Definition of centrifugal projection angle

Blok [65] defines an evacuated heat quantity for a tooth face per width unit. This energy can be deduced from Figure 4.10, depending on a dimensionless number Ψ, defined as:

$$\Psi = \left(\frac{R_p \; a \; {\theta_{proj}}^2}{\nu_{lub} \; H_{tooth}}\right)^{1/4} \tag{4.15}$$

where $R_p$is the gear pitch radius (m), a is the thermal diffusivity of oil (m²/s), θ_{proj} is the centrifugal projection angle (rad), ν_{lub} is the kinematic viscosity of oil (m²/s) and H_{tooth} is the tooth height (m).

For the complete gear, a global heat flow is then defined as:

$$Q = \frac{q \; b_{tooth} \times 2 \; Z}{2 \; \pi/\Omega} \tag{4.16}$$

where q is the evacuated heat quantity for a tooth face per width unit (W), b is the tooth width (m), Z is the gear teeth number and Ω is the gear rotational speed (rad/s).

As $Q = \Delta T/R_{proj}$, an approximation of the curve presented on Figure 4.10 can be done to obtain directly a thermal resistance:

$$if \; \Psi < 0.68 \qquad R_{proj} = \frac{2 \; \pi}{1.14 \; b_{tooth} \times 2 \; Z \; H_{tooth} \sqrt{\Omega \; \theta_{proj}} \; \chi} \tag{4.17}$$

$$if\ 0.68 < \Psi < 1.5 \qquad R_{proj} = \frac{2\,\pi}{(1.55 - 0.6\,\Psi) b_{tooth} \times 2\,Z\,H_{tooth}\sqrt{\Omega\,\theta_{proj}}\,\chi} \tag{4.18}$$

where H_{tooth} is the tooth height (m), χ is the thermal effusivity of oil ($\chi = \sqrt{k\,\rho\,c}$ N/m.s$^{1/2}$.°C) and ΔT is the temperature difference between pinion and oil (K).

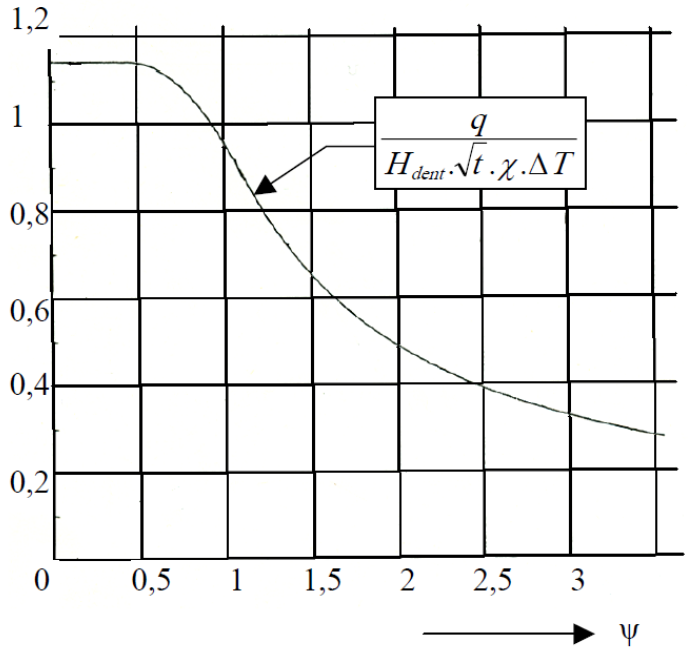

Figure 4.10: Evolution of evacuated heat quantity [65]

- **Striction:**
  $R_{th}(15{,}13), R_{th}(15{,}14)$

Striction controls the exchange between gears and their meshing point.

During meshing, the contact temperature increases a lot. However, the heat produced does not propagate deeply in gear tooth due to small contact zone and short contact duration. This has to be compared with gear size and time until the next meshing, which are really bigger. Gear bulk temperature is then not much influenced.

A distinction is thus made between gear pair and its meshing zone. Each gear has its own bulk temperature. Meshing zone is at "flash-temperature", as defined by Blok [65]. The thermal exchanges between meshing zone and each gear is driven by the thermal resistance defined as:

$$R_{striction} = \frac{0.767}{\sqrt{2\,b_c}\;b_{tooth}\,\chi\,\sqrt{V_{r\,i}}} \tag{4.19}$$

where $2\,b_c$ is the width of squeezing surface (m), b_{tooth} is the tooth width or mean contact length if several teeth mesh simultaneously (m), χ is the thermal effusivity of material ($\chi = \sqrt{k\,\rho\,c}$ N/m.s$^{1/2}$.°C) and $V_{r\,i}$ is the mean surface velocity of gear i (m/s).

2.4. Comparison between ISO technical reports and thermal network model

Several ISO technical reports address thermal issues like ISO/TR 14179-2 [9] for heat dissipation of transmissions and ISO/TR 13989-2 [35] for bulk temperature of gears. Both use only oil temperature and do not consider the system specificities (air flow, local temperatures…). Advantages of the thermal network model are highlighted hereafter.

2.4.1. Estimation of thermal dissipation

The isothermal method considers a one part housing with a uniform heat exchange, while the thermal network method allows for using a housing divided in three parts with various heat exchanges depending on air flow around it. Moreover concerning heat dissipation in the environment, the influencing element is convection and radiation between housing and air, as seen for the isothermal approach. For radiation, the ISO technical report uses a formulation which is close to but not in agreement with the linearization of Stefan-Boltzmann law [63]. For forced convection, the formulation proposed by ISO technical report (Equation (4.5)) is comparable to the one proposed by Winter et al. [64] (Equations (4.10) and (4.11)) , but with a higher coefficient, as shown below with the simplified form of Equation (4.20). This leads to an overestimated heat flow.

$$\alpha_{conv} = \frac{0.0086\ Re^{0.64}}{L} = \frac{0.0086\ \left(\frac{L\,V}{\nu_{air}}\right)^{0.64}}{L} = 10.25\frac{V^{0.64}}{L^{0.36}} \qquad (4.20)$$

To compare both models, the same steady state case as the one used in Part 2.2 is studied.

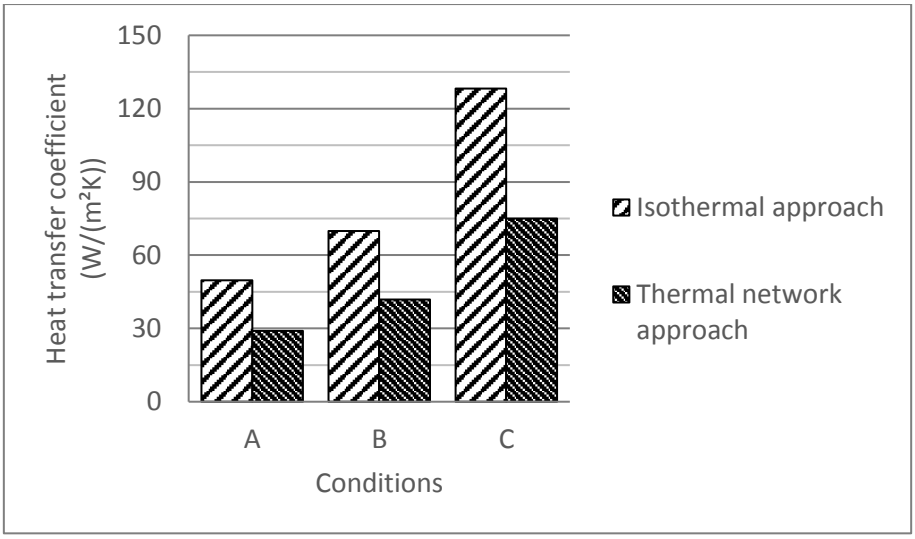

Figure 4.11: Comparison of heat transfer coefficient for radiation and convection with the air

More appropriate formulae and breakdown of the housing induce more accurate transfers with the air: the comparison of heat transfer coefficients on Figure 4.11 presents a decrease of roughly 40% between the two approaches. Thanks to this consideration of air flow, the heat exchanges are better taken into account. Finally, the oil sump temperature calculated with the thermal network is 80°C +/- 1°C for each test condition.

2.4.2. Calculation of bulk temperature

The thermal network is a way to calculate bulk temperatures of the components without using a time-consuming Finite-Element model. Standards also propose formulae in order to do so and without modelling the whole system. These two methods are compared hereafter [66].

Firstly, the gear set bulk temperature θ_M (°C) is computed with the ISO/TR 13989-2 [35]:

$$\theta_M = \theta_{oil} + C_3 \cdot X_{mp} \cdot \theta_{flaint} \cdot X_S \tag{4.21}$$

where θ_{oil} is the lubricating oil temperature (°C), θ_{flaint} is the mean flash temperature (K), C_3 is a fixed factor, X_{mp} is a contact factor, and X_S a lubrication factor. Some specificities of this formulation can be highlighted:

1) This method considers only the couple of gears (operating condition, gear geometry, surface roughness …) and the lubricating oil (lubrication mode, oil type…).
2) Oil temperature is required for this computation. This implies that a temperature measurement should be done, which is not the case with the thermal network.
3) Only a global temperature of the gear set θ_M is calculated. Indeed, it is generally assumed in gear mechanical studies that pinion and crown are at the same temperature and conduct equal heat flows from gear mesh contact. This assumption is also made for axle gear set [53]. However, as the crown wheel and the pinion have really different size, number of cycles and immersed surface, their temperature could be quite different, as well. This is supported by measurements made by Xu [3], observing up to 10°C difference.

The difference between bulk temperatures obtained with the standard and the ones determined with the thermal network is plotted on Figure 4.12 for different operating conditions. Similar results are obtained with both approaches on the prediction of crown wheel temperature: difference is less than 2°C. However, an important gap is observed on pinion bulk temperature between standard and thermal network estimations, up to almost 10°C. Even at mid power condition (condition B), a difference of more than 3°C can be critical for scuffing issues.

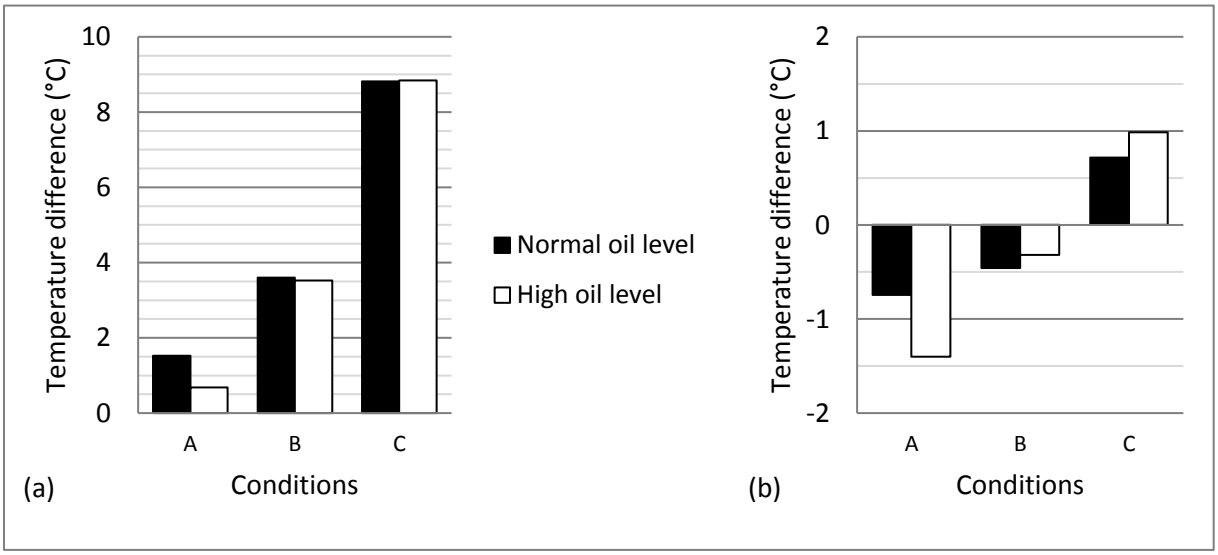

Figure 4.12: Bulk temperature difference between standard and thermal network calculation: (a) pinion and (b) crown gear

The pinion is hotter than the crown wheel. This is in agreement with the observations made by Xu et al. [3] on temperature measurements under load. To explain this phenomenon, Xu et al. suggest the influence of the difference in number of cycles between pinion and crown wheel and also the lower thermal inertia of the pinion. In addition to these explanations, another influence can be highlighted: even if the heat transfer from the contact between pinion and crown is almost equivalent, the thermal resistance between pinion and oil is 3 times bigger than the one between crown and oil. This induces a better cooling of the crown and a higher temperature of the pinion. A hotter environment also exists on the input shaft around the pinion than around the crown wheel, due to closer rolling element bearings.

2.4.3. Conclusion on thermal network application

The thermal network method gives more coherent results both in terms of thermal exchanges and temperature evaluation. However, experimental data collected until now are not sufficient to corroborate thermal network results. Indeed, only oil temperature was monitored and it has been thoroughly underlined that temperature varies locally. A more specific test campaign is needed to obtain bulk temperature of several axle components and thus to validate the thermal network of the axle.

3. Investigations on axle thermal behaviour

In order to validate the thermal network model, it is necessary to measure the temperature of several components and to characterise the thermal behaviour of the axle. As those presented in Chapter 2, usual efficiency tests only monitor oil temperature, which is not sufficient to validate the power loss breakdown. New tests are then performed.

3.1. Test definition

Test rigs similar to those of Chapter 2 are used to conduct experiments with and without an applied load. This allows for efficiency measurements. For the tests with an applied load, torque range is of 5kN.m on the input and on each output with an accuracy of +/-8.5N.m. For the no-load tests, torque range on the input is of 200N.m with an accuracy of +/-0.4N.m.

For the thermal study, several components of the axle are monitored with K-type thermocouples according to the list of Table 4.4. Their locations are represented on Figure 4.13 and Figure 4.14. The oil temperature sensor is located in the oil drain plug of the axle. The precision of these temperature sensors is +/- 0.5 °C.

Table 4.4: List of temperature sensors

Sensor number	Monitored component
1	Ambient air
2	Oil
3	Air flow
4	Drive head housing
5	Sump housing

Sensor number	Monitored component
6	Lateral housing
7	Head rolling element bearing
8	Tail rolling element bearing
9	Pilot rolling element bearing
10	Differential rolling element bearing

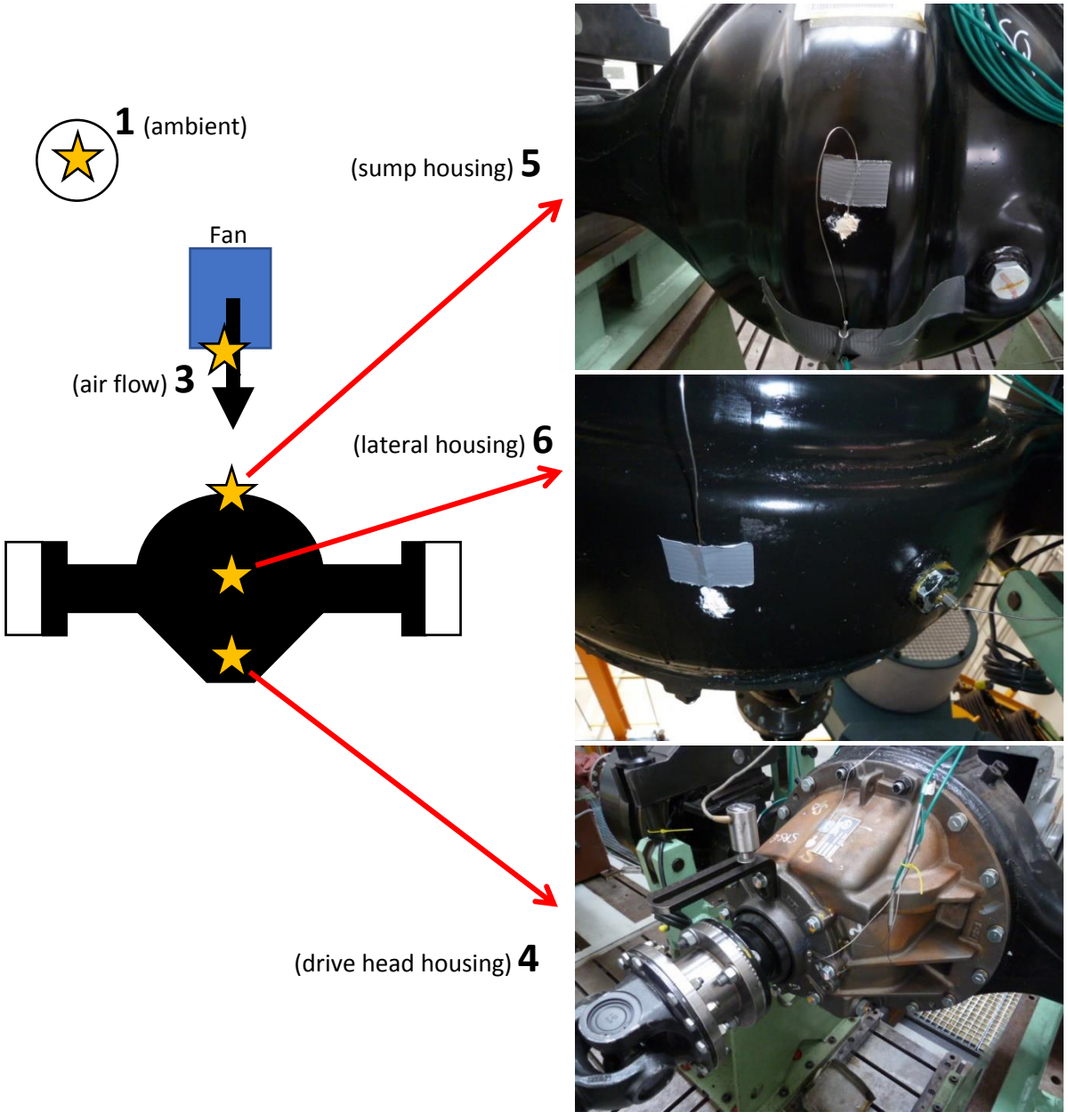

Figure 4.13: Locations of external temperature sensors

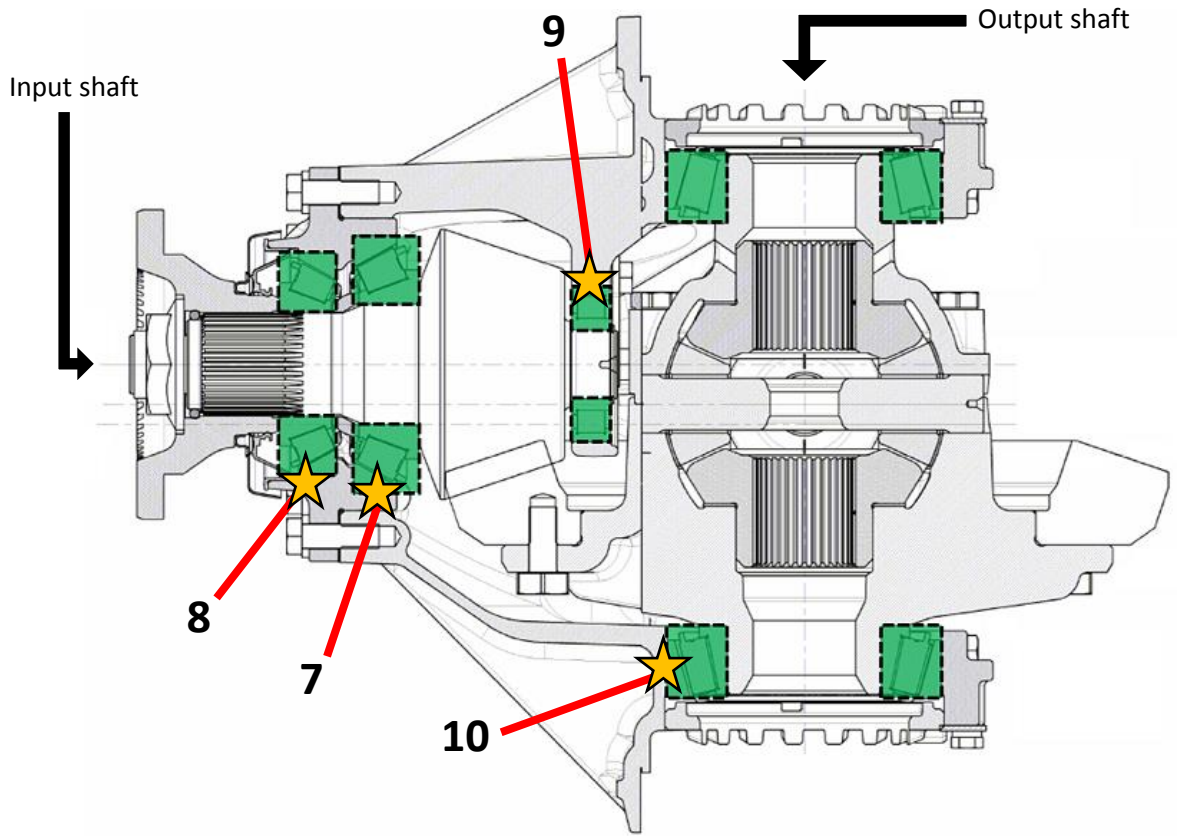

Figure 4.14: Locations of internal temperature sensors

The test procedure is composed of three power steps with different speeds, as detailed in Table 4.5. Corresponding output torques and speeds are represented on Figure 4.15. Due to the use of two different test benches, the no-load step is operated separately. For each condition, a stabilisation criteria must be fulfilled before going forward: oil temperature variation must be under 0.1°C during 3 minutes. The same procedure is repeated with a higher oil level.

Table 4.5: Test conditions

Test condition	**No-load step**		**Load steps**			
	1	2	3	4	5	6
Input power (kW)	~ 0		60		120	
Vehicle speed (km/h)	50	80	50	80	50	80

A fan prevents the axle to overheat and helps a quicker temperature stabilisation by inducing forced air convection. Even during the cooling after the tests, the fan is blowing and temperatures are recorded. Air flow is kept constant during the whole procedure in order to characterise the forced convection between air and housing. It is characterised thanks to an anemometer: its speed is of 22 m/s on load test bench and of 12 m/s on no-load test bench.

The axle and the oil used for thermal tests are the same as the one used for the efficiency tests of Chapter 2. Specification of this axle and oil volumes are presented in Table 4.6.

Table 4.6: Specification of tested axle

	Axle	**H1**
	Ratio	4.625
Gear set	**Type**	Hypoid
	Cutting method	Face-hobbed
	Number of teeth	8 x 37
Oil volume (L)	**Normal level**	14
	High level	25

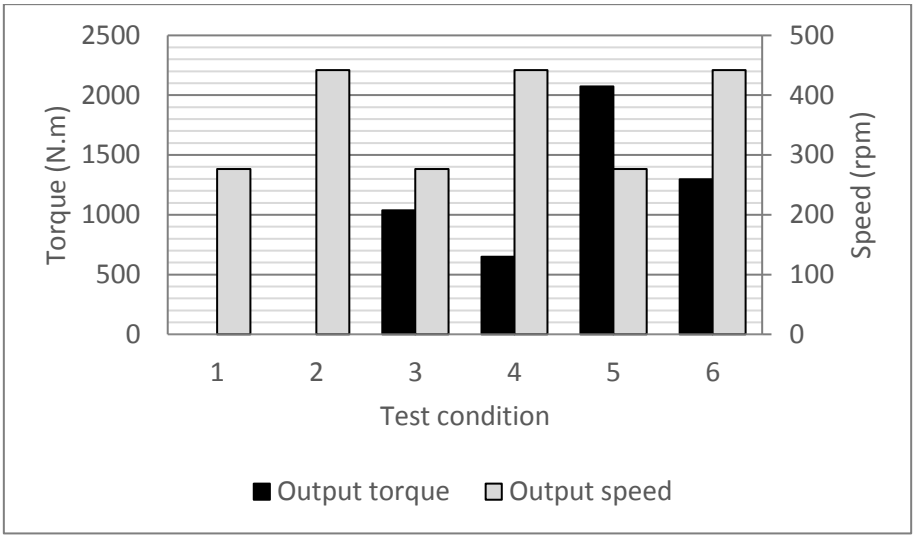

Figure 4.15: Output torque (on each output shaft) and output speed for the different test conditions

3.2. Experimental results

Two types of results are obtained thanks to these tests: global power loss of the axle and components temperatures. Measurement results for both efficiency and temperature aspects are summarized in Table 4.7 to Table 4.10.

Axle power loss is presented on Figure 4.16: hub losses are removed in order to have only drive head contribution. For each power step, power loss increases with speed. A higher oil level always induces higher losses. This is even more pronounced at higher speeds (conditions 2, 4 and 6) with differences from 400 W up to 1 kW. It is important to keep in mind that the operating temperature here is quite low (maximum oil sump temperature of 60°C). This is favourable for gear mesh efficiency while it is unfavourable for rolling elements bearings losses.

Temperature of components is now considered. A first observation can be made regarding axle housing. Figure 4.17 presents temperature measurements of the three sensors installed on different housing sides, for tests at normal oil level with the same speed but different loads. Drive head housing appears to be the hottest housing part in every condition. Indeed, this is a compact part of the axle with several rolling element bearings generating losses.

Table 4.7: Efficiency measurements at normal oil level

	INPUT			OUTPUT				
Cond.	**Speed (rpm)**	**Torque (N.m)**	**Power (kW)**	**Speed (rpm)**	**Torque (N.m)**	**Power (kW)**	**Power loss (kW)**	**Efficiency (%)**
1	1278	16.5	2.20	/	/	/	2.20	/
2	2045	17.7	3.79	/	/	/	3.79	/
3	1276	445	59.5	276	1969	56.9	2.6	95.6
4	2044	276	59.0	443	1192	55.2	3.7	93.7
5	1276	899	120.1	276	4032	116.5	3.5	97.1
6	2044	557	119.2	443	2481	115.0	4.2	96.5

Table 4.8: Efficiency measurements at high oil level

	INPUT			OUTPUT				
Cond.	**Speed (rpm)**	**Torque (N.m)**	**Power (kW)**	**Speed (rpm)**	**Torque (N.m)**	**Power (kW)**	**Power loss (kW)**	**Efficiency (%)**
1	1278	19.0	2.54	/	/	/	2.54	/
2	2045	19.5	4.18	/	/	/	4.18	/
3	1276	445	59.4	276	1956	56.6	2.9	95.2
4	2044	276	59.0	443	1172	54.3	4.7	92.1
5	1276	897	119.8	276	4017	116.2	3.7	96.9
6	2044	556	119.1	443	2467	114.3	4.8	96.0

Table 4.9: Temperature measurements regarding ambient temperature (°C) at normal oil level

Cond	**Oil**	**Head REB**	**Tail REB**	**Pilot REB**	**Differential REB**	**Drive head housing**	**Sump housing**	**Lateral housing**
1	17.4	20.3	20.9	18.0	17.2	14.9	12.1	9.1
2	28.1	30.4	31.2	30.0	28.6	24.2	20.1	16.7
3	22.7	24.9	24.6	23.9	21.7	18.6	14.9	12.8
4	30.6	32.9	32.8	32.9	30.5	25.3	20.4	16.9
5	31.4	33.3	32.8	32.7	29.5	25.7	20.5	16.7
6	35.7	37.6	37.3	38.0	34.6	29.8	24.7	21.5

Table 4.10: Temperature measurements regarding ambient temperature (°C) at high oil level

Cond.	**Oil**	**Head REB**	**Tail REB**	**Pilot REB**	**Differential REB**	**Drive head housing**	**Sump housing**	**Lateral housing**
1	18.5	19.9	20.6	19.0	18.2	15.9	12.3	11.6
2	28.9	30.8	31.3	30.2	28.3	25.0	20.1	18.9
3	22.4	23.3	23.3	23.2	21.4	18.4	14.8	13.7
4	31.0	32.8	32.7	32.4	29.9	26.0	21.0	20.0
5	29.2	29.9	29.8	30.2	27.3	23.5	18.5	17.0
6	36.3	37.9	37.5	37.8	34.5	30.3	24.1	22.4

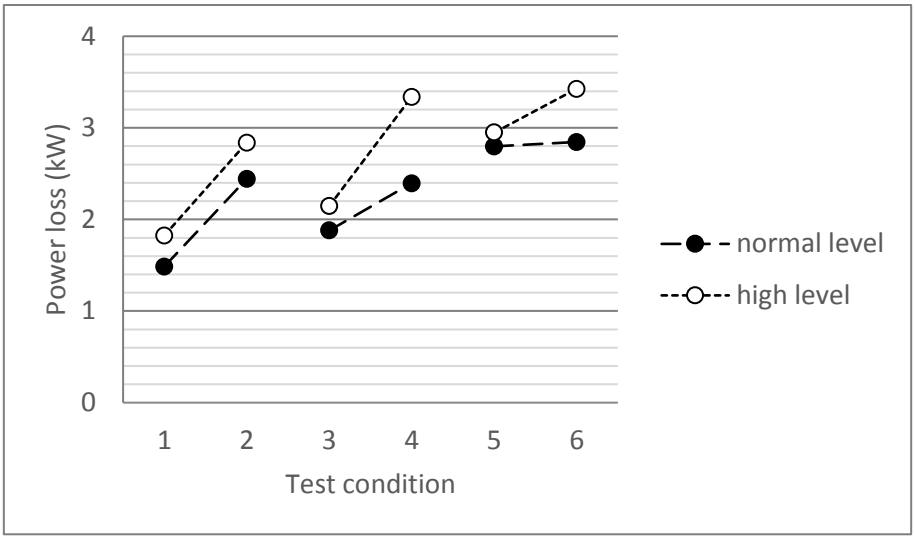

Figure 4.16: Power loss of axle for two oil levels (normal and high)

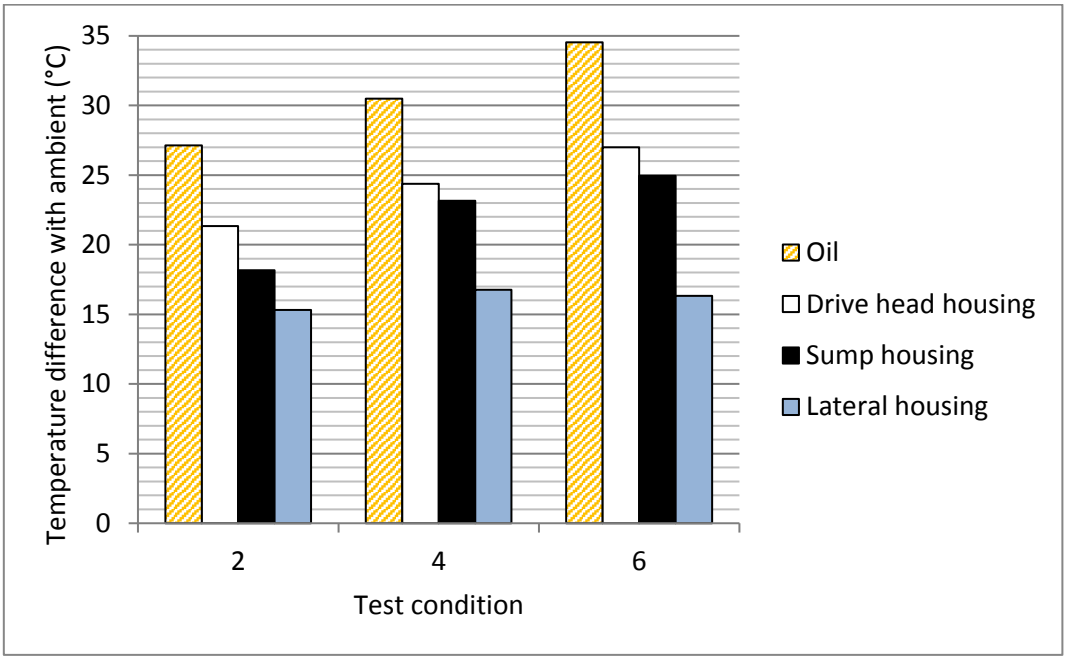

Figure 4.17: Stabilised temperatures of the different housing parts compared to oil temperature

Moreover, on test bench, air flow comes from the opposite side (see Figure 4.8). Temperature difference with sump housing is up to 8% and difference with lateral housing ranges from 14% to 23%. It seems then appropriate to consider several parts to model the housing, as proposed before. Moreover, housing is not at oil sump temperature.

A second observation can be made on rolling element bearings through a comparison with oil. Figure 4.18 presents temperatures of oil and bearings for tests at normal oil level too. Rolling element bearings located on input shaft are hotter than oil due to their power losses, while the differential rolling element bearing is colder mainly due to the lower rotational speed of output shaft.

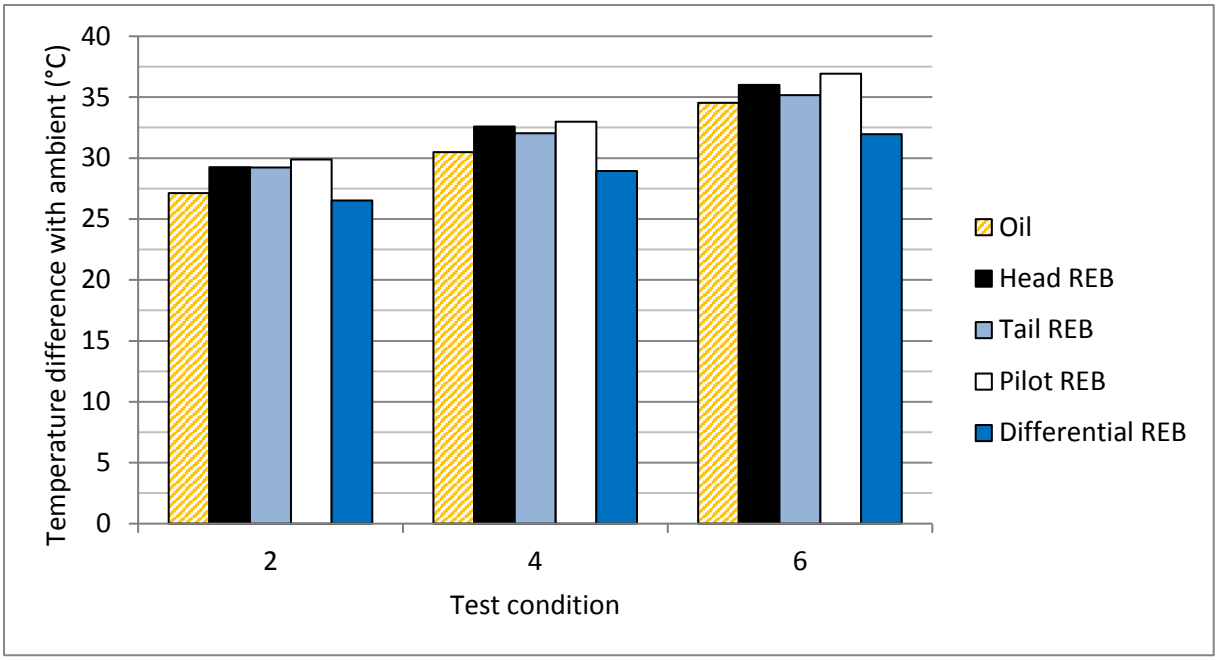

Figure 4.18: Stabilised temperatures of oil and rolling element bearings (REBs)

3.3. Validation of axle thermal network

Thanks to the test procedure, different characteristics of the axle power losses and thermal exchanges can be determined, as reported in Table 4.11.

First, thermal exchanges with the environment must be correctly estimated. As they are conditioned by forced convection with air, it is thus necessary to validate this exchange thanks to the cooling phase, after what temperatures and power losses can be compared. A good agreement between the measured and predicted temperatures of, for example, a rolling element bearing confirms the estimation of its power loss. On the contrary, if the measured temperature is higher than the predicted one, this means that the power loss estimation is lower than in the reality.

Table 4.11: Characterisation of losses and thermal exchanges during the tests

	No-load step	**Load steps**	**Cooling**
REB, churning and seal losses	X		
Gear mesh friction losses		X	
Free oil convection			X
Forced oil convection	X	X	
Forced air convection			X

3.3.1. Axle cooling

As reported in Table 4.11, free oil convection occurs inside the axle and forced air convection occurs outside during the cooling. As the air flow was kept constant, temperature derivative should be constant as well.

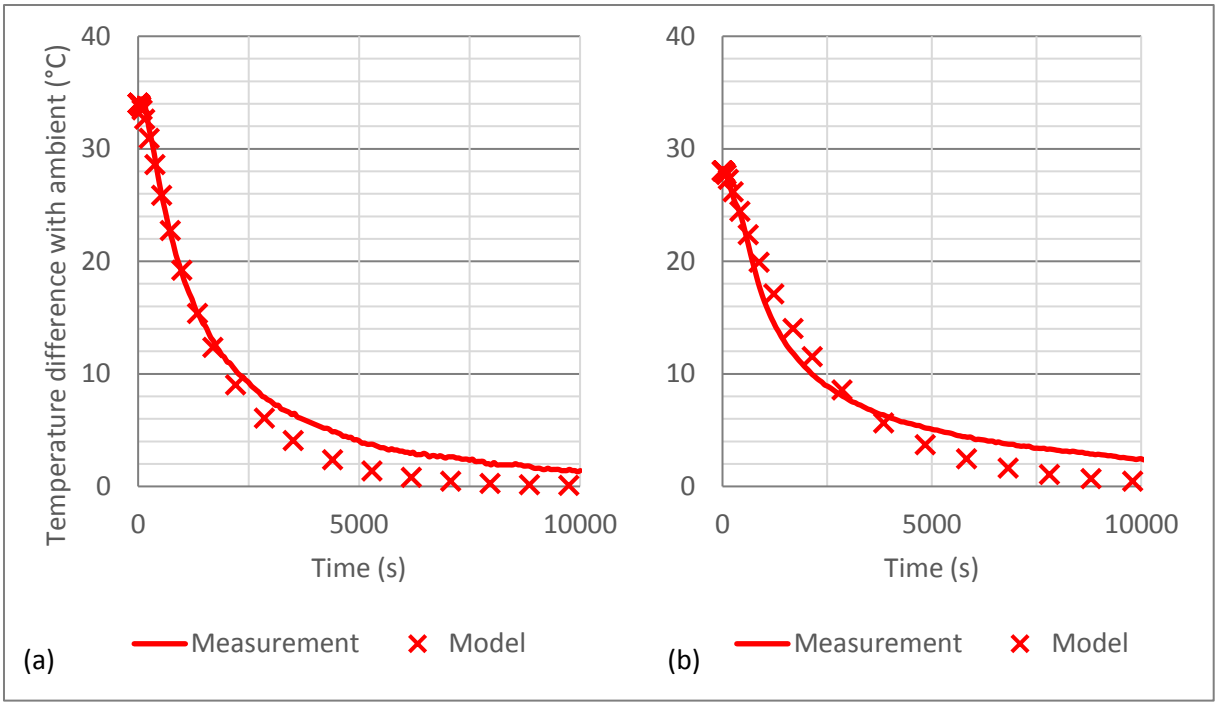

Figure 4.19: Oil cooling according to measurement and corresponding model on (a) load test bench and (b) no-load test bench

Figure 4.19 presents oil temperature measurements and model results for the cooling phase on both test benches. A good agreement is observed on the first part of the cooling (<2500 s). Temperature decrease is then slower in the reality and takes more time to reach ambient temperature (>10000 s), but overall behaviour is well reproduced.

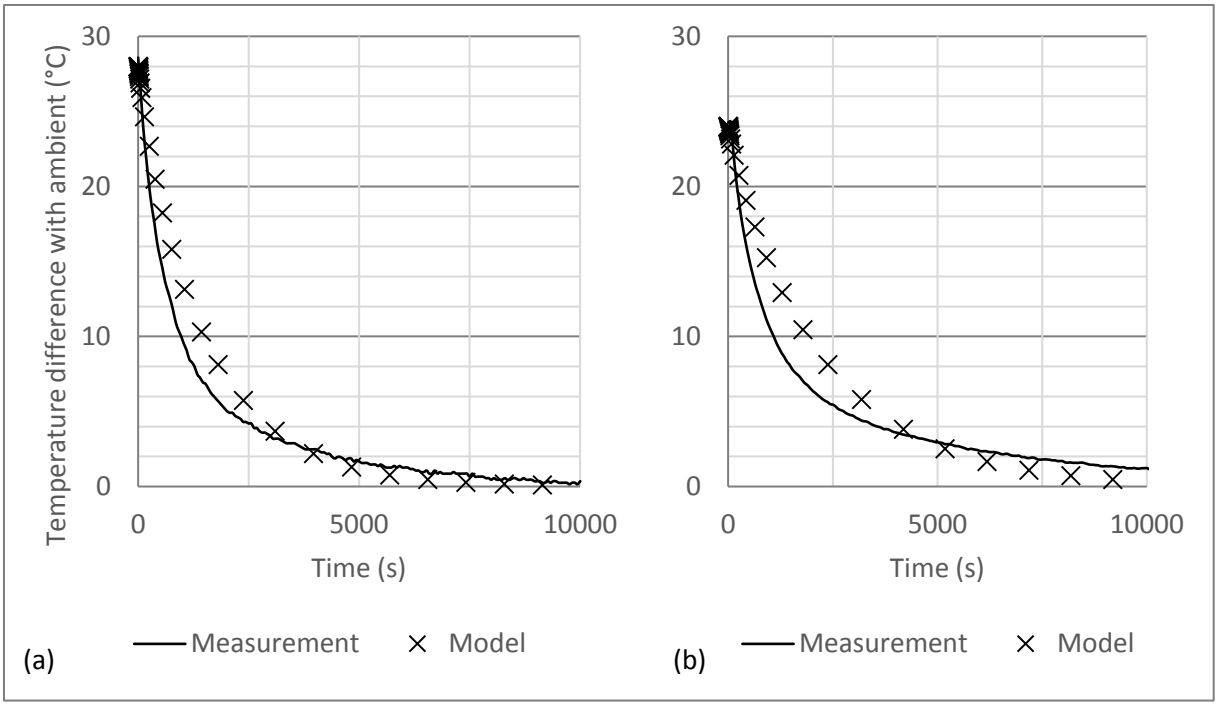

Figure 4.20: Drive head housing cooling according to measurement and corresponding model on (a) load test bench and (b) no-load test bench

Figure 4.20 presents the same comparison for drive head housing temperature. A better agreement is obtain on temperature decrease rate.

To test the model sensitivity, the heat transfer coefficient is modified by 10%. This induces an oil temperature variations of less than 1°C. The model thus gives a correct and stable approximation of axle cooling.

3.3.2. No-load step

During the no-load step, forced air convection also occurs on housing, which was already identified in the previous section. However, forced oil convection is also generated inside the housing due to shafts and gears rotation. As summarized in Table 4.11, this thermal exchange can be characterised here.

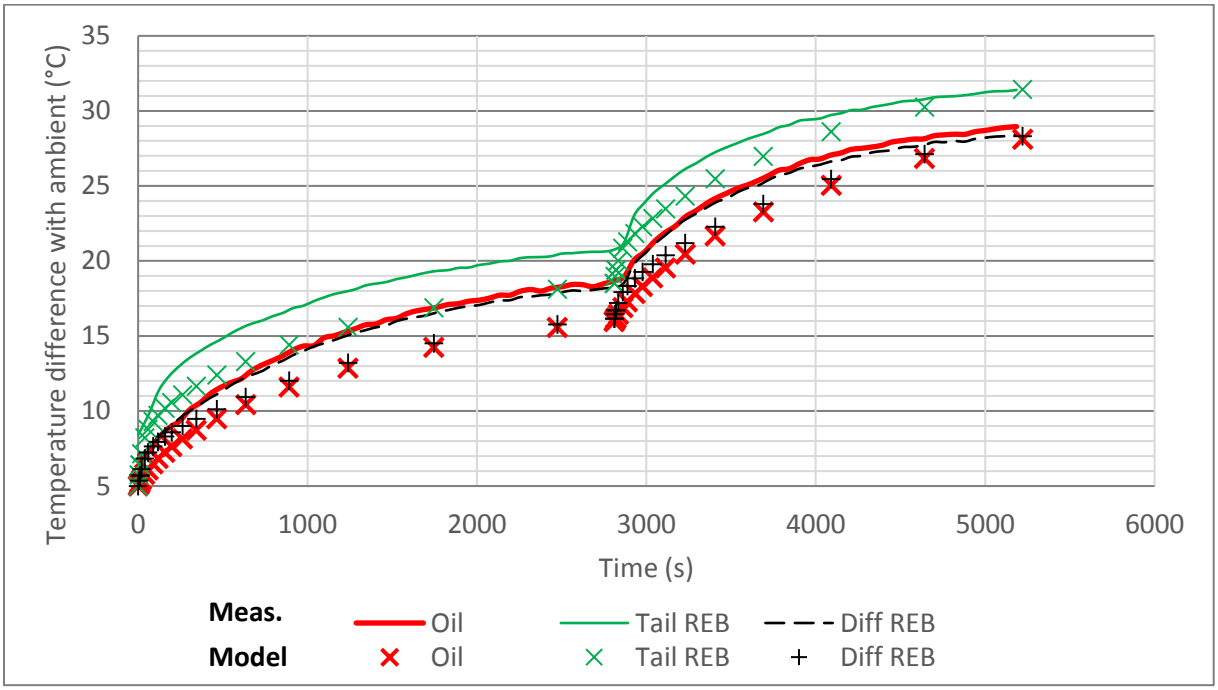

Figure 4.21: Oil and REB temperatures regarding ambient according to measurement and model for no-load step conditions (1 and 2)

Figure 4.21 illustrates temperature evolution of oil and rolling element bearings (REB) and compares measurement and model results. Temperature increase rate is slightly different but overall behaviour is close. Stabilised state is then considered for each no-load test condition. Figure 4.22 presents oil temperature comparison: a good agreement is obtained. Figure 4.23 exposes temperature difference between REB and oil: tendencies are similar for measurement and model.

Still according to Table 4.11, power losses independent from load are produced. Figure 4.24 compares these power losses according to measurement and model. Calculations underestimate the loss: there is a maximum difference of 26% with measurement point and of 11% with measurement uncertainty. This power loss underestimation explains the temperatures predicted on Figure 4.22, which are lower than measured ones.

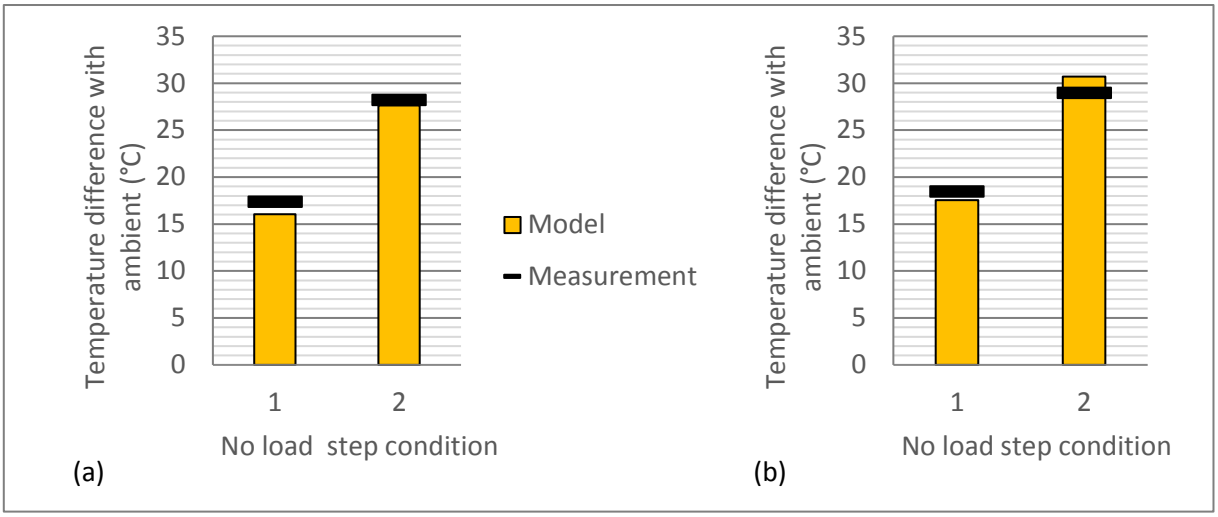

Figure 4.22: Oil temperature regarding ambient according to measurement and model for (a) normal oil level and (b) high oil level

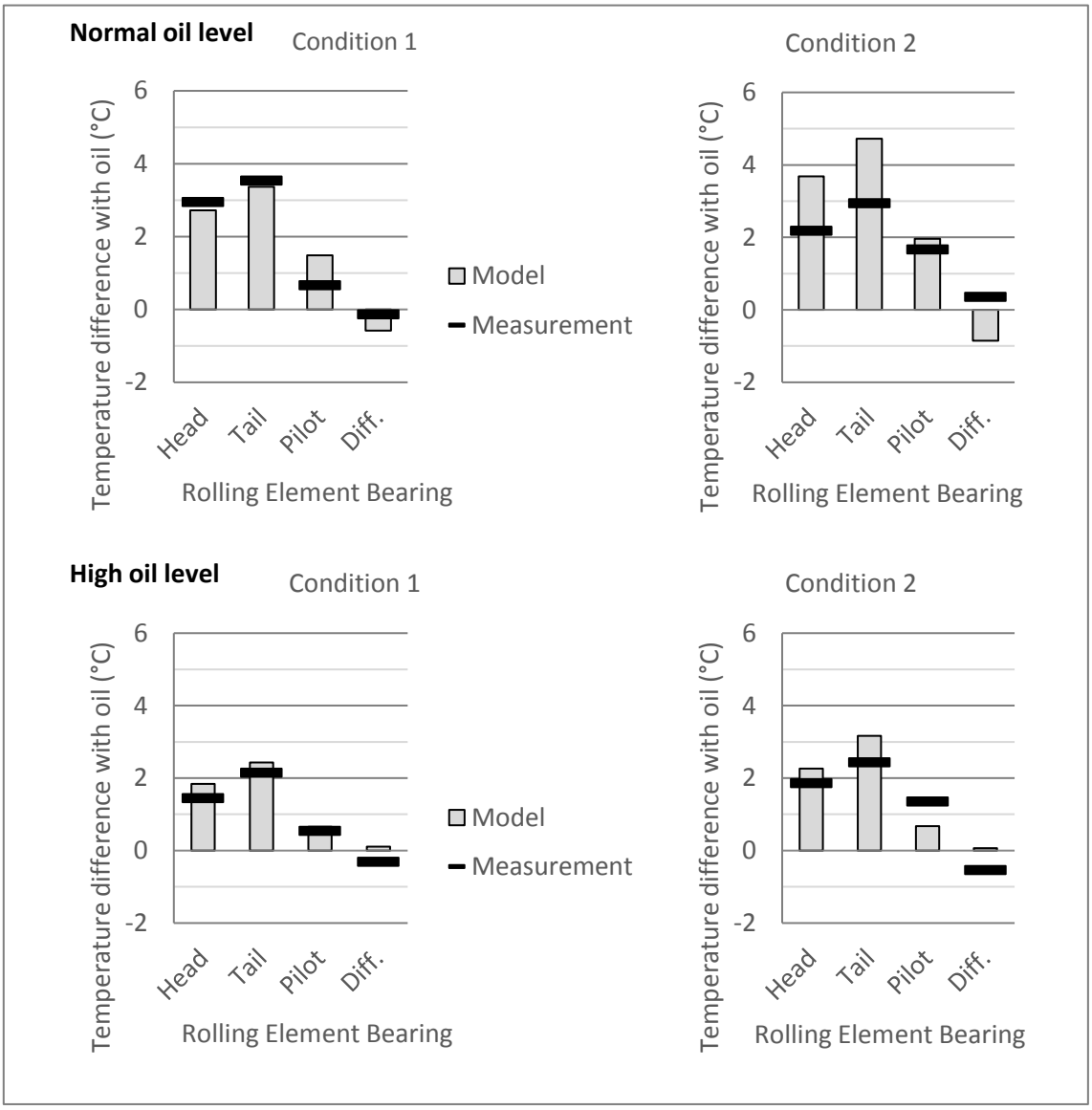

Figure 4.23: REB temperature regarding oil according to measurement and model

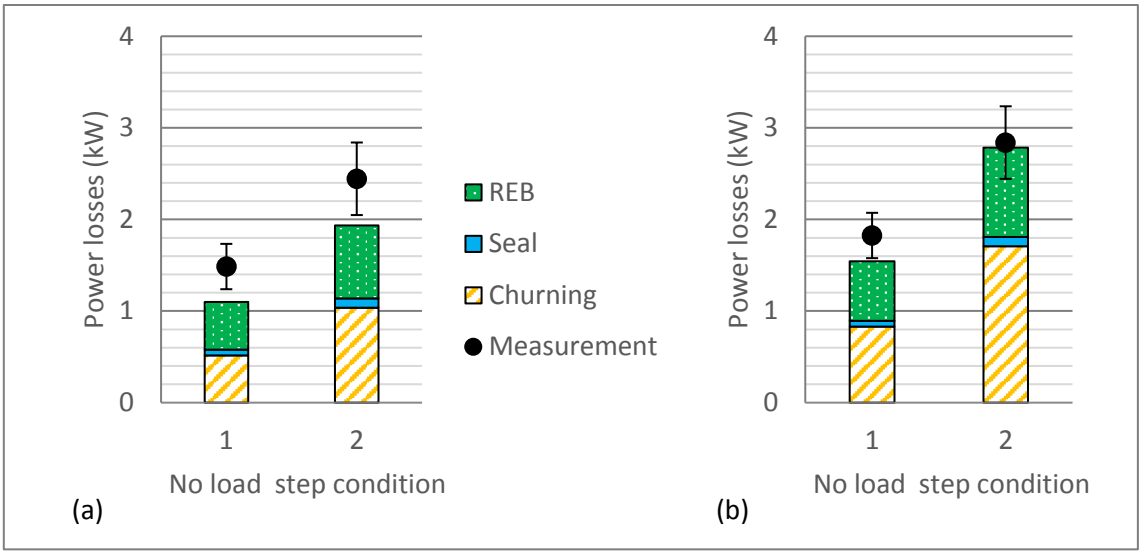

Figure 4.24: Power loss estimation and comparison with measurement for (a) normal oil level and (b) high oil level

3.3.3. Load steps

Thermal exchanges occurring during load steps are the same as for the no-load step. Temperature evolution presented on Figure 4.25 and stabilised temperature comparisons of Figure 4.26 and Figure 4.27 show good agreement between measurement and calculation for these load conditions too.

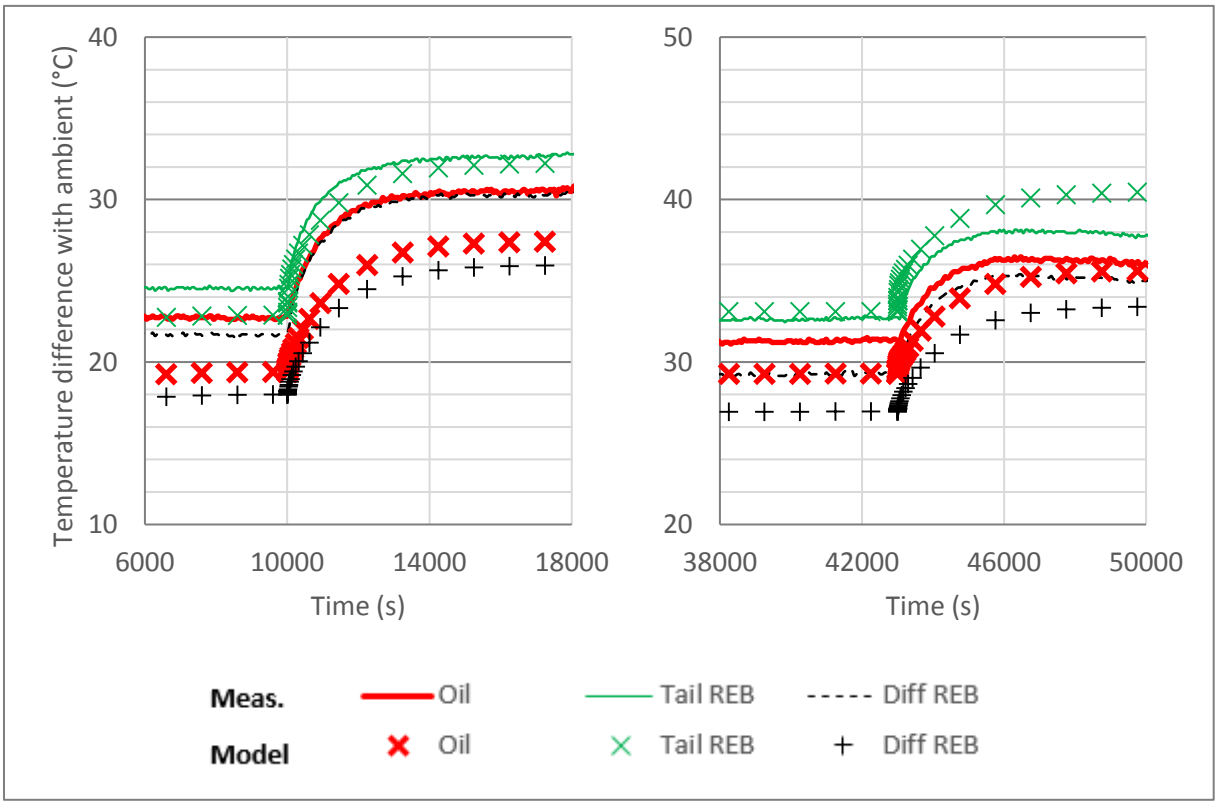

Figure 4.25: Oil and REB temperatures regarding ambient according to measurement and model for load steps conditions (3, 4, 5 and 6)

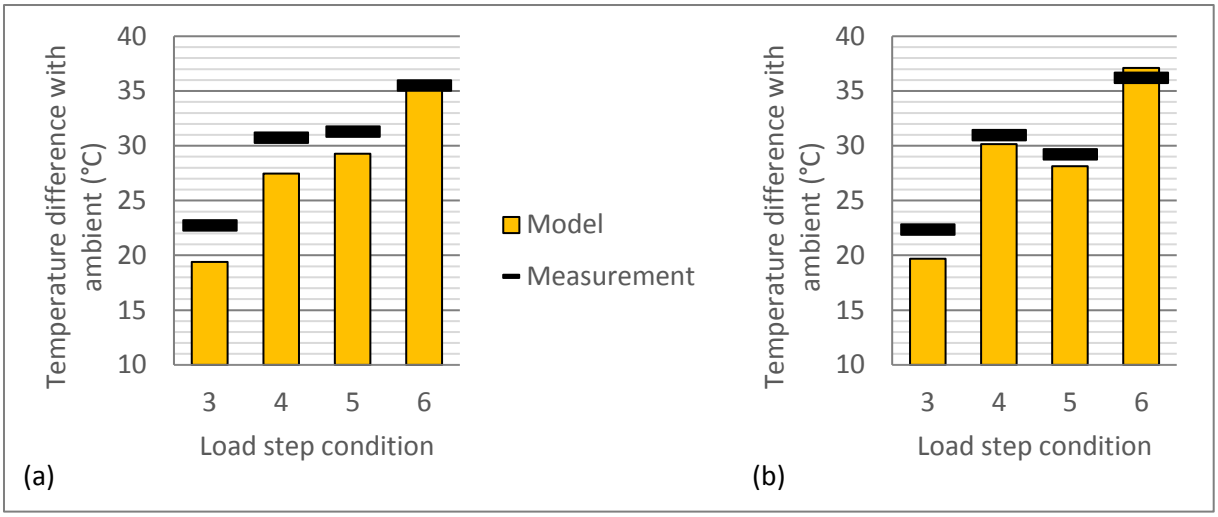

Figure 4.26: Oil temperature regarding ambient according to measurement and model for (a) normal oil level and (b) high oil level

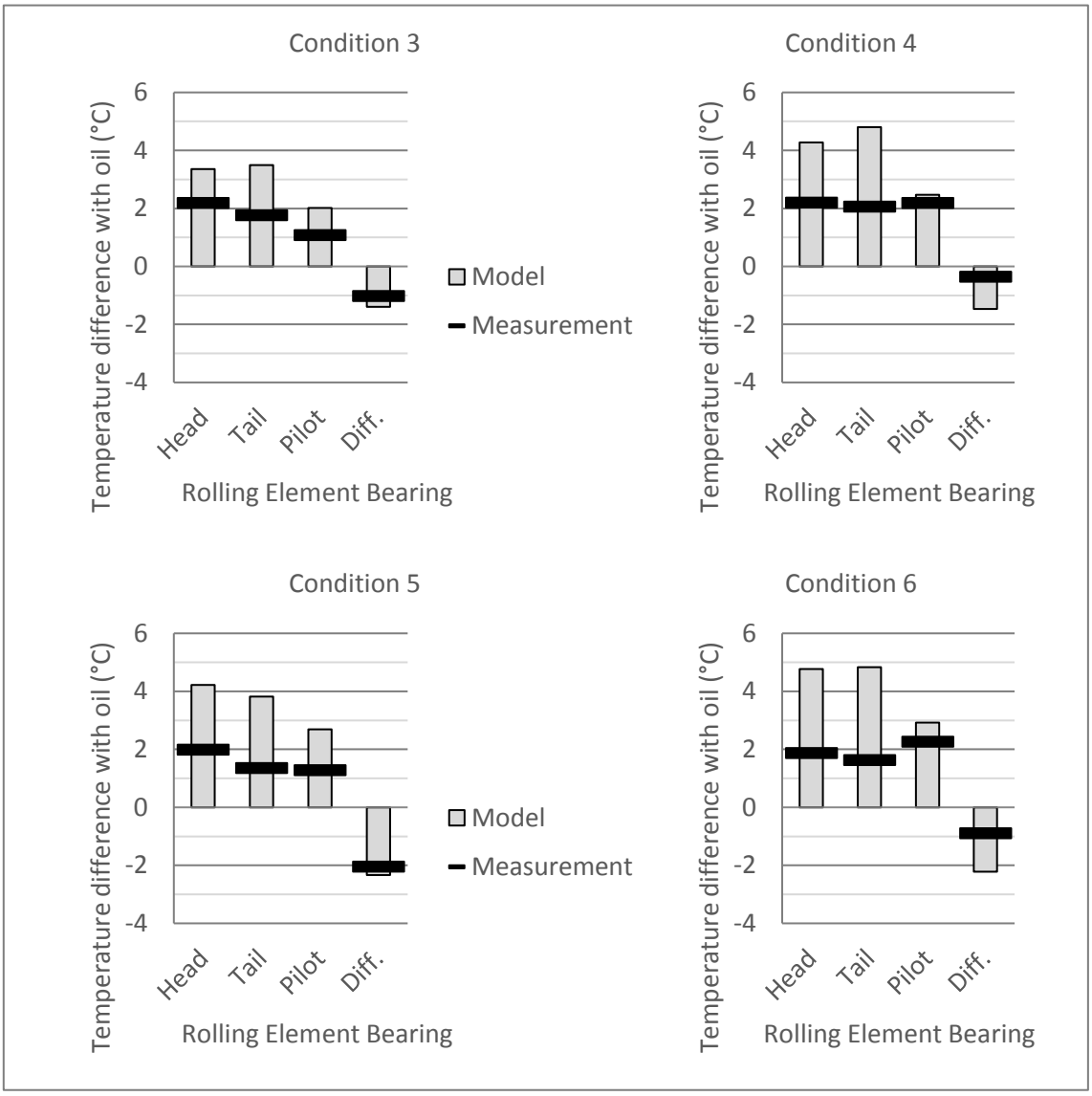

Figure 4.27: REB temperature regarding oil according to measurement and model for normal oil level

Regarding power losses, gear mesh friction is now considered. Figure 4.28 compares tests and calculations: results are close and present similar tendencies. This validates the axle thermal model for both temperature prediction and power loss estimation.

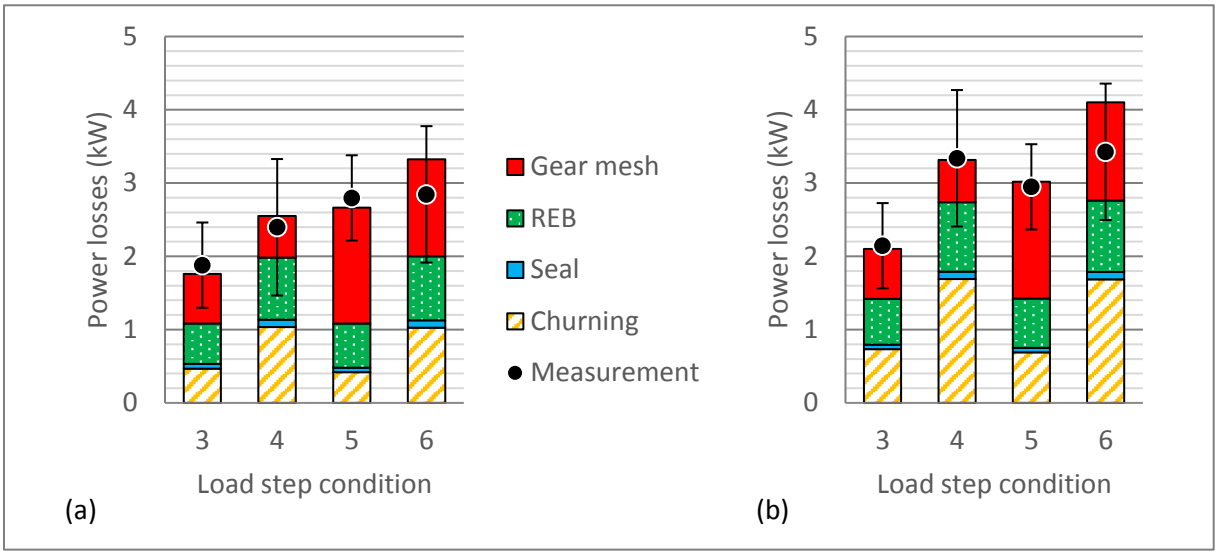

Figure 4.28: Power loss estimation and comparison with measurement for (a) normal oil level and (b) high oil level

3.4. Extending model validation

The same thermal tests are performed on a second axle called SB1. Axle ratio is identical but the gear set is a spiral bevel one. General characteristics of the axle are given in Table 4.12. Housing and rolling element bearing dimensions are slightly different from axle H1.

Table 4.12: Comparison of tested axle characteristics

	Axle	**H1**	**SB1**
	Ratio	4.625	4.625
Gear set	**Type**	Hypoid	Spiral bevel
	Cutting method	Face-hobbed	Face-milled
	Number of teeth	8 x 37	8 x 37
Oil volume (L)	**Normal level**	14	10
	High level	25	19.5

Experimental and calculated results are presented hereafter. Figure 4.29 and Figure 4.30 expose oil and REB temperature comparison: a good agreement is obtained. A point of discrepancy is solely observed on pilot REB, which is colder than oil and even than differential REB. It is unlikely that this bearing produces almost no losses, so an instrumentation issue is considered. Power loss measurements and estimations are compared successfully on Figure 4.31.

The axle thermal model is thus an efficient tool to predict both temperatures and power losses of the system.

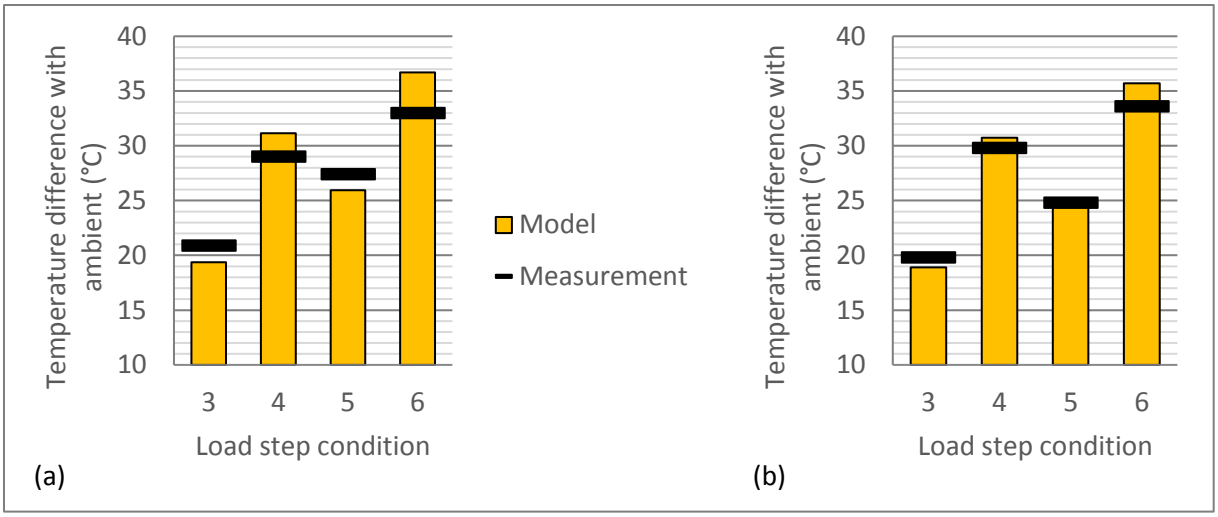

Figure 4.29: Oil temperature of axle SB1 regarding ambient according to measurement and model for (a) normal oil level and (b) high oil level

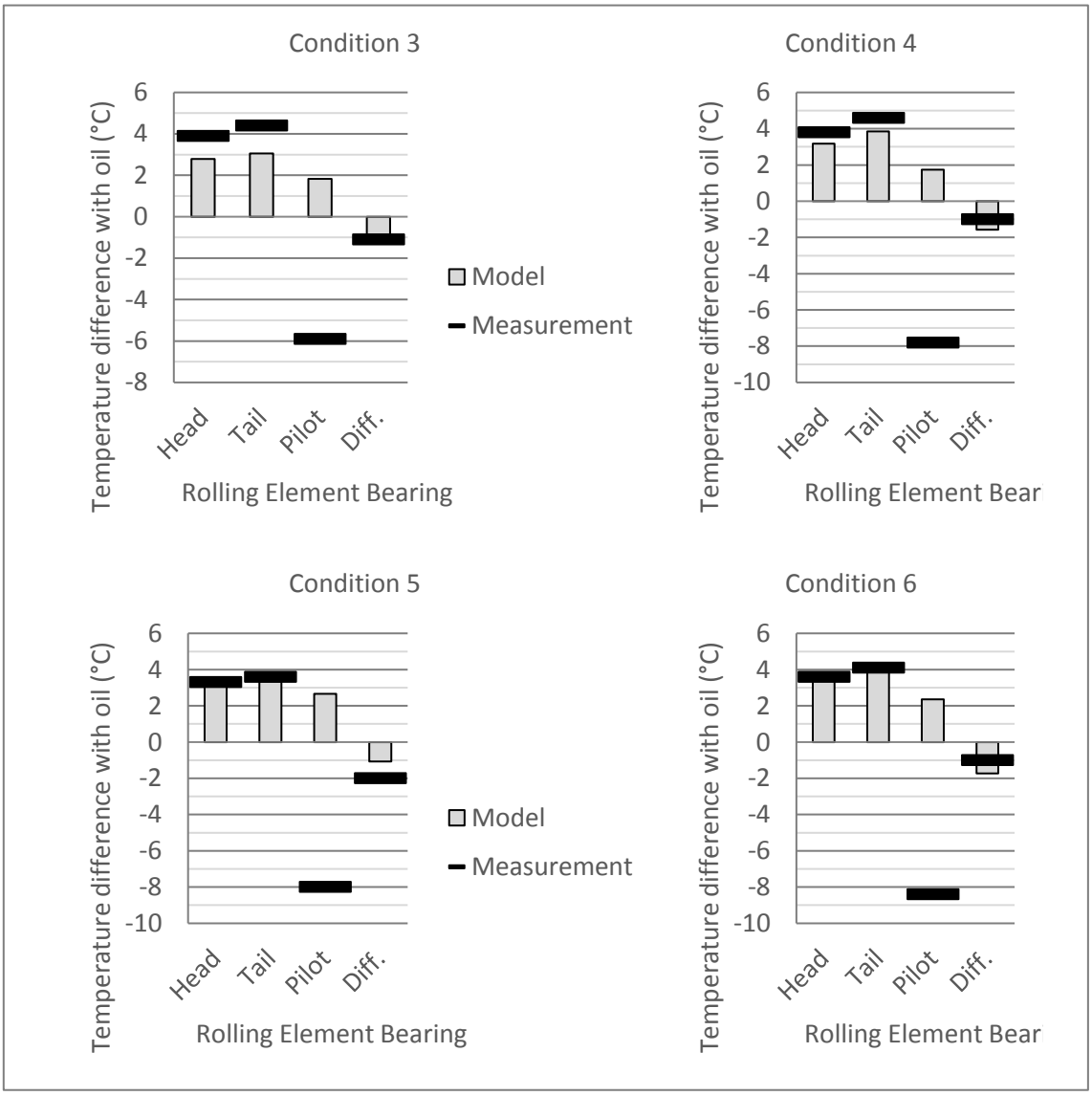

Figure 4.30: REB temperature of axle SB1 regarding oil for normal oil level

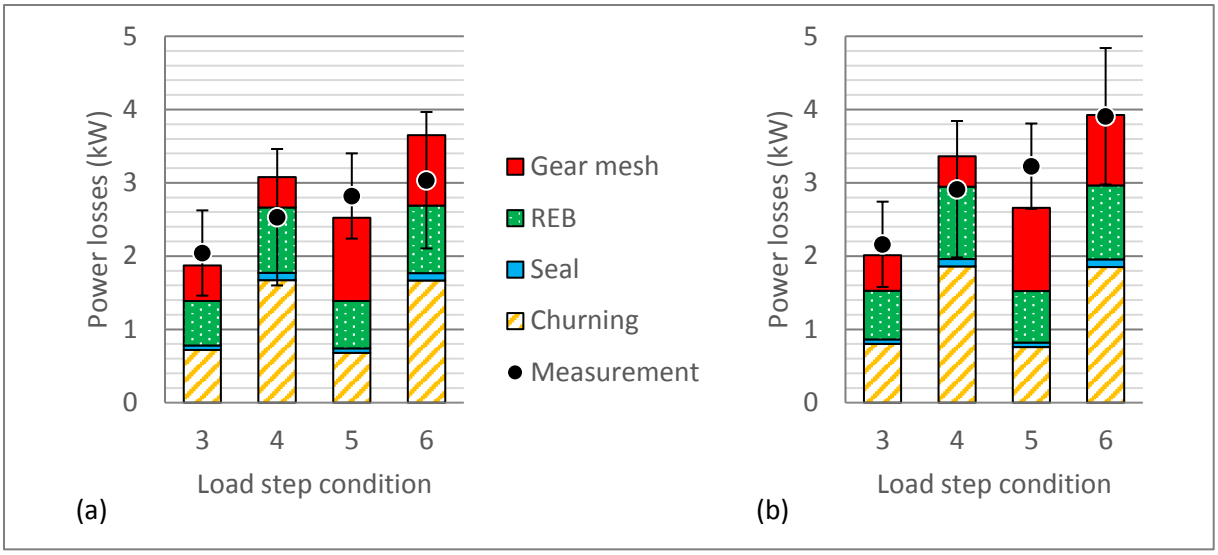

Figure 4.31: Power loss estimation of axle SB1 and comparison with measurement for (a) normal oil level and (b) high oil level

A comparison is made here between the two axles H1 and SB1. Gear mesh friction is lower on axle SB1 due to the spiral bevel gear set, while oil churning losses are higher due to a larger diameter of its crown wheel. Thus, the efficiency of these axles is similar for these test conditions.

4. Exploitation of the model

Axle is now represented thanks to a thermo-mechanical model: efficiency and bulk temperatures can be calculated for various operating conditions. The influence of some parameters are investigated hereafter on axle H1.

4.1. Oil properties

Various lubricants can be used in axles. They have different viscosities, as presented in Table 4.13: Mineral lubricant is the most viscous, Eco lubricant has a lower viscosity than Reference at low temperature. As Reference and Eco lubricant have the same viscosity at high temperature, no difference will be observed for a long haul condition (80km/h, 120kW) as oil temperature is around 80°C. A comparison is made here on a medium duty condition (50km/h, 60kW).

Table 4.13: Oil properties of considered lubricants

Oil	Type	Density	Viscosity at 40°C (cSt)	Viscosity at 100°C (cSt)
Mineral	Mineral	0.895	298	25.2
Reference	Synthetic	0.86	120	15.9
Eco	Synthetic	0.869	103	15.3

Figure 4.32 displays total power loss and temperatures. A significant decrease in power loss and temperature is observed between mineral and synthetic oils: this is due to their respective viscosity, but also to the use of a coefficient depending on oil type for the friction coefficient calculation. There is a slight decrease of temperature between the two synthetic oils but no difference of efficiency. Indeed, the equilibrium between power dissipation and temperature induces a lower temperature for the Eco lubricant. Viscosity is then similar for both lubricants, and power losses too.

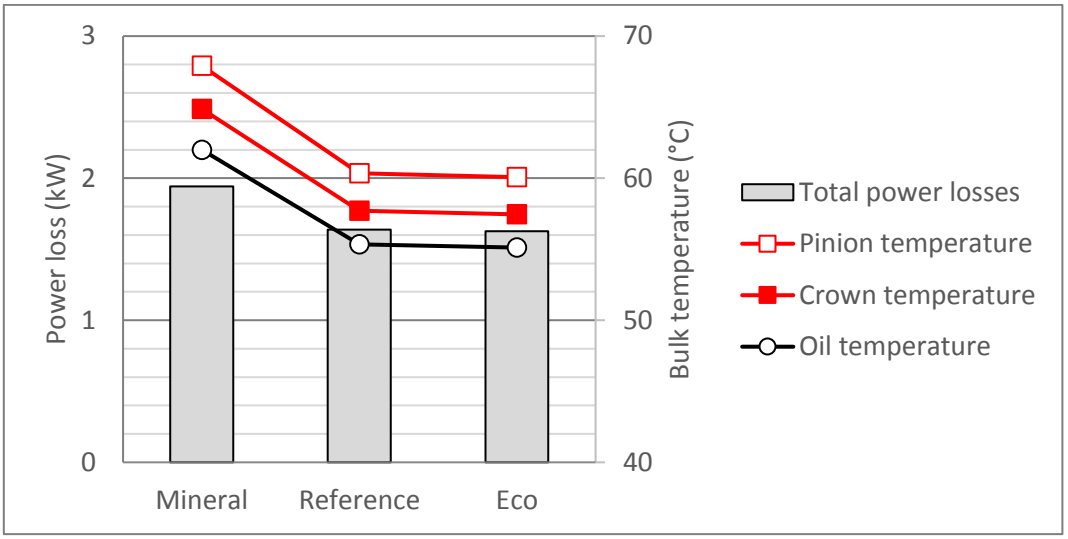

Figure 4.32: Total power losses and oil and gear set temperatures for several lubricants

4.2. Gear surface roughness

In Chapter 3, it has been shown that gear tooth surface roughness has an influence on gear mesh friction. The heat produced modifies oil viscosity and can influence even more friction losses through the friction coefficient.

Figure 4.33 illustrates the evolution with roughness of gear mesh power losses and of oil and gear set temperatures for a long haul condition (80km/h, 120kW). Both naturally decrease together.

Table 4.14 gives the different friction coefficients obtained in these conditions with temperatures of Figure 4.33 and at 80°C. The same trends are observed as in Chapter 3, but friction coefficient is increased for medium grinding, as operating temperature here is higher than 80°C. This thus worsens even more the gear mesh conditions and induces more friction losses.

Table 4.14: Gear surface roughness and friction coefficient according to ISO/TR 14179-2

Surface finishing	Ra (µm)	Friction coefficient (Figure 4.33)	Friction coefficient at 80°C
Grinding (medium)	0.8	0.03	0.026
Reference	0.3	0.023	0.023
Lapping	0.2	0.021	0.020

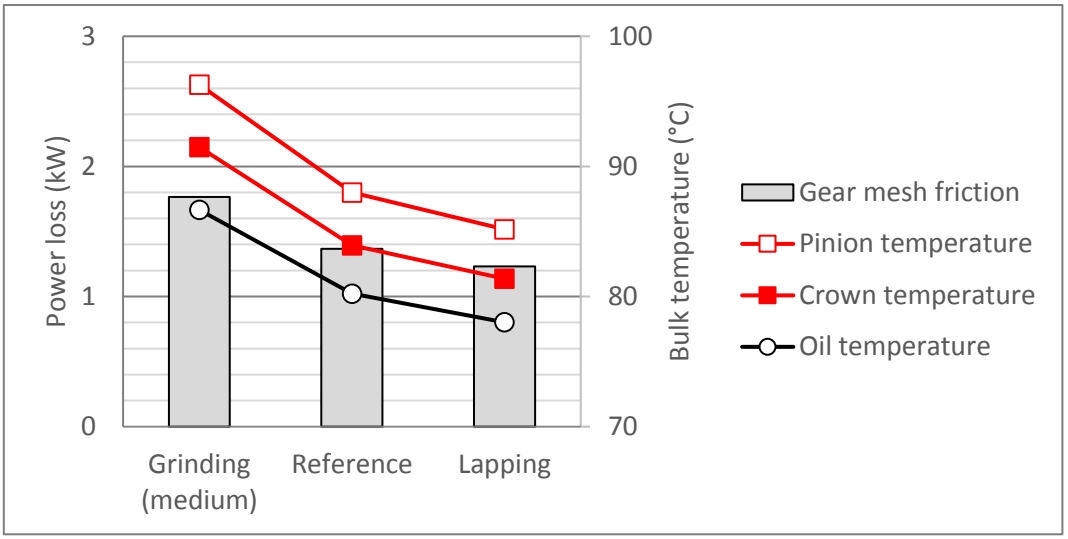

Figure 4.33: Gear mesh power losses and oil and gear set temperatures for various gear surface roughness

4.3. Air flow

The axle is located in the chassis of the vehicle. This protects it from air flow generated by truck displacement. For a truck running at 80km/h, the speed of air flow around the vehicle is 22m/s. However, only 5m/s of air flow circulates generally around the axle. This is a very small part of the flow.

Three air flow conditions are tested to see the impact on efficiency and temperatures. Results are presented on Figure 4.34 for a long haul condition (80km/h, 120kW). When air flow is lower (3m/s), bulk temperatures are increased by almost 15°C. This decreases oil viscosity and so power losses, but can induce component failures. When air flow is higher (8m/s), bulk temperatures drop by 10°C and power losses are increased.

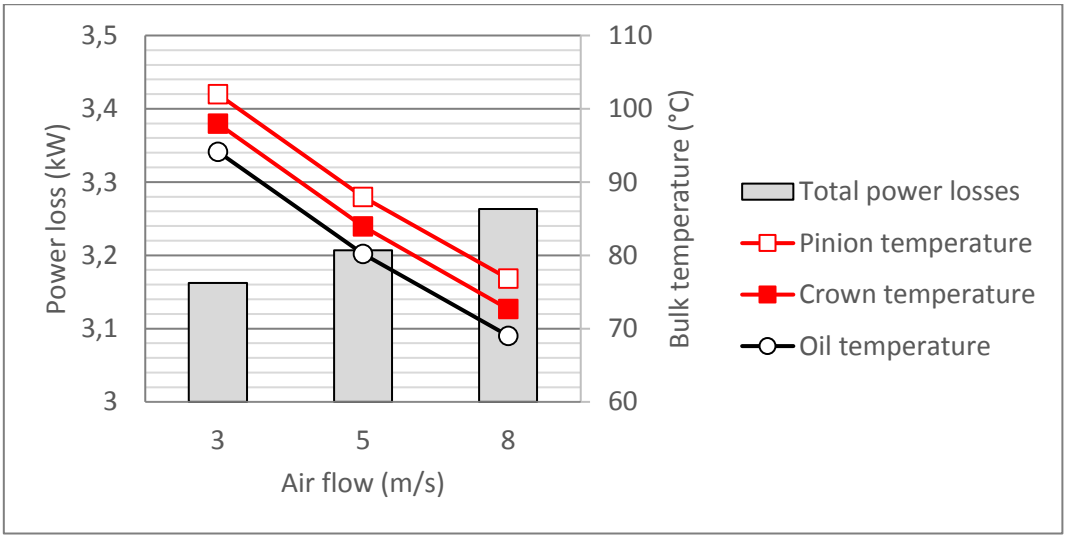

Figure 4.34: Total power losses and oil and gear set temperatures for different air flow speeds

Apart from efficiency aspects, it is important here to notice that more power losses do not always mean higher bulk temperatures. This is right only if thermal exchanges are kept identical.

5. Conclusion

This final chapter presented the development of a thermal model that uses power loss estimations established in previous chapters. This model has two objectives:

1. To be able to determine bulk temperatures of critical parts of the system like gears or bearings for both efficiency and durability concerns.
2. To validate power loss estimations based on temperature measurements. It has already been shown that oil temperature is not sufficient to confirm the power loss breakdown.

Several ISO technical reports propose formulae to address these goals. ISO/TR 14179-2 [9] uses an isothermal approach to consider thermal exchanges between axle and its surrounding environment. Oil operating temperature is calculated but it appears that radiation and convection with air are overestimated, as already reported in the literature [61]. ISO/TR 13989-2 [35] gives a formula to determine gear bulk temperature, based on oil operating temperature. This considers an identical bulk temperature for both meshing gears. However, pinion and crown can have different bulk temperatures due to their respective size and rotational speed. It will then be interesting to compare the aforementioned results to the thermal network method.

Most of the authors consider the axle as isothermal in their model, but it was underlined in the literature that it is not the case [3]. To take into account bulk temperatures of individual axle components, a thermo-mechanical model is developed, based on the thermal network method. The different components of the axle are considered as isothermal nodes of a network and linked by thermal resistances. Resistances manage various heat flows like conduction, convection with air or oil, radiation, and striction. Heat generated by dissipation sources is injected at the corresponding node. Temperatures and power losses are then calculated thanks to an algorithm. Several operating conditions can be applied to the system and steady state or transient results can be obtained.

A comparison is done between thermal network and ISO technical report methods. Thermal network shows more coherent results for thermal exchanges and allows to distinguish pinion and crown gear bulk temperatures.

To validate both bulk temperature estimations and power loss breakdown, a specific test campaign has been done. An axle was monitored with many temperature sensors located on components like rolling element bearings and housing. Different operating conditions were tested in order to characterise thermal exchanges and power dissipation: loaded and unloaded running phases, but also cooling phases. Results regarding power loss are as expected: it increases with torque and speed, but also with oil level. Concerning temperature, it is confirmed that housing temperature varies between sides and that differential rolling element bearings are colder than the one located on the input shaft. Indeed, due to their lower rotational speed, they generate less power losses.

Test results are then compared to axle thermal model for the different operating conditions: cooling, no-load step and load steps. The model shows a good agreement for both temperatures and power losses. To go further, a second axle with a spiral bevel gear set was tested and modelled: the axle thermal model gives good results as well and can be used as a design tool.

This thermo-mechanical model is now used to investigate various parameters. Their influence on power losses and on bulk temperatures is analysed. Lubricant with lower viscosity provides lower bulk temperature but not necessarily better efficiency. A smoother tooth surface is an advantage for both power losses and bulk temperature. Finally, increasing air flow around axle diminishes bulk temperatures but increases power losses. The opposite is also correct. This last case also underlines that power losses and temperature do not always increase together.

Conclusion

To fulfil customer demands but also government regulations, the truck industry must decrease fuel consumption and emissions of its products. Improvement of the powertrain efficiency is then a key development. The axle is the final part of the truck driveline and can still be improved. Indeed, optimisation of axles at design stage is mostly considered regarding durability and noise aspects.

Focus is now expanding to include efficiency: this study aims to characterise the efficiency of truck axles through a thermo-mechanical model. This model is developed to estimate both power losses and thermal exchanges. A global approach is used to consider the complete system and to allow a fast increment in order to use it at design stage. However, a local approach is also investigated to evaluate meshing friction of the gear set.

The first chapter describes the truck drive axle and its gear set: a hypoid or a spiral bevel one (without offset). As most of the previous studies are on automotive axles, the differences with truck axles are presented, like dimensions (crown gear size, oil volume) and operating conditions (speed, torque). This influences power losses but efficiency stays comparable. The literature investigates axle efficiency through experimental means first and then through theoretical methods. Influential parameters are highlighted: operating conditions, such as lubricant temperature, rotational speed, load…; gear macro-geometry parameters, like hypoid offset, spiral angle, face width, diameter, ease-off… and gear micro-geometry parameters, like surface roughness. The power loss sources of the axle are identified: shaft seal friction, rolling element bearing drag and friction, oil churning and gear mesh friction. For each

source, power loss models exist but do not always agree with each other. Depending on application and operating conditions, great discrepancies can be observed between estimations. The thermal behaviour of the axle was investigated thanks to isothermal approaches and mainly for efficiency purposes. Models consider the axle at oil sump temperature. However, it has been shown experimentally that noticeable temperature differences exist between components [3]. Cooling and durability issues must be kept in mind: local hot spots can be created and induce failure of gears and rolling element bearings. As temperature influences lubricant viscosity, this can also modify power losses generated by each component. Moreover, knowing local temperatures allows to validate the estimation of component power losses. Indeed, different power loss breakdown can match to the same global power loss of the axle. A measurement of global power loss and of oil temperature is then not sufficient to validate the results of an efficiency model.

The second chapter attempts to estimate the efficiency of truck axle. Tests are performed to measure global power losses of an axle for loaded and unloaded conditions. This allows the evaluation of load-dependent and load-independent losses. Calculations are then conducted for each source of power loss according to the different formulae reviewed in the literature and a method is selected. For shaft seal friction, the formula of Simrit is kept. For Rolling Element Bearings losses, it appears that SKF formula overestimates the losses under load; more coherent results are obtained with Harris formula, which is then used. For hypoid gear mesh friction, the estimation according to the ISO/TR 14179-2 gives a good trend, but a more thorough study is required to improve it. For the oil churning, both Mauz and Jeon solutions gives unrealistic results. Investigations are then conducted on the churning losses of spiral bevel gears: a specific test bench is used with several spiral bevel gears and cones. Experiments are done with different oils and operating conditions. The results highlight the influence of some operating conditions like speed, immersion ratio and oil viscosity, but also of a main gear geometrical parameter which is the outer diameter. By contrast, it appears that gear teeth have little influence on churning losses. A comparison between test results and Mauz and Jeon models shows discrepancies. Based on Jeon formula who has worked on axles too, a new model is proposed to better take into account the identified influential parameters. This also considers two different regimes depending on Reynolds number and the greater contribution due to the meshing gear pair. Thanks to this new formula, the power loss estimation for the truck axle case has a better agreement with test results. For example, the influence of oil level on losses is correctly taken into account. Finally, gear mesh friction contributes a lot to losses for truck operating cases (80°C), while rolling element bearings are the first dissipation source for lower operating temperature (40°C).

As gear mesh friction appears to be a major source of dissipation for truck axles, it is thoroughly investigated in the third chapter. Indeed, spiral bevel and hypoid gears are particular. Their manufacturing process is reviewed from cutting process to surface finishing. Indeed, design choices and manufacturing determine geometrical parameters. A model developed by Barday [22] allows to take most of them into account. During gear mesh, elliptical contacts occur successively along contact path. For modelling purposes, each successive contact is discretised in several line contacts: contact conditions (load, velocities, surface curvature…) are calculated thanks to Barday software. Due to conical shape and spiral angle, the kinematic of spiral bevel and hypoid gears is different from other gears: surface velocities are not oriented along the axis of contact ellipse and they are not aligned together. Angles are defined to characterise the orientation of velocities. Moreover, entrainment velocity varies along y-axis of contact ellipse and induces a global rotation of the contact. For hypoid

gears, sliding is not only transverse, as a longitudinal sliding also exists due to offset. The power loss of gear mesh is now studied with a local approach based on data from Barday software. Contact conditions and power loss along contact path are analysed. Two gear sets are compared, a hypoid and a spiral bevel one: the permanent sliding is observed on the hypoid gear, while a decrease is observed around pitch point on spiral bevel gear. A comparison is made between local approach and ISO global approach to discuss the validity of ISO technical report approximation. Global approach always overestimates the power loss, due to sliding velocity estimation: indeed, sliding velocity varies a lot along a line of contact and local approach considers the sliding only on the contacting part of the line. For higher loads, a better agreement is then expected, as contact pattern is more spread. In our case, ISO estimation obtains more coherent results for the hypoid gear than the spiral bevel one. Finally, local approach is more accurate to evaluate gear mesh power loss and gives acceptable results with a global friction coefficient calculated according to ISO technical report. However, local approach offers the possibility to use local friction coefficients: as friction coefficient influences heavily the friction loss of the gear mesh, this can be more precise. Formulae to calculate friction coefficient are based on similar parameters: load, entrainment and sliding velocities, oil viscosity, and surface roughness. In the case of hypoid gears, two specific parameters are selected: surface roughness and velocities defined by orientation angles. Surface roughness depends mainly on cutting process and on surface finishing. It is characterised by an overall roughness but also by machining grooves orientation. Friction coefficients are calculated for various overall roughness according to reviewed formulae: a decrease of friction coefficient, and so of gear mesh power losses, is observed for smoother surfaces. Orientation angles have been studied only regarding elastohydrodynamic aspects. Friction was considered for a close phenomenon: the contact between rib roller-end and flange in some rolling element bearings. Preliminary tests are performed to evaluate the influence of orientation angle: friction coefficient can be doubled for low surface velocity. This induces a great increase of gear mesh power losses too.

Finally, the fourth chapter presents the thermal model of the axle, based on the thermal network method. The different components of the axle are considered as isothermal nodes of a network and linked by thermal resistances that manage various heat flows (conduction, convection with air or oil, radiation). Power losses are estimated according to formulae established in the previous chapters and the heat generated is injected at the node corresponding to the dissipation source. Temperatures and power losses are then calculated thanks to an algorithm. Several operating conditions can be applied to the system and steady state or transient results can be obtained. A comparison is done between thermal network and ISO technical report methods. ISO/TR 14179-2 [9] overestimates the thermal exchanges between axle and its surrounding, as already reported in the literature [61]. Thermal network method obtains more coherent results. ISO/TR 13989-2 [35] gives a formula to determine gear bulk temperature, which considers an identical bulk temperature for both meshing gears. However, the thermal network method presents different bulk temperatures for pinion and crown. This can be explained by their respective size and rotational speed. A specific test campaign is conducted to validate the thermo-mechanical model of the axle. An axle was monitored with many temperature sensors located on components like rolling element bearings and housing. Different operating conditions were tested in order to characterise thermal exchanges and power dissipation: loaded and unloaded running phases, but also cooling phases. Results regarding power loss are as expected: it increases with torque and speed, but also with oil level. Concerning temperature, it is

confirmed that housing temperature varies between sides and that differential rolling element bearings are colder than the one located on the input shaft. Indeed, due to their lower rotational speed, they generate less power losses. The thermal model shows good agreement with test results for the different operating conditions (cooling, no-load and load steps): calculated temperatures and power losses are representative. This is also validated with another design of axle with a spiral bevel gear set. The axle thermal model can then be used as a design tool. The influence of some parameters on power losses and on bulk temperatures is analysed. Lubricant with lower viscosity provides lower bulk temperature but not necessarily better efficiency. A smoother tooth surface is an advantage for both power losses and bulk temperature. Finally, increasing air flow around axle diminishes bulk temperatures but increases power losses. The opposite is also correct. This last case underlines also the fact that power losses and temperature do not always increase together.

The thermo-mechanical model of truck axles developed in this study allows to obtain both efficiency and temperature distribution. Regarding industrial application for the Volvo Group, this tool can be used at design stage to:

- Optimise efficiency of the axle. By combining it with software already used at Volvo Group, optimisation can be done regarding durability and noise as well.
- Investigate on failure issues due to local hot spots on rolling element bearings or gears.

In parallel with this work, a model was also established for planetary gears [36]. Coupling it with the axle model could be considered to study hub reduction axles.

Besides model exploitation, some experimental results on complete axles must still be analysed. Indeed, two additional axles were tested during the thermal tests in order to investigate different parameters: one has a face-milled gear set and the other has a lower ratio. Two gear cutting methods (face-hobbing and face-milling) could then be compared on the axle with a hypoid gear set. Another comparison could also be done between two axle ratio (4.625 and 2.643) on the axle with a spiral bevel gear set. Test results are important to validate the consistency of the thermo-mechanical model regarding specific parameters.

The complexity of the friction in spiral bevel and hypoid gears has been underlined. Indeed, it has been shown that grooves orientation regarding rolling direction has an impact on friction coefficient [26]. On spiral bevel and hypoid gears, this is different from spur gears: it is neither perpendicular nor parallel. Moreover, pinion and crown gear appear to have different surface roughness and this can influence friction. Tests must be done to characterise friction coefficient for these particular surfaces, on a twin disc machine for example [26]. Various surface finishing could also be tested.

However, on twin disc machine, rolling direction is the same for both discs, while this is not the case for spiral bevel and hypoid gears. This specific configuration is reproduced on some test benches ([29], [30]), but only film thickness is studied. Preliminary tests presented in Chapter 3 show an influence of orientation angle on friction coefficient. It would be interesting to go further, by characterising more precisely the impact on friction coefficient. Moreover, preliminary tests were done on smooth test samples only. Test samples with rough surface can be manufactured and used to conduct a procedure

similar to the one used on twin disc machine. This would allow for a better characterisation of the contact of hypoid gears.

Another point of interest would be rolling element bearings. They are currently considered as isothermal elements. The model could be made finer by splitting bearings in several parts, to take into account the temperature difference between inner and outer races. This would allow for a more precise study of bearing failure or race expansion.

Annexes

Annex 1.A: Detail of formulae for hypoid gear mesh friction

{a} Buckingham formula

Reference [16]

Hypoid gear efficiency is expressed as:

$$E_{hypoid} = \frac{1}{1 + \phi_{spiral\ bevel} + \phi_{worm}} \tag{1.35}$$

with:

- $\phi_{spiral\ bevel}$: friction loss factor of spiral bevel gear
- ϕ_{worm}: friction loss factor of worm gear

Friction loss factor of spiral bevel gear $\phi_{spiral\ bevel}$:

$$\phi_{spiral\ bevel} = \frac{\cos\phi}{\cos\phi_n + \cos\psi}\left[\frac{1 + \left(\frac{1}{m}\right)}{(\beta_a + \beta_r)\cos\psi}\right]\left(\frac{f_{sb}}{2}\right)\left({\beta_a}^2 + {\beta_r}^2\right) \tag{1.36}$$

with:

- ϕ: pressure angle in plane of rotation of equivalent helical gear (°)
- ϕ_n: normal pressure angle at middle of gear face (°)
- ψ: spiral angle of gear at middle tooth face (°)
- m: gear ratio of equivalent helical gears
- β_a, β_r: arc of approach and recess of equivalent helical gears
- f_{sb}: average coefficient of friction for spiral bevel gear from experiments

Where:

$$\tan\phi = \frac{\tan\phi_n}{\cos\psi} \tag{1.37}$$

f_{sb} is determined from a table based on an average sliding velocity V_s'(ft/min):

$$V_s' = V\cos\phi\left(1 + \frac{R_{vp}}{R_{vg}}\right)\left(\frac{\beta_a + \beta_r}{4}\right) \tag{1.38}$$

Where:

$$R_p = \sqrt{{R'_p}^2 + {R_{hp}}^2} \tag{1.39}$$

$$R_g = \sqrt{{R'_g}^2 + {R_{hg}}^2} \tag{1.40}$$

$$R_{vp} = \frac{R'_p}{\cos \gamma_p} \tag{1.41}$$

$$R_{vg} = \frac{R'_g}{\cos \gamma_g} \tag{1.42}$$

$$m = \frac{R_{vg}}{R_{vp}} \tag{1.43}$$

with:

- $R_{p,g}$: pitch radius of hypoid pinion and gear at large ends (in.)
- $R'_{p,g}$: pitch radius of equivalent bevel pinion and gear (in.)
- $R_{hp,hg}$: radius of base cylinder of pinion and gear hypoid (in.)
- $R_{vp,vg}$: pitch radius of equivalent helical pinion and gear (in.)
- $\gamma_{p,g}$: generatrix angle of pinion and gear hypoid

And V is the pitch-line velocity (ft/min):

$$V = 0.5236 \times R_m \, n \tag{1.44}$$

with:

- R_m: mean pitch radius of hypoid pinion (in.)
- n: rpm of driving pinion (rpm)

Friction loss factor of worm gear ϕ_{worm}:

$$\phi_{worm\ gear} = \frac{2 \times f_w}{\cos \phi_n \sin 2\gamma_p + 2 \times f_w} \tag{1.45}$$

with:

- f_w: average coefficient of friction for worm gear from experiments
- ϕ_n: normal pressure angle at middle of gear face (°)
- γ_p: angle of generatrix of pinion (°)

f_w is determined from a table based on an average sliding velocity V_s (ft/min):

$$V_s = \frac{0.5236 \times R_{bp} \, n}{\sin \gamma_p} \tag{1.46}$$

with:

- R_{bp}: radius of base cylinder of pinion hypoid (in.)
- n: number of rpm of driving pinion (rpm)

{b} ISO/TR 14179-2

Reference [9]

Hypoid gear mesh power loss is defined as:

$$P_{hypoid} = F_n \, v_{gm} \, \mu_m \tag{1.47}$$

with:

- F_n: tooth normal load (N)
- v_{gm}: mean sliding speed (m/s)
- μ_m: mean friction coefficient

The following indices stand for:

- 1: pinion
- 2: crown gear

An equivalent helical gear substitutes for the hypoid one for gear mesh calculation. Specifically for hypoid gears, the ISO Technical Report defines:

Mean sliding speed v_{gm}:

$$v_{gm} = v_{gs} + \frac{\left(v_{g\gamma 1} - v_{gs}\right)^2 + \left(v_{g\gamma 2} - v_{gs}\right)^2}{2\left(v_{g\gamma 1} + v_{g\gamma 2} - 2 \times v_{gs}\right)} \tag{1.48}$$

with:

- v_{gs}: helical speed (m/s)
- $v_{g\gamma 1,2}$: total surface speed at tooth tip (m/s)

Mean friction coefficient μ_m:

$$\mu_m = 0.048 \left(\frac{F_n \cos \beta_{b2} / (0.85 \times b_2)}{v_{\Sigma m} \, R_{eq,n}} \right)^{0.2} \eta_{oil}{}^{-0.05} \, Ra^{0.25} \, X_L \tag{1.49}$$

with:

- β_{b2}: helix angle at base circle (°)
- b_2: tooth width (mm)
- $v_{\Sigma m}$: mean resultant sum velocity (m/s)
- $R_{eq,n}$: equivalent radius of curvature, normal section (mm)
- η_{oil}: dynamic viscosity of oil at operating temperature (mPa.s)
- X_L: oil lubricant factor
  - $X_L = 1.0$ for mineral oils;
  - $X_L = 0.8$ for polyalfaolefins and esters;
  - $X_L = 0.75 \, (6 \backslash v_{\Sigma m})^{0.2}$ for polyglycols;
  - $X_L = 1.3$ for phosphoric esters;
  - $X_L = 1.5$ for traction fluids;

$$Ra = 0.5\ (Ra_1 + Ra_2) \tag{1.50}$$

with:

- $Ra_{1,2}$: arithmetic average roughness

$$v_{\Sigma m} = \sqrt{{v_{\Sigma s}}^2 + {v_{\Sigma h}}^2} \tag{1.51}$$

with:

- $v_{\Sigma s}$: sum velocity in direction of tooth length (m/s)
- $v_{\Sigma h}$: sum velocity in direction of tooth depth (m/s)

$$v_{\Sigma s} = v_{t1}\left(\sin\beta_{m1} + \sin\beta_{m2}\frac{\cos\beta_{m1}}{\cos\beta_{m2}}\right) \tag{1.52}$$

$$v_{\Sigma h} = 2 \times v_{t1}\cos\beta_{m1}\sin\alpha_n \tag{1.53}$$

with:

- $\beta_{m1,2}$: helix angle at medium circle (°)
- v_{t1}: peripheral speed at pitch circle (m/s)
- α_n: normal pressure angle (°)

Annex 2.A: Experimental results on oil churning test rig

Table 0.1: Tested gears characteristics

	Gear 1	Gear 2	Gear 3	Gear 4	Cone 1	Cone 2
Number of teeth	41	37	41	37	/	/
Outer diameter (mm)	157	130	188	154	157	160
Width (mm)	22	27	30	30	22	27
Face width (mm)	27	24,5	32	27,5	27	24,5
Face angle (°)	72.4	58.1	72.4	58.1	72.4	58.1
Pressure angle (°)	20	20	20	20	/	/
Spiral angle (°)	35	35	35	35	/	/
Hand of spiral	LH	LH	LH	LH	/	/

Table 0.2: Tested oils characteristics

	Oil A	Oil B	Oil C	Oil D
Kinematic viscosity @ 40°C (cSt)	220	35	45.1	120
Kinematic viscosity @ 100°C (cSt)	19	7.5	7.7	15.9
Density @ 15°C	0.895	0.870	0.885	0.860
Oil type	Mineral	Mineral	Mineral	Synthetic

{a} Tests performed by Laruelle [67]

Various tests were performed by Laruelle on each tested gear and with different oils.

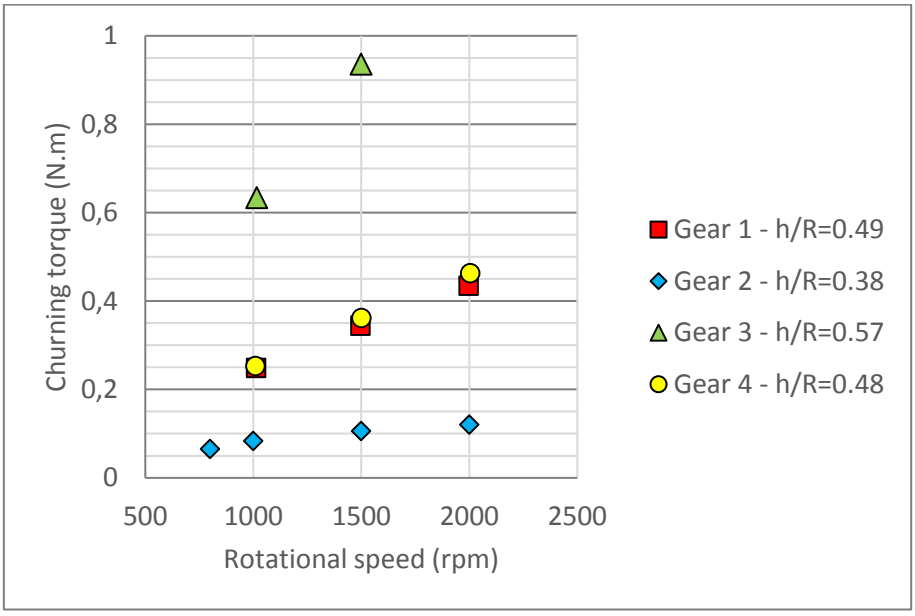

Figure 1: Churning torque depending on rotational speed (oil A, 70°C)

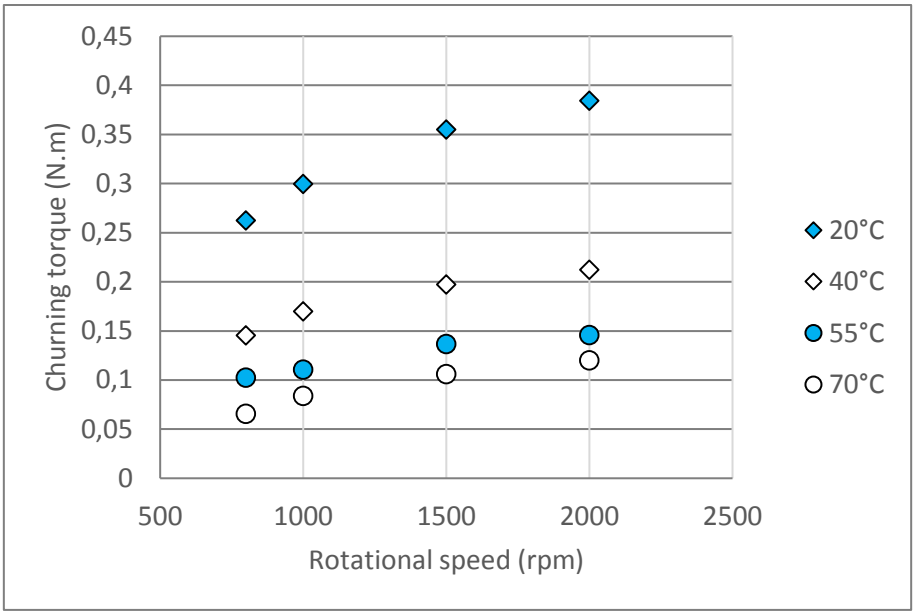

Figure 2: Churning torque depending on rotational speed and oil temperature (Gear 2, oil A, h_{lub}/R_o =0.38)

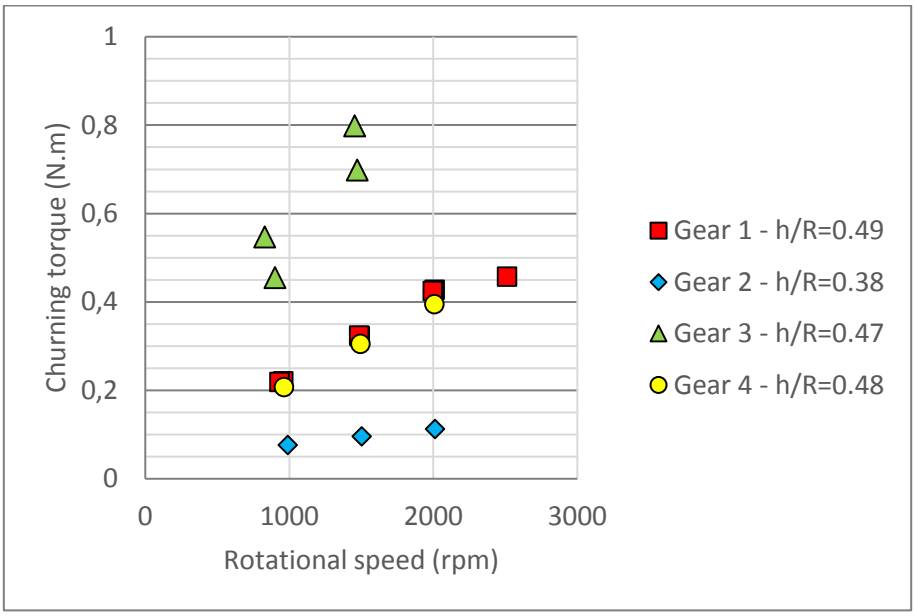

Figure 3: Churning torque depending on rotational speed (oil B, 30°C)

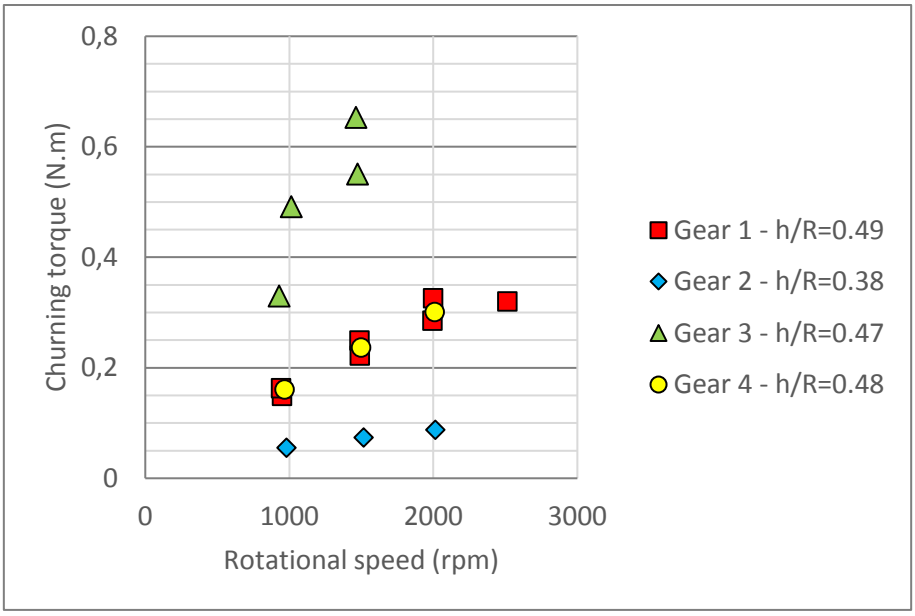

Figure 4: Churning torque depending on rotational speed (oil B, 70°C)

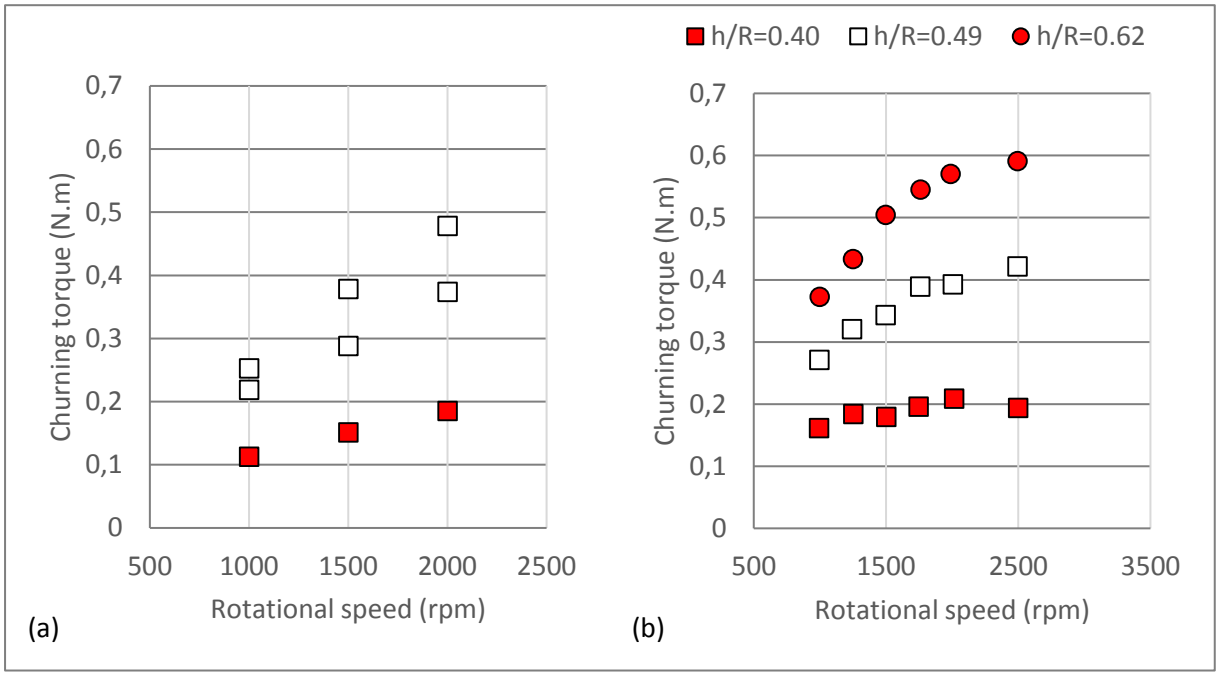

Figure 5: Churning torque depending on rotational speed and immersion (Gear 1, (a) oil C and (b) oil D, 40°C)

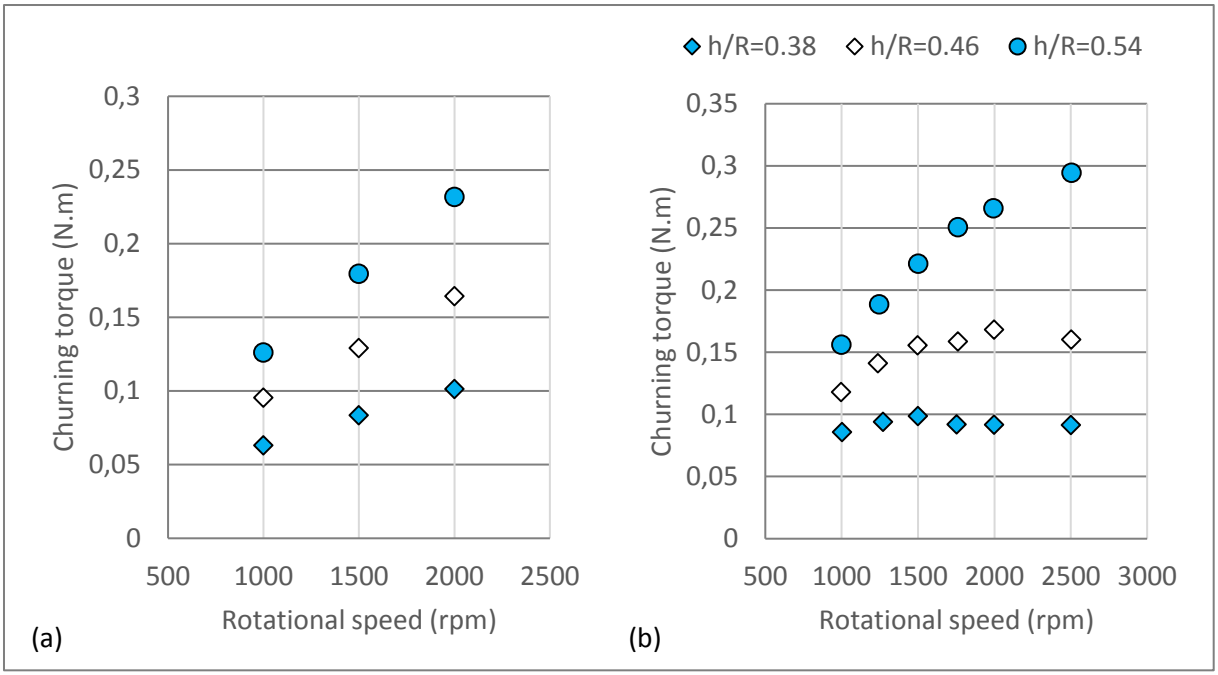

Figure 6: Churning torque depending on rotational speed and immersion (Gear 2, (a) oil C and (b) oil D, 40°C)

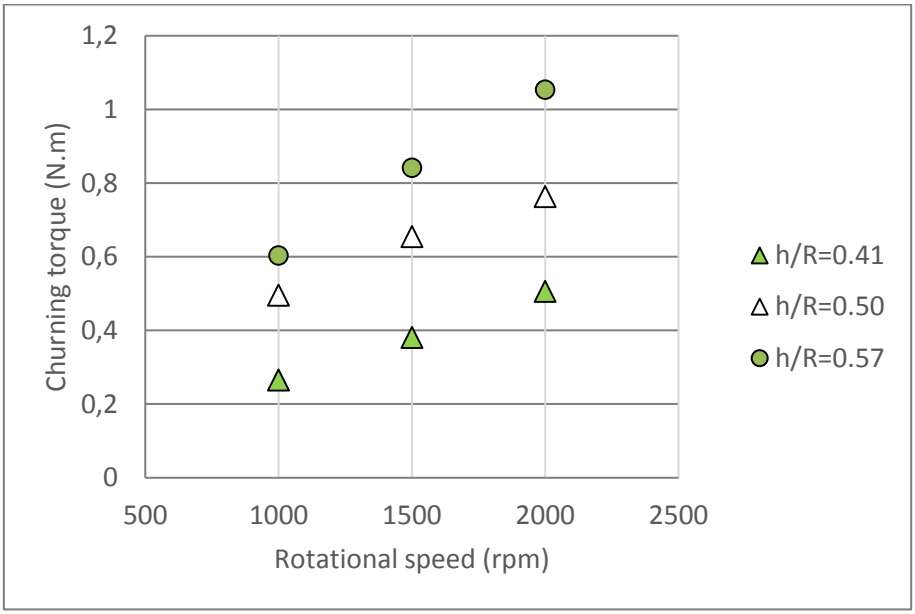

Figure 7: Churning torque depending on rotational speed and immersion (Gear 3, oil C, 40°C)

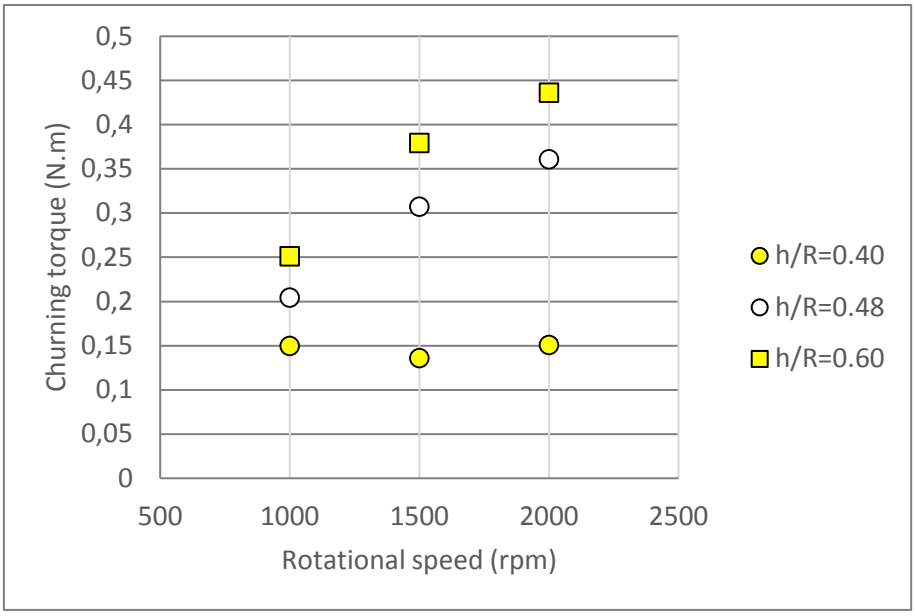

Figure 8: Churning torque depending on rotational speed and immersion (Gear 4, oil C, 40°C)

{b} Complementary tests on gear 3 and oil D

Due to its size and immersion, crown gear generates more losses than pinion gear. According to Table 2.8, gear 3 experiences similar peripheral speeds to that of crown gear. Moreover it is almost half of the crown gear size and has close geometrical characteristics. More tests are then conducted on this gear with oil D to cover the truck application.

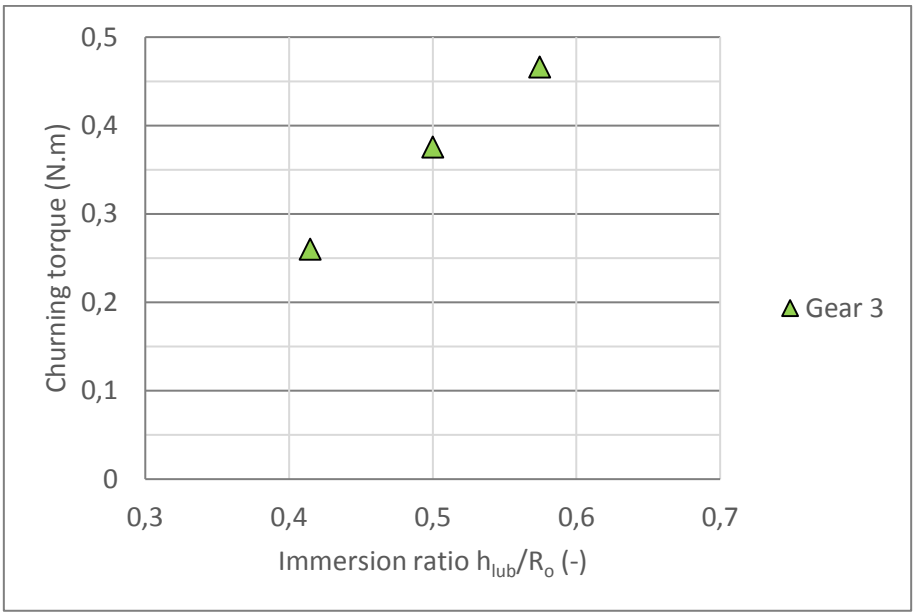

Figure 9: Churning torque depending on immersion ratio (Gear 3, oil B, 40°C, 1000 rpm)

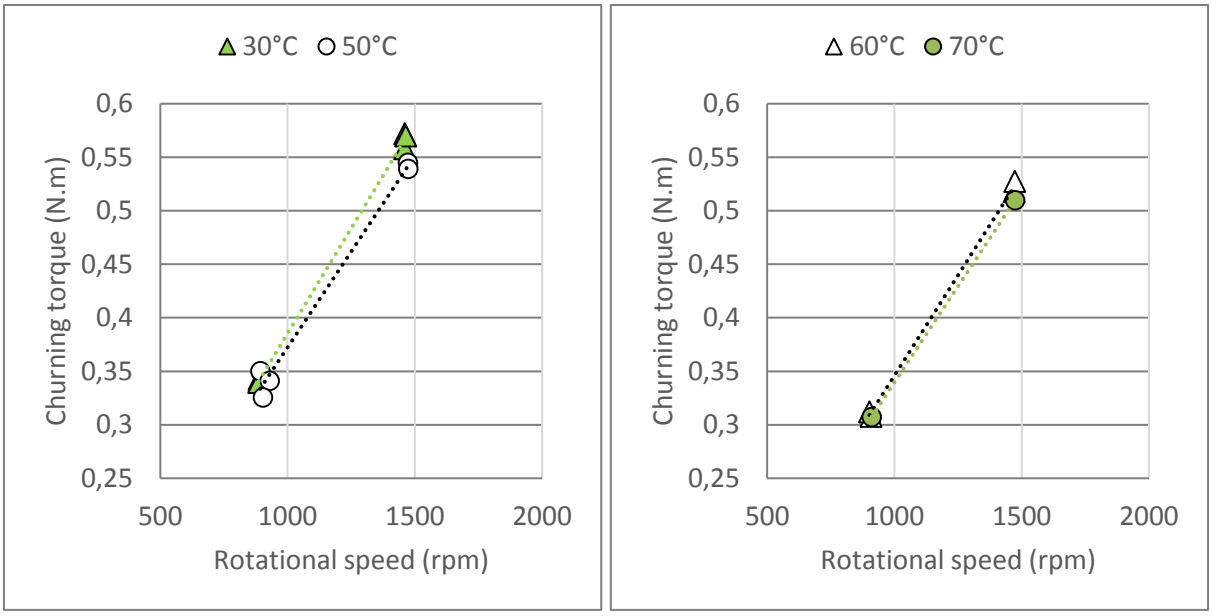

Figure 10: Churning torque depending on rotational speed and oil temperature (Gear 3, oil B, h_{lub}/R_o =0.47)

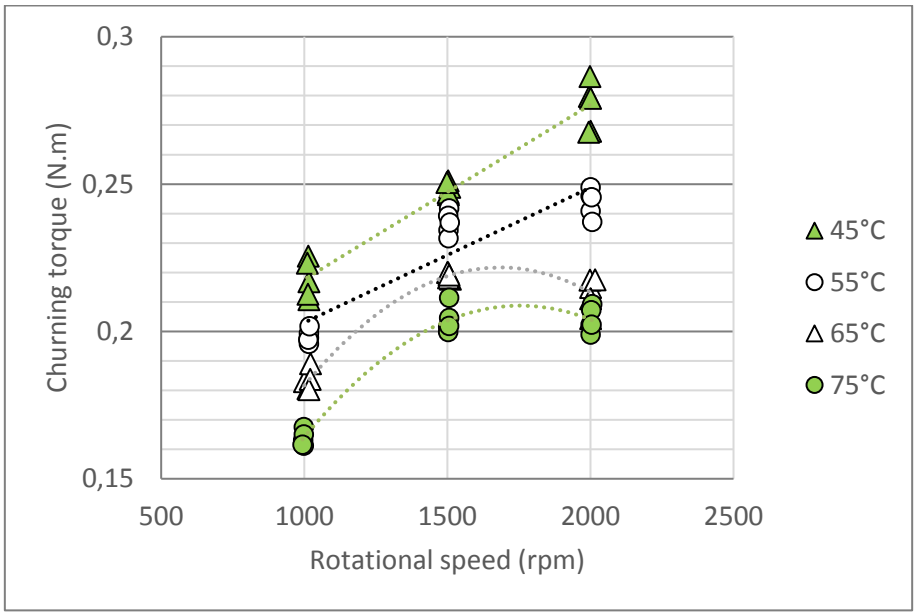

Figure 11: Churning torque depending on rotational speed and oil temperature (Gear 3, oil D, h_{lub}/R_o =0.36)

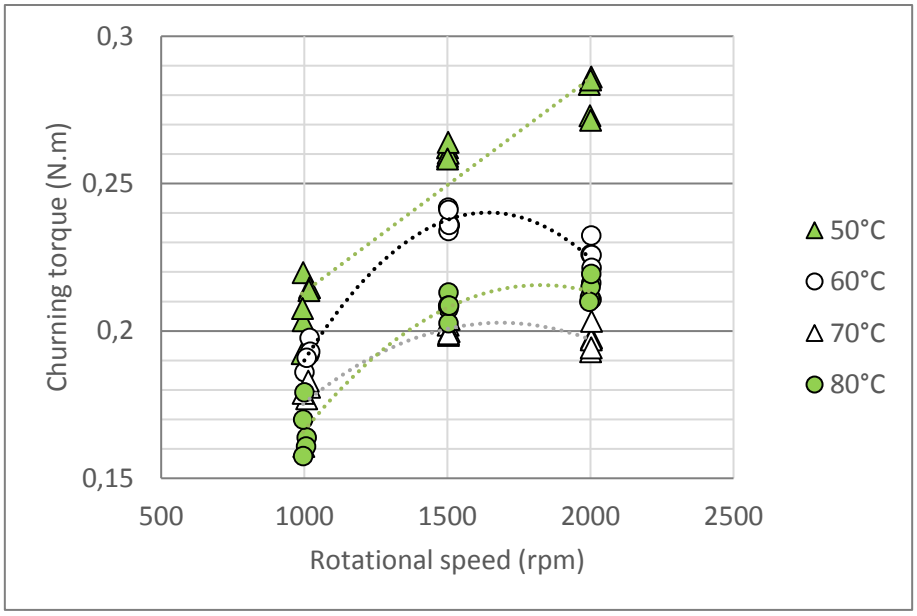

Figure 12: Churning torque depending on rotational speed and oil temperature (Gear 3, oil D, h_{lub}/R_o =0.36)

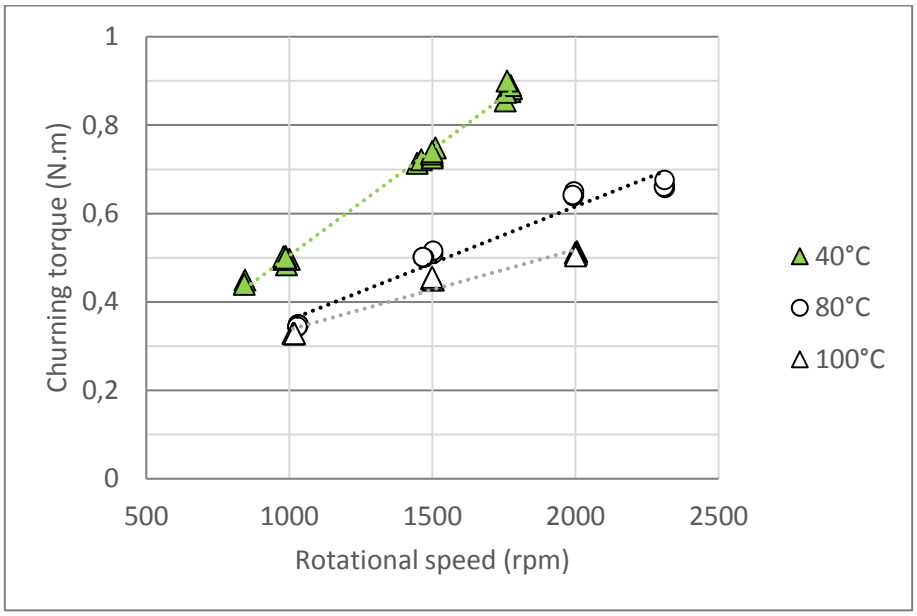

Figure 13: Churning torque depending on rotational speed and oil temperature (Gear 3, oil D, h_{lub}/R_o =0.47)

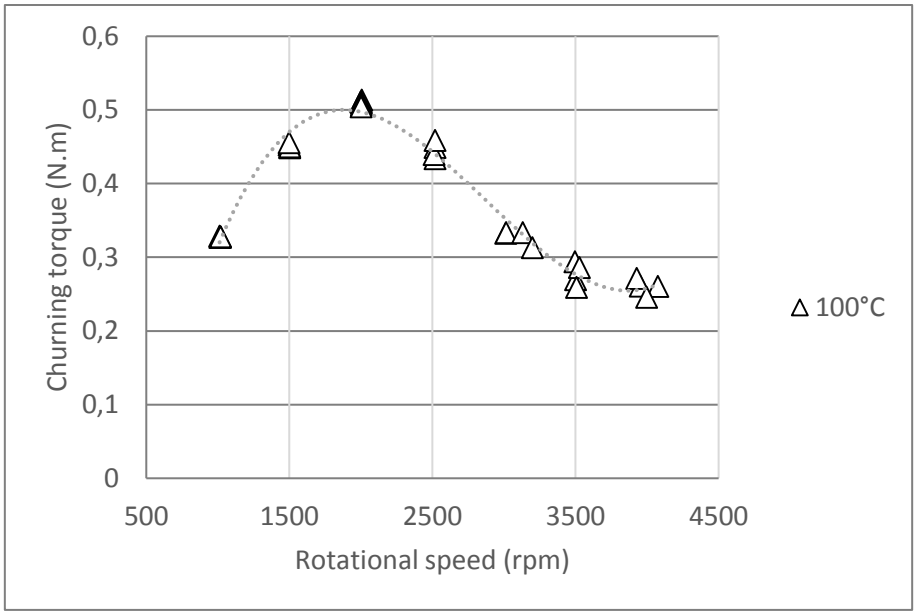

Figure 14: Churning torque decreases at high speed (Gear 3, oil D, h_{lub}/R_o =0.47)

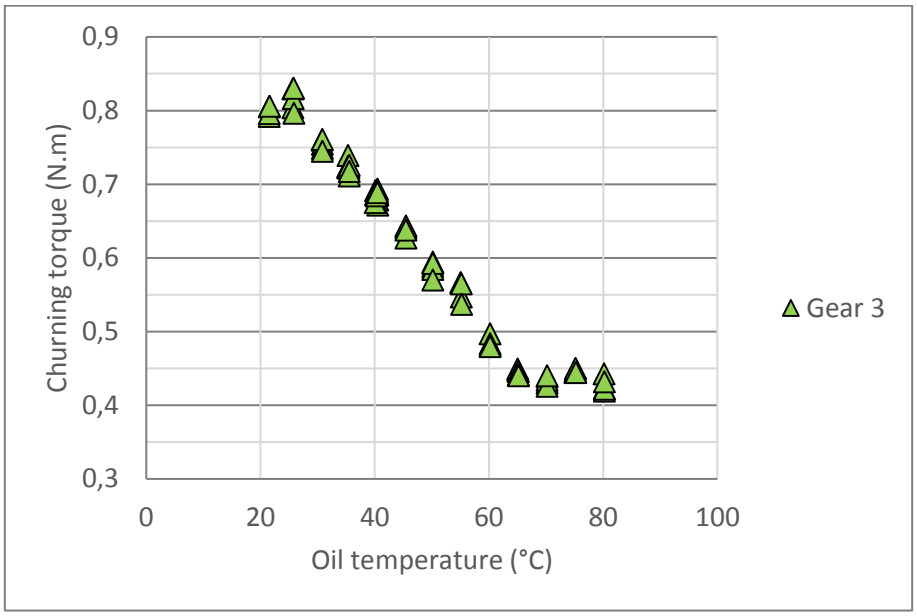

Figure 15: Churning torque depending on oil temperature (Gear 3, oil D, h_{lub}/R_o =0.57, 1000 rpm)

{c} Tests with a deflector

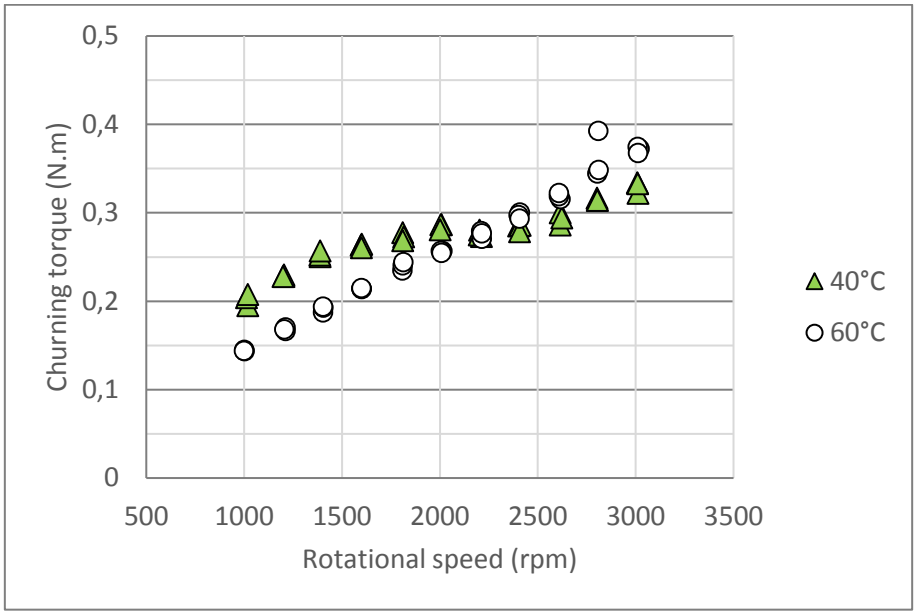

Figure 16: Churning torque depending on rotational speed and oil temperature (Gear 1, oil D, h_{lub}/R_o =0.49, with deflector)

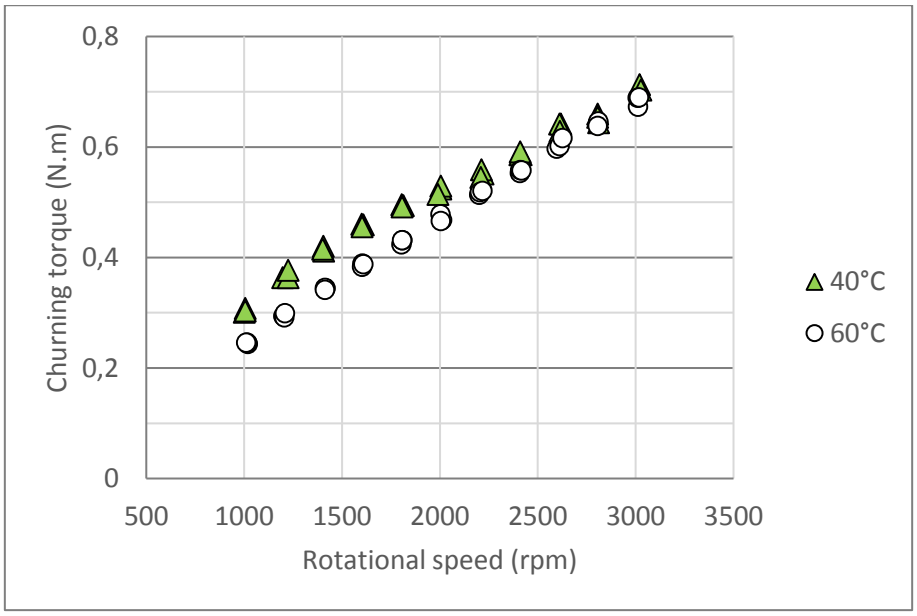

Figure 17: Churning torque depending on rotational speed and oil temperature (Gear 1, oil D, h_{lub}/R_o =0.62, with deflector)

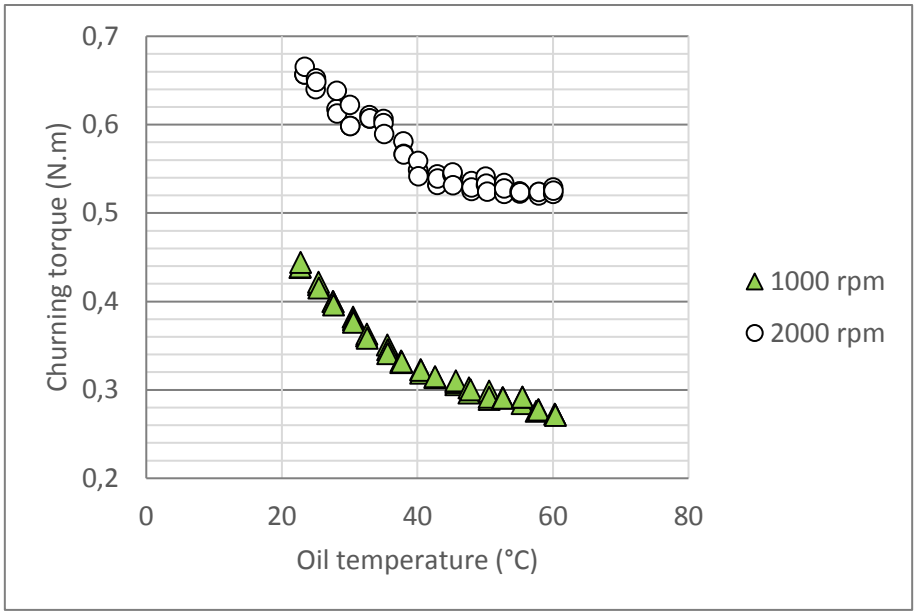

Figure 18: Churning torque depending on oil temperature and rotational speed (Gear 1, oil D, h_{lub}/R_o =0.62, with deflector)

Annex 2.B: Calculation of immersed surface area

The immersed areas of a bevel gear are identified on Figure 19. To simplify the problem, two areas are isolated: the front and back areas {a} highlighted with dots, the peripheral area {b} highlighted with stripes.

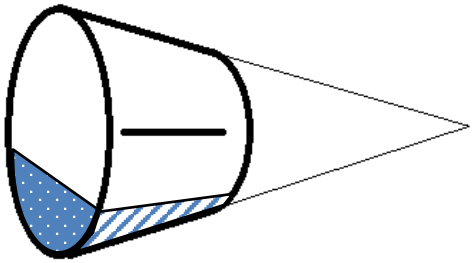

Figure 19: Scheme from the back side of the pinion (tooth not represented) with the cone angle

{a} Front and back areas

The areas are computed as follows for the front and back side of the gear. Some useful geometrical parameters are illustrated on Figure 20.

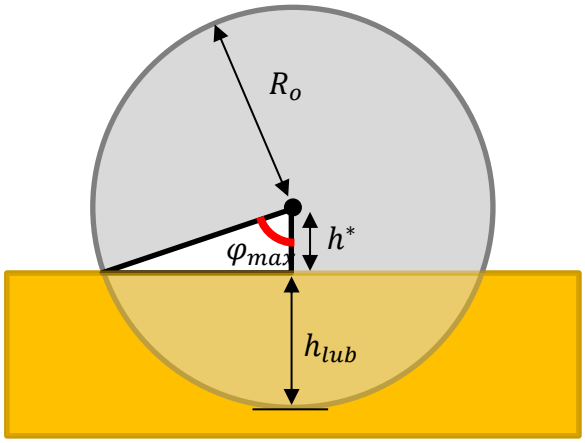

Figure 20: Definition of geometrical parameters

- R_o: gear outer radius (m)
- φ_{max}: immersion angle of back side (rad)
- φ_{max2}: immersion angle of front side (rad)
- h^*: dry level (m)
- h_{lub}: immersion depth of gear (m)

h^* is defined as a constant value computed from back end of gear:

$$h^* = R_o - h_{lub} \tag{2.13}$$

Immersion angles φ_{max} and φ_{max2} are defined as:

$$\cos \varphi_{max} = \frac{h^*}{R_o} \tag{2.14}$$

$$\cos \varphi_{max2} = \frac{h^*}{e_o} \tag{2.15}$$

with:

- e_o: radius of the front side of the truncated cone associated to the cone of base radius R_o (m)

Then, the back side area $A1$ (m²) is:

$$A1 = \frac{1}{2} {R_o}^2 (2\,\varphi_{max} - \sin(2\,\varphi_{max})) \tag{2.16}$$

For the front side $A2$ (m²), it is:

$$A2 = \frac{1}{2} e_o^2 (2\,\varphi_{max2} - \sin(2\,\varphi_{max2})) \tag{2.17}$$

{b} Peripheral area

It represents the area of the side face of the truncated cone which is immersed in the lubricant sump. Figure 21 represents the main parameters for this area.

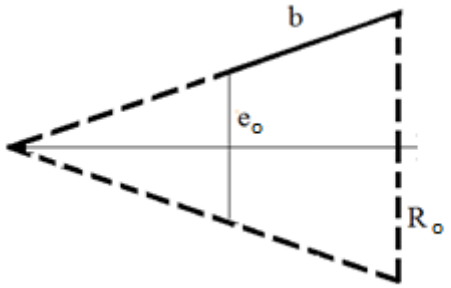

Figure 21: Main parameters of peripheral area

Finally, the peripheral area $A3$ (m²) can be approximated by:

$$A_3 = (\varphi_{max}\, R_o + \varphi_{max2}\, e_o)\, b \tag{2.18}$$

with:

- b: tooth width (m)

Annex 3.A: Hertzian contacts

An equivalent geometry is generally used for Hertzian contacts: gear teeth are reduced to two parabolical bodies. Each have radii of curvature in two directions, generally x and y axis. The pressure distribution in such contact depends only on gap height between surfaces. Thus the body 2 can be considered as plane in a particular direction if an equivalent radius of curvature is defined for the body 1 in the same direction:

$$\frac{1}{R_d} = \frac{1}{R_{d1}} + \frac{1}{R_{d2}} \tag{3.12}$$

with:

- R_{d1}, R_{d2}: curvature radius in direction d of body 1 or 2

An equivalent elastic modulus E' (Pa) is also defined:

$$\frac{1}{E'} = \frac{1}{2}\left(\frac{1-{\nu_1}^2}{E_1} + \frac{1-{\nu_2}^2}{E_2}\right) \tag{3.13}$$

with:

- ν_1, ν_2: Poisson ratio of body 1 or 2
- E_1, E_2: elastic modulus of body 1 or 2 (Pa)

Then, characteristics of Hertzian contacts can be calculated according to the following formulae.

{a} Line contact

Maximum Hertz pressure p_h (Pa) is:

$$p_h = \frac{2\,w_1}{\pi\,b_c} \tag{3.14}$$

with:

- w_1: load per unit width (N/m)
- b_c: half-width of the contact (m)

$$b_c = \sqrt{\frac{8\,w_1\,R}{\pi\,E'}} \tag{3.15}$$

with :

- R: equivalent radius of curvature (m)

{b} Elliptical contact

Maximum Hertz pressure p_h (Pa) is:

$$p_h = \frac{3\,w}{2\,\pi\,a\,b_c} \tag{3.16}$$

with:

- w: load per unit width (N/m)
- a: half-width of the contact (m)
- b_c: half-width of the contact (m)

$$b_c = \sqrt[3]{\frac{6\,k^2\,\varepsilon\,w\,\bar{R}}{\pi\,E'}} \tag{3.17}$$

$$a = \frac{b_c}{k} = \sqrt[3]{\frac{6\;\varepsilon\,w\,\bar{R}}{\pi\,k\,E'}} \tag{3.18}$$

with :

- k: ratio of contact semi-axes
- ε: elliptical integral
- $\bar{R}$: equivalent radius of curvature (m)

$$k = {}^{b}/_{a} \tag{3.19}$$

$$\frac{1}{\bar{R}} = \frac{1}{R_x} + \frac{1}{R_y} \tag{3.20}$$

with :

- R_x: equivalent radius of curvature in direction x (m)
- R_y: equivalent radius of curvature in direction y (m)

Annex 3.B: Detail of friction coefficient formulae

{a} ISO/TR 14179-2

Reference [9]

$$\mu_m = 0.048 \left(\frac{F/b}{v_\Sigma \, R_{eq}} \right)^{0.2} {\eta_{oil}}^{-0.05} \, Ra^{0.25} \, X_L \tag{3.21}$$

with:

- F: tooth normal force (N)
- b: tooth width (mm)
- v_Σ: resultant sum velocity (m/s)
- R_{eq}: equivalent radius of curvature (mm)
- η_{oil}: lubricant dynamic viscosity at operating temperature (mPa.s)
- Ra: arithmetic average roughness (µm)
- X_L: oil lubricant factor
  - $X_L = 1.0$ for mineral oils;
  - $X_L = 0.8$ for polyalfaolefins and esters;
  - $X_L = 0.75 \, (6 \backslash v_{\Sigma m})^{0.2}$ for polyglycols;
  - $X_L = 1.3$ for phosphoric esters;
  - $X_L = 1.5$ for traction fluids;

$$Ra = 0.5 \, (Ra_1 + Ra_2) \tag{3.22}$$

with:

- $Ra_{1,2}$: arithmetic average roughness (µm)

For hypoid gears geometry, an equivalent helical gear is used. Specific formulae are defined:

$$F = F_n \cos \beta_{b2} \tag{3.23}$$

$$b = 0.85 \times b_2 \tag{3.24}$$

$$v_\Sigma = v_{\Sigma m} = \sqrt{{v_{\Sigma s}}^2 + {v_{\Sigma h}}^2} \tag{3.25}$$

$$\rho = \rho_n \tag{3.26}$$

with:

- F_n: tooth normal force, normal section (N)
- β_{b2}: helix angle at base circle (°)
- b_2: crown gear tooth width (mm)
- $v_{\Sigma m}$: mean resultant sum velocity (m/s)
- $v_{\Sigma s}$: sum velocity in direction of tooth length (m/s)
- $v_{\Sigma h}$ the sum velocity in direction of tooth depth (m/s)
- ρ_n: equivalent radius of curvature, normal section (mm)

$$v_{\Sigma s} = v_{t1}\left(\sin\beta_{m1} + \sin\beta_{m2}\frac{\cos\beta_{m1}}{\cos\beta_{m2}}\right) \quad (3.27)$$

$$v_{\Sigma h} = 2 \times v_{t1}\cos\beta_{m1}\sin\alpha_n \quad (3.28)$$

with:

- $\beta_{m1,2}$: helix angle at medium circle (°)
- v_{t1}: peripheral speed at pitch circle (m/s)
- α_n: normal pressure angle (°)

{b} Diab formula

Reference [26]

$$\mu = \frac{1}{p_{moy}}\left[\frac{A_c}{A_0}\cdot\tau_{dry} + \left(1 - \frac{A_c}{A_0}\right)\cdot\tau_{fluid}\right] \quad (3.29)$$

with:

- $p_{moy} = {}^{W}/_{A_0}$: mean contact pressure (Pa)
- A_c: actual average contact area (m²)
- A_0: apparent contact area (m²)
- τ_{dry}: shear stress due to dry friction (Pa)
- τ_{fluid}: shear stress due to fluid friction (Pa)
- W: total load on the contact (N)

Area ratio ${}^{A_c}/_{A_0}$:

$$\frac{A_c}{A_0} = \frac{1}{2}\left[\frac{1}{2}\left(1 - \mathrm{erf}\left(\frac{\phi_T \cdot h_c}{\sqrt{2\cdot m_0}}\right)\right)\right] \quad (3.30)$$

with:

- ϕ_T: thermal correction factor [Gupta et al., 1992]
- h_c: central lubricant film thickness (m)
- m_0: average square value of the height of roughness (corresponds to rms²) (m²)

Dry friction shear stress τ_{dry}:

$$\tau_{dry} = \frac{W_{dry}}{A_c}\cdot cf_{dry}\cdot\left[1 - \exp\left(\frac{1}{S_{crit}}\cdot\frac{\Delta U}{U}\right)\right] \quad (3.31)$$

$$\frac{W_{dry}}{A_c} = 0.1\cdot E'\sqrt{\frac{m_2}{\pi}} \quad (3.32)$$

$$S_{crit} = \frac{0.1}{a}\sqrt{\frac{m_0}{m_2}} \tag{3.33}$$

with:

- W_{dry}: total applied load on the asperities (N)
- cf_{dry}: Coulomb friction coefficient, determined from experiments
- S_{crit}: critical slide-to-roll ratio
- $\Delta U = U_1 - U_2$: sliding velocity (m/s)
- $U = U_1 + U_2$: rolling velocity (m/s)
- E': equivalent Young's modulus (Pa)
- m_0: average square value of the height of roughness (corresponds to rms²) (m²)
- m_2: average square value of the slope of roughness profile
- a: half width of contact (m)

Fluid friction shear stress τ_{fluid}:

$$\tau_{fluide} = \tau_L \cdot \sinh^{-1}\left(\frac{\tau_N}{\tau_L}\right) \tag{3.34}$$

$$\tau_N = \eta\left(p_{moy}, T_{fluide}\right)\frac{\Delta U}{\phi_T \cdot h_c} \tag{3.35}$$

$$\tau_L = C_0 \cdot \exp\left(C_p \cdot p_{moy}\right) \cdot \exp\left(C_t\left(\frac{1}{T_{fluide}} - \frac{1}{T_0}\right)\right) \tag{3.36}$$

with:

- τ_N: shear stress assuming a Newtonian fluid lubrication (Pa)
- τ_L: limiting shear stress (Pa)
- $\eta(p_{moy}, T_{fluide})$: viscosity depending on pressure and temperature (Pa.s)
- C_0: limiting shear stress parameter for ambient pressure and reference temperature (Pa)
- C_p: limiting shear stress parameter for pressure (Pa^{-1})
- C_t: limiting shear stress parameter for temperature (K^{-1})
- T_{fluide}, T_0: fluid and reference temperatures (K)

{c} Xu formula

Reference [45]

$$\mu = e^{f(SR, P_h, \eta_{oil}, Ra)}\, {P_h}^{b_2}\, |SR|^{b_3}\, {V_e}^{b_6}\, {\eta_{oil}}^{b_7} R^{b_8} \tag{3.37}$$

$$with \qquad f = b_1 + b_4\, |SR|\, P_h \log_{10}(\eta_{oil}) + b_5\, e^{-|SR|\, P_h \log_{10}(\eta_{oil})} + b_9\, e^{Ra} \tag{3.38}$$

with:

- SR: slide-to-Roll Ratio
- P_h: maximum Hertzian pressure (GPa)
- η_{oil}: dynamic viscosity at oil inlet under ambient pressure (Pa.s)
- Ra: surface roughness (µm)
- V_e: entrainment velocity (m/s)
- R: effective radius of curvature (m)
- b_i: coefficients of EHL-based formula, see Table 0.3

Table 0.3: Coefficients of EHL-based formula

b1	-8.916465
b2	1.03303
b3	1.036077
b4	-0.354068
b5	2.812084

b6	-0.100601
b7	0.752755
b8	-0.390958
b9	0.620305

$$P_h = \sqrt{\frac{W' E'}{2\,\pi\, R}} \times 10^{-9} \tag{3.39}$$

$$\frac{1}{E'} = \frac{1}{2}\left(\frac{1-{\nu_1}^2}{E_1} + \frac{1-{\nu_2}^2}{E_2}\right) \tag{3.40}$$

with:

- W': load per length (N/m)
- E' : effective modulus of elasticity (Pa)
- $E_{1,2}$: modulus of elasticity of respectively pinion and gear (Pa)
- $\nu_{1,2}$: Poisson's ratio of respectively pinion and gear (-)

$$V_e = \frac{U_1 + U_2}{2} \tag{3.41}$$

$$SR = 2\frac{V_s}{V_r} = 2\frac{U_1 - U_2}{U_1 + U_2} \tag{3.42}$$

with:

- $U_{1,2}$: surface velocity of respectively pinion and gear (m/s)

$$R = \frac{R_1\, R_2}{R_1 + R_2} \tag{3.43}$$

with:

- $R_{1,2}$: radius of curvature of respectively pinion and gear (m)

Annex 4.A: Heat dissipation through the housing

Reference: ISO/TR 14179-2 [9]

The heat flow dissipated through the housing is:

$$Q = U\, A_{ca}\, (T_{oil} - T_{air}) \tag{4.22}$$

with:

- Q: heat flow across housing surface (W)
- U: overall heat transmission coefficient (W/(m²K))
- A_{ca}: external housing surface (m²)
- T_{oil}: oil temperature (K)
- T_{air}: ambient air temperature (K)

$$\frac{1}{U} = \frac{1}{\alpha_{oil}}\frac{A_{ca}}{A_{oil}} + \frac{\delta_{wall}}{\lambda_{wall}}\frac{A_{ca}}{A_{oil}} + \frac{1}{\alpha_{ca}} \tag{4.23}$$

with:

- α_{oil}: oil-side heat transfer coefficient (W/(m²K))
  Reference value: $\alpha_{oil} = 200$ W/(m²K)
- α_{ca}: air-side heat transfer coefficient (W/(m²K))
- A_{oil}: internal housing area (m²)
- δ_{wall}: mean housing wall thickness (m)
- λ_{wall}: thermal conductivity of housing (W/(m.K)

The ISO technical report recommends as a rule to determine the heat dissipation via the housing by the larger value air-side thermal resistance at the housing surface. The first two terms in the above equation can then be neglected. For high air velocities and thus good external heat transfer, it will possibly be necessary to take into account the oil-side heat transfer as well. The heat conduction through the housing should only be taken into account in special cases (double-walled housings, housings with sound insulation, non-metallic housings...).

The air-side heat transmission α_{ca} is composed of:

$$\alpha_{ca} = \alpha_{conv} + \alpha_{rad} \tag{4.24}$$

with:

- α_{conv}: convection heat transfer coefficient (W/(m²K))
- α_{rad}: radiation heat transfer coefficient (W/(m²K))

$$\alpha_{rad} = 0.23 \times 10^{-6}\, \varepsilon \left(\frac{T_{wall} + T_{air}}{2}\right)^3 \tag{4.25}$$

$$\alpha_{conv} = \alpha_{K,free}\left(1 - \frac{A_{air}}{A_{ca}}\right) + \alpha_{K,forced}\frac{A_{air}}{A_{ca}}\,\eta^* \tag{4.26}$$

with:

- ε: housing emission ratio
- T_{wall}: housing wall temperature (K)
- $\alpha_{K,free}$: heat transfer coefficient due to free convection (W/(m²K))
- $\alpha_{K,forced}$: heat transfer coefficient due to forced convection (W/(m²K))
- A_{air}: ventilated housing area (m²)
- η^*: temperature ratio

$$\eta^* = \frac{T_{wall} - T_{flow}}{T_{wall} - T_{air}} \tag{4.27}$$

with:

- T_{flow}: cooling air temperature (K)

Here, only housings without thermal finning are considered. For free convection ($v_{air} < 1.5$ m/s):

$$\alpha_{K,free} = 18\ {h_{ca}}^{-0.1} \left(\frac{T_{wall} - T_{air}}{T_{air}}\right)^{0.3} \tag{4.28}$$

For forced convection ($v_{air} > 1.5$ m/s):

$$\alpha_{K,forced} = \frac{0.0086\ (Re')^{0.64}}{l_x} \tag{4.29}$$

with:

- h_{ca}: overall height of housing (m)
- l_x: flow length (m)

$$Re' = \sqrt{Re^2 + \frac{Gr}{2.5}} \tag{4.30}$$

$$Re = \frac{v_{flow}\ l_x}{v_{ref}} \tag{4.31}$$

$$Gr = \frac{g\ {h_{ca}}^2\ (T_{wall} - T_{air})}{T_{air}\ {v_{flow}}^2} \tag{4.32}$$

with:

- Re: Reynold's number
- Gr: Grashoff number
- v_{flow}: cooling air flow velocity (m/s)
- v_{ref}: impingement velocity ($= 15.6 \times 10^{-6}$m²/s)
- g: standard gravity (=9.81 m/s²)

Annex 4.B: Thermal network method

Reference [34], [62]

Thermal network method is detailed here for a mechanical transmission application.

{a} Method principle

The thermal network method uses a conceptual view-point for Fourier's law of heat transfer [63]. A transposition can be done between an electric circuit and a thermal network, according to Table 0.4.

Table 0.4: Analogy from an electric circuit to a thermal network

Electric circuit		
Potential difference	ΔU	(V)
Electrical resistance	R	(Ω)
Current	I	(A)

Thermal network		
Temperature difference	ΔT	(K)
Thermal resistance	R_{th}	(K/W)
Heat flow	Q	(W)

Like Ohm's law for electric circuit, the Fourier equation then becomes:

$$\Delta T = R_{th} \times Q \tag{4.33}$$

This analogy is helpful to solve network problems. Indeed, the relationships for series and parallel thermal resistances are also valid:

$$R_{series} = R_1 + R_2 \tag{4.34}$$

$$\frac{1}{R_{parallel}} = \frac{1}{R_1} + \frac{1}{R_2} \tag{4.35}$$

where R_{series} and $R_{parallel}$ are the equivalent resistances respectively for series resistances and for parallel resistances.

The network is composed of nodes linked by thermal resistances. Each node is isothermal and represents an element of the modelled system. The heat generated by dissipation sources is injected in the network at the corresponding node.

According to the first law of thermodynamics, the total energy of an isolated system is constant. The internal energy of an element of the system then varies due to its own power dissipation and to heat exchanges with other elements of the system:

$$M_i \, c_i \, \frac{dT_i}{dt} = Q_i + \sum_{j=1 \; and \; j \neq i}^{nb} \frac{T_j - T_i}{R_{th}(i,j)} \tag{4.36}$$

with:

- M_i: mass of element i (kg)
- c_i: specific heat (J/kg.K)
- T_i, T_j: temperature of element i or j (K)

- t: time (s)
- Q_i: heat flow injected at node i (W)
- $R_{th}(i,j)$: thermal resistance between elements i and j (K/W)
- nb: number of thermal network nodes

It is noteworthy that the heat sink of the system (generally ambient air) is a particular element. If its temperature is imposed and constant, it is necessary to define its thermal inertia as infinite: $M_i\ c_i = 10^{30}$ J/K for example. Moreover, as all the heat evacuates through this element, its Q_i will be negative.

This system of differential equations can be solved numerically thanks to Runge-Kutta or Adams methods [34].

In case of steady state conditions, Equation (4.36) simplifies to:

$$Q_i = \sum_{j=1\ and\ j\neq i}^{nb} \frac{T_i - T_j}{R_{th}(i,j)} \tag{4.37}$$

{b} Definition of thermal resistances

Various thermal exchanges can happen inside a mechanical transmission. Thus, different kinds of thermal resistances are defined to manage the heat flows between the nodes:

- Convection and radiation with ambient air
- Convection with oil
- Conduction
- Striction

1) Convection and radiation with ambient air

Thermal exchange between housing and ambient air occurs through convection and radiation. The corresponding thermal resistances are then parallel. Depending on the existence of an air flow around the housing, the convection is forced or free.

The housing is decomposed in a set of flat plates to take into account the different air flows around it. For each plate, the characteristic dimension is then plate length or height, depending on its orientation. To consider this assembly, a global thermal resistance is calculated for each type of thermal exchange (convection and radiation):

$$R_{th\ housing} = \frac{1}{\sum h_i\ A_i} \tag{4.38}$$

with:

- h_i: heat transmission coefficient of plate i (W/(m²K))
- A_i: surface of plate i (m²)

❖ **Radiation:**

The radiation coefficient is determined from the Stefan-Boltzmann law [63]:

$$h_{rad} = \epsilon\, \sigma \left({T_{ca}}^2 + {T_{air}}^2\right)(T_{ca} + T_{air}) \tag{4.39}$$

with:

- ϵ: material emissivity (some values are given in Table 0.5)
- σ: Stefan-Boltzmann constant (5.67×10^{-8} W/(m²K⁴))
- T_{ca}: housing temperature (K)
- T_{air}: ambient air temperature (K)

Table 0.5: Emissivity properties of some materials

Material	State	Emissivity
Steel	Polished	0.066
	Oxydised	0.8
Iron	Polished	0.14-0.38
	Oxydised	0.61
Cast iron	Polished	0.21
	Oxydised	0.64
	Casing	0.81
Aluminum	Polished	0.09
	Oxydised	0.20-0.31

❖ **Free convection:**

Free convection happens when ambient air around the housing is static. The free convection coefficient is defined after the formulae proposed by Winter et al. [68]. The thermal exchange with air depends on the orientation of the surface, as heat dissipation is not the same depending on surface inclination.

Thus, for vertical surfaces, it is:

$$h_{conv} = 11.06 \cdot L^{-0.1} \cdot \left[\frac{T_{ca} - T_{air}}{T_{air}}\right]^{0.3} \tag{4.40}$$

For top horizontal surfaces:

$$h_{conv} = 12.87 \cdot L^{-0.04} \cdot \left[\frac{T_{ca} - T_{air}}{T_{air}}\right]^{0.32} \tag{4.41}$$

For bottom horizontal surfaces:

$$h_{conv} = 1.86 \cdot L^{-0.4} \cdot \left[\frac{T_{ca} - T_{air}}{T_{air}}\right]^{0.2} \tag{4.42}$$

with:

- L: characteristic length (m)
- T_{ca}: housing temperature (K)
- T_{air}: ambient air temperature (K)

❖ **Forced convection:**

Forced convection is due to an air flow occurring around the housing. The forced convection coefficient is also defined according to formulae of Winter et al. [64]. For this thermal exchange, the distinction is made between surfaces normal and tangential to the air flow.

For surfaces normal to the flow:

$$h_{conv} = 5.6 \cdot L^{-0.34} \cdot V^{0.66} \tag{4.43}$$

For surfaces tangential to the flow:

$$h_{conv} = 7.6 \cdot L^{-0.37} \cdot V^{0.63} \tag{4.44}$$

with:

- L: characteristic length (m)
- V: air flow velocity (m/s)

For the particular case of forced convection with a surface normal to the flow, the characteristic length is: $L = {}^{A}/_{P}$ with A the normal surface area (m²) and P its perimeter (m).

2) Convection with oil

A dip lubricated transmission is considered here. Convection then occurs between oil and different parts of the system: housing, gears, rolling element bearings… If gears are running, which is generally the case, convection with oil is forced. Otherwise convection is free.

Air is considered as inviscid, but oil is a viscous fluid. The same approximation cannot be done and fluid mechanics characteristics should be taken into account. Thus for convection with the oil, Holman [63] defines the different heat transfers with:

$$h_{oil} = \frac{Nu\ k}{L} \tag{4.45}$$

with:

- Nu: Nusselt number
- k: lubricant thermal conductivity (W/m.K)
- L: characteristic dimension (m)

Nusselt number is linked to Reynolds number Re for forced convection or Grashof number Gr for free convection and to Prandtl number Pr. Formulae are detailed for each particular heat exchange in the following parts.

$$Gr = \frac{g\ \beta\ \Delta T\ L^3}{\nu^2} \tag{4.46}$$

$$Pr = \frac{\mu\ c}{k} \tag{4.47}$$

$$Re = \frac{V\ L}{\nu} \tag{4.48}$$

with:

- g: standard gravity (=9.81 m/s²)
- β: volume coefficient of expansion (/K)
  (=0.0007 for oil; equal to the inverse of fluid temperature for an ideal gas)
- ΔT: temperature difference between wall and fluid (K)
- L: characteristic dimension (m)
- ν: fluid kinematic viscosity (m²/s)
- μ: fluid dynamic viscosity (Pa.s)
- c: specific heat (J/kg.K)
- k: lubricant thermal conductivity (W/m.K)
- V: flow velocity (m/s)

❖ **Convection with housing:**

The housing is still considered as an assembly of flat plate. A global thermal resistance is again calculated according to Equation (4.38). For each plate, the characteristic dimension is also plate length or height, depending on its orientation.

Free oil convection inside the oil bath is due to density variations that induce oil motion. This also depends on surface orientation. For horizontal surfaces, Nusselt number is defined as:

$$if\ (Gr\ Pr) < 8 \cdot 10^6, \qquad Nu = 0.54\ (Gr\ Pr)^{0.25} \tag{4.49}$$

$$else\quad Nu = 0.15\ (Gr \cdot Pr)^{1/3} \tag{4.50}$$

For vertical surfaces:

$$if\ (Gr\ Pr) < 1 \cdot 10^9, \qquad Nu = 0.59\ (Gr\ Pr)^{0.25} \tag{4.51}$$

$$else\quad Nu = 0.1\ (Gr \cdot Pr)^{1/3} \tag{4.52}$$

For forced convection inside the oil bath, a flow is generated by running gears. Nusselt number is then:

$$if\ Re < 5 \cdot 10^5, \qquad Nu = 0.664\ \sqrt{Re}\ \ Pr^{1/3} \tag{4.53}$$

$$else\quad Nu = \ Pr^{1/3}\ (0.037\ (Re^{0.8}) - 850) \tag{4.54}$$

For Reynolds calculation, the fluid velocity to take into account is due to running gears:

$$V = \Omega\ R_p \tag{4.55}$$

with:

- Ω: gear rotational speed (rad/s)
- R_p: gear pitch radius (m)

Oil is also projected on housing wall due to gears rotation. For this oil trickling along non-immersed surfaces, the oil displacement is due to gravity. A mean velocity of the fluid film is then defined:

$$V = 2.95\sqrt{L} \tag{4.56}$$

❖ **Convection with rolling element bearings:**

As rolling element bearings are partially immersed in oil bath, convection with oil must be considered. Rolling element bearings are treated in the same manner as the housing for the heat transmission coefficient calculation: free oil convection when system is at rest, forced oil convection and oil trickling when system is rotating. The characteristic dimension considered is bearing radius. Thermal resistance of convection with oil is then:

$$R_{oil} = \frac{1}{h\,A} \tag{4.57}$$

with A the surface of transfer (m²), which is the bearing immersed surface for convection with oil bath or the non-immersed surface for oil trickling.

❖ **Convection with gears:**

When the system is stopped, free convection occurs between oil and gear immersed surface. This thermal exchange follows the same rules as for the housing in Equations (4.51) and (4.52). The characteristic dimension to be used is the gear immersion depth.

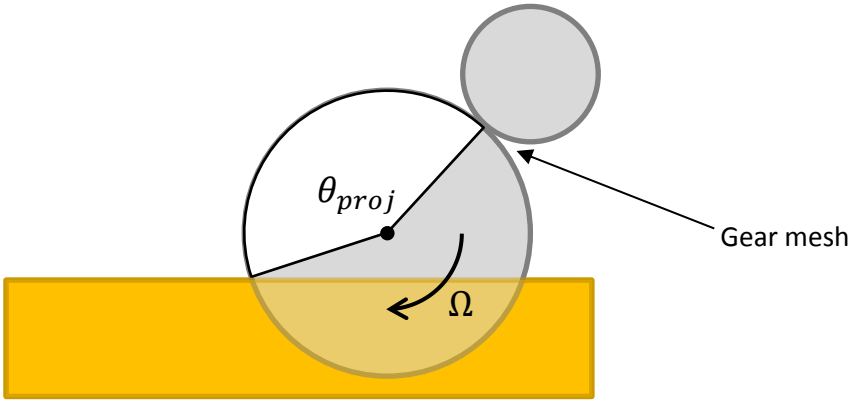

Figure 22: Definition of centrifugal projection angle

When gears are rotating, forced convection with oil takes place in a particular way: centrifugal projection of oil along gear teeth flanks evacuates the major amount of heat. Convection with oil bath can be also considered, but this contributes a few.

Oil projection is notably characterised by the angle of rotation where the gear projects oil. For dip lubricated gears, this angle θ_{proj} begins at gear teeth emergence from oil and ends at gear mesh point, as illustrated on Figure 22. Projection duration is also important and is defined as: t= θ_{proj}/Ω .

Blok [65] defines an evacuated heat quantity for a tooth face per width unit. This energy can be deduced from Figure 23, depending on a dimensionless number Ψ, defined as:

$$\Psi = \left(\frac{R_p \, a \, {\theta_{proj}}^2}{\nu_{lub} \, H_{tooth}} \right)^{1/4} \tag{4.58}$$

with:

- R_p: gear pitch radius (m)
- a: thermal diffusivity of oil (m²/s)
- θ_{proj}: angle of centrifugal projection (rad)
- ν_{lub}: kinematic viscosity of oil (m²/s)
- H_{tooth}: tooth height (m)

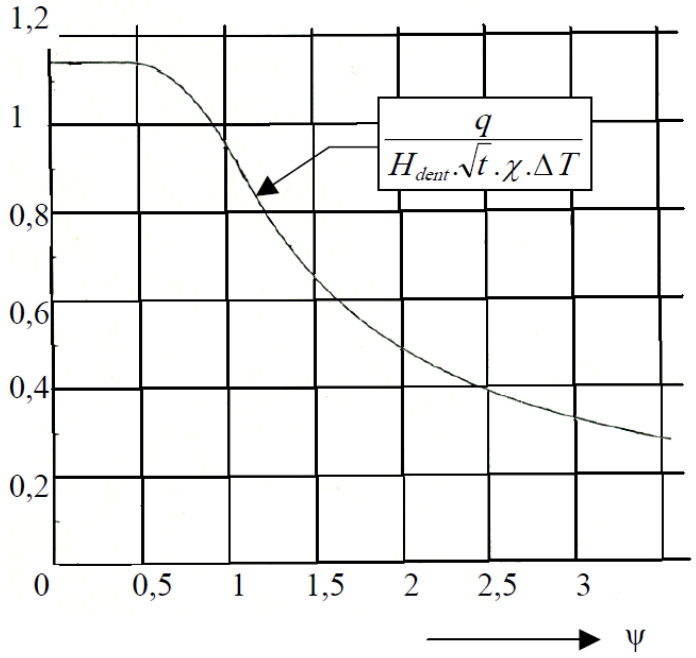

Figure 23: Evolution of evacuated heat quantity [65]

For the complete gear, a global heat quantity is then defined as:

$$Q = \frac{q \, b_{tooth} \times 2 \, Z}{2 \, \pi / \Omega} \tag{4.59}$$

with:

- q: Evacuated heat quantity for a tooth face per width unit (W)
- b_{tooth}: tooth width (m)
- Z: gear teeth number
- Ω: gear rotational speed (rad/s)

As $Q = \Delta T / R_{proj}$, an approximation of the curve presented on Figure 23 can be done to obtain directly a thermal resistance:

$$if\ \Psi < 0.68 \qquad R_{proj} = \frac{2\,\pi}{1.14\,b_{tooth} \times 2\,Z\,H_{tooth}\sqrt{\Omega\,\theta_{proj}}\,\chi} \tag{4.60}$$

$$if\ 0.68 < \Psi < 1.5 \qquad R_{proj} = \frac{2\,\pi}{(1.55 - 0.6\,\Psi) b_{tooth} \times 2\,Z\,H_{tooth}\sqrt{\Omega\,\theta_{proj}}\,\chi} \tag{4.61}$$

with:

- χ: thermal effusivity of oil ($\chi = \sqrt{k\,\rho\,c}$ N/m.s$^{1/2}$.°C)
- ΔT: temperature difference between pinion and oil (K)

3) Conduction

Conduction happens inside elements when a temperature gradient exists. This mainly depends on element geometry.

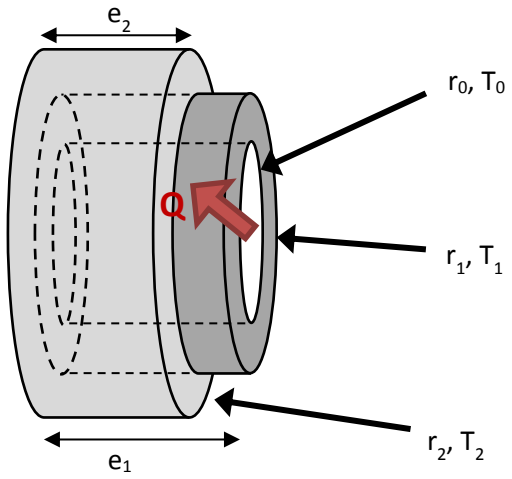

Figure 24: Heat conduction through a cylindrical solid with various widths

❖ **Radial conduction:**

Radial conduction occurs through cylindrical solids: for example, gears and rolling element bearings. Heat conduction through a solid with several widths is illustrated on Figure 24 and the corresponding thermal resistance is expressed as:

$$R_{radial} = \sum_{i=1}^{2} \frac{\ln\left(\frac{r_i}{r_{i-1}}\right)}{2\,\pi\,k\,e_i} \tag{4.62}$$

with:

- r_i: radius of cylinder i (m)
- k: material thermal conductivity (W/m.K)
- e_i: width of cylinder i (m)

❖ **Axial conduction:**

Axial conduction occurs through solids of constant section: for example, housing. Heat conduction through a solid constituted of blocks with different conductivities is illustrated on Figure 25 and the corresponding thermal resistance is expressed as:

$$R_{axial} = \sum_i \frac{e_i}{k_i A_d} \tag{4.63}$$

with:

- e_i: width of block i (m)
- k_i: material thermal conductivity (W/m.K)
- A_d: block section (m²)

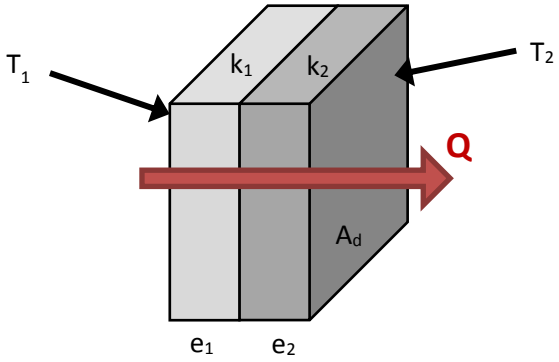

Figure 25: Heat conduction between two blocks

❖ **Contact conduction:**

Contact conduction occurs between solids in contacts at different temperatures: for example, between drive head housing and the remaining housing, as they are bolted together.

This is a complex type of conduction due to notably to surface roughness. For a metal-metal contact with air in between, thermal resistance is expressed as:

$$R_{contact} = \frac{x}{\bar{k} A} \tag{4.64}$$

with:

- x: contact width depending on pressure (m)
  varies from 3.10^{-3} to 6.10^{-3}m for metal-metal contact
- $\bar{k}$: equivalent thermal conductivity (W/m.K)
  Calculated according to conductivities of contacting material: $\bar{k} = 2\frac{k_1 k_2}{k_1 + k_2}$
- A: apparent contact area (m²)

4) Striction

Striction controls the exchange between gears and their meshing point.

During meshing, the contact temperature increases a lot. However, the heat produced does not propagate deeply in gear tooth due to small contact zone and short contact duration. This has to be compared with gear size and time until the next meshing, which are really bigger. Gear bulk temperature is then not much influenced.

A distinction is thus made between gear pair and its meshing zone. Each gear has its own bulk temperature. Meshing zone is at "flash-temperature", as defined by Blok [65]. The thermal exchanges between meshing zone and each gear is driven by the thermal resistance defined as:

$$R_{striction} = \frac{0.767}{\sqrt{2\ b_c}\ b_{tooth}\ \chi\ \sqrt{V_{r\,i}}} \tag{4.65}$$

with:

- $2\ b_c$: width of squeezing surface (m)
- b_{tooth}: tooth width or mean contact length if several teeth mesh simultaneously (m)
- χ: thermal effusivity of material ($\chi = \sqrt{k\ \rho\ c}$ N/m.s$^{1/2}$.°C)
- $V_{r\,i}$: mean surface velocity of gear i (m/s)

The half-width of contact l_h is calculated according to data obtained with Barday software.

References

[1] European Commission, “Reducing CO2 emissions from Heavy-Duty Vehicles.” [Online]. Available: https://ec.europa.eu/clima/policies/transport/vehicles/heavy_en. [Accessed: 11-Dec-2017].

[2] A. S. Kolekar, A. V. Olver, A. E. Sworski, and F. E. Lockwood, “The efficiency of a hypoid axle - a thermally coupled lubrication model,” *Tribology International*, vol. 59, pp. 203–209, 2013.

[3] H. Xu, A. Singh, D. Maddock, A. Kahraman, and J. Hurley, “Thermal Mapping of an Automotive Rear Drive Axle,” *SAE International Journal of Engines*, vol. 4, no. 1, pp. 888–901, 2011.

[4] D. E. Hobson, “Axle Efficiency - Test Procedures and Results,” *SAE Technical Paper*, no. 790744, 16p., 1979.

[5] H. Winter and L. Wech, “Measurements and Optimization of the Efficiency of Hypoid Axle Drives of Vehicles,” *SAE Technical Paper*, no. 885127, 10p., 1988.

[6] H. Xu, A. Singh, A. Kahraman, J. Hurley, and S. Shon, “Effects of Bearing Preload, Oil Volume, and Operating Temperature on Axle Power Losses,” *Journal of Mechanical Design*, vol. 134, no. 5, pp. 54501–54508, 2012.

[7] I. Kakavas, A. V. Olver, and D. Dini, “Hypoid gear vehicle axle efficiency,” *Tribology International*, vol. 101, pp. 314–323, 2016.

[8] Simrit, *Radialwellendichtringe, Katalog Nr. 100*. 1976.

[9] “Gears - Thermal capacity Part 2 : Thermal load-carrying capacity,” *ISO/TR 14179-2*, 2001.

[10] H. Linke, *Stirnradverzahnung*. Hanser Verlag, 1996.

[11] J. Kettler, “Planetengetriebe-Sumpftemperatur,” *FVA-Forschungsvorhaben Nr. 313, Heft 639, Forschungsbericht*, 2002.

[12] T. A. Harris, *Rolling bearing analysis*. John Wiley and sons, 2001.

[13] SKF Group, *General Catalogue 6000/I EN*. 2008.

[14] “Gears - Thermal capacity Part 1 : Rating gear drives with thermal equilibrium at 95°C sump temperature,” *ISO/TR 14179-1*, 2001.

[15] S. Jeon, “Improving Efficiency in Drive Lines: an Experimental Study on Churning Losses in Hypoid Axle,” PhD Thesis, Imperial College London, 230p., 2010.

[16] E. Buckingham, *Analytical Mechanics of Gears*. McGraw-Hill, 530p., 1949.

[17] W. Coleman, “Effect of mounting displacements on bevel and hypoid gear tooth strength,”

SAE Technical Paper, no. 750151, 16p., 1975.

[18] M. Mohammadpour, S. Theodossiades, H. Rahnejat, and P. Kelly, “Transmission efficiency and noise, vibration and harshness refinement of differential hypoid gear pairs,” *Proceedings of the IMechE, Part K: Journal of Multi-body Dynamics*, vol. 228, no. 1, pp. 19–33, 2014.

[19] J. Hurley, “An Experimental Investigation of Thermal Behavior of an Automotive Rear Axle,” MS Thesis, The Ohio State University, 106p., 2009.

[20] R. F. Handschuh, “Thermal behaviour of spiral bevel gears,” PhD Thesis, Case Western Reserve University, 286p., 1993.

[21] Y. Wang, W. Tang, Y. Chen, T. Wang, G. Li, and A. D. Ball, “Investigation into the meshing friction heat generation and transient thermal characteristics of spiral bevel gears,” *Applied Thermal Engineering*, vol. 119, pp. 245–253, 2017.

[22] D. Barday, “Meshing of Bevel and Hypoid Gear Sets,” in *4th world congress on gearing*, 1999.

[23] H. Xu, A. Kahraman, and D. R. Houser, “A Model to Predict Friction Losses of Hypoid Gears,” *AGMA Technical Paper*, pp. 1–15, 2005.

[24] M. Kolivand, S. Li, and A. Kahraman, “Prediction of mechanical gear mesh efficiency of hypoid gear pairs,” *Mechanism and Machine Theory*, vol. 45, no. 11, pp. 1568–1582, 2010.

[25] G. H. Benedict and B. W. Kelley, “Instantaneous Coefficients of Gear Tooth Friction,” *Tribology Transactions*, vol. 4, no. 1, pp. 59–70, 1961.

[26] Y. Diab, F. Ville, and P. Velex, “Prediction of Power Losses Due to Tooth Friction in Gears,” *Tribology Transactions*, vol. 49, no. 2, pp. 260–270, 2006.

[27] H. Xu, “Development of a Generalized Mechanical Efficiency Prediction Methodology for Gear Pairs,” PhD Thesis, The Ohio State University, 233p., 2005.

[28] R. Chittenden, D. Dowson, J. Dunn, and C. Taylor, “A Theoretical Analysis of The Isothermal Elastohydrodynamic Lubrication of Concentrated Contacts II General Case, with Lubricant Entrainment along either Principal Axis of the Hertzian Contact Ellipse or at some Intermediate Angle,” *Proceedings of the Royal Society of London*, vol. 397 A, pp. 271–294, 1985.

[29] M. Omasta, I. Křupka, and M. Hartl, “Effect of surface velocity directions on elastohydrodynamic film shape,” *Tribology Transactions*, vol. 56, no. 2, pp. 301–309, 2013.

[30] K. Stahl, K. Michaelis, J. Mayer, A. Weigl, T. Lohner, M. Omasta, M. Hartl, and I. Krupka, “Theoretical and Experimental investigations on EHL point contacts with different entrainment velocity directions,” *Tribology Transactions*, vol. 56, pp. 728–738, 2013.

[31] W. Pu, J. Wang, Y. Zhang, and D. Zhu, “A Theoretical Analysis of the Mixed Elastohydrodynamic Lubrication in Elliptical Contacts With an Arbitrary Entrainment Angle,” *Journal of Tribology*, vol. 136, no. 4, p. 41505, 2014.

[32] M. Carli, K. J. Sharif, E. Ciulli, H. P. Evans, and R. W. Snidle, “Thermal point contact EHL analysis of rolling/sliding contacts with experimental comparison showing anomalous film shapes,” *Tribology International*, vol. 42, no. 4, pp. 517–525, 2009.

[33] T. Doki-thonon, “Thermal effects in elastohydrodynamic spinning circular contacts,” PhD Thesis, INSA Lyon, 133 p., 2012.

[34] C. Changenet, “Modélisation du comportement thermique des transmissions par engrenages,” PhD Thesis, INSA Lyon, 167p., 2006.

[35] “Calculation of scuffing load capacity of cylindrical, bevel and hypoid gears - Part 2: Integral temperature method,” *ISO/TR 13989-2*, 2000.

[36] J.-B. Boni, A. Neurouth, C. Changenet, and F. Ville, “Experimental investigations on churning power losses generated in a planetary gear set,” *Journal of Advanced Mechanical Design, Systems, and Manufacturing*, vol. 11, no. 6, pp. 1–12, 2017.

[37] K. Takaki, M. Sugimoto, and A. Hayata, “Optimization of Hypoid Gear Design for High Efficiency Drives,” *International Conference on Gears - VDI-Berichte*, vol. 2255, 2015.

[38] B.-R. Höhn, K. Michaelis, and T. Vollmer, *Thermal rating of gear drives: balance between power loss and heat dissipation*. American Gear Manufacturers Association, 1996.

[39] J. W. Daily and R. E. Nece, “Chamber Dimension Effects on Induced Flow and Frictional Resistance of Enclosed Rotating Disks,” *Journal of Basic Engineering*, vol. 82, no. 1, pp. 217–230, Mar. 1960.

[40] P. Luke and A. V. Olver, “A study of churning losses in dip-lubricated spur gear,” *Proceedings of the Institution of Mechanical Engineers, Part G: Journal of Aerospace Engineering*, vol. 213, pp. 337–346, 1999.

[41] C. Changenet, G. Leprince, F. Ville, and P. Velex, “A Note on Flow Regimes and Churning Loss Modeling,” *Journal of Mechanical Design*, vol. 133, no. 12, pp. 1210091–1210095, 2011.

[42] C. Changenet and P. Velex, “Housing Influence on Churning Losses in Geared Transmissions,” *Journal of Mechanical Design*, vol. 130, pp. 0626031–0626036, 2008.

[43] C. Changenet and P. Velex, “A Model for the Prediction of Churning Losses in Geared Transmissions—Preliminary Results,” *Journal of Mechanical Design*, vol. 129, no. 1, pp. 128–133, 2007.

[44] P. Velex and F. Ville, “An Analytical Approach to Tooth Friction Losses in Spur and Helical Gears—Influence of Profile Modifications,” *Journal of Mechanical Design*, vol. 131, no. 10, p. 101008, 2009.

[45] H. Xu and A. Kahraman, “Prediction of friction-related power losses of hypoid gear pairs,” *Proceedings of the Institution of Mechanical Engineers, Part K: Journal of Multi-body Dynamics*, vol. 221, no. 3, pp. 387–400, 2007.

[46] R. F. Handschuh, “Effect of Lubricant Jet Location on Spiral Bevel Gear Operating Temperatures,” *NASA TM-105656, AVSCOM TR 91-C-033*, 1992.

[47] C. Fossier, C. Changenet, F. Ville, D. Barday, and V. Berier, “Investigations on drive axle thermal behaviour: power loss and heat-transfer estimations,” *accepted for publication in SAE International Journal of Engines*.

[48] S. Laruelle, C. Fossier, C. Changenet, F. Ville, and S. Koechlin, “Experimental investigations and analysis on churning losses of splash lubricated spiral bevel gears,” *Mechanics & Industry*, vol.

18, no. 4, pp. 41201–41210, 2017.

[49] T. Misic, M. Najdanovic-Lukic, and L. Nesic, “Dimensional analysis in physics and the Buckingham theorem,” *European Journal of Physics*, vol. 31, no. 4, 893p., 2010.

[50] B.-R. Höhn, K. Stahl, and C. Wirth, “New methods for the calculation of the load capacity of bevel and hypoid gears,” 2011.

[51] M. Kolivand, “Development of Tooth Contact and Mechanical Efficiency Models for Face-Milled and Face-Hobbed Hypoid and Spiral Bevel Gears,” PhD Thesis, The Ohio State University, 190p., 2009.

[52] Y. Chen, A. Yamamoto, and K. Omori, “Improvement of Contact Fatigue Strength of Gears by Tooth surface Modification Processing,” in *12th IFToMM Wolrd Congress*, 2007.

[53] I. Karagiannis, S. Theodossiades, and H. Rahnejat, “On the dynamics of lubricated hypoid gears,” *Mechanism and Machine Theory*, vol. 48, pp. 94–120, 2012.

[54] M. Mohammadpour, S. Theodossiades, and H. Rahnejat, “Elastohydrodynamic lubrication of hypoid gear pairs at high loads,” *Proceedings of the Institution of Mechanical Engineers, Part J: Journal of Engineering Tribology*, vol. 226, no. 3, pp. 183–198, 2012.

[55] J. Astoul, E. Mermoz, M. Sartor, J. M. Linares, and A. Bernard, “New methodology to reduce the transmission error of the spiral bevel gears,” *CIRP Annals - Manufacturing Technology*, vol. 63, pp. 165–168, 2014.

[56] A. Bahramighahnavieh, P. Mosaddegh, and S. Akbarzadeh, “Investigation of the Hertzian Stress Distribution on the Surface of the Straight Bevel Gear,” *Applied Mechanics and Materials*, vol. 307, pp. 304–307, 2013.

[57] D. Barday, “Noise optimization of a rear axle gear set,” in *Internoise*, 2000.

[58] R. Stribeck, “Die wesentlichen Eigenschaften der Gleit- und Rollenlager,” *VDI-Zeitschrift*, vol. 46, pp. 1341–48, 1432–38, 1463–70, 1902.

[59] C. Fossier, C. Changenet, F. Ville, D. Barday, and V. Berier, “Investigations on truck axle efficiency: thermal behaviour and hypoid gears parameters influence,” in *43nd Leeds-Lyon Symposium on Tribology, Leeds*, 2016.

[60] H. J. Stadtfeld, “Less Energy Consumption with High-Efficiency Bevel Gears and their Usage in the U.S.,” *Gear Technology*, no. October, pp. 42–49, 2014.

[61] J. Bendzulla, B. Bouché, and R. Thiele, “New analysis on the heat balance of industrial gearboxes - Optimized calculation-method of a gearbox manufacturer,” *International Conference on Gears - VDI-Berichte*, vol. 2255.2, pp. 859–869, 2015.

[62] C. Changenet, X. Oviedo-Marlot, and P. Velex, “Power Loss Predictions in Geared Transmissions Using Thermal Networks-Applications to a Six-Speed Manual Gearbox,” *Journal of Mechanical Design*, vol. 128, no. 3, pp. 618–625, 2006.

[63] J. P. Holman, *Heat transfer*, 10th ed. New York: Mac Graw - Hill Book company, 2010.

[64] H. Winter, K. Michaelis, and G. Funck, “Wärmeabführung bei Getrieben unter Quasistationären Betriebsbedingungen. Teil II : Untersuchungen zur Wärmeabführung über

Stahlfundamente und Übertragung der Prüfstandsergebnisse auf die Praxis," *Antriebstechnik*, vol. 26, no. 6, pp. 49–55, 1987.

[65] H. Blok, "Transmission de chaleur par projection centrifuge d'huile," *Société d'Etudes de l'Industrie de l'Engrenage*, vol. 59, pp. 14–23, 1970.

[66] C. Fossier, C. Changenet, F. Ville, D. Barday, and V. Berier, "Thermal behaviour of an Axle Gear Set," in *STLE 71th Annual Meeting & Exhibition, Las Vegas*, 2016.

[67] S. Laruelle, "Study of the thermal behavior of a gear unit," PhD Thesis, Université de Lyon (INSA Lyon), 276p., 2017.

[68] H. Winter, K. Michaelis, and G. Funck, "Wärmeabführung bei Getrieben unter Quasistationären Betriebsbedingungen. Teil I : Systematische Untersuchungen zur Wärmeabführung bei Natürlicher und Erzwungener Zuftströmung mit Hilfe eines Modellprüfstandes," *Antriebstechnik*, vol. 25, no. 12, pp. 36–42, 1986.

[69] Volvo Group, "Internal communication," 2017.

Scientific contributions

Scientific papers

S. Laruelle, C. Fossier, C. Changenet, F. Ville, and S. Koechlin, “Experimental investigations and analysis on churning losses of splash lubricated spiral bevel gears,” *Mechanics & Industry*, vol. 18, no. 4, pp. 412.01–412.10, 2017.

C. Fossier, C. Changenet, F. Ville, D. Barday, and V. Berier: “Investigations on drive axle thermal behaviour: power loss and heat-transfer estimations”, accepted for publication in SAE International Journal of Engines.

Presentations and posters

STLE 70th Annual Meeting & Exhibition (May 17-21, 2015, Dallas)
C. Fossier, F. Ville, C. Changenet, V. Berier, and D. Barday: "Thermal Influence on Friction Losses of an Axle Gear Set". (Poster)

22ème Congrès Français de Mécanique (August 24-28, 2015, Lyon)
C. Fossier, F. Ville, C. Changenet, V. Berier, D. Barday: "Analyse du rendement d’un pont de camion : des paramètres de dentures spiro-conique et hypoïde à l’influence de la thermique". (Oral)

42nd Leeds-Lyon Symposium on Tribology (September 7-9, 2015, Lyon)
C. Fossier, F. Ville, C. Changenet, V. Berier, and D. Barday: "Thermal behaviour of an axle gear set". (Poster)

STLE 71th Annual Meeting & Exhibition (May 15-19, 2016, Las Vegas)
C. Fossier, C. Changenet, F. Ville, D. Barday, and V. Berier: "Thermal Behaviour of an Axle Gear Set". (Oral)

Journées ‘Transmissions Mécaniques’ (July 11-12, 2016, Lyon / Villeurbanne)
C. Fossier, C. Changenet, F. Ville, D. Barday, and V. Berier: "Comportement thermique du couple conique de pont". (Oral)

43nd Leeds-Lyon Symposium on Tribology (September 6-9, 2016, Leeds)
C. Fossier, C. Changenet, F. Ville, D. Barday, and V. Berier: "Investigations on truck axle efficiency: thermal behaviour and hypoid gears parameters influence". (Oral)

FOLIO ADMINISTRATIF

THESE DE L'UNIVERSITE DE LYON OPEREE AU SEIN DE L'INSA LYON

NOM : FOSSIER
(avec précision du nom de jeune fille, le cas échéant)

DATE de SOUTENANCE : 14/03/2018

Prénom : Charlotte

TITRE : Investigations on the efficiency of truck axles and their hypoid gear set: A thermo-mechanical model

NATURE : Doctorat

Numéro d'ordre : 2018LYSEI019

Ecole doctorale : MEGA (Mécanique, Energétique, Génie Civil, Acoustique)

Spécialité : Génie Mécanique

RESUME :
Pour répondre au besoin des clients ainsi qu'aux réglementations gouvernementales, les constructeurs de camions doivent diminuer la consommation et les émissions de leurs véhicules. Une solution-clé est d'améliorer le rendement de la transmission du camion, dont le pont fait partie. Leur design n'a longtemps été optimisé qu'en fonction de critères de durabilité et de bruit.
L'objectif de ce travail est donc de caractériser le rendement des ponts de camion. La dissipation de puissance au sein du pont est causée par l'engrènement, les roulements, les joints et le barbotage. Des méthodes permettent d'estimer globalement ces pertes de puissance, mais elles ne sont pas forcément adaptées aux ponts. En effet, l'élément principal du pont est un engrenage spiro-conique ou hypoïde et son impact est étudié : sa forme influe sur le barbotage, tandis que sa géométrie de denture et sa cinématique gouvernent le frottement à l'engrènement. Il semble ainsi important d'évaluer le frottement de ces couples coniques par une approche locale et d'étudier l'influence des paramètres de denture.
Cependant, les pertes de puissance dépendent de la température, via les propriétés de l'huile. Des expériences montrent un important écart de température entre les composants. Il faut donc considérer des températures locales plutôt qu'une température d'huile globale. Le rendement et la durabilité peuvent être impactés par des points chauds. La méthode des réseaux thermiques permet de modéliser les échanges thermiques du pont ainsi que la distribution de températures. Les tests classiques de rendement mesurent uniquement la perte globale et la température d'huile : rien ne permet de confirmer la répartition des pertes entre sources. Une campagne d'essais avec mesures de température est donc réalisée et valide le modèle pour le calcul des températures locales et pour l'estimation des pertes de chaque composant. Ce modèle peut alors être utilisé lors du design de futurs ponts.

MOTS-CLÉS : pertes de puissance, réseaux thermiques, échanges thermiques, pont, engrenage hypoïde, frottement à l'engrènement

Laboratoires de recherche :
- LaMCoS (INSA-LYON), Laboratoire de Mécanique des Contacts et des Structures
- LabECAM (ECAM LYON), Laboratoire d'Énergétique et des Matériaux de l'ECAM LYON

Directeurs de thèse: Christophe CHANGENET et Fabrice VILLE

Président de jury : à préciser après la soutenance

Composition du jury :
Denis BARDAY; Christophe CHANGENET; Daniele DINI; Agnès FABRE; Jorge SEABRA; Fabrice VILLE